UNIVERSITY OF SOUTHAMPTON

FACULTY OF ENGINEERING, SCIENCE AND MATHEMATICS

School of Chemistry

Enhanced Structural Characterisation of Supported Catalysts

by

Stephen William Thomas Price

Thesis for the degree of Doctor of Philosophy

March 2011

Abstract

Faculty of Engineering, Science and Mathematics

School of Chemistry

Doctor of Philosophy

Enhanced Structural Characterisation of Supported Catalysts

By Stephen William Thomas Price

Complex materials are emerging for use in heterogeneous catalysis and electrocatalysis with order on the atomic scale. One of the central issues for continued growth in this area is the ability to precisely control the size and shape of the nanoparticles, especially for sub 10 nm particles. Understanding the structure of these materials is of key importance in understanding their activity and developing this precise control, with which the exploitation of the key properties of nanoparticles becomes possible.

The body of the work conducted in this thesis aimed to provide more accurate characterisation of the size and shape of carbon supported nanoparticle catalysts. Both monometallic (Pt or Au) and bimetallic (PtPd) catalysts were studied. In the first results chapter the strengths and weaknesses of various structural characterisation methods, TEM, XRD and EXAFS were explored. Subsequent chapters focussed on improving the EXAFS analysis by (i) using molecular dynamics simulations as the inputs for structural fitting and (ii) by using a Cu UPD layer to cap the surface of the nanoparticles, thereby reducing the effects of termination of the metallic structure on the EXAFS. The latter study also enabled the Cu UPD structure on nanoparticles to be compared to that obtained on single crystal surfaces.

Contents

DECLARATION OF AUTHORSHIP

I, **Stephen William Thomas Price,** declare that the thesis entitled

Enhanced Structural Characterisation of Supported Catalysts

and the work presented in the thesis are both my own, and have been generated by me as the result of my own original research. I confirm that:

- This work was done wholly or mainly while in candidature for a research degree at this University;
- Where any part of this thesis has previously been submitted for a degree or any other qualification at this University or any other institution, this has been clearly stated;
- Where I have consulted the published work of others, this is always clearly attributed;
- Where I have quoted from the work of others, the source is always given. With the exception of such quotations, this thesis is entirely my own work;
- I have acknowledged all main sources of help;
- Where the thesis is based on work done by myself jointly with others, I have made clear exactly what was done by others and what I have contributed myself;
- None of this work has been published before submission

Signed: ……..

Date:……..

Acknowledgements

First of all I would like to thank my supervisor, Professor Andrea E. Russell, for giving me the opportunity to study for this PhD, and for her support, advice and motivation. To those at Johnson Matthey who have helped make this work possible, I would like to thank Tim Hyde, Don Ozkaya, Pete Ash, Brian Theobald and Gopinathan Sankar. I am deeply indebted to Dr Bruce Ravel for writing the software that made this work possible, for many interesting discussions about EXAFS and football, and for telling us about the best places to eat at whilst on the long synchrotron visits to the NSLS! My thanks also go to Bruce and to Dr Kumi Pandya for their help collecting data at the NSLS. Special thanks go to Nikos Zonias for giving up a lot of his time to run molecular dynamics simulations and for teaching me how to run them.

To the members of the Russell group for their friendship; they have made my time here enjoyable and supported me on many a conference and synchrotron visit. Jon, with whom there was never a dull moment, Fabrice for being so welcoming when I arrived, and Katie for helping me survive being thrown in at the deep end. Anna and Pete for getting stuck in and running many night shifts for me - the middle of the night phone call after blowing out the cryostat cell windows at the NSLS deserves a special mention! Gael and Praba for their advice and help in the lab, and also to Rosie, Laura and Rob. All of the support staff at the university whose work behind the scenes kept everything running smoothly; Karl, Graham, Tony, Clive, Alastair, Jan, Sally, Nanou, Mary, Bevy, Rob, Alan, Pat for a great cup of tea, Pzemyslaw, Lee and everyone at the travel office (particularly during the incident with the volcano!).

To my family, who have encouraged and supported me in all I've done, and finally to Holly who has been with me through the highs and lows of doing a PhD. Thank you.

CHAPTER ONE: INTRODUCTION

Complex materials are emerging for use in heterogeneous catalysis and electrocatalysis with order down to the atomic scale. One of the central issues for continued growth in this area is being able to precisely control the size and shape of the nanoparticles, down to below 1 nm. Understanding the structure of these materials is of key importance in understanding their activity and developing this precise control, with which the exploitation of the key properties of nanoparticles becomes possible[1,2]. The development of this understanding has been limited by the ability to characterise them on the nanoscale, as there are currently no broadly applicable quantitative methods for doing so[3-5]. In this chapter, an introduction will be given to nanoparticles and their use as catalysts followed by a brief introduction into characterisation, and finally a brief outline of the thesis. Literature reviews relevant to the results presented later in this thesis can be found at the start of each of the results chapters (Chapters Three to Six).

1 Catalysis

A catalyst is a compound that can decrease the activation energy of a reaction without being permanently changed itself. The thermodynamics of the reaction are unchanged; the catalyst influences the rate of reaction by changing the nature of the transition state(s) or intermediate product(s). A schematic of a reaction with a lowered activation energy is in **Figure 1**.

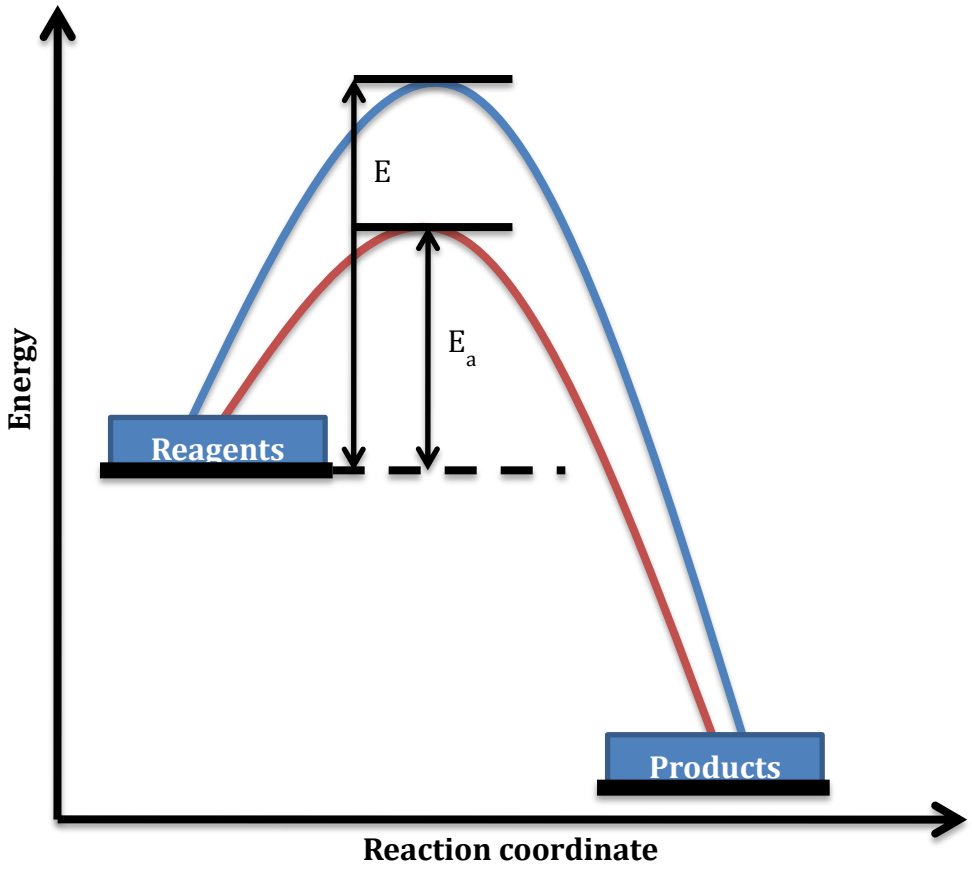

Figure 1: Schematic of the potential energy of an exothermic reaction with (red) and without (blue) a catalyst.

Types of catalysis include biocatalysis, such as reactions catalysed by enzymes, homogenous catalysis, where the catalyst is in the same phase as the reactants, such as the hydrolysis of esters, and heterogeneous catalysis, where the catalyst is in a different phase to the reactants. Examples of heterogeneous catalysis include catalytic converters for engine exhausts and the cracking, isomerisation and reforming of hydrocarbons to form petrol.

Electrocatalysis is the use of catalysts to increase the rate of an electrochemical reaction such as those at the anode and cathode in fuel cells or batteries[6-11].

2 Nanoparticles

The term nanoparticle refers to particles in which all the dimensions are below 100 nm and they often show new or improved properties compared with larger particles of the same material[12]. Nanoparticles exist in a wide variety of forms in nature, from volcanic activity to plant by-products and as products of human activities such as cooking, burning, and engine exhaust emissions. The amount of directly manufactured

nanoparticles is small in comparison[12]. As techniques in synthesising nanoparticles have advanced, a second generation of nanoparticles has come about, all with dimensions below 10 nm. It is at these sizes where the really significant non-bulk-like properties of nanoparticles dominate[12,13].

There are two main reasons for these changes in properties and behaviour. One is the relatively large proportion of surface atoms which may lead to an increased chemical reactivity or may give rise to stronger or more electrically active materials. The second reason is the increased dominance of quantum effects which change optical, magnetic and electrical properties. Some of the unusual properties not seen in the corresponding bulk materials include[13]: a) If the mean free path of the electron is larger than the crystal size, there is a decrease in electrical conductivity as a result of grain boundary (interface between two particles) scattering; b) Strength and malleability can improve in metal nanoparticles (and therefore performance) as a result of increasing grain boundaries, for particles of less than 100 nm; c) Matter transport by atomic diffusion through interfaces and membranes becomes an efficient mechanism at lower temperatures than with conventional matter. This effect can be used, for example, to considerably improve the kinetics of hydrogen diffusion in a hydrogen storage device, or lower the operation temperature of solid oxide fuel cells[13].

The area of specific interest here is the use of nanoparticles as catalysts. Catalysis occurs on the surface of particles[14], and the higher surface area to volume ratio of nanoparticles when compared with large particles often gives them a much higher catalytic activity per unit weight[15]. Many metals for use in catalysis have been known of for some time, such as Pd and Pt[16] (c. 1820), others, such as Au (1980's), are more recent[17]. Whilst bulk metallic Au is generally too inert to be used as a catalyst, it has been shown that nanoparticles of Au between 2 and 8 nm have useful catalytic properties[18], for example in the oxygen reduction reaction (ORR). Advanced synthetic techniques, such as thiol protected Au nanoparticle formation[19,20], or physical vapour deposition[11], allow for narrow size distributions of nanoparticles. This allows for enhanced size and chemical structure selectivity, the desirable goal from this being selective or specific activity, for example for a particular reaction. Given the limited availability of precious metals, in particular the Pt group metals, any reduction in the amount of catalyst used will be financially beneficial.

3 Particle Size Effect

The term "particle size effect" refers to a change in catalytic activity or selectivity as a function of particle size. This change can be a steadily increasing/decreasing trend, or a peaked function with an optimum size or size range. The particle size effect is not currently predictable from first principles and therefore highlights the need for accurate size determination to give a clearer understanding of the correlation between size and catalytic activity/selectivity. The change in activity may also be caused by a change in the crystallographic orientation of the catalyst surface[10,21].

Some general examples of particle size effects include significant changes in melting point with decreasing particle size[22]; contraction in inter-atomic bond lengths[23]; a change in reactivity, for example the kinetics for the oxygen reduction reaction in acidic medium exhibit a clear particle size effect[8,24]; elements that are inert as a bulk material can become catalytically active when nanoparticles[17,25-28].

The particle size effect in catalysis has been widely studied[9,23,29-32]. Kinoshita[33] investigated the electrocatalytic oxygen reduction reaction on cuboctahedral Pt/C catalysts. The study illustrates both a clear particle size effect and an increased mass activity with an optimum size between 3 and 5 nm.

The study of the particle size effect on Au nanoparticles is particularly interesting. Not only does Au become catalytically active on the nanoscale, but a change in particle size results in a change in reaction product, for example Hayashi *et al*.[34] demonstrated Au nanoparticles have a critical size of 2 nm for vapour phase epoxidation of propylene. Above 2 nm propylene oxide is formed, below 2 nm propane is formed. This is in contrast to the use of Pd or Pt catalysts for the same reaction where propane is the only product irrespective of the particle size of the catalyst. The critical dependence of activity and/or selectivity of size underlines the importance of accurate size determination; an error as small as 0.5 nm during catalyst preparation would result in a completely different epoxidation product from the intended one being formed.

Recently greatly increased activities for nanoislands on electrode surfaces[6,7] have been reported, for example demonstrating increased hydrogen evolution with decreasing Pd coverage[7], particularly for sub-monolayer coverage attributed to a nanoparticle-support interaction. The relationship between the interaction and support and therefore its effect on the activity is unclear, highlighting the need for accurate characterisation.

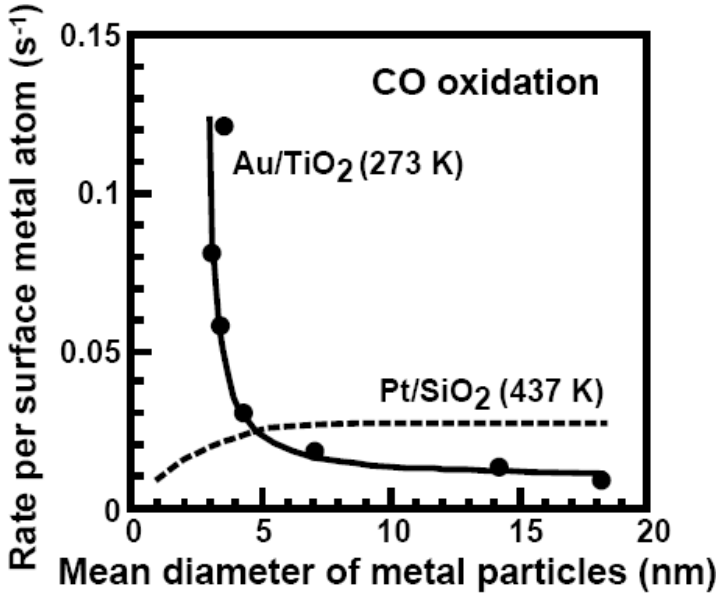

Figure 3: Turnover frequency (TOF) for CO oxidation on Au/TiO_2 as a function of average Au particle diameter[28].

Much work has been done by Haruta[17,28] on the particle size effect for Au nanoparticles. **Figure 3** plots the TOFs of CO oxidation for both Au and Pt nanoparticles as a function of size. Au exhibits a sharp increase in activity for sizes below 5 nm diameter, in contrast to the decrease observed for Pt.

Size determination becomes increasingly complex below 5 nm. Gibbs free energy calculations by Ajayan and Marks[35] demonstrated the presence of a quasi-molten phase well below the melting temperature with the particles fluctuating between different structures (**Figure 4**). This quasi-molten phase won't give rise to the degree of coherent X-ray diffraction required for analysis and therefore illustrates the need for the use of other techniques.

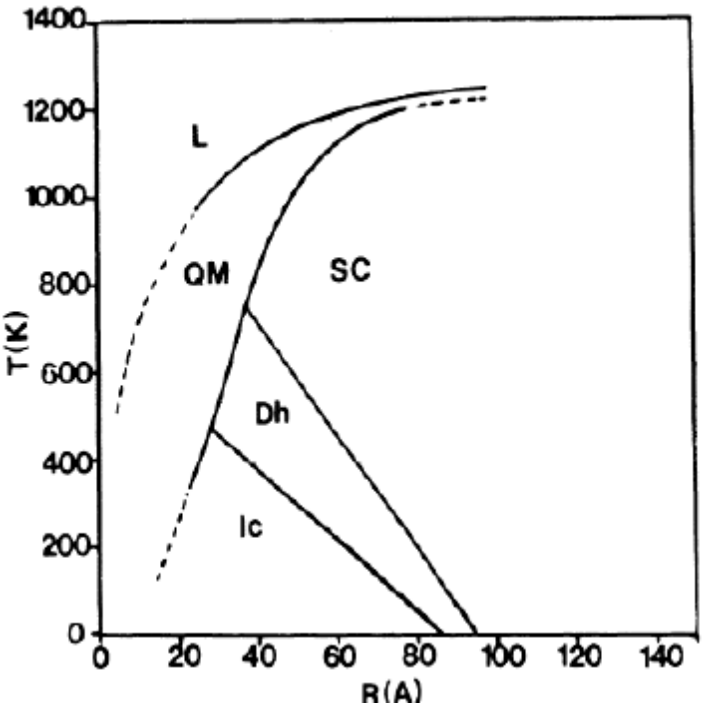

Figure 4: Phase diagram for small Au particles taken from Ajayan and Marks[35]; liquid (L), quasimelt (QM), icosahedral multiply twinned particle (Ic), decahedral multiply twinned particle (Dh) and single crystal (SC). Dotted lines represent extrapolated phase boundaries.

Transmission electron microscopy (TEM) can routinely achieve sub-nanometre resolution but is limited by the area it can probe as well as the strict conditions required for measurements. Extended X-ray Absorption Fine Structure (EXAFS) has been widely used for nanoparticle catalyst characterisation[4,18,36-44]. It has been shown to be a useful tool in studying the particle size effect[8,23] as it has increasing sensitivity towards coordination number determination (and therefore size determination[45,46]) with decreasing size. Increasingly the comparison of two or more characterisation techniques is being used to determine nanoparticle size and structure[15,44,47-49].

4 Aims and Objectives

This introduction highlights the importance of particle size in catalysis and the need to understand the relationship between structure and activity. Improved characterisation of nanoparticle catalysts will aid in the understanding of the particle size effect through enhanced structural analysis. This work primarily focuses on characterisation of nanoparticles using EXAFS, the primary aim being a clearer understanding of particle size determination and the methods by which they are determined.

Chapter Two describes the various synthetic, computational and analytical techniques used throughout this thesis.

Chapter Three will focus on the current methods of particle size determination. Correlation between different characterisation techniques (TEM, XRD, and EXAFS) for several series of nanoparticle catalysts will highlight the strengths and limitations of each technique, and the similarities and differences in particle size determined will be rationalised. This will allow for quantitative comparison of results derived by different techniques when time or circumstances only permit a single method of characterisation.

Chapter Four seeks to address some of the current assumptions inherent in EXAFS analysis by applying molecular dynamics (MD) to the problem of size determination. Cross-correlation of the results with TEM and XRD will be used as a means of evaluating the effectiveness of the MD methodology.

Chapter Five extends the MD approach to the analysis of more complicated bimetallic systems, and again uses cross-correlation with XRD and TEM data to evaluate the approach and gain a better understanding of the nanoparticle structure.

Chapter Six investigates the surface modification of Au nanoparticles by underpotential deposition (UPD) of Cu using *in situ* EXAFS characterisation. The nanoparticle structure will be studied before and after capping of the surface with Cu to investigate the contribution to the EXAFS signal from the nanoparticle surface to gain an insight into the surface structure of the nanoparticle.

5 References

(1) Fernandez-Garcia, M.; Martinez-Arias, A.; Hanson, J. C.; Rodriguez, J. A. *Chemical Reviews* **2004**, *104*, 4063.

(2) Poole, C. P.; Owens, F. J. *Introduction to Nanotechnology*; John Wiley & Sons Inc: Hoboken, New Jersey, 2003.

(3) Billinge, S. J. L.; Levin, I. *Science* **2007**, *316*, 1698.

(4) Frenkel, A. I.; Hills, C. W.; Nuzzo, R. G. *Journal of Physical Chemistry B* **2001**, *105*, 12689.

(5) Juhas, P.; Cherba, D. M.; Duxbury, P. M.; Punch, W. F.; Billinge, S. J. L. *Nature* **2006**, *440*, 655.

(6) Wolfschmidt, H.; Weingarth, D.; Stimming, U. *ChemPhysChem* **2010**, *11*, 1533.

(7) Pandelov, S.; Stimming, U. *Electrochimica Acta* **2007**, *52*, 5548.

(8) Mukerjee, S.; McBreen, J. *Journal of Electroanalytical Chemistry* **1998**, *448*, 163.

(9) Mukerjee, S. *Journal of Applied Electrochemistry* **1990**, *20*, 537.

(10) Markovic, N. M.; Adzic, R. R.; Cahan, B. D.; Yeager, E. B. *Journal of Electroanalytical Chemistry* **1994**, *377*, 249.

(11) Guerin, S.; Hayden, B. E.; Pletcher, D.; Rendall, M. E.; Suchsland, J.-P.; Williams, L. J. *Journal of Combinatorial Chemistry* **2006**, *8*, 791.

(12) *Nanoscience and nanotechnologies: opportunities and uncertainties*, The Royal Society, 2004.

(13) Lojkowski, W.; Turan, R.; Proykova, A.; Daniszewska, A. *Eighth Nanoforum Report: Nanometrology*, Institute of Nanotechnology, 2006.

(14) Taylor, H. S. *Proceedings of the Royal Society A* **1925**, *108*, 105.

(15) Díaz-Moreno, S.; Koningsberger, D. C.; Muñoz-Páez, A. *Nuclear Instruments and Methods in Physics Research Section B: Beam Interactions with Materials and Atoms* **1997**, *133*, 15.

(16) Davy, H. *Philosophical Transaction of the Royal Society* **1817**, *107*, 77.

(17) Haruta, M.; Kobayashi, T.; Sano, H.; Yamada, M. *Chemistry Letters* **1987**, *16*, 405.

(18) Cortie, M. B.; Lingen, E. v. d. *Materials Forum* **2002**, *26*, 1.

(19) Brust, M.; Walker, M.; Bethell, D.; Schriffin, D. J.; Whyman, R. *Journal of the Chemical Society-Chemical Communications* **1994**, 801.

(20) Hostetler, M. J.; Wingate, J. E.; Zhong, C. J.; Harris, J. E.; Vachet, R. W.; Clark, M. R.; Londono, J. D.; Green, S. J.; Stokes, J. J.; Wignall, G. D.; Glish, G. L.; Porter, M. D.; Evans, N. D.; Murray, R. W. *Langmuir* **1998**, *14*, 17.

(21) Strbac, S.; Adzic, R. R. *Electrochimica Acta* **1996**, *41*, 2903.

(22) Buffat, P.; Borel, J. P. *Physical Review A* **1976**, *13*, 2287.

(23) Miller, J. T.; Kropf, A. J.; Zha, Y.; Regalbuto, J. R.; Delannoy, L.; Louis, C.; Bus, E.; van Bokhoven, J. A. *Journal of Catalysis* **2006**, *240*, 222.

(24) Durand, R.; Faure, R.; Gloaguen, F.; Aberdam, D. In *Oxygen Electrochemistry*; Adzic, R. R., Kinoshita, K., Anson, F. C., Eds.; The Electrochemical Society: 1995; Vol. 26, p 27.

(25) Akolekar, D. B.; Bhargava, S. K.; Foran, G. *Radiation Physics and Chemistry* **2006**, *75*, 1948.

(26) Thompson, D. T. *Nano Today* **2007**, *2*, 40.

(27) Bus, E.; van Bokhoven, J. A. *The Journal of Physical Chemistry C* **2007**, *111*, 9761.

(28) Haruta, M. *The Chemical Record* **2003**, *3*, 75.

(29) Karim, A. M.; Prasad, V.; Mpourmpakis, G.; Lonergan, W. W.; Frenkel, A. I.; Chen, J. G. G.; Vlachos, D. G. *Journal of the American Chemical Society* **2009**, *131*, 12230.

(30) Leont'ev, I.; Guterman, V.; Pakhomova, E.; Guterman, A.; Mikheikin, A. *Nanotechnologies in Russia* **2009**, *4*, 170.

(31) Guerin, S.; Hayden, B. E.; Pletcher, D.; Rendall, M. E.; Suchsland, J.-P. *Journal of Combinatorial Chemistry* **2006**, *8*, 679.

(32) Frelink, T.; Visscher, W.; van Veen, J. A. R. *Journal of Electroanalytical Chemistry* **1995**, *382*, 65.

(33) Kinoshita, K. *Journal of The Electrochemical Society* **1990**, *137*, 845.

(34) Hayashi, T.; Tanaka, K.; Haruta, M. *Journal of Catalysis* **1998**, *178*, 566.

(35) Ajayan, P. M.; Marks, L. D. *Physical Review Letters* **1988**, *60*, 585.

(36) Davis, R. J.; Landry, S. M.; Horsley, J. A.; Boudart, M. *Physical Review B* **1989**, *39*, 10580.

(37) Menacherry, P. V.; FernandezGarcia, M.; Haller, G. L. *Journal of Catalysis* **1997**, *166*, 75.

(38) Li, Z. Y.; Young, N. P.; Di Vece, M.; Palomba, S.; Palmer, R. E.; Bleloch, A. L.; Curley, B. C.; Johnston, R. L.; Jiang, J.; Yuan, J. *Nature* **2008**, *451*, 46.

(39) Shido, T.; Prins, R. *Journal of Physical Chemistry B* **1998**, *102*, 8426.

(40) Bus, E.; Miller, J. T.; Kropf, A. J.; Prins, R.; van Bokhoven, J. A. *Physical Chemistry Chemical Physics* **2006**, *8*, 3248.

(41) Safonova, O. V.; Tromp, M.; van Bokhoven, J. A.; de Groot, F. M. F.; Evans, J.; Glatzel, P. *Journal of Physical Chemistry B* **2006**, *110*, 16162.

(42) Ankudinov, A. L.; Rehr, J. J.; Low, J. J.; Bare, S. R. *Journal of Chemical Physics* **2002**, *116*, 1911.

(43) Russell, A. E.; Rose, A. *Chemical Reviews* **2004**, *104*, 4613.

(44) Frenkel, A. I. *Journal of Synchrotron Radiation* **1999**, *6*, 293.

(45) Benfield, R. E. *Journal of the Chemical Society-Faraday Transactions* **1992**, *88*, 1107.

(46) Jentys, A. *Physical Chemistry Chemical Physics* **1999**, *1*, 4059.

(47) Calvin, S.; Luo, S. X.; Caragianis-Broadbridge, C.; McGuinness, J. K.; Anderson, E.; Lehman, A.; Wee, K. H.; Morrison, S. A.; Kurihara, L. K. *Applied Physics Letters* **2005**, *87*.

(48) Weibel, A.; Bouchet, R.; Boulc'h, F.; Knauth, P. *Chemistry of Materials* **2005**, *17*, 2378.

(49) Tauster, S. J.; Fung, S. C.; Garten, R. L. *J. Am. Chem. Soc.* **1978**, *100*, 170.

CHAPTER TWO: EXPERIMENTAL METHODS AND TECHNIQUES

This chapter describes the theoretical and practical aspects of the experimental methods that were used throughout this project. This includes descriptions of the physical characterisation (X-ray Absorption Spectroscopy, Transmission Electron Microscopy and X-ray diffraction) as well as the electrochemical studies (Cyclic Voltammetry and Underpotential Deposition) and computer modelling.

1 Reagents and Materials

The materials and reagents used during this work, along with their respective suppliers, are detailed in **Table 1** below.

Table 1: List of materials and reagents used along with suppliers

Material/Reagent	**Supplier**
Hydrogen Tetrachloroaurate (95%)	Alfa Aesar
Tetraoctylammonium Bromide (98%)	Sigma Aldrich
Toluene (reagent grade)	Fisher Scientific
Dodecanethiol (98%)	Sigma Aldrich
Sodium Borohydride (general purpose grade)	Acros Organics
Ethanol (HPLC grade)	Rathburn
Hexane (95%)	Fisher Scientific
Water (18 MΩ cm)	Purified using a Pur1te system
XC-72R carbon black	Cabot Corporation
Nafion® (10.85 wt% solids in water)	Johnson Matthey
Sulphuric Acid (Lab reagent grade)	Fisher Scientific
Trisodium Citrate	Alfa Aesar
Copper Sulphate Pentahydrate (95%)	Sigma Aldrich
Boron Nitride (1μ 99%)	Sigma Aldrich

2 X-ray Absorption Spectroscopy (XAS)

The technique known as XAS has been known since the 1920's, when Fricke reported XAS oscillations in an X-ray absorption spectra[1] followed by Kronig[2] developing the first theory of EXAFS. It was not until bright tuneable sources of X-rays at synchrotrons were built in the 1970's that its development really took off, with the modern theory being developed by Sayers *et al.* [3] that allowed for the extraction of local structural information. This work was built upon by Lee *et al*.[4] and Stern *et al*.[5]. This initial theory of EXAFS was based on a plane wave assumption (simplified from a spherical wave), which assumed that single scattering effects dominated. That is, the photoelectron emitted is only scattered once before returning to the central atom. The plane wave approximation allowed for a greater simplification for deriving structural parameters, but fails below k (wavenumber) values of 3 $Å^{-1}$. As a result of this, and thanks to faster computing, modern models are based upon spherical wave theory, and can include multiple scattering effects. This is where the photoelectron scatters off more than one atom before returning to the central atom, and allows for more reliable determination of structural information beyond the first shell where a multiple scattering paths have an equivalent path length to a single scattering path[4,6].

XAS measurements are independent of sample complexity and environment, with the signal coming from all of the atoms of a single element. Data can be collected on mixtures of gases, liquids or solids, and under a variety of conditions. The term XAS covers both X-ray Absorption Near Edge Structure (XANES) and Extended X-ray Absorption Fine Structure (EXAFS). XANES provides information on the electronic structure of the sample, and EXAFS provides near-neighbour structural information of the sample.

2.1 Theory of XAS

2.1.1 General principles

When X-rays pass through a sample, there is a reduction in the incident intensity (I_0). The number of X-rays transmitted (I_t) through a sample decreases exponentially by the thickness of the sample (x) and the absorption coefficient of the sample (μ), shown in **Equation 1**.

$$I_t = I_0 e^{-\mu x}$$

Equation 1

An X-ray absorption edge occurs when all the energy of an X-ray is absorbed by an atom, and used to excite an electron into a higher unoccupied orbital, or into the continuum. The excited electrons are known as photoelectrons, and the empty electron orbital is called a hole; when a core electron is excited, the resultant hole is known as a core hole.

As the incident photon energy is increased, absorption will decrease until the binding energy of a core electron is reached. Excitation of a core electron will result in a sharp rise in absorption, known as the absorption edge. The excited electron has energy (E_k) defined by **Equation 2**.

$$E_k = h\nu - E_{binding}$$

Equation 2

Where hν is the energy of the incident X-rays and $E_{binding}$ is the binding energy.

Beyond the absorption edge, increasing the energy results in a decrease in absorption until the next binding energy is reached. The intensity of the absorption edge is determined by the absorption coefficient μ, which is proportional to the probability of absorbing a photon according to Fermi's golden rule[6] (**Equation 3**)

$$\mu \propto \sum_f \left|\langle \varphi_f | p.A(r) | \varphi_i \rangle\right|^2 \delta\left(E_f - E_i - \hbar\omega\right)$$

Equation 3

where φ_i and φ_f describe the initial and final states, p is the momentum operator, and $A(r)$ the vector potential of the incident electromagnetic field. This is known as the photoelectric effect. The absorption edges are named and ordered in terms of decreasing energy from K, L_I, L_{II}, L_{III} etc., based on the principal quantum number from

which the electron was ejected. The K shell (n=1) corresponds to an excitation from the 1s orbital, the L shell (n=2) can contain the 2s, $2p_{1/2}$ and $2p_{3/2}$ corresponding to the L_I, L_{II} and L_{III} edges respectively (**Figure 1**).

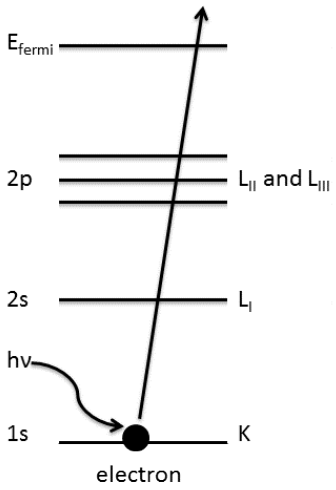

Figure 1: Schematic of the photoelectric effect, excitation of a 1s electron giving rise to a K edge.

The outgoing photoelectron can be thought of as a spherical wave, with a vector k related to the energy of the photon (**Equation 4**) where E_0 is the energy of the point of inflection of the absorption edge, normally the maximum of the first derivative, and m_e is the mass of an electron.

$$k = \sqrt{\left(\frac{8\pi^2 m_e}{h^2}\right)(h\nu - E_0)}$$

Equation 4

The outgoing photoelectron scatters off surrounding atoms, resulting in interference that creates modulations of the final state of the photoelectron wave (**Figure 2**).

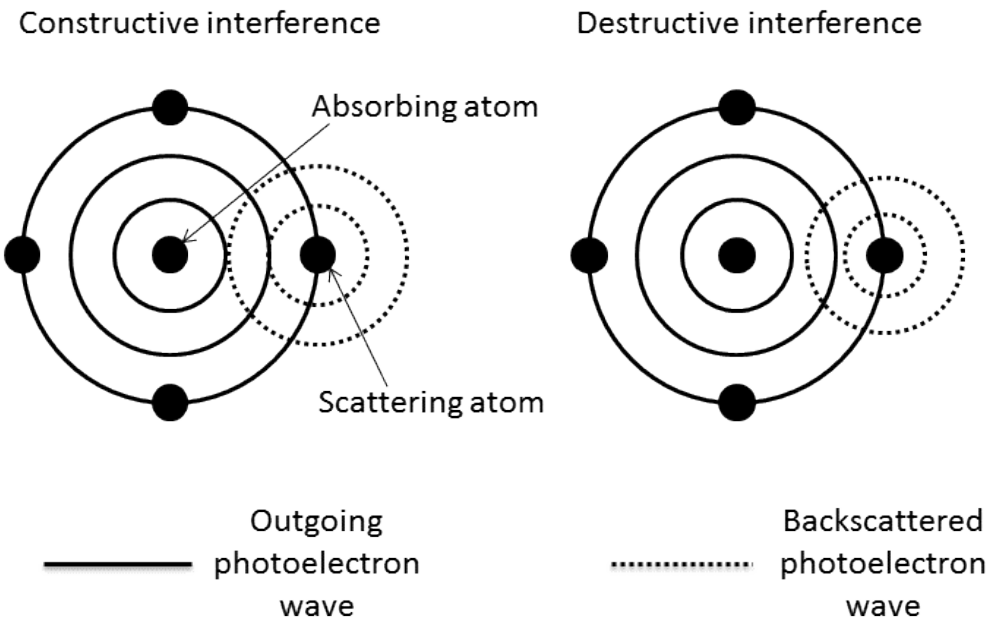

Figure 2: Schematic of constructive and destructive interference of an outgoing photoelectron. The circles represent the maxima of the photoelectron waves.

At energies where there is positive interference the absorption increases, and at energies where there is negative interference the absorption decreases. This absorption can be defined in terms of the wave vector k, and is given as:

$$\chi(k) = \frac{\mu_{tot}(k) - \mu_0(k)}{\mu_0(k)}$$

Equation 5

Where $\mu_0(k)$ is the background absorption, $\mu_{tot}(k)$ is the total absorption and $\chi(k)$ is the EXAFS that is extracted. A typical XAS spectrum is shown in **Figure 3**.

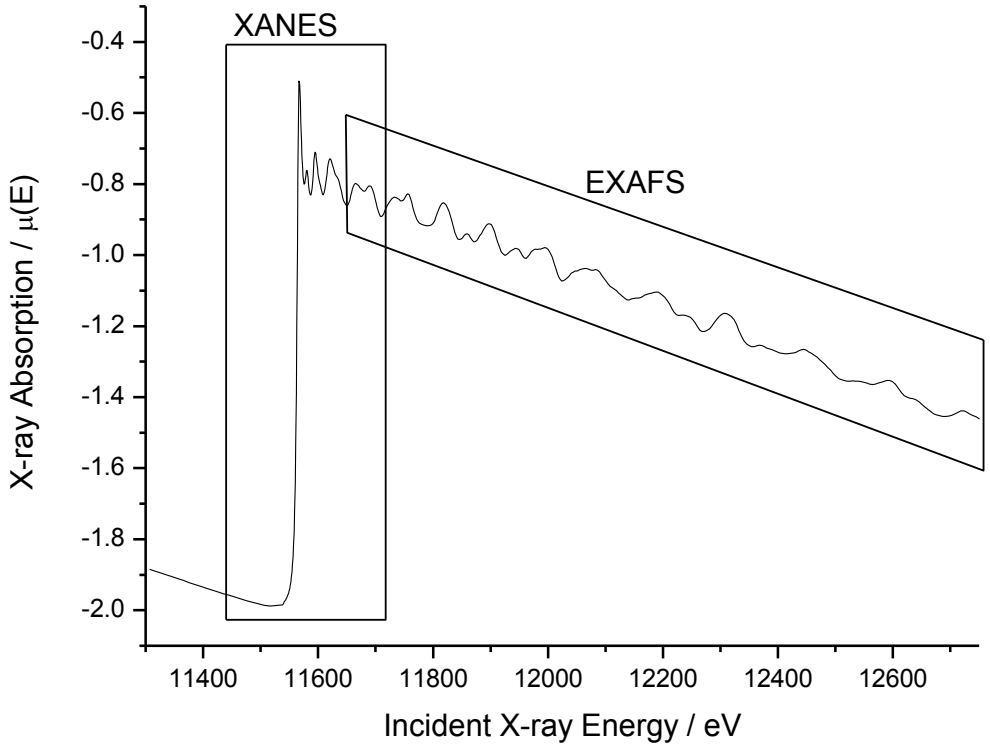

Figure 3: XAS spectrum of a Pt foil at the Pt LIII edge showing XANES and EXAFS regions.

The XANES region includes the pre-edge region where the incident X-rays are not energetic enough to excite an electron, and continues to around 200 eV beyond the edge. The shape of the absorption edge is related to the local density of states available for the photoelectron excitation; as such binding geometry and oxidation state of the absorbing atom affect the XANES region. For atoms of higher oxidation states, the edge energy is increased by a few electronvolts as the remaining electrons are in lower energy states (and hence harder to excite). Multiple scattering and multiple photon absorption complicate the analysis of the XANES region.

The EXAFS region of the spectrum is the oscillating part above the edge to over 1000 eV. The EXAFS region is used to determine local bonding environments, containing information on types and numbers of surrounding atoms, interatomic distances and the degree of disorder. In this region, single scattering normally dominates.

Each atom at the same radial distance from the absorber contributes to the same part of the EXAFS signal, with these atoms known as a shell. The number of atoms in each shell is known as the coordination number. Single scattering paths are from one shell

of atoms, with the degeneracy being the coordination number. Multiple scattering path degeneracy is the number of equivalent paths with that scattering length/phase.

2.1.2 The EXAFS Equation

The EXAFS equation allows for the quantitative determination of the structural content of the EXAFS signal, and can be written as the sum of all the photoelectron scattering paths.[7]

$$\chi(k) = \sum_i \chi_i(k)$$

Equation 6

Each scattering path can be written as:

$$\chi_i(k) = \frac{(N_i S_0^2) F_{eff_i}(k)}{k R_i^2} \sin[2kR_i + \varphi_i(k)]\, e^{-2\sigma_i^2 k^2} e^{\frac{-2R_i}{\lambda(k)}}$$

Equation 7

with

$$R_i = R_{0i} + \Delta R_i$$

Equation 8

and

$$k^2 = \frac{2m_e(E - E_0 + \Delta E_0)}{\hbar}$$

Equation 9

The terms $\boldsymbol{F_{eff}}$, $\boldsymbol{\varphi_i(k)}$ and $\boldsymbol{\lambda(k)}$ are, respectively, the effective scattering amplitude, the phase shift, and the mean free path of the photoelectron, and are computed by a program such as FEFF 6.0[6]. $\boldsymbol{R_i}$ is the photoelectron's half path length, that is the distance between absorbing and scattering atom. $\boldsymbol{R_{0i}}$ is the theoretical path length that is modified by $\boldsymbol{\Delta R_i}$. **Equation 9** is used to convert the photoelectron energy above the absorption edge into wavenumber *k*. The remaining variables can be determined by modelling the EXAFS spectrum, and are described below. The subscript ***i*** denotes that the value can change for each scattering path.

$\boldsymbol{N_i S_0^2}$: N denotes the scattering amplitude for single scattering, and the effective amplitude for multiple scattering. S_0^2 is the amplitude reduction factor, and accounts for the slight relaxation of the remaining electrons around the core hole left by the

photoelectron. It differs between elements, although can be transferred between different species of the same element (and edge)[8] and is generally between 0.7 and 1.0.

$\mathbf{1/R_i^2}$: contribution from a shell decreases with distance from the absorber.

$\mathbf{\sin[2kR_i + \varphi_i(k)]}$: reflects the dependence of the scattered photoelectron on both distance and phase shift $\varphi_i(k)$.

$e^{-2\sigma_i^2 k^2}$: Debye-Waller term. Not all of the coordinating atoms in a shell are at fixed positions of R_i from the absorber; σ^2 accounts for the disorder in interatomic distance, and is the mean-square relative displacement (MSRD) of the bond length R_i. It contains both thermal (dynamic) and structural (static) contributions. A distribution of distances within a single coordination shell increases σ^2.

$e^{\frac{-2R_i}{\lambda(k)}}$: accounts for inelastic scattering losses relating to the distance the photoelectron travels after excitation; is responsible for the short (~10 Å) range analysed by EXAFS.

$\mathbf{\Delta R_i}$: represents a change in interatomic distance relative to theoretical path length R

$\mathbf{\Delta E_i}$: relates to a change in photoelectron energy; is used to align theoretical and experimental spectra.

2.2 Experimental aspects of XAS

2.2.1 Synchrotrons

X-ray absorption measurements are almost always made at synchrotron radiation facilities. The measurements used in this study were performed at two beamlines at the National Synchrotron Light Source (NSLS), Brookhaven National Laboratory, USA. A schematic overview of a synchrotron facility is in **Figure 4** below. Bunches of electrons are accelerated by a linear accelerator and then fed into the inner booster ring that further accelerates them to near the speed of light and injects them into the outer storage ring. A series of bending magnets around the ring keep the electrons travelling in a closed loop. The conservation of angular momentum of the electrons results in the emission of synchrotron radiation (X-rays) at tangents. These X-rays are highly intense, collimated and cover a wide range of energies[9]. A series of optics is then used to tune the X-rays to the desired energy and profile.

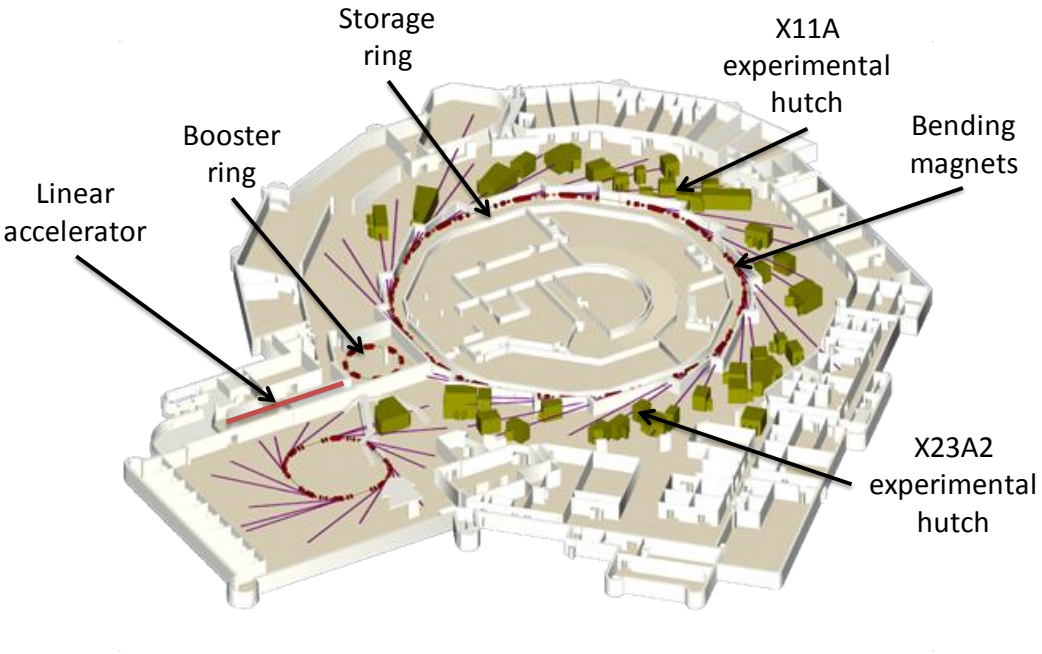

Figure 4: Annotated schematic of the NSLS experimental floor[10].

2.2.2 X11A

Station X11A has a double crystal monochromator using a Huber goniometer containing Si(111) crystals, detuned to 75% to minimise higher harmonics and can measure an energy range of 4.5-26 keV. The NSLS operates with a ring energy of 2.58 GeV and a maximum current of 350 mA.

The station scientist on X11A was Kumi Pandya (Brookhaven National Laboratories), and the experiments were conducted by Anna Wise, Gael Chouchelamane and myself (University of Southampton).

2.2.3 X23A2

Station X23A2 has a upward reflecting, fixed exit Golovchenko-Cowan design[11] monochromator containing Si(311) crystals stabilised by piezo-electric feedback with a single bounce harmonic rejection mirror to reduce higher harmonics and can measure an energy range of 4.9-30 keV.

The station scientist on X23A2 was Bruce Ravel (Brookhaven National Laboratories), and the experiments were conducted by Jon Speed, Andrea Russell, Peter Richardson and myself (University of Southampton).

2.2.4 XAS Transmission Experiments

Transmission measurements are the simplest acquisition mode for XAS collection, and works by measuring the difference in X-ray intensity between two chambers as the energy is changed. A basic schematic is shown in **Figure 5**. Transmission XAS measurements involve measuring the X-ray absorption coefficient (μ) as a function of X-ray energy.

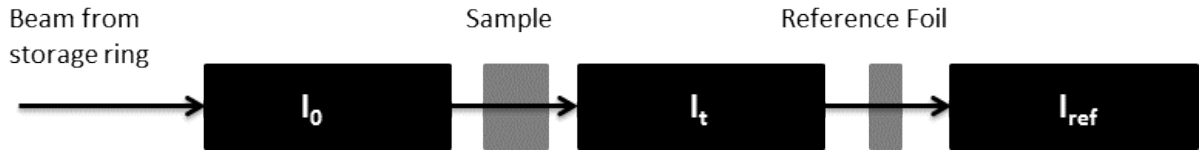

Figure 5: Schematic of transmission mode XAS experiment. I_0, I_t and I_{ref} are the incident, transmission, and reference ionisation chambers respectively.

The number of incident X-rays are measured before (I_0) and after (I_t) the sample, and the X-ray absorption coefficient (μ) is determined by rearranging **Equation 1**:

$$\mu x = \ln\left(\frac{I_0}{I_t}\right)$$

Equation 10

The gases within the ion chambers are mixed to absorb a proportion of the X-ray intensity based on the energy of the absorption edge, typically 10% absorption in I_0 and 70% absorption in I_t or I_{ref}.

Transmission experiments are used when the sample is concentrated. For more dilute samples, the signal to noise ratio will be poor, and so fluorescence measurements are needed (described below). Too concentrated a sample will result in all the X-rays being absorbed and therefore the thickness of the sample is important. For samples with more than one element present, the absorption characteristics of the other elements need to be considered. An ideal absorption edge of the element being studied should have μx between 0.25 and 1.0, with the total sample absorption being less than 2.5. The appropriate mass of sample needed can be calculated using **Equation 11**.

$$mass = \frac{(\mu x)(sample\ area)}{(\mu_\rho)}$$

Equation 11

where μ_ρ is the mass absorption coefficient of the element being studied. X-ray absorption coefficient values have been taken from McMasters tables[12].

Sample homogeneity is very important for transmission measurements, as any small holes in the sample would result in increased noise in the data. As such, all samples for transmission measurements were prepared as pellets mixed with boron nitride (BN is gas permeable and has a low X-ray absorption coefficient at Pt and Au L_{III} edges). The pellets were prepared by mixing a set amount of catalyst (calculated using **Equation 11**) with BN to form a homogenous mixture that was then compacted using a purpose built press.

2.2.5 XAS Fluorescence Experiments

For samples too dilute to be measured in transmission mode, a fluorescence detector is needed. X-ray fluorescence occurs when an electron from a higher energy orbital relaxes to fill the core hole left by the ejected photoelectron[9]. This process can emit either an Auger electron or an X-ray photon with energy equal to the difference between the two orbitals; the emitted X-ray photon is detected in fluorescence mode. The detector is usually set at 90° to the incident beam, with the sample positioned at 45° (**Figure 6**). The fluorescence X-rays are emitted isotropically from the sample whilst the Compton scattering is at a minimum at 90°. Solid state detectors are most commonly used, and for the data used in this work, a 4-element silicon drift detector was used on beamline X23A2. The detector utilises a strip of semi-conducting material behind a beryllium window to detect the X-rays, and the software allows for selection of a single X-ray energy to be recorded.

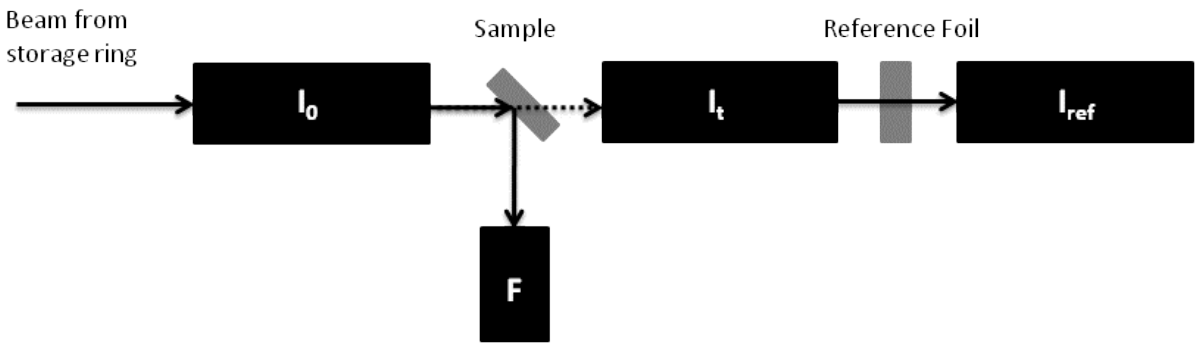

Figure 6: Schematic of fluorescence mode XAS experiment. I_0, I_t and I_{ref} are the incident, transmission, and reference ionisation chambers respectively, F is the fluorescence detector.

2.2.6 Cryostat

To collect EXAFS spectra in both a reducing hydrogen environment and at low temperature, a specially designed cryostat shroud was used (**Figure 7**). The shroud is made of steel with Kapton windows for entry and exit of X-ray beam, and with gas inlet

and outlet valves. The cell has a larger window on the reverse that can be used for fluorescence measurements if required. The pressed sample pellet was attached to the cold finger of the displex unit inside the cryostat shroud. To collect spectra under hydrogen, the cell was purged with pure hydrogen for 30 minutes with the exhaust gas being diluted with nitrogen to <2.5% before closing the gas valves. To collect low temperature EXAFS, the vacuum of the displex unit was activated after hydrogen purging and the temperature controller set to the required temperature.

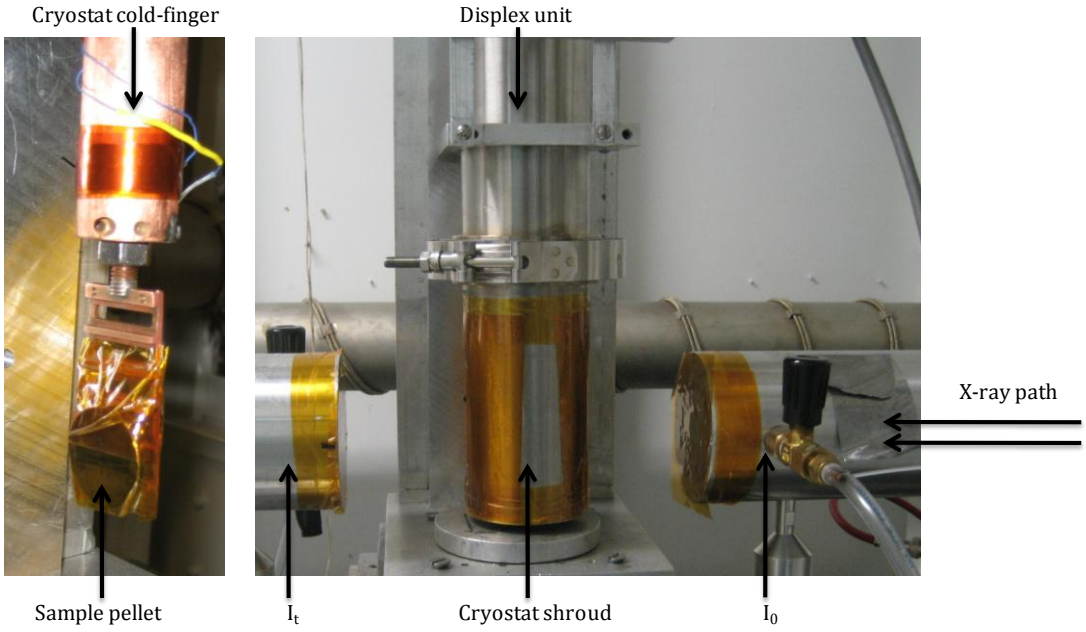

Figure 7: Cryostat shroud for hydrogen reduction and low temperature measurements. (Gas inlets are on reverse of shroud).

2.2.7 *In situ* Electrochemical Cell

An *in situ* electrochemical cell (designed by Anna Wise, **Figure 8**) was used to collect XANES and EXAFS data during the underpotential deposition of Cu on Au. The working electrode (WE) was held in place by a Au wire contact, and a Pt wire served as the counter electrode (CE). A mercury mercurous sulphate (MMS), Hg/Hg_2SO_4, reference electrode (RE) was used to define the potential. To operate the cell, the electrolyte was first purged with nitrogen for 15 minutes to remove all oxygen. A peristaltic pump was used to flush the electrolyte through the cell. All three electrodes were connected to a μAutolab type III potentiostat running off General Purpose Electrochemistry Software 4.9 (GPES). Full details of the electrochemistry follow later in this chapter.

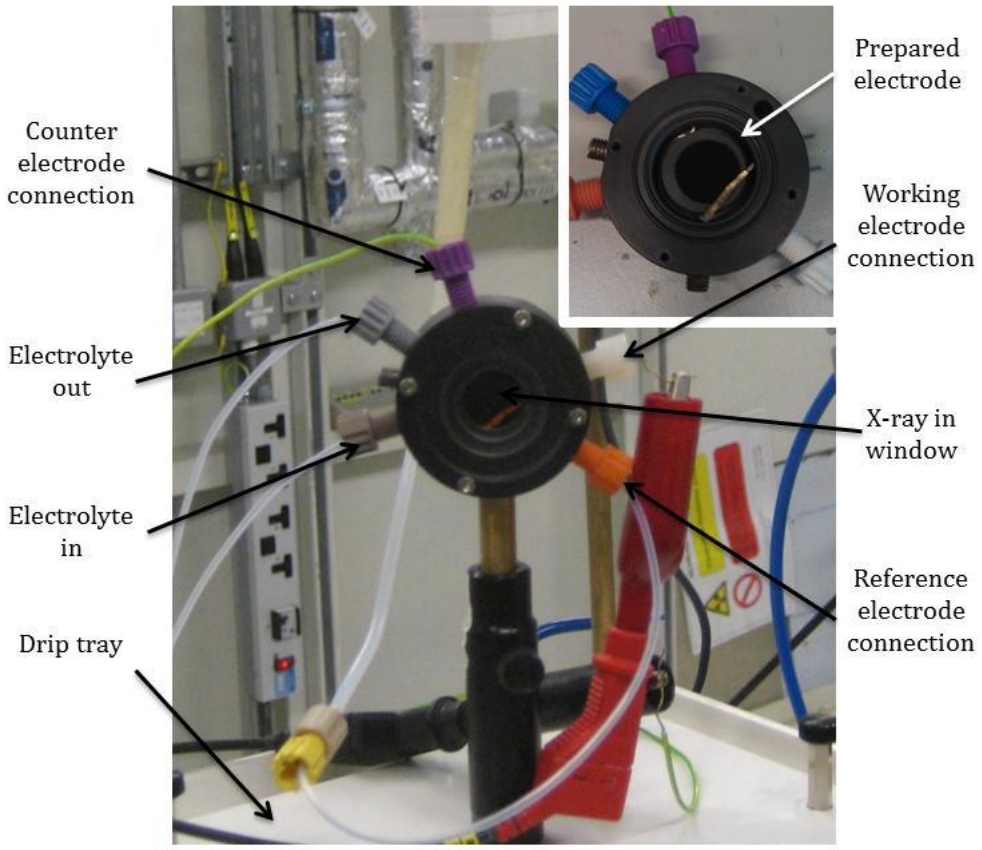

Figure 8: *In situ* electrochemistry/XAS cell. Inset is opened cell with electrode in place.

2.3 Data Analysis

Data was processed and analysed using the Horae software package(ATHENA, ATOMS, ARTEMIS)[6,13-15]. The basic processing procedure is outlined below.

After importing the raw data file into ATHENA, a linear pre-edge and a quadratic post-edge function are fitted to the data. These functions are subtracted from the data and the spectrum normalised to give an edge step of 1 (**Figure 9**).

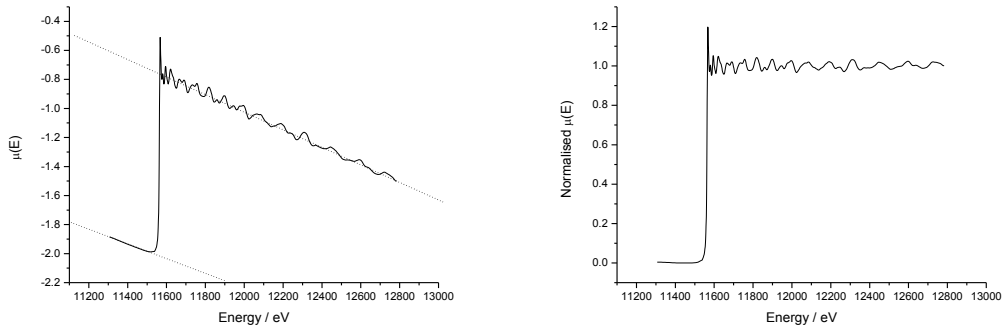

a) b)

Figure 9: Raw EXAFS data a) before and b) after background subtraction and normalisation.

The energy scale was calibrated to a reference foil, with the first derivative maximum being used to mark the absorption edge (**Figure 10**). The background was subtracted using the AUTOBK algorithm[16] present in ATHENA, automatically fitting a spline function to pass through the nodes of the EXAFS oscillations without following the oscillations of the data.

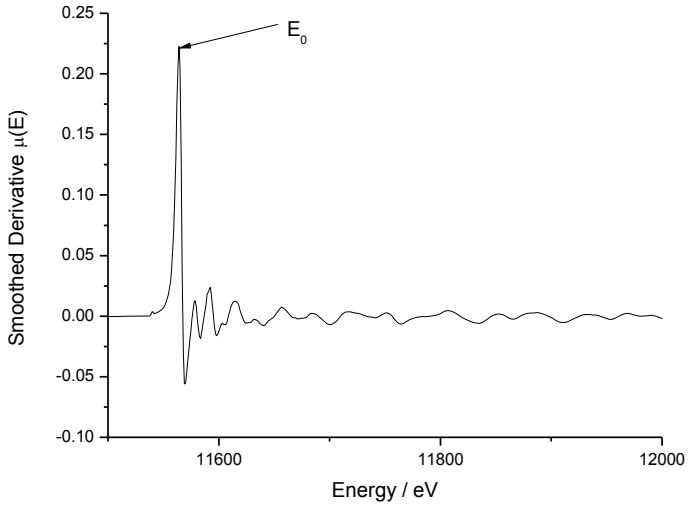

Figure 10: Determination of first derivative maximum to rescale EXAFS data.

Where more than one scan was taken, the second file could be imported, with all of the processing parameters copied from the first file, aligned along the energy axis and then merged to average the scan(s) and improve the signal to noise ratio. Once processed the data can then be analysed in ARTEMIS using the FEFF 6.0 code to fit the experimental data to theory. The energy scale is converted (using **Equation 9**) from electronvolts (eV) to wavenumber ($Å^{-1}$). The resulting $\chi(k)$ plot can be varyingly weighted, and Fourier transformed to give a plot similar to a radial distribution function (**Figure 11**).

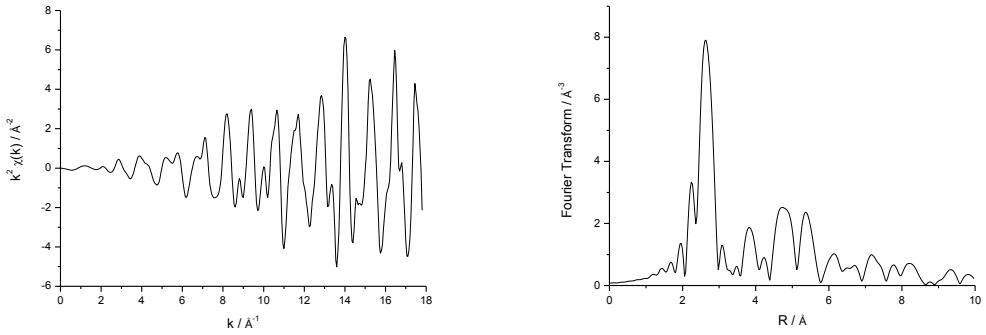

Figure 11: a) k² weighted χ(k) data and b) corresponding Fourier transform.

The values of coordination number (N_i), neighbouring shell distance (R_i), MSRD (σ^2) and energy shift (E_0) are calculated from the fit, and refined using a Levenberg-Marquardt non-linear least squares minimization, with a reduced χ^2 fitting metric to compare the difference of quality of fit (**Equation 12**) and an R factor (R_f) to evaluate goodness of fit (**Equation 13**).

$$\chi^2 = \frac{N_{idp}}{\epsilon N_{data}} \sum_{i=min}^{max} [Re(\chi_d(r_i) - \chi_t(r_i))^2 + Im(\chi_d(r_i) - \chi_t(r_i))^2]$$

Equation 12

where N_{idp} is the number of independent data points, N_{data} the number of points in the data, ϵ the measurement uncertainty, χ_d the experimental EXAFS, and χ_t the theoretical EXAFS.

$$R_f = \frac{\sum_{i=min}^{max} [Re(\chi_d(r_i) - \chi_t(r_i))^2 + Im(\chi_d(r_i) - \chi_t(r_i))^2]}{\sum_{i=min}^{max} \left[Re\left(\chi_d(r_i)\right)^2 + Im\left(\chi_d(r_i)\right)^2\right]}$$

Equation 13

The reduced χ^2 is not normally reported, whilst an R_f of less than 0.03 can be considered a good fit. For noisier data, slightly higher is acceptable.

3 Transmission Electron Microscopy (TEM) and Energy Dispersive X-ray Analysis (EDX)

TEM was used to determine the particle size distribution (PSD) within each sample and also to determine 2-dimensional shape. EDX was used to examine the proportion of different elements within the sample.

3.1 TEM

3.1.1 Principles of TEM

TEM uses electrons instead of light to image a sample. The wavelength associated with high energy electrons is smaller than inter-atomic distances, and this can give rise to diffraction effects, resulting in an image that does not necessarily represent the shape of the particle as optical microscopy would (effectively limiting the resolution[17]). Higher energy electrons are capable of achieving greater spatial resolution up to 0.1 nm, but are more likely to damage the sample, thus not all catalysts can be routinely imaged at atomic resolution[18]. Depending on sample thickness, a fraction of electrons pass through the sample without losing energy. As the attenuation of the beam depends on density and thickness, transmitted electrons form a 2D projection of the sample (i.e. size and shape) – typical transmission images are bright field (BF).

TEM can also operate in high angle annular dark field (HAADF) mode where back-scattered electrons are detected. The intensity of the back scattered electrons is proportional to the atomic mass of the scatterer.

3.1.2 Scanning Transmission Electron Microscopy

Scanning transmission electron microscopy (STEM) operates by rastering a narrow electron beam across the surface of the sample, and can operate in both BF and HAADF modes. STEM can have resolution comparable to TEM with the advantage that selected areas of the sample can be investigated separately (whereas TEM cannot).

3.1.3 Aberration Corrected STEM

Standard TEM lenses are spherical. Aberration corrected TEM uses non-spherical lenses. This corrects for the spherical aberration caused by normal electron microscope lenses[19] and allows for enhanced spatial resolution to below 0.1 nm.

3.1.4 TEM Data Analysis

A histogram representing the number of particles of a certain size is generated from a selection of images of the sample to gain a more representative view of the PSD, from which the average particle size and standard deviation are calculated. An example of a TEM image and PSD is given in **Figure 12**.

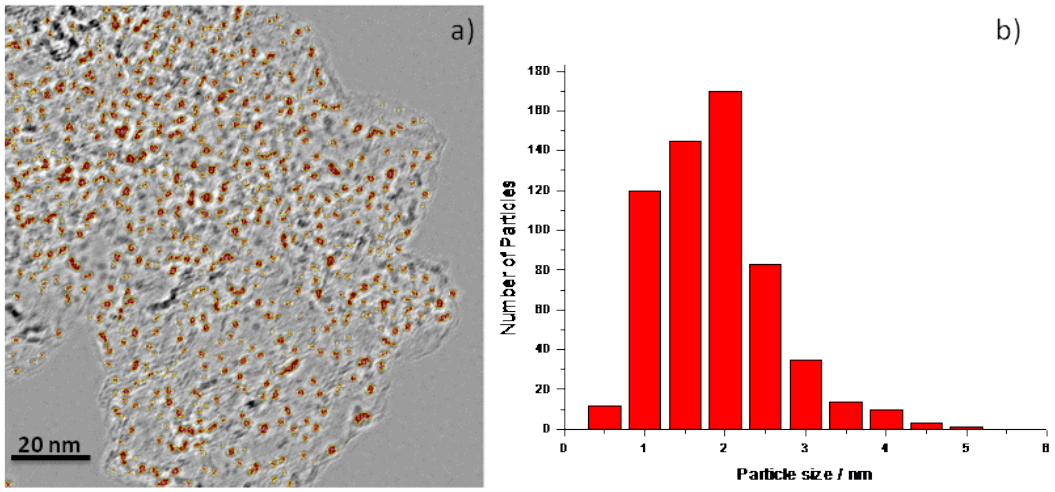

Figure 12: a) TEM micrograph used to calculate particle size distribution and b) typical particle size distribution. The particles included in the size analysis are marked in red.

3.2 EDX

3.2.1 Principles of EDX

EDX operates similar to the XAS fluorescence detector, in that it uses a solid state detector such as a germanium strip to detect X-rays emitted from the sample when it is bombarded by electrons. The X-rays emitted by the sample are isotropic, however the closer the detector can be to 90° the less Compton scattering will be present. EDX can be used to determine the identity of different materials present within a sample.

3.2.2 EDX Data Analysis

The darker areas in an EDX image are the carbon support, the bright white areas the metal catalyst, an example of a typical image being given in **Figure 13**. The image is acquired by narrowing down the electron beam and focussing on a small area of the sample and scanning across. The number of counts for a specific element can be plotted against the distance the EDX spot has been scanned to give an elemental profile of the sample.

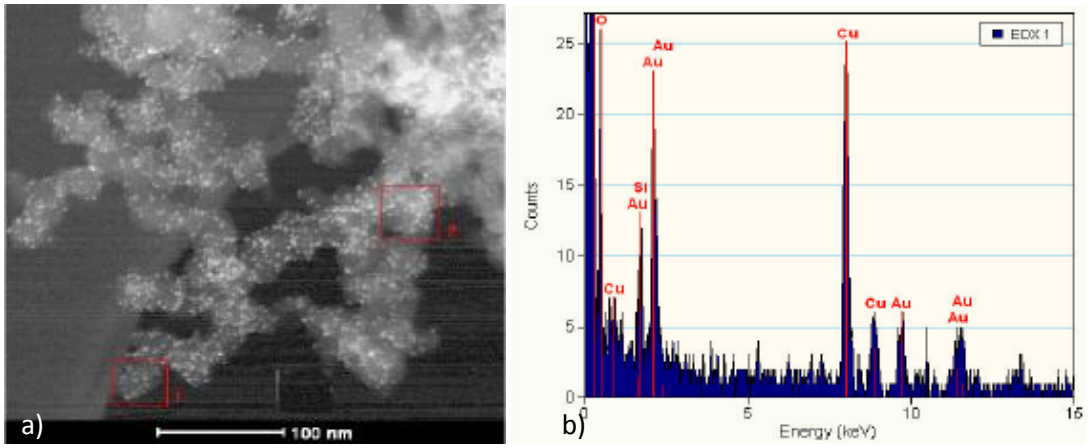

Figure 13: a) Typical TEM HAADF image, and b) EDX response from red box labelled 1 in TEM image. Cu contribution to signal is from grid.

3.2.3 Experimental of TEM and EDX

Powder samples for TEM-EDX were crushed between two glass slides and samples positioned onto a lacey carbon coated Cu "finder" grid with the aid of a micromanipulator. The samples were examined for particle size analysis in a Tecnai F20 transmission electron microscope. The microscope was operating with a voltage of 200 kV and C2 apertures of 30 & 50 m. Bright field, high-resolution electron microscopy, EDX and HAADF modes were used. TEM EDX work was carried out at the Johnson Matthey Technology Centre by Greg Goodlet and Don Ozkaya.

Aberration corrected images were obtained using a Jeol JEM-2100 LaB6 scanning transmission electron microscope. Bright field, high-resolution electron microscopy and HAADF modes were used. AC-STEM work was carried out at the Nanoscale Physics Research Laboratory, University of Birmingham by Don Ozkaya and myself.

4 X-ray Diffraction (XRD)

XRD is a non-destructive technique commonly used in catalyst characterisation. It relies on long range order to provide information on crystallite size and any phase(s) present[20].

4.1 Theory of XRD

X-rays have wavelengths in the Å range, similar to interatomic distances, and can penetrate solids due to their high energy, making them suitable to probe internal structure. X-ray diffraction (XRD) is used to identify long range order, bulk phases, monitor kinetics of bulk transformations, estimate particle sizes and can be applied *in situ*[17,21]. XRD is the scattering of X-ray photons by atoms in a periodic lattice giving rise

to interference effects. **Figure 14** shows how the lattice spacings can be derived from X-ray diffraction using the Bragg equation (**Equation 14**).

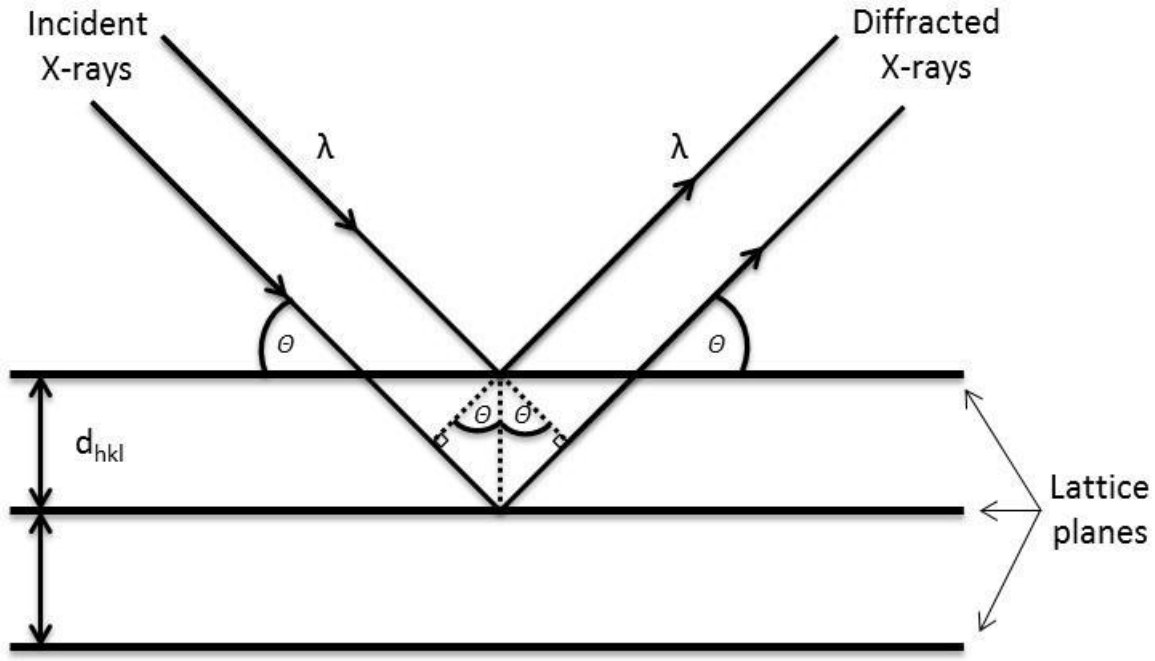

Figure 14: Schematic illustration of Braggs law

$$n\lambda = 2d\sin\theta$$

Equation 14

Where λ is the wavelength of the X-rays, d is the distance between two lattice planes, θ is the angle between the incoming X-rays the reflecting lattice plane, n is an integer called the order of the reflection.

A powder sample for XRD consists of a large number of very small crystals with random orientations. Over all the crystals in the sample, for a given set of *hkl* planes, a few of the crystals (with spacing d_{hkl}) will be aligned in the correct direction with the incoming beam to allow Bragg reflection at angle $2\theta_{hkl}$ to the incoming beam (creating a diffracted cone of radiation). The intensity is obtained from summing over all unit cells of the crystal (then integrated)[17,20].

4.2 Experimental Aspects of XRD

The XRD analysis used a Bruker AXS D8 Advance diffractometer in parallel beam mode with a 60 mm Gobel mirror, and a Ni filtered Cu K_α X-ray source. XRD patterns were collected over a scan range of 10° to 170° 2Θ with a 0.022° step size at a scan rate of 0.264° 2Θ per minute. The diffracted beam was collected using a Vantec Position

Sensitive Detector. All XRD data reported here was collected by Tim Hyde of Johnson Matthey Technology Centre.

4.3 Data Analysis

Crystallite size was determined by both the Rietveld Method (Topas V3), and Formfit V5.5, and was supplied by Tim Hyde of Johnson Matthey Technology Centre.

5 Nanoparticle Synthesis

5.1 Theoretical aspects

Au nanoparticles can be synthesised using a variety of amines or thiols to control the particle size. A schematic of this is shown in **Figure 15**.

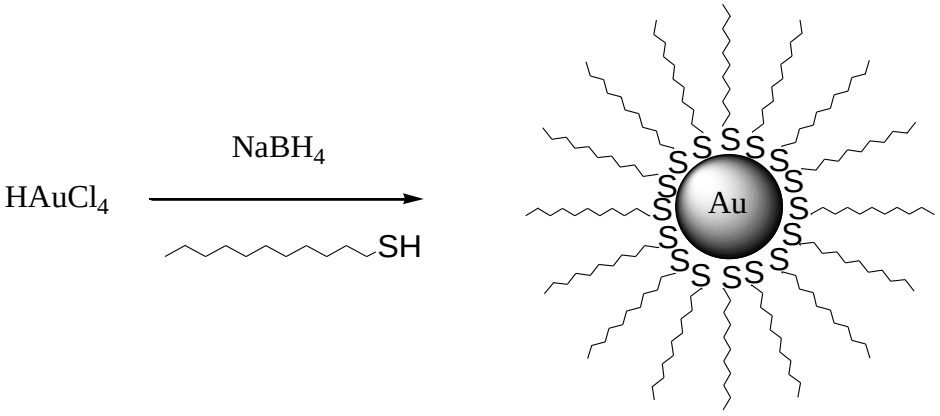

Figure 15: Synthesis of thiol monolayer protected Au nanoparticles.

Thiols have a strong affinity to the Au surface, and so make a good protecting layer on the surface[22]. The exact mechanism is still unclear, though it has been suggested that the Au core atoms each donate a single electron to delocalised orbitals and the protecting thiol groups accept the electrons into a localised orbital[23,24]. The initial two phase mixing is to transfer the chloroaurate anion ($AuCl_4^-$) from the aqueous to the organic layer by means of the tetraoctylammonium bromide (TOAB) acting as a phase transfer reagent. The anion is then reduced by sodium borohydride ($NaBH_4$, acting as a source of electrons) in the presence of dodecanethiol. This is shown in **Equation 15** and **Equation 16** below[25]:

$$AuCl_{4\,(aq)}^{-} + [N\,Br(C_8H_{17})_4]^{+}C_6H_5Me \rightarrow [N\,(C_8H_{17})_4]^{+} + [AuCl_4^-]\cdot(C_6H_5Me)^{+}Br^{-} \quad \textbf{Equation 15}$$

$$mAuCl_4^- (C_6H_5Me) + nC_{12}H_{25}SH (C_6H_5Me) + 3\ me^-$$

$$\rightarrow 4mCl^-(aq) + (Au)_m (C_{12}H_{25}SH)_n (C_6H_5Me) \qquad \textbf{Equation 16}$$

Au chloride can also be reduced by citrate in aqueous solutions to form colloidal nanoparticles[26]. The citrate is oxidised to dicarboxy acetone, and the Au (III) is reduced by the borohydride to Au (I). The Au (I) chloride then disproportionates to form metallic Au and Au (III) chloride, facilitated by the dicarboxy acetone molecules bringing the Au (I) species in close proximity (**Figure 16**).

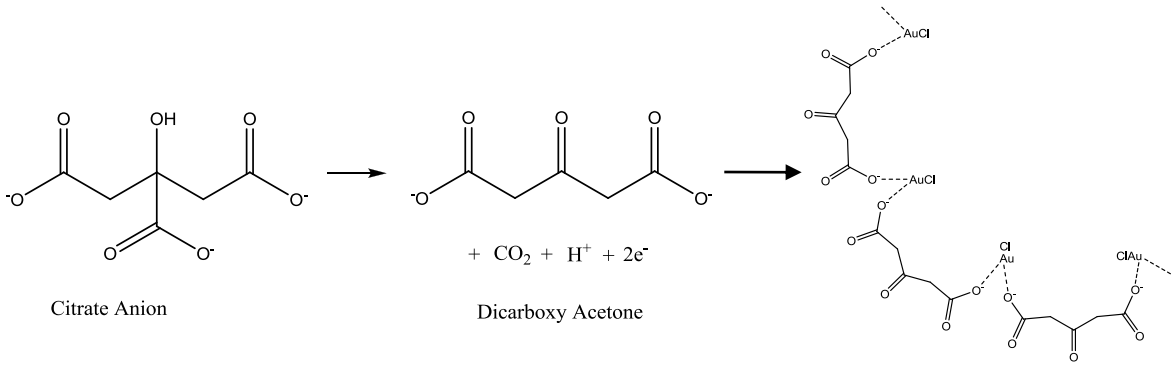

Figure 16: Illustration of binding of aurous species with dicarboxy acetone[26].

5.2 Synthesis of Dodecanethiol Stabilised Au Nanoparticles by Borohydride reduction

The thiol encapsulated nanoparticles were prepared by the method of Brust *et al.* [25]. An aqueous solution of hydrogen tetrachloroaurate (0.178 g, 15 ml, 30 mmol dm^{-3}) was mixed with a solution of tetraoctylammonium bromide (1.094 g) in toluene (40 ml, 50 mmol dm^{-3}). The two-phase mixture was vigorously stirred and transferred to a separating funnel until all the tetrachloroaurate was transferred into the organic layer. The aqueous solution was initially yellow, but quickly faded as the toluene phase became deep orange/brown in colour. Dodecanethiol (85 mg, ~0.1ml) was added in to the organic phase. A freshly prepared aqueous solution of sodium borohydride (0.19 g, 12.5 ml, 0.4 mol dm^{-3}) was slowly added with vigorous stirring.

The mixture was magnetically stirred for 3 hours. The organic phase was then separated, reduced to ~10 ml under vacuum, forming a dark red/brown waxy liquid, and mixed with 200 ml ethanol. The mixture was kept overnight at 255 K to remove excess thiol and precipitate the nanoparticles. The dark brown precipitate was filtered off and washed with ethanol to remove any remaining thiol, then dissolved in 10 ml toluene and again precipitated with 200 ml ethanol before being kept at 255 K for 4

hours. The resultant black waxy solid was filtered, dissolved in ~10 ml hexane and the solvent removed under vacuum.

The nanoparticles were supported on carbon black (Vulcan XC – 72 R). The Au colloid dispersion and a suspension of Vulcan carbon XC – 72 R were combined in ethanol. The mixture was sonicated for 30 minutes, and refluxed at 353 K under vigorous stirring for 10 h. The powders were separated by filtration and then thoroughly washed with purified water, before being dried at 383 K for 2 h.

5.3 Synthesis of Citrate Stabilised Au Nanoparticles

Aqueous solutions of $HAuCl_4$ (0.15g, 750 ml) and trisodium citrate (0.11g, 750 ml) were prepared, and mixed together. Sodium borohydride (0.170 g) was dissolved in water (45 ml) and kept in ice. The borohydride solution was added drop wise over a period of 20 minutes under vigorous stirring.

The nanoparticles were supported on carbon black (Vulcan XC – 72 R). The carbon (0.3g) was added to the reduced aqueous gold/citrate solution and left to stir for 48 hrs. The mixture was filtered and washed with water. The black powder obtained was left to dry at room temperature overnight.

5.4 Preparation of Painted Electrodes

The required amount of catalyst (approx. 60 mg) was finely ground and then dispersed in a small amount of deionised water (0.75 ml). Nafion® (10.85 wt% solids in water) was added to the solution to give an ink with 30 wt% Nafion® solids when dry, according to **Equation 17**.

$$V_{Nafion®}(\mu L) = \frac{Mass_{Catalyst}(mg) \times wt\%\ Nafion®\ w.r.t.solid\ \times 1000}{wt\%\ Nafion® \times Density\ of\ Nafion®}$$

Equation 17

The mixture was sonicated for 20 minutes followed by mixing with a Fisher PowerGen 125 homogeniser. The resulting mixture was painted onto carbon paper (TGHP 090) which was then painted, dried, weighed, the process being repeated until the desired loading was obtained. The electrodes were pressed at 450 K and 1 bar for 3 minutes. Small circular electrodes (1.32 cm^2) were then cut to fit into the electrochemical cells and hydrated in deionised water.

6 Molecular Dynamics

6.1 Theoretical Aspects

The Gupta[27] and Sutton-Chen[28] potentials are semi-empirical potentials based on the second moment approximation to tight binding theory, containing a repulsive pair-wise and an attractive many body term. The tight-binding method (TB) assumes very short range interactions (first shell interactions, around the range of the lattice constant), and so each lattice site is treated independently. The second moment approximation extends this cut-off up to the fifth shell, improving the quality of results[27].

The Gupta potential has the form;

$$U_i(r) = \frac{1}{2}\sum_{j\neq i} A\exp\left(-p\frac{r_{ij}-r_0}{r_0}\right) - B\sqrt{\sum_{j\neq i}\exp\left(-2q_{ij}\frac{r_{ij}-r_0}{r_0}\right)}$$

Equation 18

where $\boldsymbol{A}$ is the repulsive pair-wise energy, $\boldsymbol{p}$ is the range exponent for the pair potential, $\boldsymbol{B}$ is the many-body attractive energy, $\boldsymbol{q_{ij}}$ is the range exponent for many-body potential, and $\boldsymbol{r_0}$ is the equilibrium bond length; $\boldsymbol{r_{ij}}$ is the distance between atoms *i* and *j*. The parameters are taken from Cleri & Rosato[27], with the modification of the $\boldsymbol{A}$ parameter being doubled due to a different representations of potential in the molecular dynamics program.

The Sutton-Chen potential has the form;

$$U_i = \varepsilon\sum_i\left[\frac{1}{2}\sum_{j\neq i}\left(\frac{a}{r_{ij}}\right)^n - c\sqrt{\sum_{j\neq i}\left(\frac{a}{r_{ij}}\right)^m}\right]$$

Equation 19

where $\boldsymbol{\epsilon}$ is a parameter with the units of energy, $\boldsymbol{a}$ is a parameter with the dimensions of length, $\boldsymbol{c}$ is a positive dimensionless parameter, and $\boldsymbol{m}$ and $\boldsymbol{n}$ are positive integers. The parameters are taken from Sutton & Chen[28].

The potentials were tested on a bulk system containing 256 face-centred-cubic packed atoms in a cube using periodic boundary conditions (PBC). PBC are used to simulate large systems (in this case bulk metal) by modelling a small part of the system distant from all edges/surfaces. In effect, the atoms that appear to be on the "surface" of the

simulation cell act as if they are within an infinite matrix of atoms and so surface effects are negligible.

6.2 Experimental Aspects

Classical molecular dynamics (MD) simulations have been performed using the DL_POLY 2.0[29] software package. The simulations were carried out within the micro-canonical (NVE) ensemble, with an integration time-step of 1 fs. The atomic forces and velocities were equilibrated for 50 ps after which the molecular dynamic simulation was run for 2 ns. Data were collected during the simulation after confirming that both the energy and temperature were stabilised.

The simulations were performed on "spherical" nanoparticles 55, 177, 381 and 767 atoms for both Au and Pt corresponding to average nanoparticle diameters of 1.44 nm, 2.02 nm, 2.60 nm and 3.17 nm for gold, and of 1.39 nm, 1.94 nm, 2.50 nm and 3.05 nm for platinum, respectively. These sizes cover the range of the experimentally determined diameters of the nanoparticles.

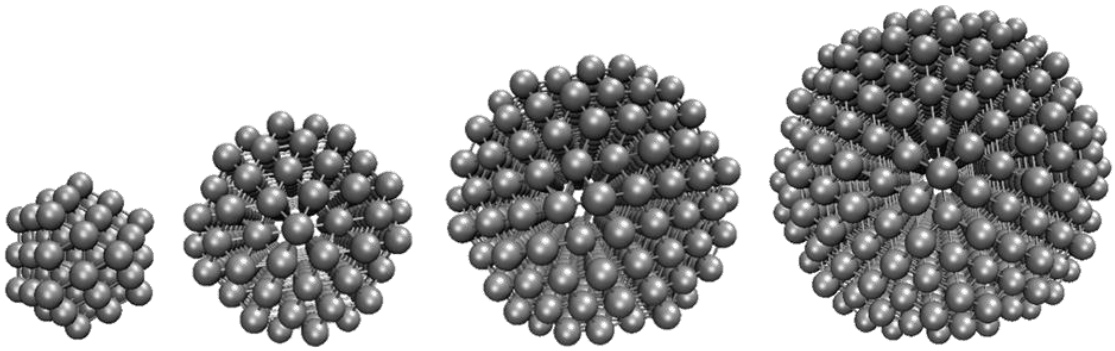

55 atom 177 atom 381 atom 767 atom

Figure 17: Starting configurations of "spherical" nanoparticles.

The initial structures for the simulated nanoparticles were constructed with ATOMS[14] (**Figure 17**). The lattice parameters for constructing the nanoparticles were obtained from a unit cell representation of the face-centred cubic (fcc) structure of the corresponding bulk metal. The Gupta potential was used to simulate both Au and Pt nanoparticles, and the Sutton-Chen potential for the Pt nanoparticles only. The MD simulations were conducted at temperatures from 20 K to 300 K. Work using the Gupta potential for Au was carried out by Nicholas Zonias and myself. All Pt nanoparticle simulations were carried out by Nicholas Zonias (University of Southampton).

7 Electrochemical Methods

Electrochemical techniques are key in studying the behaviour and structure of nanoparticle electrocatalysts, and also provide a means of modifying the surface and properties of these particles. Firstly cyclic voltammetry is used to characterise the nanoparticles; secondly, underpotential deposition is used to modify the surface of the nanoparticles to investigate the contribution of the surface structure to the EXAFS signal.

7.1 Cyclic Voltammetry

7.1.1 Basic Principles

Cyclic voltammetry (CV) is a potentiodynamic voltammetric measurement, used in particular to study the redox properties of electroactive species. CV consists of cycling the potential of an electrode (**Figure 18**) in an unstirred solution and measuring the resulting current.

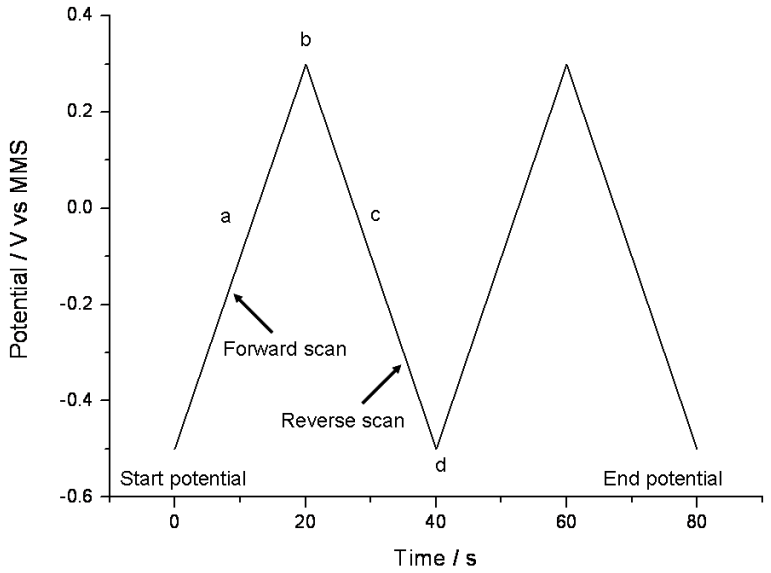

Figure 18: Typical waveform for cyclic voltammetry – a triangular potential waveform with switching potentials at 0.3 and -0.5 V vs. MMS.

The start potential is chosen at a suitable limit for the system under study, generally the open circuit potential (OCP - where there is no current flowing). The voltage is then increased linearly as a function of time (a) up to the potential at (b) oxidising the system, but stopping before electrolysis of the supporting electrolyte occurs. The

potential is swept back (c) to the start potential (d) reducing the system. Measurements may also be done where the system is first reduced then oxidised.

7.1.2 Experimental Aspects

A three electrode electrochemical cell (**Figure 19**) was used to test the electrochemical techniques in the lab before the *in situ* electrochemical cell was used for the EXAFS studies (**Figure 9**, section 2.2.7). An Autolab PGSTAT30 potentiostat was used to connect and control all three electrodes. The painted electrode served as the working electrode (WE), held in place to the Pt wire contact by a screw cap. A Pt wire mesh served as the counter electrode (CE), and a mercury mercurous sulphate (MMS) Hg/Hg_2SO4 was used as the reference electrode (RE). The RE was calibrated prior to use against a reversible hydrogen electrode (RHE) system of Pt wire in hydrogen purged 1M H_2SO_4; the MMS had a potential of 0.69 V vs RHE. The RE was used in conjunction with a Luggin capillary to reduce any errors resulting from resistance in the electrolyte solution. The cell had a total volume of 150 ml.

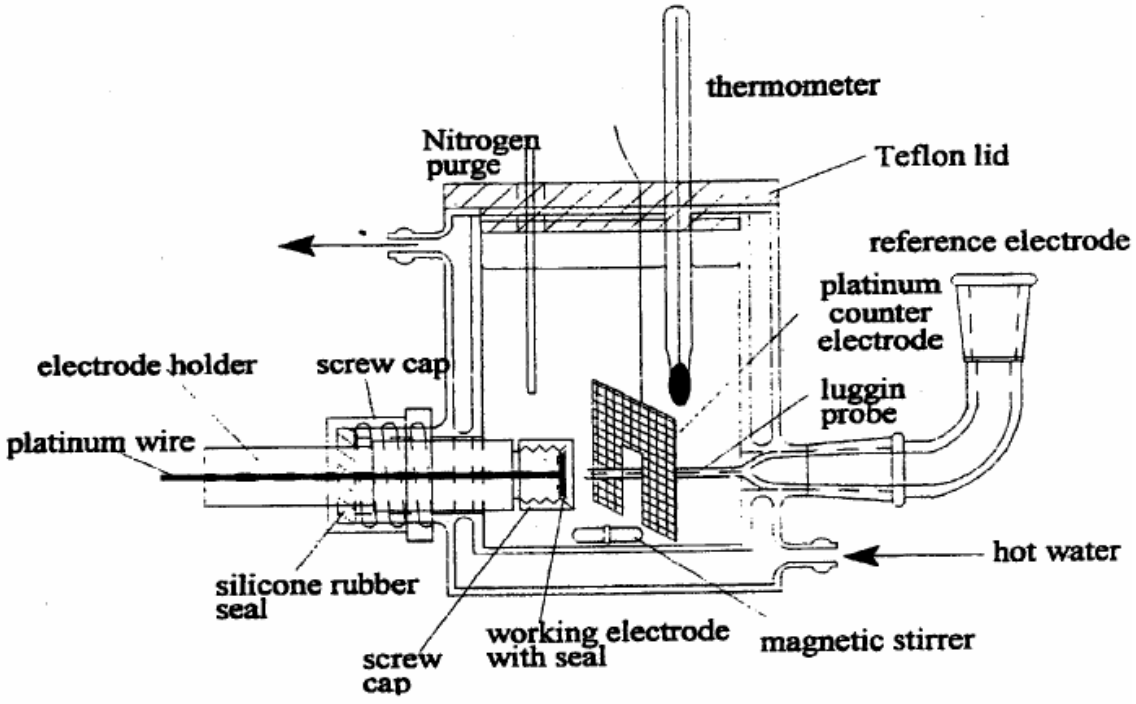

Figure 19: Example of the three electrode electrochemical cell[30].

The three electrode cell was filled with 1.0 M H_2SO_4, and purged with N_2 for 15 minutes whilst stirring to remove any dissolved oxygen. After this the gas was left to bleed over the surface of the electrolyte and the stirring stopped. CVs were taken between -0.69 and 0.90 V vs. MMS until the scans overlaid.

7.1.3 Cyclic Voltammetry of Au in Acid

The cyclic voltammetry of Au in acid is fairly straightforward, with only oxide formation/removal and double layer charging effects present (**Figure 20**).

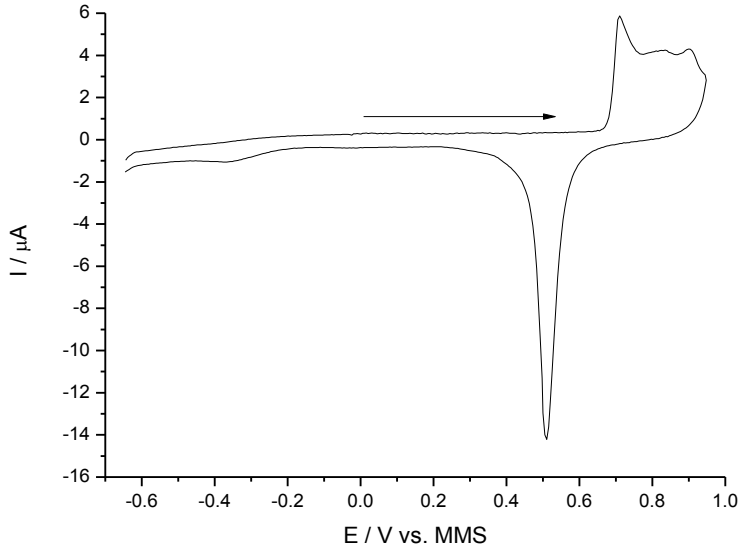

Figure 20: CV of bulk Au (mm diameter disc) in 1 M H_2SO_4. Scan rate 10 mV s^{-1}, forward scan indicated by arrow.

The double layer region extends from -0.1 V to +0.3 V vs. MMS, and arises from build-up of charge on the electrode surface. Oxide monolayer formation begins at 0.65 V vs. MMS, with oxygen evolution beginning at +1.0 V vs. MMS (not shown). The broad anodic peak, and presence of hysteresis indicate that the process does not occur very reversibly. The maximum anodic limit for the Au nanoparticle electrochemistry was chosen to be 0.90 V vs. MMS as beyond this dissolution of the nanoparticles occurs at an appreciable rate.

7.2 Underpotential Deposition

7.2.1 Basic Principles

Underpotential deposition (UPD) of Cu occurs positive to the bulk deposition potential[31], and is visible as a small current peak occurring upon the deposition of the first monolayer on the electrode which is slightly positive in relation to the peak associated the bulk deposition. On single crystal surfaces the technique reliably deposits a monolayer coverage of Cu, that can then be exchanged for a more noble metal. In terms of modifying electrocatalysts this is extremely useful, though for this

study, a complete surface capping for structural investigation[32] is the desired state, and so the technique was stopped at the Cu deposition stage.

7.2.2 Experimental Aspects

The electrochemical cell was set up as in section 7.1.2, and CVs collected at 10 mV s^{-1} in 0.5M H_2SO_4 until they overlaid. The anodic limit was decreased until no Au oxide formation/removal was present and a further CV collected. The solution was changed to one of 2mM $CuSO_4$ in 0.5 M H_2SO_4 that was purged in N_2 for 15 minutes, and the same set of CVs collected. The open circuit, monolayer and bulk deposition potentials were taken from these scans, as well as the onset of the stripping peaks, and were used as potential hold points for the *in situ* EXAFS studies.

7.2.3 *In situ* EXAFS Studies of Cu UPD on Au Nanoparticles

The *in situ* cell was set up on the beamline as detailed in section 2.2.7 with a pre-prepared painted electrode placed inside the cell. The electrode was cycled in 0.5 M H_2SO_4 between -0.625 V and +0.900 V vs. MMS at 50 mVs^{-1} until the scans overlaid. For each desired measurement, a CV was collected between -0.625 V and +0.900 V vs. MMS, and between -0.625 and +0.200 V vs. MMS at 10 mV s^{-1} followed by holding the potential at the desired limit whilst recording the current profile.

Once the current had stabilised the EXAFS was collected. After each set of EXAFS scans the electrolyte was pumped through the cell and the potential slowly moved to the next desired limit. The procedure was run once with 0.5 M H_2SO_4 as the supporting electrolyte at the Au L_{III} edge, and once with 2 mM $CuSO_4$ in 0.5 M H_2SO_4 as the electrolyte on a single painted electrode at both the Au L_{III} and Cu K edges

8 References

(1) Lytle, F. W. *Journal of Synchrotron Radiation* **1999**, *6*, 123.

(2) Kronig, R. d. L. *Zeitschrift für Physik A Hadrons and Nuclei* **1932**, *75*, 191.

(3) Sayers, D. E.; Stern, E. A.; Lytle, F. W. *Physical Review Letters* **1971**, *27*, 1204.

(4) Lee, P. A.; Pendry, J. B. *Physical Review B* **1975**, *11*, 2795.

(5) Stern, E. A.; Sayers, D. E. *Physical Review Letters* **1973**, *30*, 174.

(6) Rehr, J. J.; Albers, R. C. *Reviews of Modern Physics* **2000**, *72*, 621.

(7) Stern, E. A. *Contemporary Physics* **1978**, *19*, 289

(8) Li, G. G.; Bridges, F.; Booth, C. H. *Physical Review B* **1995**, *52*, 6332.

(9) Teo, B. K. *EXAFS: Basic Principles and Data Analysis*; Springer Verlag: Berlin, 1986; Vol. 9.

(10) Brookhaven National Laboratory: 2010, p http://www.nsls.bnl.gov/about/imagelibrary/images/lr/NSLS_Experimental_Floor_lowres.jpg.

(11) Golovchenko, J. A.; Levesque, R. A.; Cowan, P. L. *Review of Scientific Instruments* **1981**, *52*, 509.

(12) McMaster, W. H.; Grande, N. K. D.; Mallett, J. H.; Hubbell, J. H. *Compilation of X-ray Cross Sections*; Lawrence Livermore National Laboratory Report UCRL-50174 Section II Revision I, 1969.

(13) Newville, M. *Journal of Synchrotron Radiation* **2001**, *8*, 322.

(14) Ravel, B. *Journal of Synchrotron Radiation* **2001**, *8*, 314.

(15) Ravel, B.; Newville, M. *Journal of Synchrotron Radiation* **2005**, *12*, 537.

(16) Newville, M.; Limacrvincedilscaron, P.; Yacoby, Y.; Rehr, J. J.; Stern, E. A. *Physical Review B* **1993**, *47*, 14126.

(17) Niemantsverdriet, J. W. *Spectroscopy in Catalysis*; 2 ed.; Wiley-VCH, 2000.

(18) *Nanoscience and nanotechnologies: opportunities and uncertainties*, The Royal Society, 2004.

(19) Hetherington, C. *Materials Today* **2004**, *7*, 50.

(20) Warren, B. E. *X-Ray Diffraction*; Dover Publications Inc.: New York, 1990.

(21) Azaroff, L. V.; Kaplow, R.; Kato, N.; Weiss, R. J.; Wilson, A. J. C.; Young, R. A. *X-Ray Diffraction*; McGraw-Hill, Inc.: USA, 1974.

(22) Luo, Y. *Materials Letters* **2007**, *61*, 1039.

(23) Whetten, R. L.; Price, R. C. *Science* **2007**, *318*, 407.

(24) Jadzinsky, P. D.; Calero, G.; Ackerson, C. J.; Bushnell, D. A.; Kornberg, R. D. *Science* **2007**, *318*, 430.

(25) Brust, M.; Walker, M.; Bethell, D.; Schriffin, D. J.; Whyman, R. *Journal of the Chemical Society-Chemical Communications* **1994**, 801.

(26) Kumar, S.; Gandhi, K. S.; Kumar, R. *Industrial & Engineering Chemistry Research* **2007**, *46*, 3128.

(27) Cleri, F.; Rosato, V. *Physical Review B* **1993**, *48*, 22.

(28) Sutton, A. P.; Chen, J. *Philosophical Magazine Letters* **1990**, *61*, 139.

(29) Smith, W.; Forester, T. R. *Journal of Molecular Graphics* **1996**, *14*, 136.

(30) Hogarth, M. P. PhD, University of Newcastle upon Tyne, 1995.

(31) Brankovic, S. R.; Wang, J. X.; Adzic, R. R. *Surface Science* **2001**, *474*, L173.

(32) Lee, J. R. I.; O'Malley, R. L.; O'Connell, T. J.; Vollmer, A.; Rayment, T. *The Journal of Physical Chemistry C* **2009**, *113*, 12260.

CHAPTER THREE: CHARACTERISATION OF MONOMETALLIC CATALYSTS

Chapter One gave an introduction into the growing use of nanoparticles in catalysis and the need for accurate characterisation of particle size to feed into models of structure and property relationships. Chapter Two introduced the characterisation techniques; this chapter details the characterisation of a series of monometallic nanoparticle catalysts and cross correlation between results. The samples studied were two series of Pt/C nanoparticle catalysts, and two Au/C nanoparticle catalysts prepared by different methods.

1 Introduction

Characterisation is vital if a quantitative link is to be made between a material's structure and properties. There is a large body of research detailing the different methods of structural characterisation currently available, and also of the most recent advances. Problems encountered when seeking to determine atomic structure on the nanoscale include the physical limitations of techniques, non-uniform size distribution within the samples coupled with a variety of means to weight data (resulting in differences in the sizes obtained), and the on-going development in the interpretation of results such as with EXAFS[1,2]. Line broadening with XRD[3-5] effectively places a lower limit on the size of particle that can be resolved. TEM is a direct probe[6] and can regularly attain resolutions of below 1 nm, and even down to 0.1 nm with the use of aberration correction, but particle instability within the electron beam along with the inherent local nature of TEM[3,7-9] limits the technique. XRD and EXAFS, as bulk probes, are able to provide a much more representative picture of the sample under study but, unlike TEM and EXAFS, XRD cannot detect amorphous materials, and therefore is unable to detect the smallest catalyst particles[1]. EXAFS is an indirect probe of particle size[10], and the coordination numbers determined need interpretation to provide a means of particle size determination. The interpretation of particle size from coordination number is discussed in depth later on in the chapter.

To complicate matters further, each technique is weighted differently. Therefore average particle size is not a unique quantity for a polydisperse sample as a consequence of the different weighting methods that can be employed. The effect of polydispersity is such that if a sample consists primarily of small particles with a small

proportion of large particles the average number weighted size will be small. However if the results are volume weighted the average size will be much larger (as a result of the few large particles present) resulting in a discrepancy between the determined sizes. Volume weighting counts each atom equally, whereas number weighting counts each crystallite/particle equally (e.g. TEM/XRD); in this sense, EXAFS can be said to be a volume weighted technique[3]. XRD and TEM can be converted into volume weighted results for a more direct comparison and the process is discussed later in this chapter. Therefore the more polydisperse a sample is, the greater the difference in sizes seen by each technique will be.

The desired goal in characterisation is the ability to constrain a unique structural solution for both size and shape from only one technique. With the current limitations for each technique, this is rarely possible. Li *et al*. imaged an Au 309 atom cluster in three dimensions with aberration corrected scanning transmission electron microscopy (AC-STEM[9]) by comparing the integrated intensity of the signal with theoretical modelling. This process was however very time intensive, was even more local in its probing than TEM, and required size selected nanoparticles (by mass spectrometry) to ensure monodispersity and simplification of analysis. As such, it fails to be a viable method for routine large scale characterisation of polydisperse samples.

Cervera Gontard *et al*. used three-dimensional tomographic reconstruction of HAADF-TEM (Chapter Two, section 3.1.1) images to determine a particle size distribution[11] and a complete shape analysis of a small sampling of nanoparticles. Whilst not requiring a pre-selection of the most suitable particles to study (as was the case with Li *et al*.) this too is time consuming, due to the complexity of tomographic measurements on a nanoscale, to be able to image enough particles for a measurement that is representative of the sample. The same study illustrated the use of bulk probes such as XRD and SAXS (small angle X-ray scattering) to determine a particle size distribution as well as that derived from the TEM micrographs. The combination of the detailed structural characterisation of the TEM reconstructions coupled with the bulk probes of the XRD and SAXS allow for a more complete picture of the sample on a local and bulk scale, provided the similarities and differences between the characterisation techniques are understood.

Electron microscope methods offer perhaps the most complete structural solution for single nanoparticles, but their local nature and the strict conditions the measurements must be performed under diminish their effectiveness and applicability when looking

at catalysts, since increasingly there is a desire to characterise nanoparticle catalysts *in situ*. *In situ* XRD measurements are routinely carried out and *in situ* TEM is possible under mild conditions however the equipment to do so is not standard. Synchrotron methods such as XAS (but also small angle X-ray scattering) offer improvements over XRD for *in situ* measurements as any number of experimental conditions are possible, and are not limited by the need for sample crystallinity[12-15]. Techniques may be combined for *in situ* measurements such as EXAFS and XRD to offer powerful characterisation solutions under a range of experimental conditions[16-18]. The cross correlation of techniques allows for a much deeper understanding of the sample under study, if complementary methods are chosen, for example:

XRD vs. TEM

- Bulk probe
- Limited to larger crystallites (>2 nm)
- Amorphous material invisible
- Usually no beam damage

- Local Probe
- 0.1 Å resolution
- Amorphous material visible
- Beam damage at highest resolutions

XRD vs. EXAFS

- Long range order
- Crystalline only
- Not element specific
- Able to distinguish different crystallographic sites and phases
- Averages different elements in the same crystallographic sites

- Short range order
- Crystalline and amorphous
- Element specific
- Averages over all sites and phases
- Able to distinguish different elements in the same crystallographic sites (dopants)

This chapter will look at the cross- correlation between TEM, XRD and EXAFS of a series of monometallic nanoparticle catalysts supported on carbon, with the aim of rationalising the similarities and differences in size determined by each technique.

2 Experimental procedures

2.1 Catalyst preparation

The series of Pt/C nanoparticle catalysts were supplied by Johnson Matthey and the Au/C catalysts were prepared by two different methods. The details of all catalysts used in this work are in **Table 1**.

Table 1: Nominal loadings and nomenclature of monometallic nanoparticle catalyst samples investigated.

Sample	Nominal Loading / wt%	Treatment
Au/XC72R carbon (Thiol)	4	None
Au/ XC72R carbon (Citrate)	16	
Pt/Ketjen carbon	5	
	10	
	20	
	40	
	60	
Pt/Ketjen carbon (treated)	10	None
	10	Heated in N_2, 973 K
	10	Heated in N_2, 1273 K
	10	Heated in N_2, 1473 K

2.3 TEM and XRD

All samples for TEM and XRD were submitted to the Johnson Matthey Technology Centre for analysis. Data collection and analysis were completed by Don Ozkaya (TEM) and Tim Hyde (XRD).

2.4 EXAFS

The absorption edges of interest were the Au L_{III} (11919 eV) and Pt L_{III} (11564 eV) edges. Investigations were carried out on beamline X11A for the Au measurements and X23A2 for the Pt measurements. All EXAFS measurements in this chapter were collected in transmission mode using the cryostat cell. The samples were all prepared as boron nitride pellets. The Pt/C samples were reduced at room temperature by exposure to pure H_2 prior to data collection.

2.5 Sample Nomenclature

The focus in this work is on the sample size and structure and the characterisation of these properties rather than the behaviour of the samples as catalysts; as such samples will be referred to in terms of their nominal metal loading throughout, i.e. 10 wt% Pt/C for simplicity (**Table 1**).

3 Characterisation of Pt/C nanoparticle catalysts

3.1 TEM

TEM was used to give an indication of the average nanoparticle size and distribution in each sample. Micrographs were taken between 5 nm and 200 nm scale; an example micrograph for each sample is given in **Figure 1** below.

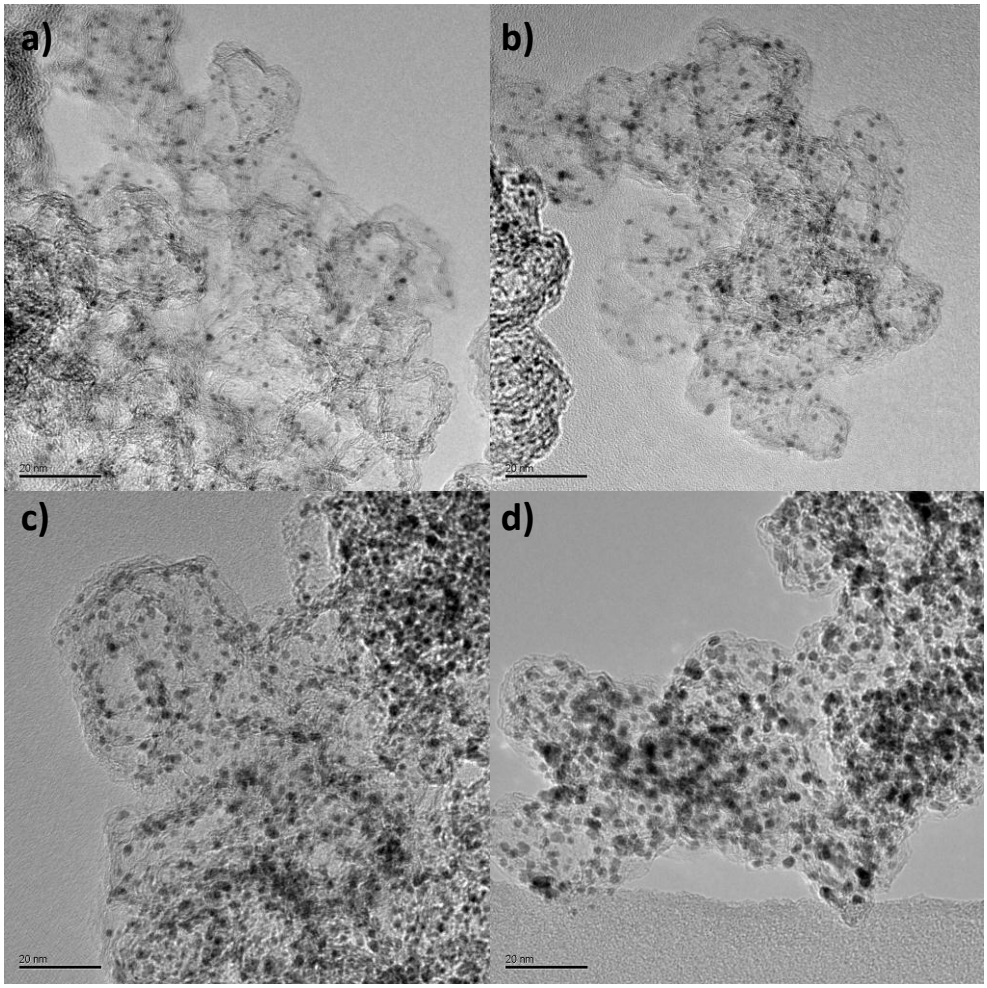

Figure 1: TEM micrographs of a) 10 wt% Pt/C, b) 20 wt% Pt/C, c) 40 wt% Pt/C and d) 60 wt% Pt/C. Scale bar is 20 nm.

Bright field (BF) micrographs at 10 and 20 nm scale were used for the particle size analysis (**Figure 2**), with between 350 and 600 particles being sampled. The samples all show the catalyst is well dispersed over the support, the distributions are all narrow, with small numbers of particles measured at either end of the distribution. These factors result in little change in average particle size when varying the weighting of the results (**Table 2**). The narrow distribution and even dispersion suggest that the whole of each sample is uniform, which is useful for studying the particle size effect, but also ideal for applying more advanced EXAFS characterisation methods (discussed in Chapter Four).

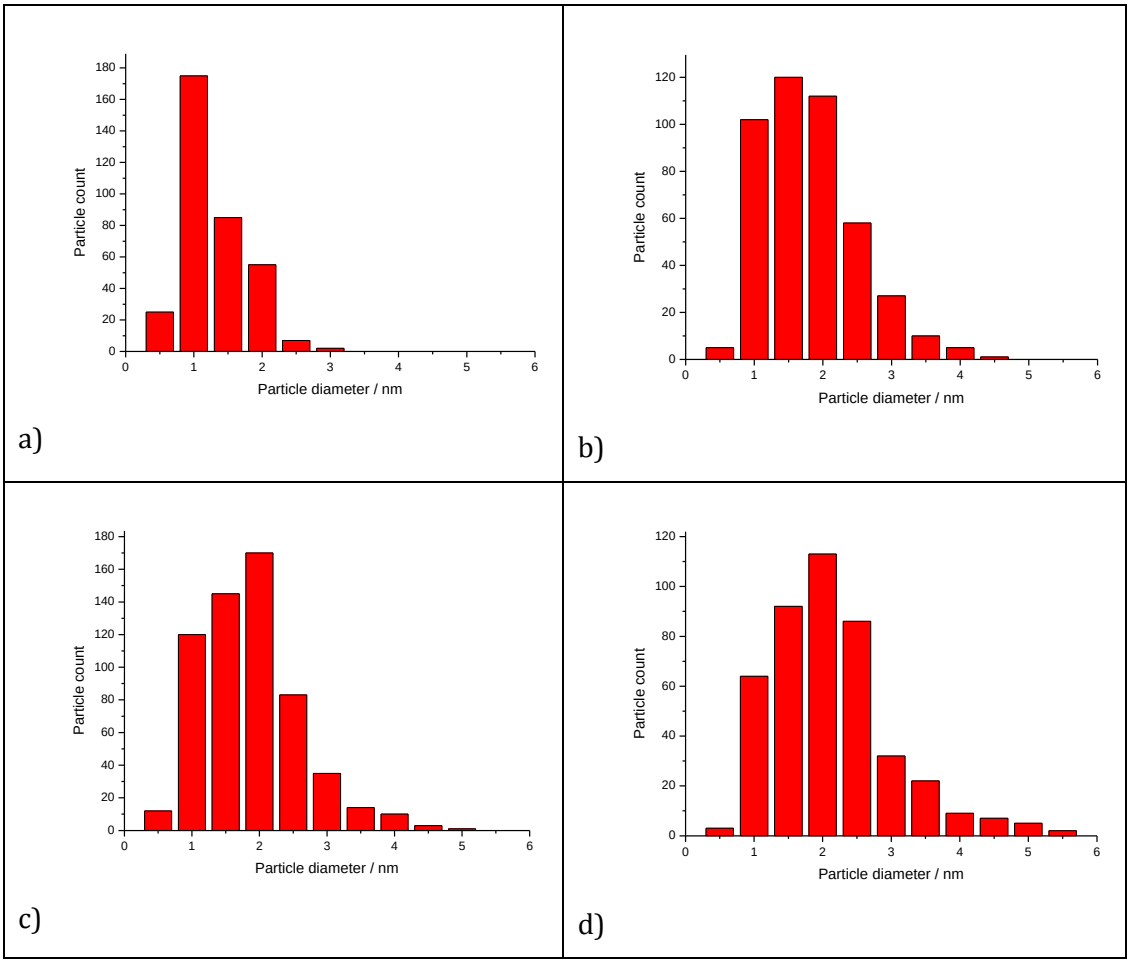

Figure 2: Particle size distribution of a) 10 wt% Pt/C, b) 20 wt% Pt/C, c) 40 wt% Pt/C and d) 60 wt% Pt/C.

Table 2: Comparison of particle size determinations from varying TEM weighting approaches.

Sample loading / wt% Pt/C	Number of observed particles	Average TEM particle size / nm				Standard deviation / nm
		D_0	D_n	D_a	D_{Vol}	
10	354	0.98	1.03	1.43	1.61	0.45
20	445	1.46	1.57	2.15	2.43	0.69
40	600	1.53	1.92	2.26	2.57	0.73
60	433	1.74	1.84	2.58	2.95	0.82

The various weightings for particle size distributions were calculated using TEMdist software[19], with the following definitions of each weighting as follows:

$$D_n = \text{number weighted average} = D_0 e^{0.5(\ln\sigma)^2}$$

Equation 1

$$D_a = \text{area weighted average} = D_0 e^{2.5(\ln\sigma)^2}$$

Equation 2

$$D_{Vol} = \text{volume weighted average} = D_0 e^{3.5(\ln\sigma)^2}$$

Equation 3

where,

D_0 is the mean of lognormal distribution and σ is the variance of lognormal distribution of spheres (measure of distribution width) as calculated in the TEMdist software.

In all cases the error (calculated as standard deviation of the particle sizes measured) is less than a third of the average particle size, a result of the narrow size distribution. Analysis of the distribution from BF images is complicated by distinguishing the particles from the carbon support[20], as well as contrast between adjacent particles and overlap between particles in projection[11].

All various weightings are dependent on the particle size distribution of the sample, and therefore the quality of the sample itself will heavily influence the effect the weighting procedure has. The means by which the weightings are calculated also clearly illustrates how one very large particle can greatly increase the variance and thus skew the average particle size.

The method by which the TEM derived particle size is weighted is not commonly reported although the simplest interpretation of a PSD is the mean of the lognormal distribution as it requires the least amount of data processing (The distribution is influenced by whether the sample is dominated by small or large particles, and this affects the position of the mean). Such a skew can lead to inconsistencies when correlating and comparing results that are inherently weighted in a different manner. Often, mean number weighted TEM results are compared with volume weighted XRD results erroneously, giving rise to a disagreement between the two methods[21]. This will be discussed further in **Section 6.3** of this chapter.

3.2 AC-STEM Pt/C

Aberration correction was used to gain a more detailed understanding of the exact morphology of the nanoparticles. With resolution capable of going below 0.1 nm, imaging of the packing of atoms is possible. **Figures 3** through **5** contain some sample micrographs.

Micrographs were collected in both BF and HAADF mode. The dark field mode, sensitive to backscattered electrons works particularly well at such high magnification, and was able to detect atomic debris on the support that was not bound in a nanoparticle (**Figure 3**).

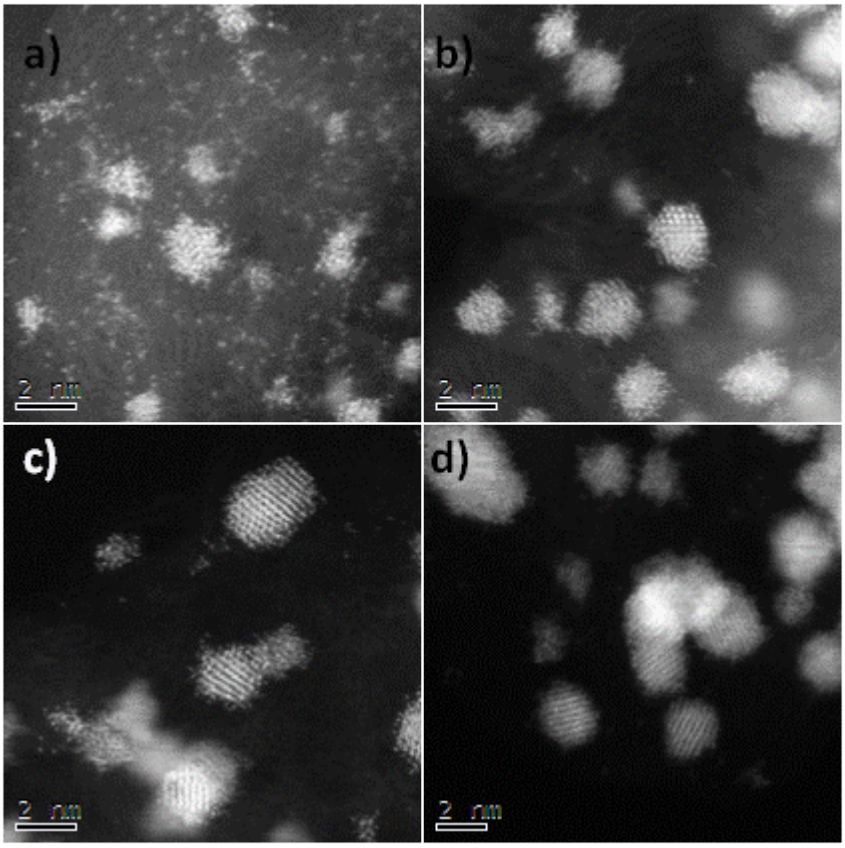

Figure 3: AC-STEM micrographs of a) 10 wt% Pt/C, b) 20 wt% Pt/C, c) 40 wt% Pt/C and d) 60 wt% Pt/C in HAADF mode. Scale bar is 2 nm.

The particles are non-spherical, tending towards hexagonal, suggesting cuboctahedral or icosahedral geometries, although intensity profiling[22] is required for determination of exact morphology. Characterising the morphology and support interaction would prove useful in preparing the molecular dynamics simulations to be detailed in Chapter Four. The aim of collecting AC-STEM micrographs was to gain more detailed images of the nanoparticle morphology, both top-down and side-on to the support. Unfortunately, this met with limited success for a number of reasons. The power of the electron beam at highest magnification caused the samples to vibrate, blurring the images. Scanning the beam faster reduced the image blur due to vibrations, but introduced scanning artefacts (**Figure 4**).

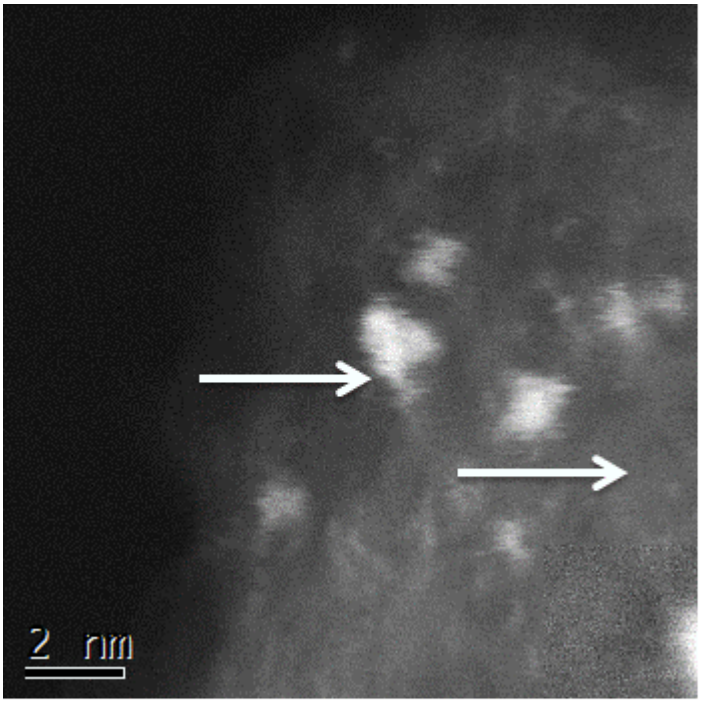

Figure 4: AC-STEM beam scanning artefacts in HAADF mode, direction marked by white arrows.

The smaller nanoparticles (lower loading Pt/C) having poorer crystallinity were much less stable to the electron beam, and began to disintegrate on imaging (Figure 5a-c), the electron beam breaking bonds within the nanoparticle and knocking atoms off the edges, and destroying any crystallinity that was initially present.

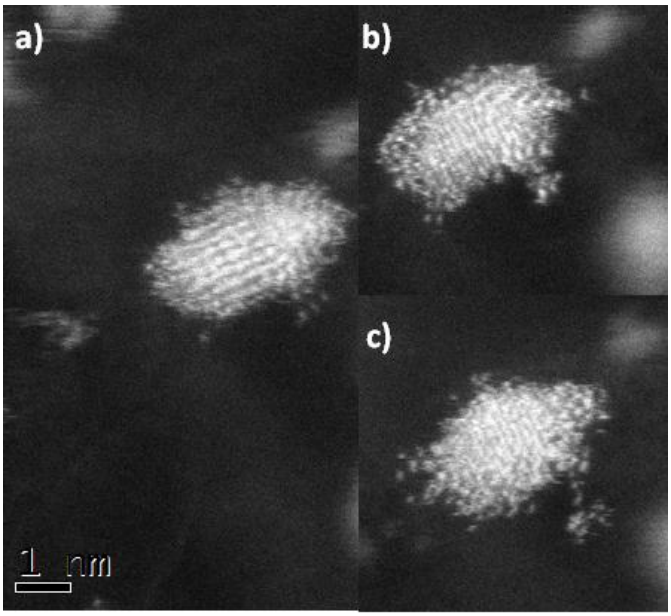

Figure 5: Beam damage at highest magnification, the time sequence of micrograph imaging runs a), b) then c).

The amount of atomic debris visible decreases with increased Pt loading, suggesting that increasing the loading during the synthesis stage forces the debris and nanoparticles to aggregate together, resulting in the increased particle sizes observed. Although much more crystalline and resilient to beam damage, the extent of the loading caused a large degree of overlapping of particles, and made identification of a stable side-on particle (for support interaction/morphology) highly improbable.

3.3 XRD

XRD was used to identify which phases were present in the samples, and to determine crystallite size, although due to the size of the nanoparticles, the latter was for cross-correlation purposes rather than absolute size determination. XRD patterns of the 10-60 wt% Pt/C samples are presented in **Figure 6**.

The broad diffraction peak at $2\Theta \sim 25°$ due to the Ketjen carbon support (**Figure 6e**) is observed in all patterns. The lowest loaded sample - 10 wt% (**Figure 6a**) - exhibits a small amount of (face centred cubic – *fcc*) crystalline Pt, although this is overlaid with some poorly tetragonal platinum oxide, most probably PtO. The amount of "crystalline" Pt is too small to be resolved and the convolution of the broad diffraction peaks makes crystallite size determination unfeasible, highlighting a limitation of using XRD to characterise very small particles.

As the sample loading is increased to 20 wt% (**Figure 6b**), the corresponding slight increase in size is enough to make the poorly crystalline Pt detectable by XRD, with more appreciable amounts detectable for the 40 wt% and 60 wt% samples (**Figure 6c** and **6d** respectively). The crystallite sizes were determined by a Rietveld analysis and presented in **Table 3**. In all samples, there is still some poorly defined PtO present.

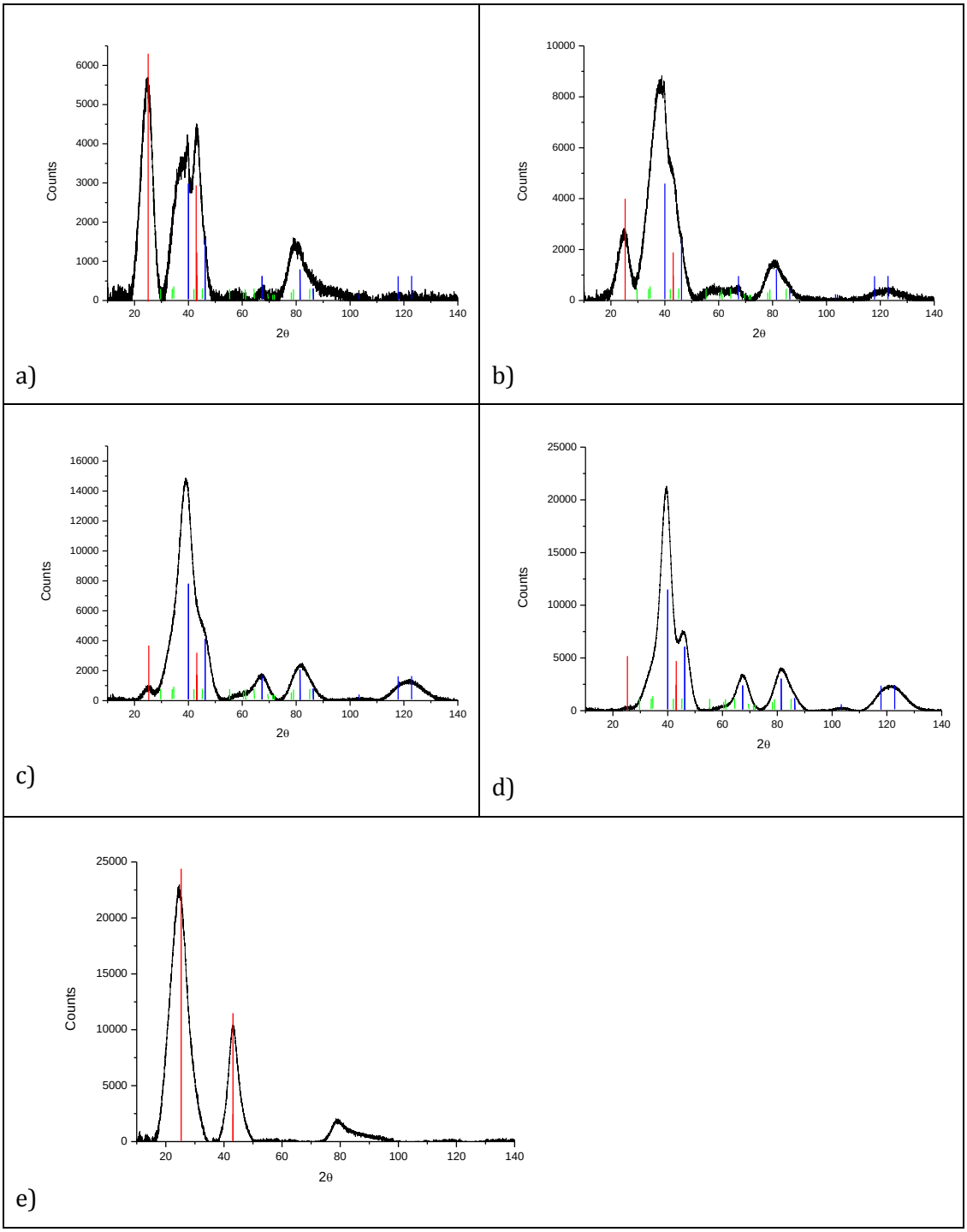

Figure 6: XRD patterns of a) 10 wt% Pt/C, b) 20 wt% Pt/C, c) 40 wt% Pt/C, and d) 60 wt% Pt/C. Data is the black line, | refers to cubic Pt (PDF No. 00-04-0802, a = 3.92 Å), | refers to tetragonal PtO (PDF No. 01-085-0714, a = 3.04 Å, c = 5.34 Å), and | refers to the Ketjen (EC600JD) carbon support in panel e).

The presence of the poorly defined oxide phases hinders the calculation of crystallite size, as does the relatively high contribution from the carbon support for the lower

loaded samples. Consequently, all crystallite sizes can only be regarded as approximations rather than absolute values.

Table 3: Rietveld derived XRD crystallite sizes. Size determination was not possible due to very poor crystallinity for the 10 wt% sample.

Sample / wt% Pt/C	Crystallite size / nm	
	L_{Vol} average crystallite size	**$D_{Vol} = 4/3*L_{Vol}$ (sphere) – mean volume weighted diameter**
10	---	---
20	1.10	1.46
40	1.36	1.81
60	1.69	2.25

where,

D_{Vol} = mean volume weighted diameter = $4/3*L_{Vol}$

The quantity L_{Vol} can be related to D_0 and σ (found in **Equations 1-3**) as follows:

$$L_{Vol} = \frac{3}{4} D_0 e^{3.5(\ln\sigma)^2}$$

Equation 4

The factor of $4/3$ in the XRD D_{Vol} calculation is related to the crystal shape, usually assumed to be spherical. By converting the weightings of XRD crystallite size to the D_{Vol} weighted method, a direct means of comparing results from TEM (**Equation 3**) and XRD is obtained[23], linked by the same two parameters, D_0 and σ. This is an improvement in general terms for cross-correlation, although a direct comparison can still not be provided as XRD measures crystallite size whilst TEM measures particle size (with the possible existence of twinned crystals or overlapping particles).

3.4 Standard EXAFS

The following section contains EXAFS fit by standard means up to the 4th coordination shell. In this work, standard analysis refers to using a bulk *fcc* structure to generate the theoretical scattering paths that FEFF calculates, and that are used to fit the experimental data to theory. None of the surface termination effects or anharmonic behaviour present in the nanoparticles are accounted for in this approach. These effects will be considered later in Chapter Four.

Data was fitted between 2-6 Å in R, 3-18 $Å^{-1}$ in *k* (cryostat data) and 3-17 $Å^{-1}$ (300 K data), with multiple *k*-weighting. The data was fitted starting at the first coordination shell, evaluating the fit by minimising the R_f and reduced χ^2, then moving radially outwards from the absorbing atom to the fourth coordination shell, including all single scattering paths and all major multiple scattering paths. The path degeneracy was also used as a fitting parameter due to the termination effects present in nanoparticles. To minimise the number of parameters in the fit the multiple scattering path σ^2 parameters were constrained based on the photoelectron mean free path length (**Table 4**. **Figure 7**).

Table 4: Fitting parameter constraints for standard EXAFS fits.

Scattering Path	Amplitude	Path length	Energy shift	Disorder
$Pt_{abs} - Pt_1 - Pt_{abs}$	N_1	$R_{eff} * \alpha$	E_0	σ^2_1
$Pt_{abs} - Pt_2 - Pt_{abs}$	N_2			σ^2_2
$Pt_{abs} - Pt_{1a} - Pt_{1b} - Pt_{abs}$	N_{MS}			$1.5*\sigma^2_1$
$Pt_{abs} - Pt_3 - Pt_{abs}$	N_3			σ^2_3
$Pt_{abs} - Pt_{1a} - Pt_{1c} - Pt_{abs}$	N_{MS}			$\sigma^2_1 + 0.5*\sigma^2_3$
$Pt_{abs} - Pt_{3a} - Pt_{1d} - Pt_{abs}$	$N_{MS}*2$			$\sigma^2_1 + 0.5*\sigma^2_3$
$Pt_{abs} - Pt_4 - Pt_{abs}$	N_4			σ^2_4
$Pt_{abs} - Pt_{1e} - Pt_{4a} - Pt_{abs}$	N_4*2			$\sigma^2_1 + 0.5*\sigma^2_4$
$Pt_{abs} - Pt_{1f} - Pt_{abs} - Pt_{1g} - Pt_{abs}$	N_4			$2*\sigma^2_1$
$Pt_{abs} - Pt_{1h} - Pt_{1i} - Pt_{1j} - Pt_{abs}$	N_4			$2*\sigma^2_1$
$Pt_{abs} - Pt_{1k} - Pt_{abs} - Pt_{1k} - Pt_{abs}$	N_4			$2*\sigma^2_1$

R_{eff} is the theoretical bond length for the scattering path, and α is the isotropic expansion coefficient.

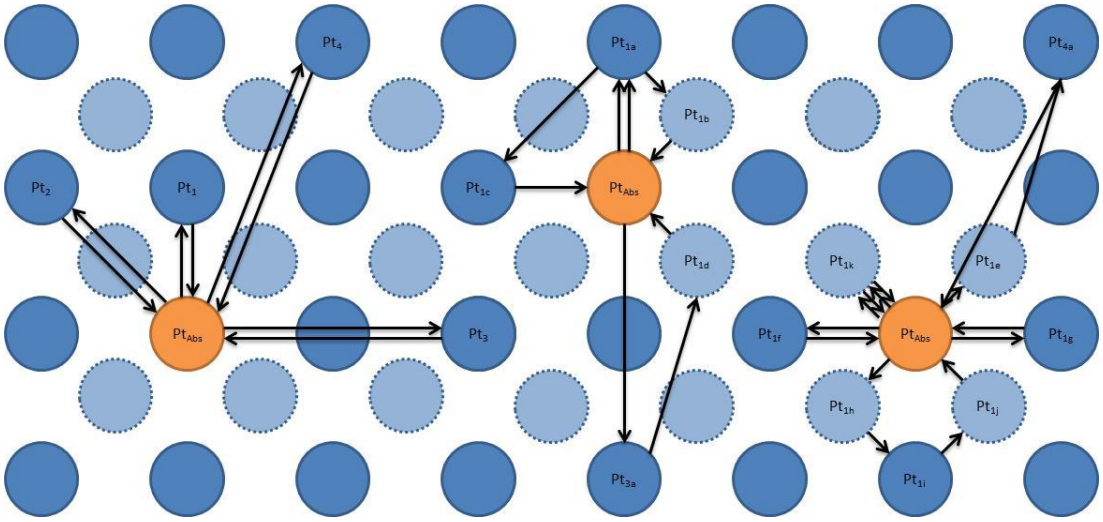

Figure 7: Representation of single and multiple scattering paths in Table 4. Orange circles denote absorbing atoms, dark blue circles are scattering atoms in plane of the absorbing atom and light blue (dashed outline) circles are beneath the plane of the absorbing atom.

Prior to collecting the nanoparticle data, a Pt foil was run to determine the amplitude reduction factor (S_0^2), without the which the coordination number cannot be accurately determined[24]. The amplitude reduction factor was found to be 0.85 ± 0.03 at the Pt L_{III} edge and all coordination numbers reported in this work were corrected using this amplitude reduction.

The EXAFS signal contained some noise with a low R component that could not be removed during data processing without affecting the amplitude of the data. This resulted in a slight misfit around 2 Å. Thermal vibrations damp down the EXAFS oscillations at higher *k* values in the 300 K data, and cause a decrease in the signal to noise ratio, hence the reduced fitting range.

The experimental data and fits for the 10-60 wt% Pt/C catalysts are presented in **Figures 8-11**, with the corresponding fitting parameters in **Tables 5-8**. All data was collected on beamline X23A2 of the NSLS.

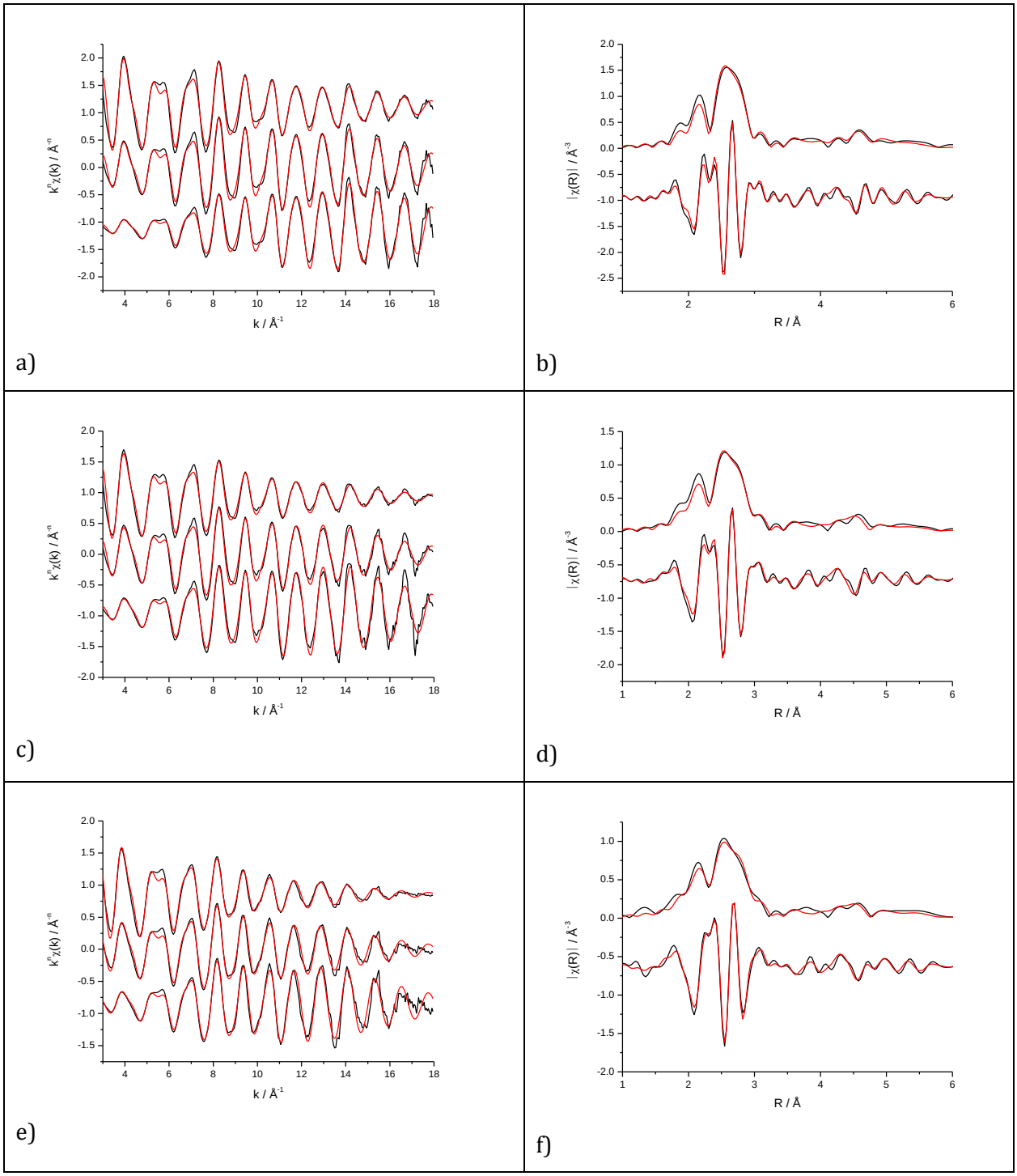

Figure 8: k^n weighted (k^1 top, k^2 middle, k^3 bottom of panel) experimental data (black) and fit (red) along with k^2 weighted magnitude and real Fourier transform for 10 wt% Pt/C at a-b) 20 K, c-d) 150 K and e-f) 300 K.

Table 5: Structural parameters for room temperature H_2 reduced 10 wt% Pt/C nanoparticles at 20 K, 150 K and 300 K, acquired at the Pt L_{III} edge, corresponding to the data in Figure 8.

Condition	10 wt% Pt/C					
	Shell	***N***	***R* / Å**	**σ^2 / Å^2**	**ΔE_0 / eV**	**R_f**
20 K vacuum	Pt-Pt_1	7.45 ± 0.43	2.73 ± 0.01	0.0048 ± 0.0002	8.25 ± 0.55	0.022
	Pt-Pt_2	2.72 ± 0.70	3.87 ± 0.01	0.0065 ± 0.0022		
	Pt-Pt_3	6.80± 2.04	4.74 ± 0.01	0.0058 ± 0.0016		
	Pt-Pt_4	4.38 ± 2.08	5.47 ± 0.01	0.0121 ± 0.0049		
150 K vacuum	Pt-Pt_1	7.53 ± 0.39	2.73 ± 0.01	0.0059 ± 0.0008	7.62 ± 0.48	0.022
	Pt-Pt_2	1.98 ± 0.79	3.87 ± 0.01	0.0065 ± 0.0024		
	Pt-Pt_3	7.68 ± 2.11	4.74 ± 0.01	0.0079 ± 0.0018		
	Pt-Pt_4	4.84 ± 1.91	5.47 ± 0.01	0.0128 ± 0.0049		
300 K	Pt-Pt_1	7.81 ± 0.49	2.75 ± 0.01	0.0068 ± 0.0003	5.53 ± 0.46	0.019
	Pt-Pt_2	2.24 ± 1.36	3.90 ± 0.01	0.0085 ± 0.0040		
	Pt-Pt_3	6.41 ± 3.84	4.77 ± 0.01	0.0087 0.0033		
	Pt-Pt_4	5.28 ± 1.79	5.51 ± 0.01	0.0121 ± 0.0043		

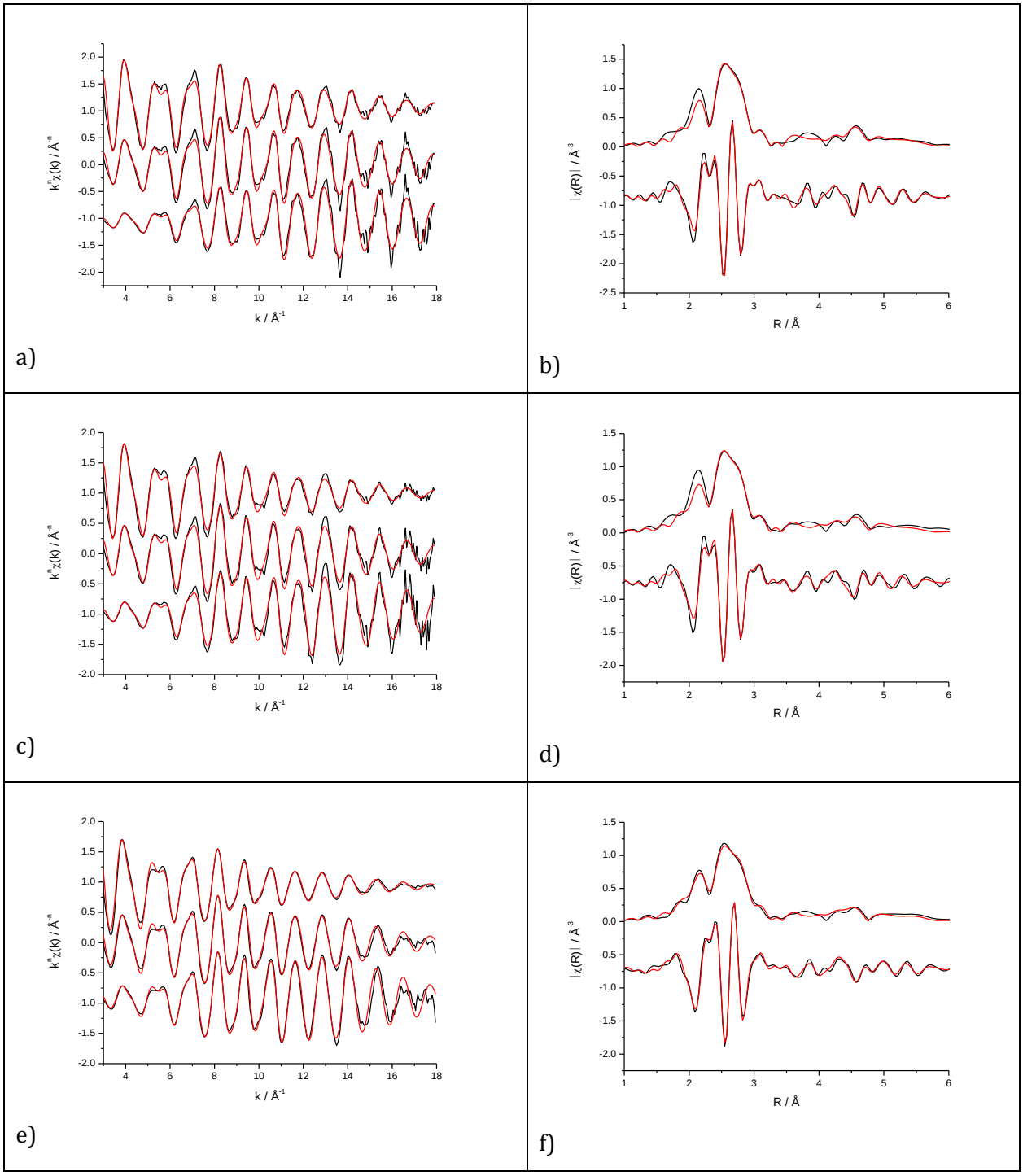

Figure 9: k^n weighted (k^1 top, k^2 middle, k^3 bottom of panel) experimental data (black) and fit (red) along with k^2 weighted magnitude and real Fourier transform for 20 wt% Pt/C at a-b) 20 K, c-d) 150 K and e-f) 300 K.

Table 6: Structural parameters for room temperature H_2 reduced 20 wt% Pt/C nanoparticles at 20 K, 150 K and 300 K, acquired at the Pt L_{III} edge, corresponding to the data in Figure 9.

Condition	20 wt% Pt/C					
	Shell	***N***	***R* / Å**	**σ^2 / Å^2**	**ΔE_0 / eV**	**R_f**
20 K vacuum	Pt-Pt_1	7.76 ± 0.38	2.74 ± 0.01	0.0053 ± 0.0002	7.66 ± 0.45	0.016
	Pt-Pt_2	1.91 ± 0.85	3.87 ± 0.01	0.0056 ± 0.0017		
	Pt-Pt_3	7.91 ± 2.54	4.74 ± 0.01	0.0069 ± 0.0014		
	Pt-Pt_4	5.79 ± 1.27	5.48 ± 0.01	0.0113† ± 0.0035		

	Shell	***N***	***R* / Å**	**σ^2 / Å^2**	**ΔE_0 / eV**	**R_f**
150 K vacuum	Pt-Pt_1	7.91 ± 0.41	2.73 ± 0.01	0.0060 ± 0.0002	7.27 ± 0.46	0.017
	Pt-Pt_2	3.40 ± 1.44	3.87 ± 0.01	0.0094** ± 0.0033		
	Pt-Pt_3	7.43 ± 3.60	4.74 ± 0.01	0.0088 ± 0.0029		
	Pt-Pt_4	4.95 ± 1.13	5.47 ± 0.01	0.0169†** ± 0.0056		

No fitting model could break the trend in σ^2 being higher for 2nd shell than 3rd**, or for the very high 4th shell value†.

	Shell	***N***	***R* / Å**	**σ^2 / Å^2**	**ΔE_0 / eV**	**R_f**
300 K	Pt-Pt_1	8.27 ± 0.41	2.76 ± 0.01	0.0065 ± 0.0002	5.10 ± 0.36	0.011
	Pt-Pt_2	2.31 ± 1.03	3.90 ± 0.01	0.0077 ± 0.0026		
	Pt-Pt_3	8.78 ± 3.79	4.78 ± 0.01	0.0095 ± 0.0024		
	Pt-Pt_4	5.60 ± 1.39	5.52 ± 0.01	0.0110 ± 0.0029		

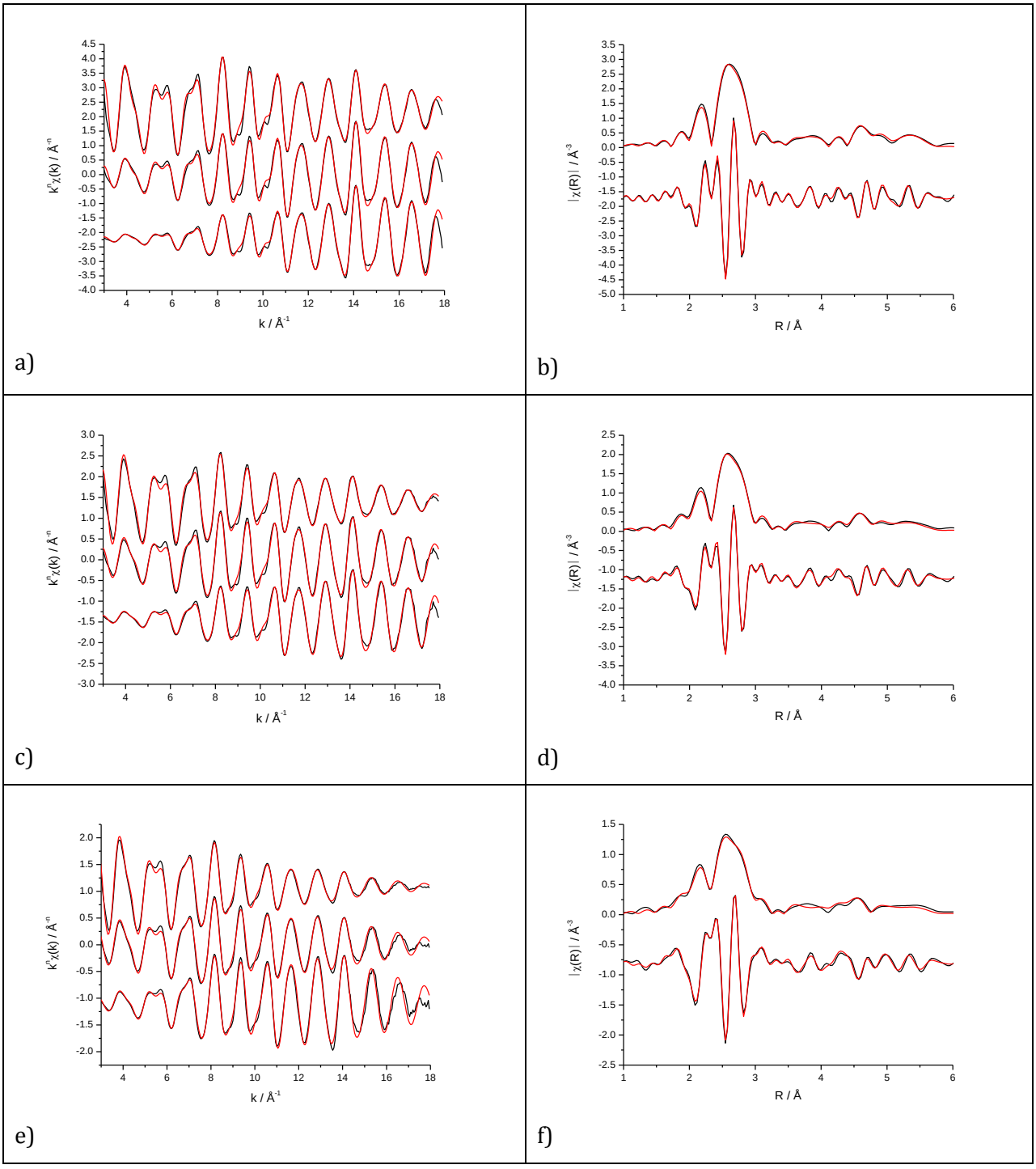

Figure 10: k^n weighted (k^1 top, k^2 middle, k^3 bottom of panel) experimental data (black) and fit (red) along with k^2 weighted magnitude and real Fourier transform for 40 wt% Pt/C at a-b) 20 K, c-d) 150 K and e-f) 300 K.

Table 7: Structural parameters for room temperature H_2 reduced 40 wt% Pt/C nanoparticles at 20 K, 150 K and 300 K, acquired at the Pt L_{III} edge, corresponding to the data in Figure 10.

Condition	**40 wt% Pt/C**					
	Shell	***N***	***R* / Å**	**σ^2 / Å^2**	**ΔE_0 / eV**	**R_f**
20 K vacuum	Pt-Pt_1	9.13 ± 0.41	2.75 ± 0.01	0.0034 ± 0.0001	8.44 ± 0.43	0.008
	Pt-Pt_2	3.06 ± 0.96	3.89 ± 0.01	0.0037 ± 0.0010		
	Pt-Pt_3	10.50 ± 2.46	4.76 ± 0.01	0.0039 ± 0.0008		
	Pt-Pt_4	6.07 ± 1.29	5.49 ± 0.01	0.0065 ± 0.0010		

	Shell	***N***	***R* / Å**	**σ^2 / Å^2**	**ΔE_0 / eV**	**R_f**
150 K vacuum	Pt-Pt_1	8.78 ± 0.37	2.75 ± 0.01	0.0046 ± 0.0002	7.96 ± 0.38	0.008
	Pt-Pt_2	2.82 ± 0.97	3.89 ± 0.01	0.0058 ± 0.0014		
	Pt-Pt_3	10.05 ± 2.42	4.76 ± 0.01	0.0060 ± 0.0010		
	Pt-Pt_4	6.08 ± 1.38	5.49 ± 0.01	0.0080 ± 0.0017		

	Shell	***N***	***R* / Å**	**σ^2 / Å^2**	**ΔE_0 / eV**	**R_f**
300 K	Pt-Pt_1	8.47 ± 0.41	2.76 ± 0.01	0.0060 ± 0.0002	5.47 ± 0.37	0.009
	Pt-Pt_2	2.68 ± 1.02	3.90 ± 0.01	0.0074 ± 0.0022		
	Pt-Pt_3	10.16 ± 2.12	4.77 ± 0.01	0.0087 ± 0.0018		
	Pt-Pt_4	6.20 ± 1.52	5.51 ± 0.01	0.0101 ± 0.0023		

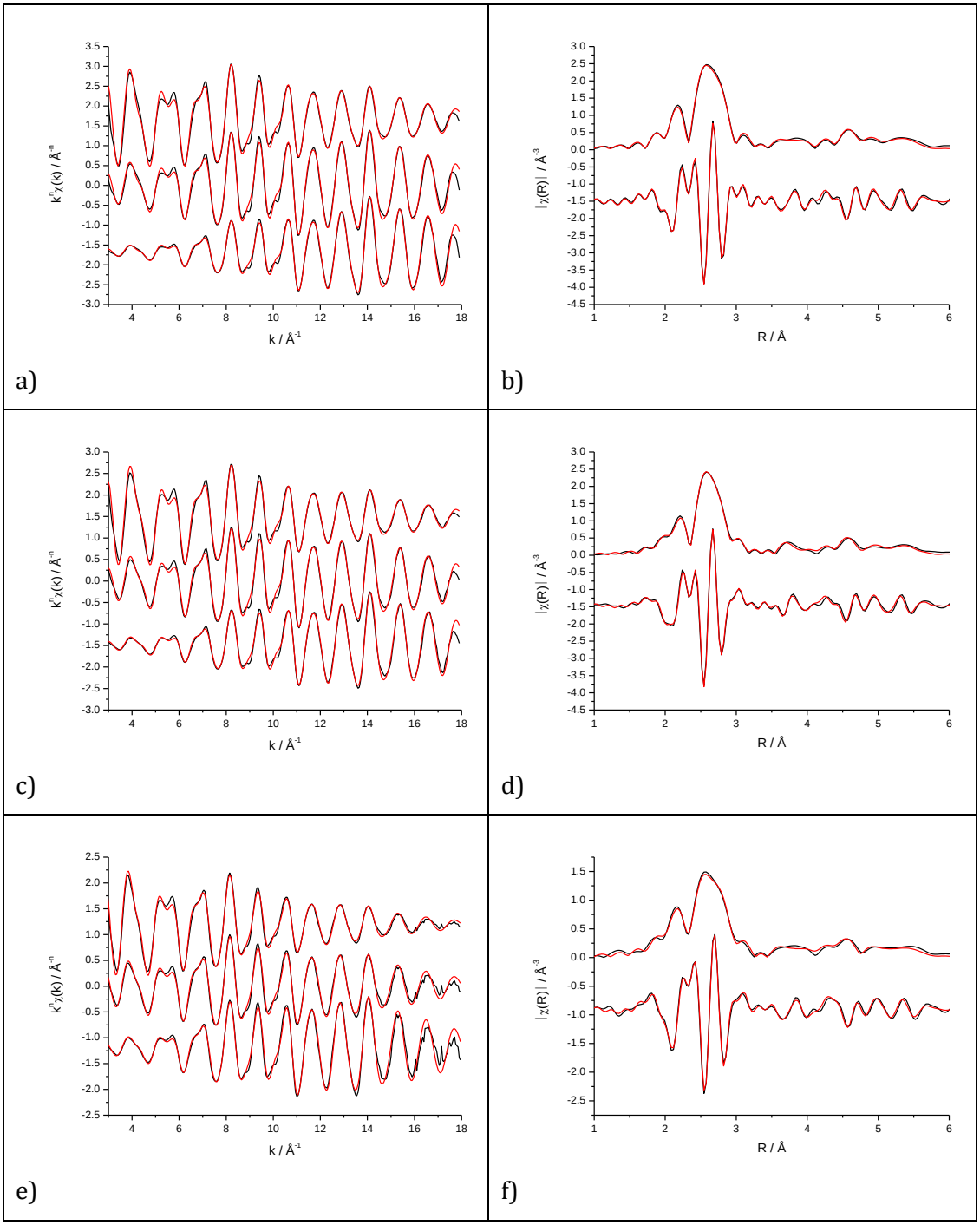

Figure 11: k^n weighted (k^1 top, k^2 middle, k^3 bottom of panel) experimental data (black) and fit (red) along with k^2 weighted magnitude and real Fourier transform for 60 wt% Pt/C at a-b) 20 K, c-d) 150 K and e-f) 300 K.

Table 8: Structural parameters for room temperature H_2 reduced 60 wt% Pt/C nanoparticles at 20 K, 150 K and 300 K, acquired at the Pt L_{III} edge, corresponding to the data in Figure 11.

Condition	60 wt% Pt/C					
	Shell	***N***	***R* / Å**	**σ^2 / Å^2**	**ΔE_0 / eV**	**R_f**
20 K vacuum	Pt-Pt_1	9.54 ± 0.41	2.75 ± 0.01	0.0041 ± 0.0002	7.56 ± 0.40	0.009
	Pt-Pt_2	3.03 ± 1.04	3.89 ± 0.01	0.0048 ± 0.0013		
	Pt-Pt_3	12.14 ± 2.82	4.76 ± 0.01	0.0053 ± 0.0009		
	Pt-Pt_4	6.90 ± 1.40	5.50 ± 0.01	0.0070 ± 0.0013		

	Shell	***N***	***R* / Å**	**σ^2 / Å^2**	**ΔE_0 / eV**	**R_f**
150 K vacuum	Pt-Pt_1	9.32 ± 0.40	2.75 ± 0.01	0.0046 ± 0.0002	8.09 ± 0.39	0.009
	Pt-Pt_2	3.08 ± 0.82	3.89 ± 0.01	0.0056 ± 0.0015		
	Pt-Pt_3	11.97 ± 2.88	4.76 ± 0.01	0.0066 ± 0.0011		
	Pt-Pt_4	7.07 ± 1.44	5.50 ± 0.01	0.0132 ± 0.0015		

	Shell	***N***	***R* / Å**	**σ^2 / Å^2**	**ΔE_0 / eV**	**R_f**
300 K	Pt-Pt_1	8.71 ± 0.42	2.76 ± 0.01	0.0057 ± 0.0002	5.65 ± 0.41	0.009
	Pt-Pt_2	5.43 ± 0.56	3.90 ± 0.01	0.0067 ± 0.0015		
	Pt-Pt_3	12.74 ± 1.98	4.78 ± 0.01	0.0086 ± 0.0012		
	Pt-Pt_4	8.03 ± 1.69	5.52 ± 0.01	0.0094 ± 0.0017		

On fitting a bulk *fcc* material, the coordination numbers would be expected to follow the theoretical values of 12, 6, 24 and 12 for the first to fourth shells respectively. Moving radially outwards from the absorbing atom, the probability that the photoelectron will scatter and return to the absorber is reduced, and so the actual coordination numbers measured will be slightly lower than the theoretical values. With the finite size of nanoparticles, there are significantly less atoms at the third and fourth coordination shell distances, and so the measured values will be further reduced. This is the "termination effect" with respect to coordination number.

Fitting of the higher coordination shells gives much higher errors in coordination number and disorder compared with those for the first shell. Since the fourth shell is greatly under-coordinated (as a result of the particle size) the multiple scattering contributions, both at this distance and between the third and fourth shells, are significantly reduced. These scattering paths are still needed for a physically reasonable fit, as without the contribution of their amplitudes and phases, unrealistic values such as negative disorder and coordination are obtained for the higher shells. The unknown degree of termination and the constraints imposed on these paths (to reduce the number of fitting variables below the Nyquist theorem limit) contribute to the higher error values. This effect is observed in all samples measured, with the larger errors being obtained for both measurements at higher temperature and for the smaller nanoparticles (i.e. lower coordination number)

Some of the higher coordination shell results appear anomalous, such as those in **Table 6** (data in **Figure 9a, 9c**). The data recorded at 20 and 150 K is noisier beyond 12 $Å^{-1}$ than for similar samples, and harder to fit to theory, resulting in the disorder not following the expected trends; i.e. increasing with temperature, or increasing as the radial distance between absorber and scatterer is increased. The cryostat relied on a vacuum and displex unit to reach the required temperature, and it is likely that the physical nature of the cooling process damaged the pellet, introducing sample inhomogeneities that resulted in the increased noise[25]. A more severe effect was observed with a 5 wt% Pt/C sample on activation of the displex unit that rendered the final EXAFS data too distorted to be useable and this data has not been reported herein.

Whilst modelling the disorder with the correlated Debye function[26,27] would facilitate a reduction in the number of variables and therefore lower the reduced χ^2, its use was deemed inappropriate for such poorly crystalline nanoparticles given that it was developed for crystalline systems[28]. This is evidenced by the large degree of surface

atoms with anharmonic bond vibration combined with the poor crystallinity seen in the XRD patterns and the AC-STEM micrographs. The cryostat was used to reduce the degree of thermal disorder in the sample to allow for more accurate determination of coordination number, and to shed light on the degree of structural disorder present in in the nanoparticles. Even at 20 K, the fits reveal a very large degree of disorder present in the system, e.g. the 20 wt% Pt/C at 20 K has a greater σ^2 value (0.0053 Å^2) than bulk Pt at room temperature (0.0049 Å^2). The majority contribution to this increase is from structural strain, and as such suggests that an improved fitting model is needed to account for this.

A decrease in average bond length is observed at lower temperatures, and as the Pt loading is reduced. Given that the average coordination number (and thus size) reduces with Pt loading, the lattice contraction is both temperature and size dependent.

Table 9: Decrease in lattice parameter determined from the EXAFS fits with size and temperature.

Sample / wt% Pt/C	Temperature / K	Lattice parameter *a* / Å
Bulk Pt	*20*	*3.91± 0.01*
	300	*3.92± 0.01*
10	20	3.87 ± 0.01
	150	3.87 ± 0.01
	300	3.90 ± 0.01
20	20	3.87 ± 0.01
	150	3.87 ± 0.01
	300	3.90 ± 0.01
40	20	3.89 ± 0.01
	150	3.89 ± 0.01
	300	3.90 ± 0.01
60	20	3.89 ± 0.01
	150	3.89 ± 0.01
	300	3.90 ± 0.01

The isotropic expansion coefficient measured by EXAFS shows a contraction in the unit cell of the Pt crystallites, with noticeable differences between the reference foil and nanoparticles at 300 K, and an even greater contraction at 20 K (**Table 9**). This contraction of the lattice as a function of both temperature and size is well established[29,30].

3.5 Particle Size Calculation from EXAFS

Particle size calculations were carried out based on the work of Benfield[31] and Jentys[32]. A cluster with a complete outer shell is commonly known as a "magic number cluster"[33]. Assuming an approximately spherical shape, this allows for a size calculation based on the atomic radius of the element of which the cluster is composed, as shown in **Figure 12** below. Of course, this does not take into account any non-bulk type behaviour such as contraction of the surface bonds[29,34], however it does provide a reliable means of converting average EXAFS coordination numbers into average particle sizes.

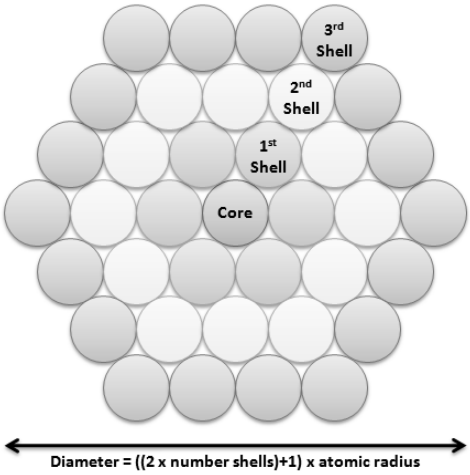

Figure 12: Schematic of cluster size (diameter) calculation.

Both Benfield[31] (**Equation 5**) and Jentys[32] (**Equation 6**) have derived formulae for calculating the coordination number based on the number of atoms in the cluster.

$$N_1 = \frac{12(m-1)(10m^2 - 14m + 6)}{(2m-1)(5m^2 - 5m + 3)}$$

Equation 5

where m is the edge length of the cluster. And;

$$N_i = \frac{aN_{at}}{b + N_{at}} + \frac{cN_{at}}{d + N_{at}}$$

Equation 6

where a = 8.981, b = 9.640, c = 3.026, d = 1462.61 for the 1st coordination shell. Values of a-d not shown for the other coordination shells.

A plot of the functions determining coordination number based on Jentys's formula for the first four coordination shells is shown in **Figure 13**.

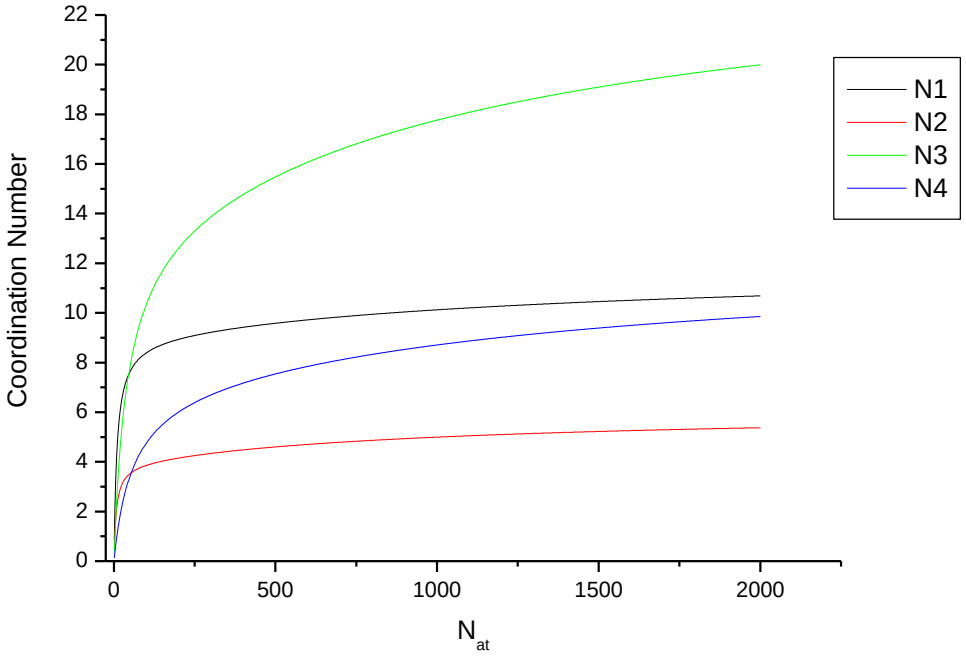

Figure 13: Average coordination numbers as a function of the number of atoms for 1st through 4th coordination shells, N1, N2, N3 and N4.

These formulae give rise to the coordination numbers seen in **Table 10**. Whilst the exact coordination number predicted by these formulae differs, it is by much less than 10 %, and so well within the accepted limits for coordination number determination from EXAFS[35]. Inverting the formulae, a coordination number determined from an EXAFS spectrum can then be used to estimate the average number of atoms present in the nanoparticles and thus the average diameter. The technique is inherently limited by the assumption of a "spherical" structure, a complete outer shell of atoms and no size dependent bond length contraction, but there is enough tolerance in the calculations that the method provides a reasonable approximation of particle size. By varying the metal-metal bond length used, the method can be applied easily to any monometallic nanoparticle system.

Table 10: Calculation of first shell coordination number from Benfield[31] and Jentys[32] (based on Equation 5 and Equation 6 respectively).

Complete shells around core (Cluster Order)	Edge Length	Total Number of Atoms in Cluster	Diameter of Cluster* / nm	1st Shell Coordination Number	
				Benfield	Jentys
0	1	1	0.277	0	0
1	2	13	0.832	5.54	5.17
2	3	55	1.386	7.85	7.75
3	4	147	1.940	8.98	8.70
4	5	309	2.495	9.63	9.24
5	6	561	3.049	10.05	9.67
6	7	923	3.604	10.35	10.06
7	8	1415	4.158	10.57	10.41
8	9	2057	4.712	10.73	10.71
9	10	2869	5.267	10.87	10.96

*based on Pt –Pt bond length of 2.772 Å

Particle size determination involved averaging over all coordination numbers determined for each sample; if the error in each coordination number was taken into account, the error would be far greater than the value in some cases, as the errors in the higher shell coordination numbers determined in this work were at times large. Therefore only the first coordination shell was used for particle size determination, and the reported error taken to be the variance of the coordination numbers rather than the sum of each individual error.

As the coordination numbers near their theoretical values (first nearest neighbour = 12 for an *fcc* metal), and this determination then becomes less challenging (for non-complex systems such as monometallic catalysts), and the error associated with the fit decreases. However, the error in the size estimation methods begins to increase as particle size increases. The size estimation methods are most sensitive below approximately 4 nm where large changes in coordination number correspond to small changes in size (**Table 10**). Above this limit, small changes in coordination number can result in large changes in size. Thus with the inherent degree of uncertainty in coordination number determination, sizes of larger nanoparticles determined using

this method become less reliable. The upper limit of reliability for particle size determination by EXAFS is therefore between 4 and 5 nm

A list of the particle sizes determined from the EXAFS fits for the unheated Pt/C series is presented in **Table 11** below.

Table 11: Particle sizes for Pt/C samples determined from EXAFS fits.

Sample / wt% Pt/C	Average diameter / nm	
	Standard 4 shell fit	**Standard 1 shell fit**
10	1.32 ± 0.09	1.52 ± 0.14
20	1.51 ± 0.15	1.87 ± 0.26
40	2.10 ± 0.29	2.29 ± 0.33
60	2.49 ± 0.43	2.66 ± 0.34

4 Characterisation of Pt/C (treated) nanoparticle catalysts

A series of Pt/C nanoparticle catalysts that had undergone heat treatment, designed to increase the average particle size without a change in the metal loading, was studied to aid the analysis of the cross-correlation of techniques, and in particular the effect of weighting results.

4.1 TEM

TEM was performed to determine average particle size and particle size distribution. Micrographs were taken between 5 nm and 200 nm; an example micrograph for each sample is given in **Figure 14** below.

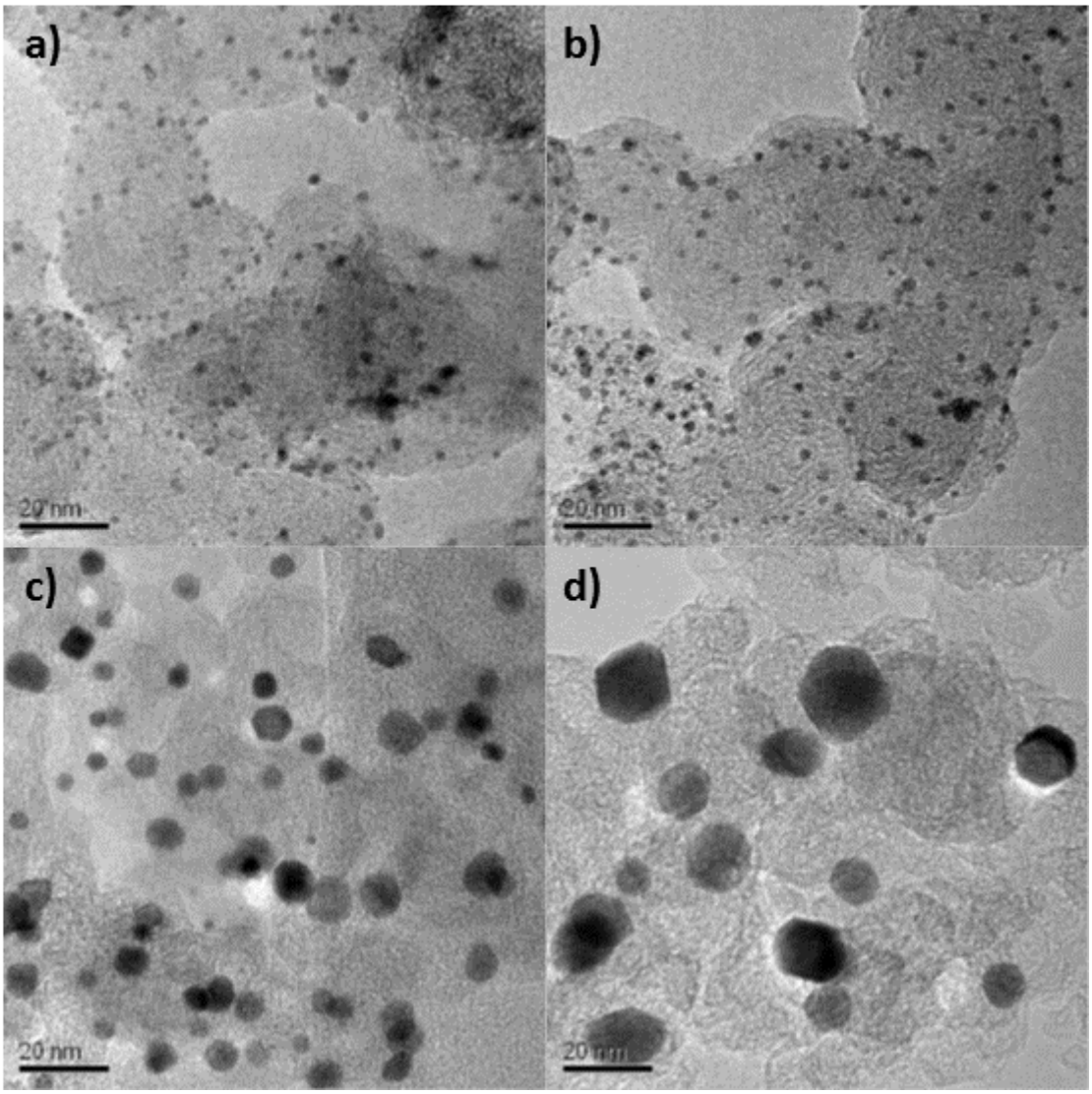

Figure 14: TEM micrographs of a) 10 wt% Pt/C unheated, b) 10 wt% Pt/C heated to 973 K, c) 10 wt% Pt/C heated to 1273 K and d) 10 wt% Pt/C heated to 1473 K. Scale bar is 20 nm.

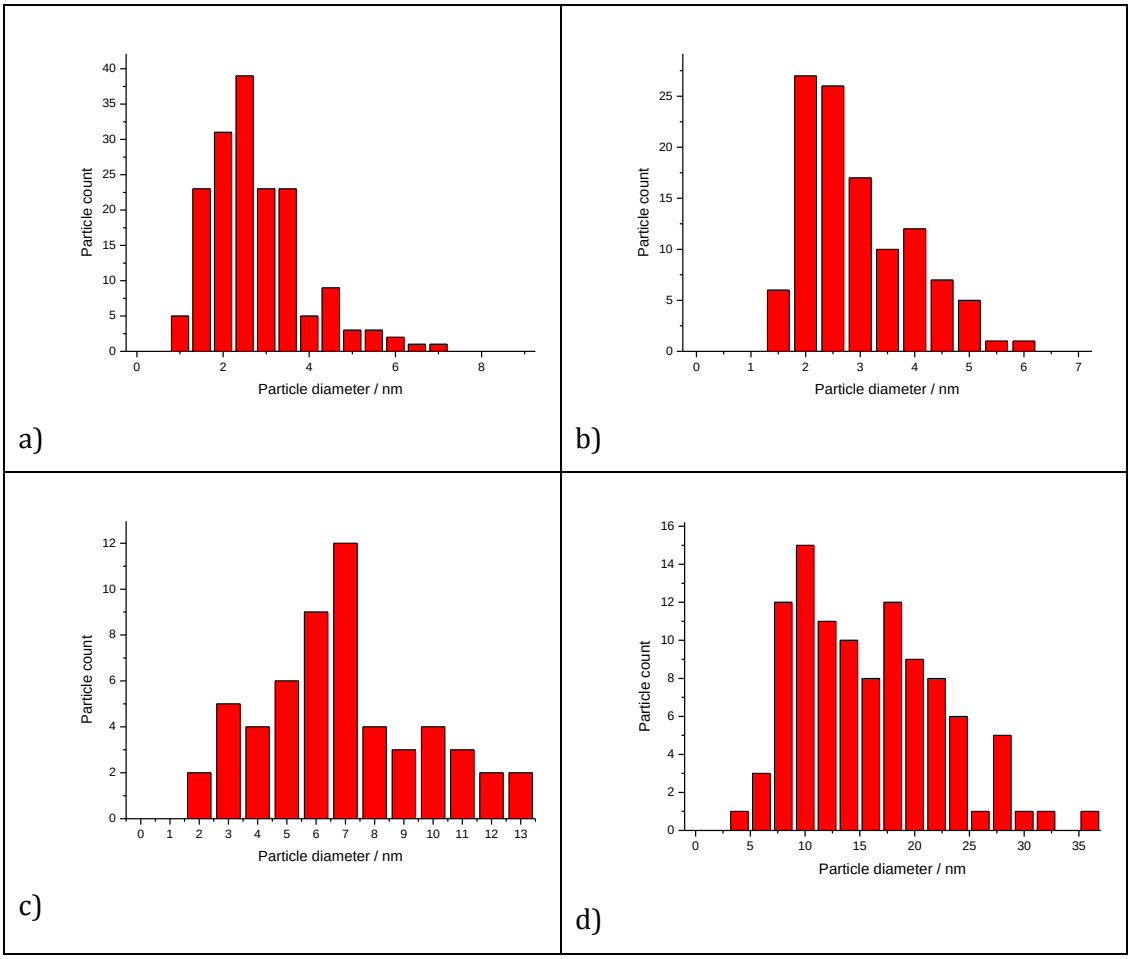

Figure 15: Particle size distribution of a) 10 wt% Pt/C unheated, b) 10 wt% Pt/C heated to 973 K, c) 10 wt% Pt/C heated to 1273 K and d) 10 wt% Pt/C heated to 1473 K.

Table 12: Comparison of particle size determinations from varying TEM weighting approaches for treated 10 wt% Pt/C.

Sample treatment	Number of observed particles	Average TEM particle size / nm				Standard deviation / nm
		D_0	D_n	D_a	D_{Vol}	
None	168	2.37	2.52	3.51	4.03	1.10
973 K	104	2.55	2.70	3.43	3.77	0.99
1273 K	112	6.06	6.38	8.56	9.34	2.79
1473 K	56	13.87	14.86	20.31	22.50	6.57

On heating, the Pt nanoparticles aggregate together on the support to form larger particles. Depending on the uniformity of dispersion across the support, the aggregation can lead to a broadening of the distribution and possibly a splitting

(**Figure 15d**). The dependency of the result weighting on the variance (and therefore the sample quality) is highlighted in the differences between the unheated sample and the sample heated to 973 K (**Table 12**). The typical number weighted approach leads the 973 K heated sample to have a larger average particle diameter, yet because the observed variance was smaller than the unheated sample, the D_{Vol} weighted average diameter was smaller. It is clear to see that with such a large variance, as in the 1473 K heated sample, the effect of weighting the results is more profound than with uniform samples (**Figure 2**, **Table 2**).

4.2 XRD

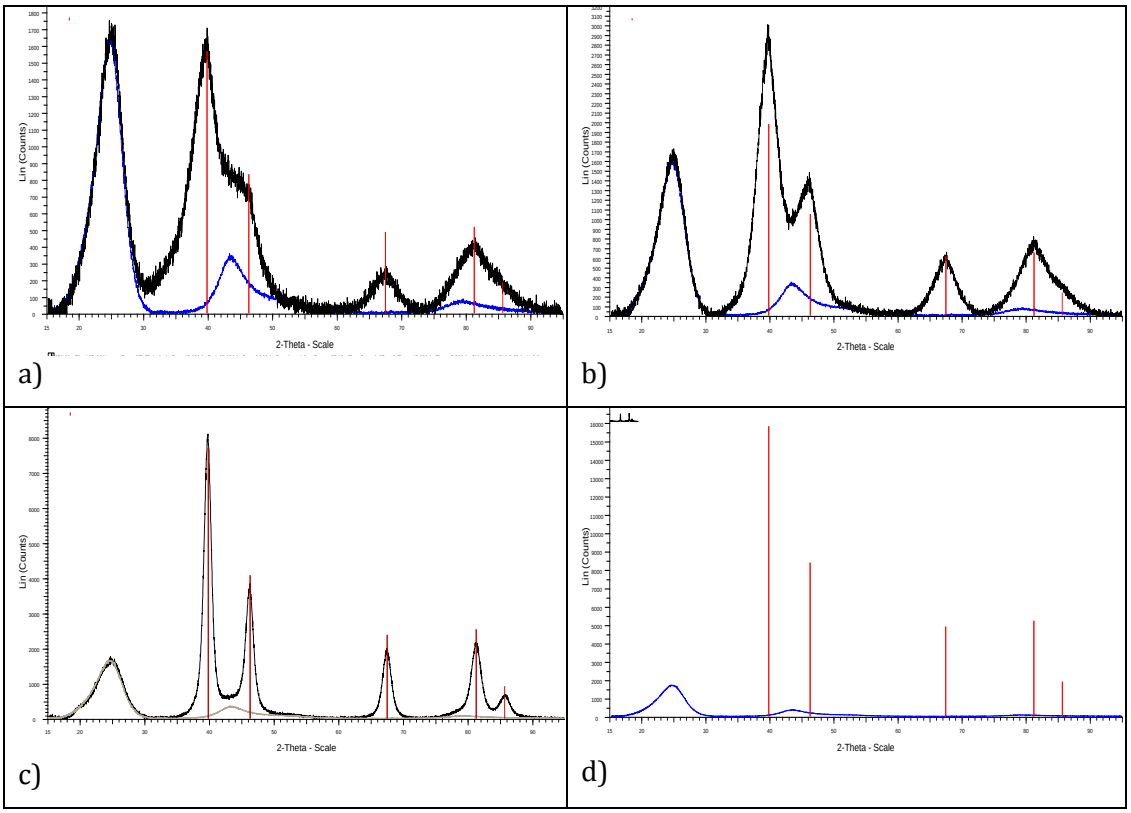

Figure 16: XRD patterns of a) 10 wt% Pt/C unheated, b) 10 wt% Pt/C heated to 973 K, c) 10 wt% Pt/C heated to 1273 K and d) 10 wt% Pt/C heated to 1473 K. Data is the black line, | refers to cubic Pt (PDF No. 00-04-0802, a = 3.92 Å),), and | refers to the carbon support (fit to data).

The unheated sample consists of very poorly crystalline Pt with no other phases present. The aggregation caused by increased heat treatments results in much more crystalline Pt particles, with the 1473 K sample in particular having much improved crystallinity (**Figure 16**).

As with the previous series of Pt/C nanoparticles, the average crystallite sizes reported in **Table 13** can only be regarded as estimates due to the poorly crystalline nature of many of the samples.

Table 13: Rietveld derived XRD crystallite sizes.

10 wt% Pt/C treatment	**Crystallite size / nm**	
	L_{Vol} average crystallite size	**$D_{Vol} = 4/3*L_{Vol}$ (sphere) – mean volume weighted diameter**
None	1.61	2.15
973 K	2.20	2.93
1273 K	5.18	6.91
1473 K	10.80	14.40

4.3 Standard EXAFS

Data was fitted as in section 3.4 **Table 4**, but over a range of 3-16 Å^{-1} in *k* space due to the slightly poorer data quality and glitches in the EXAFS data beyond 16.4 Å^{-1} originating from the monochromator. All data was collected on beamline X11A of the NSLS.

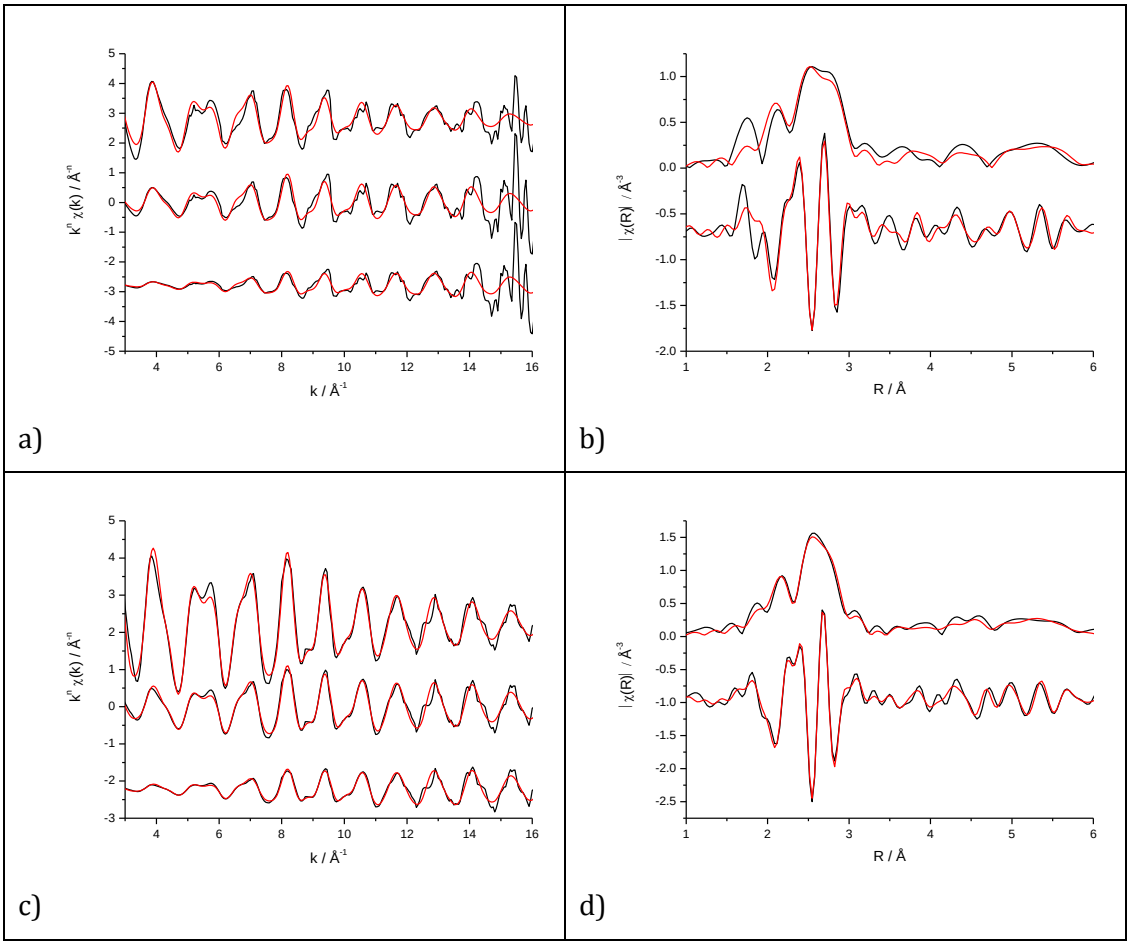

Figure 17 : k^n weighted (k^1 top, k^2 middle, k^3 bottom of panel) experimental data (black) and fit (red) along with k^2 weighted magnitude and real Fourier transform at 300 K for a-b) 10 wt% Pt/C unheated, and c-d) 10 wt% Pt/C heated to 973 K.

Table 14: Structural parameters for 10 wt% Pt/C nanoparticles unheated and heated to 973 K, acquired at the Pt L_{III} edge, corresponding to the data in Figure 17.

Condition	**10 wt% Pt/C no heat treatment***					
	Shell	***N***	***R* / Å**	**σ^2 / Å^2**	**ΔE_0 / eV**	**R_f**
300 K H_2	Pt-Pt_1	8.71 ± 0.90	2.76 ± 0.01	0.0059 ± 0.0006	5.58 ± 0.96	0.047
	Pt-Pt_2	2.08 ± 1.04	3.90 ± 0.01	0.0060 ± 0.0045		
	Pt-Pt_3	19.96 ± 8.82	4.77 ± 0.01	0.0133 ± 0.0098		
	Pt-Pt_4	7.28 ± 3.41	5.51 ± 0.01	0.0401 ± 0.0131		

*fitting range finished at k_{max} 14 Å^{-1}

Condition	**10 wt% Pt/C heated to 973 K**					
	Shell	***N***	***R* / Å**	**σ^2 / Å^2**	**ΔE_0 / eV**	**R_f**
300 K H_2	Pt-Pt_1	9.56 ± 0.62	2.75 ± 0.01	0.0059 ± 0.0003	5.85 ± 0.58	0.027
	Pt-Pt_2	3.15 ± 1.84	3.89 ± 0.01	0.0095 ± 0.0056		
	Pt-Pt_3	21.46 ± 10.45	4.77 ± 0.01	0.0113 ± 0.0029		
	Pt-Pt_4	8.29 ± 1.69	5.51 ± 0.01	0.0393 ± 0.0080		

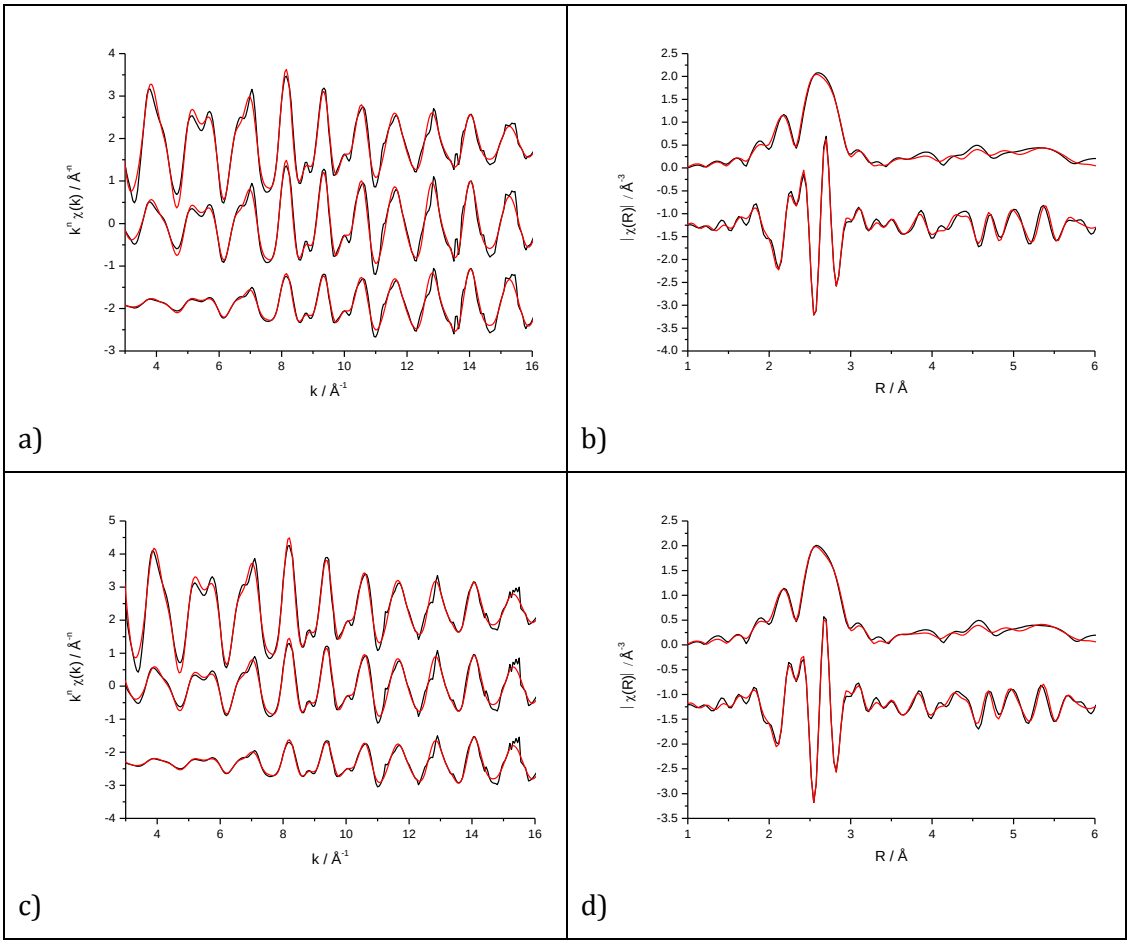

Figure 18 : k^n weighted (k^1 top, k^2 middle, k^3 bottom of panel) experimental data (black) and fit (red) along with k^2 weighted magnitude and real Fourier transform at 300 K for a-b) 10 wt% Pt/C heated to 1273 K and c-d) 10 wt% Pt/C heated to 1473 K.

Table 15: Structural parameters for 10 wt% Pt/C nanoparticles heated to 1273 K and to 1473 K, acquired at the Pt L_{III} edge, corresponding to the data in Figure 18.

Condition	**10 wt% Pt/C heated to 1273 K**					
	Shell	***N***	***R* / Å**	**σ^2 / Å^2**	**ΔE_0 / eV**	**R_f**
300 K H_2	Pt-Pt_1	10.73 ± 0.58	2.76 ± 0.01	0.0053 ± 0.0002	6.94 ± 0.50	0.019
	Pt-Pt_2	4.48 ± 2.05	3.90 ± 0.01	0.0076 ± 0.0026		
	Pt-Pt_3	21.46 ± 7.34	4.77 ± 0.01	0.0088 ± 0.0017		
	Pt-Pt_4	9.18 ± 1.55	5.51 ± 0.01	0.0455 ± 0.0094		

Condition	**10 wt% Pt/C heated to 1473 K**					
	Shell	***N***	***R* / Å**	**σ^2 / Å^2**	**ΔE_0 / eV**	**R_f**
300 K H_2	Pt-Pt_1	10.87 ± 0.64	2.76 ± 0.01	0.0051 ± 0.0003	4.72 ± 0.56	0.021
	Pt-Pt_2	4.92 ± 1.66	3.90 ± 0.01	0.0082 ± 0.0030		
	Pt-Pt_3	21.66 ± 7.74	4.78 ± 0.01	0.0085 ± 0.0016		
	Pt-Pt_4	9.86 ± 1.71	5.52 ± 0.01	0.0419 ± 0.0086		

There is very little change in lattice parameter and bond lengths across this series of catalysts, although, as before there, is a slight contraction when compared with the bulk values. As is clearly seen in the TEM micrographs, the particles increase in size with heat treatment, and a clear increase in coordination number is observed in the EXAFS fits. The first and third shells show a corresponding decrease in σ^2 but the trend is less clear for the second and fourth shells. The lower occupancy of the second shell and termination effects present in the fourth shell result in them being harder to fit and could explain this poor agreement.

A list of the particle sizes determined from the EXAFS fits for the unheated Pt/C series is presented in **Table 16** below.

Table 16: Particle sizes for Pt/C samples determined from EXAFS fits.

10 wt% Pt/C treatment	Average diameter / nm	
	Standard 4 shell fit	Standard 1 shell fit
None	2.01 ± 0.93	1.38 ± 0.81
973 K	2.86 ± 0.88	2.63 ± 0.85
1273 K	4.77 ± 1.37	4.17 ± 1.27
1473 K	5.07 ± 1.63	4.22 ± 1.03

6 Characterisation of Au/C

6.1 TEM

Bright field micrographs for each of the 4 wt% and 16 wt% Au/C samples are included below in **Figure 19**, with the associated particle size distributions in **Figure 20**.

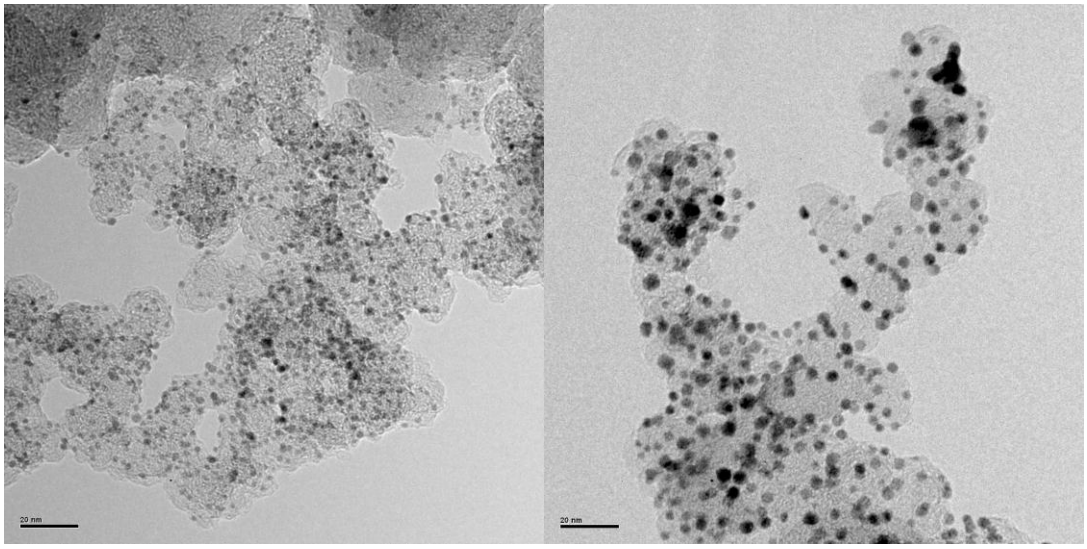

a) b)

Figure 19: TEM micrographs of a) 4 wt% Au/C, and b) 16 wt% Au/C. Scale bar is 20 nm.

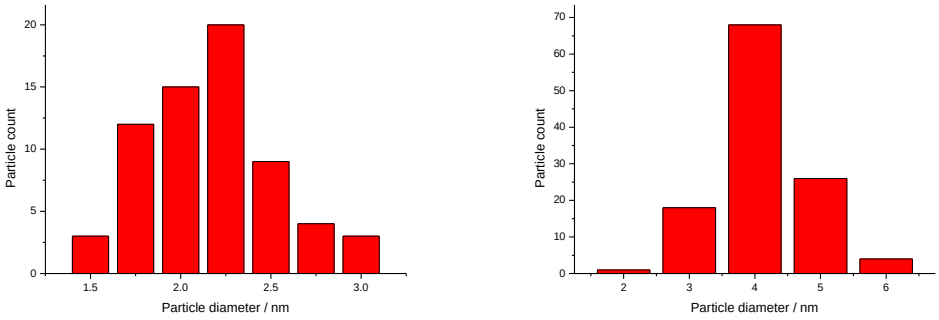

a) b)

Figure 20: Particle size distribution of a) 4 wt% Au/C, and b) 16 wt% Au/C.

TEM shows both Au samples to be well dispersed across the carbon support, with relatively evenly shaped particles. The higher loading of the 16 wt% sample has resulted in some overlap that could give erroneous results during the particle size calculation. EDX confirmed the particles consisted of Au.

Table 17: Comparison of particle size determinations from varying TEM weighting approaches.

Sample loading / wt% Au/C	Number of observed particles	Average TEM particle size / nm				Standard deviation / nm
		D_0	D_n	D_a	D_{Vol}	
4	70	2.07	2.11	2.29	2.38	1.22
16	119	3.63	3.70	3.99	4.14	1.22

The sample variance is reasonable (**Table 17**), with not much change seen as the weighting is increased. No trace of the thiol or citrate used during the synthesis are seen in the EDX results, and any presence in the TEM is not distinguishable from the Au core.

6.2 XRD

XRD patterns of both Au/C samples are in **Figure 21** below.

a) 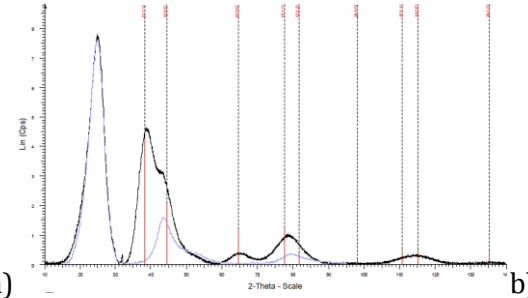 b) 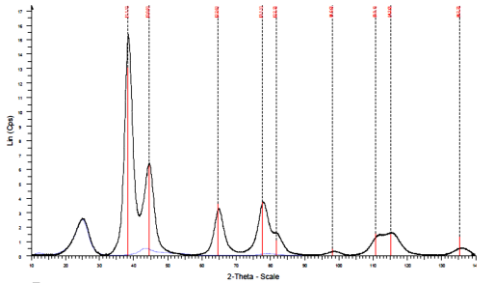

Figure 21: XRD patterns of a) 4 wt% Au/C and b) 16 wt% Au/C. Data is the black line, | refers to cubic Au (PDF No. 03-065-2870, a = 4.08 Å), and | refers to the carbon support (fit to data).

The 4 wt% Au/C sample XRD pattern is dominated by the carbon support due to both the low Au loading and the poorly crystalline nature of the nanoparticles. The 16 wt% Au/C sample is more crystalline compared to the 4 wt% sample, although in general terms it is still poorly crystalline. There is still a noticeable contribution to the XRD pattern from the carbon support. Rietveld determined average crystallite sizes are reported in **Table 18**. Given the poor crystallinity, XRD appears unsuitable for size determination of the smallest nanoparticles, as was the case with the smallest Pt/C samples.

Table 18: Rietveld derived XRD crystallite sizes. Errors in average crystallite size not supplied in analytical report.

Sample / wt% Au/C	Crystallite size / nm	
	L_{Vol} average crystallite size	$D_{Vol} = 4/3*L_{Vol}$ (sphere) – mean volume weighted diameter
4	1.81	2.41
16	3.14	4.19

6.3 Standard EXAFS

Data was fitted as in section 3.4 **Table 4**, but using an Au *fcc* input and over a range of 3-14 Å^{-1} in *k* space for the 300 K measurements due to the poorer data quality. Data was collected on beamline X23A2 for the 4 wt% Au/C sample and beamline X11A for the 16 wt% Au/C sample.

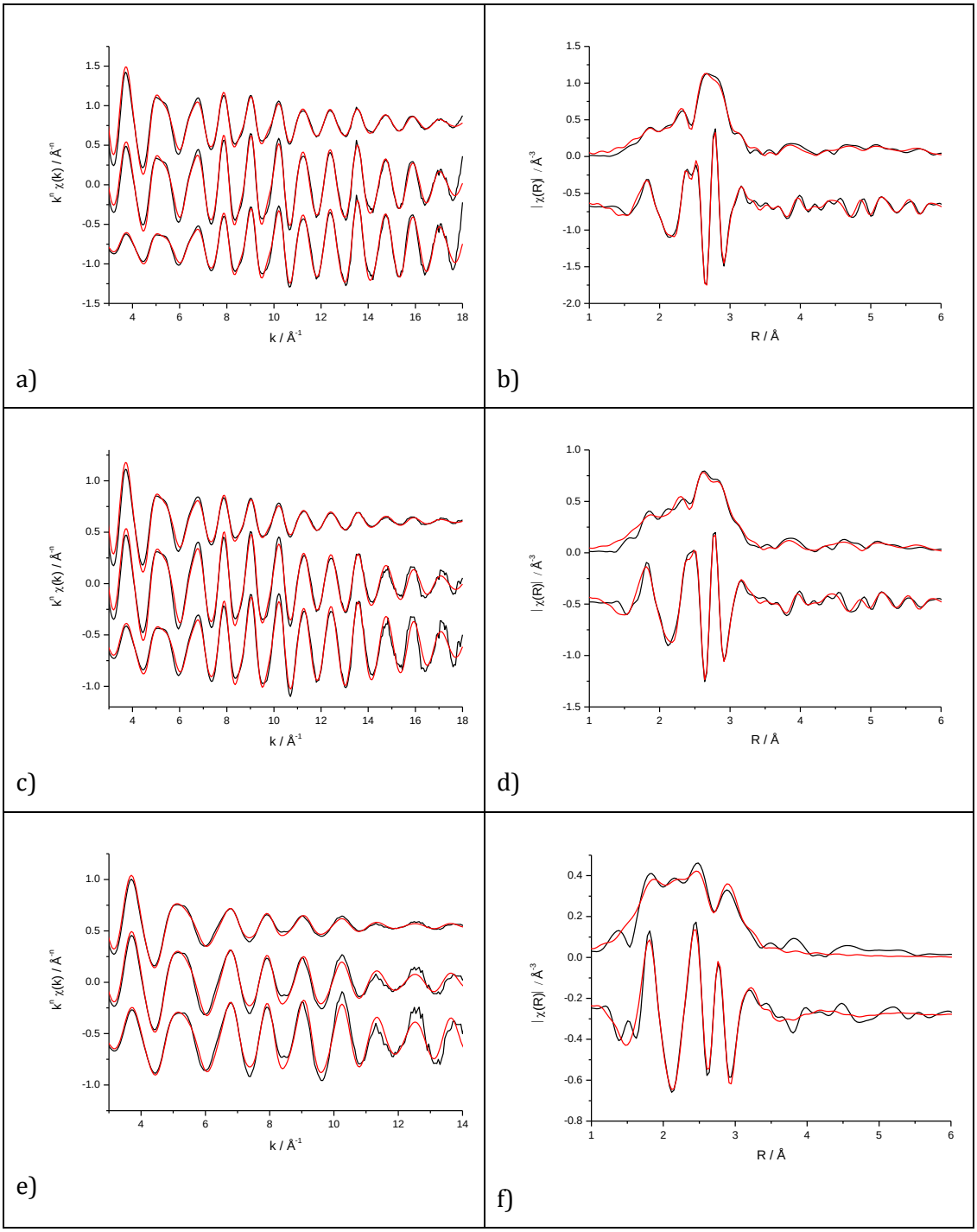

Figure 22: k^n weighted (k^1 top, k^2 middle, k^3 bottom of panel) experimental data (black) and fit (red) along with k^2 weighted magnitude and real Fourier transform for 4 wt% Au/C at a-b) 85 K c-d) 150 K, and e-f) 300 K.

Table 19: Structural parameters for 4 wt% Au/C nanoparticles at 85 K, 150 K and 300 K, at the Au L_{III} edge, corresponding to the data in Figure 22.

Condition	4 wt% Au/C					
	Shell	***N***	***R* / Å**	**σ^2 / Å^2**	**ΔE_0 / eV**	**R_f**
85 K	Au-Au_1	6.86 ± 0.43	2.85 ± 0.01	0.0056 ± 0.0002	6.43 ± 0.32	0.017
	Au-S_1	1.04 ± 0.31	2.31 ± 0.01	0.0083 ± 0.0037		
	Au-Au_2	1.48 ± 0.72	4.03 ± 0.01	0.0059 ± 0.0025		
	Au-Au_3	11.01 ± 3.84	4.94 ± 0.01	0.0104 ± 0.0023		
	Au-Au_4	4.05 ± 1.07	5.70 ± 0.01	0.0188 ± 0.0074		
150 K	Au-Au_1	6.77 ± 0.45	2.85 ± 0.01	0.0070 ± 0.0003	5.91 ± 0.31	0.021
	Au-S_1	1.04 ± 0.30	2.31 ± 0.01	0.0088 ± 0.0036		
	Au-Au_2	1.18 ± 0.85	4.02 ± 0.01	0.0070 ± 0.0037		
	Au-Au_3	13.55 ± 5.20	4.93 ± 0.01	0.0147 ± 0.0034		
	Au-Au_4	4.15 ± 1.17	5.69 ± 0.01	0.0230 ± 0.0098		
300 K*	Au-Au_1	6.58 ± 0.64	2.83 ± 0.01	0.0124 ± 0.0018	4.10 ± 0.40	0.017
	Au-S_1	1.04 ± 0.42	2.30 ± 0.01	0.0094 ± 0.0094		

*Data could not be reasonably fitted beyond 1st shell as *N*, σ^2 and associated errors were too large.

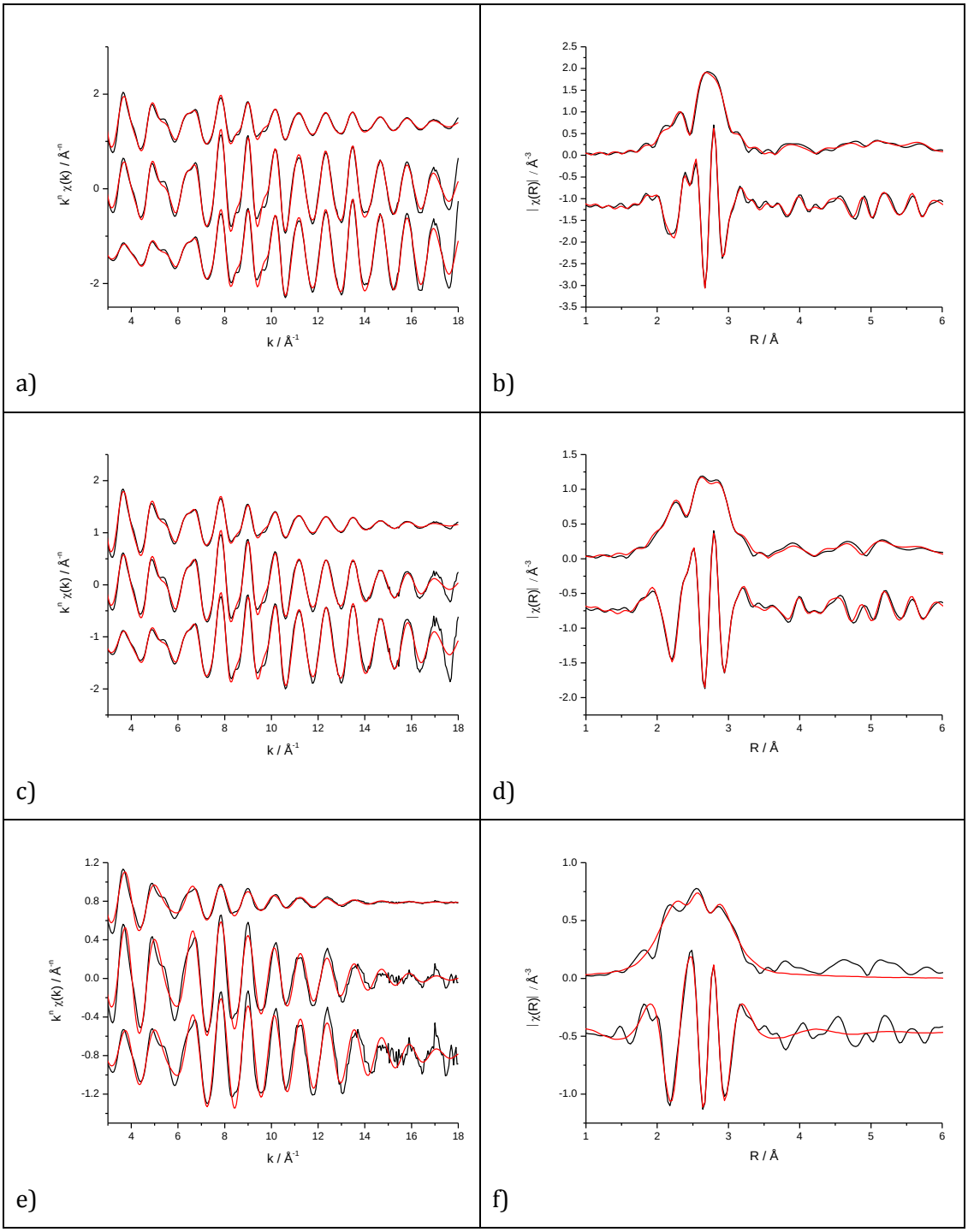

Figure 23: k^n weighted (k^1 top, k^2 middle, k^3 bottom of panel) experimental data (black) and fit (red) along with k^2 weighted magnitude and real Fourier transform for 16 wt% Au/C at a-b) 85 K c-d) 150 K, and e-f) 300 K.

Table 20: Structural parameters for 16 wt% Au/C nanoparticles at 85 K, 150 K and 300 K, at the Au L_{III} edge, corresponding to the data in Figure 23.

Condition	16 wt% Au/C					
	Shell	***N***	***R* / Å**	**σ^2 / Å^2**	**ΔE_0 / eV**	**R_f**
85 K	Au-Au_1	10.28 ± 0.47	2.86 ± 0.01	0.0053 ± 0.0002	5.61 ± 0.33	0.018
	Au-Au_2	2.90 ± 1.31	4.05 ± 0.01	0.0063 ± 0.0023		
	Au-Au_3	22.05 ± 6.74	4.96 ± 0.01	0.0099 ± 0.0018		
	Au-Au_4	9.83 ± 7.72	5.73 ± 0.01	0.0174 ± 0.0042		
150 K	Au-Au_1	10.72 ± 0.47	2.86 ± 0.01	0.0070 ± 0.0002	4.70 ± 0.30	0.015
	Au-Au_2	2.17 ± 1.10	4.04 ± 0.01	0.0065 ± 0.0025		
	Au-Au_3	23.49 ± 8.12	4.95 ± 0.01	0.0125 ± 0.0024		
	Au-Au_4	11.06 ± 1.75	5.72 ± 0.01	0.0229 ± 0.0053		
300 K	Au-Au_1	10.52 ± 0.54	2.85 ± 0.01	0.0094 0.0004	4.40 ± 0.30	0.019
	Au-Au_2	1.69 ± 1.02	4.03 ± 0.01	0.0111 ± 0.0079		
	Au-Au_3	12.94 ± 6.18	4.94 ± 0.01	0.0132 ± 0.0035		
	Au-Au_4	11.76 ± 5.06	5.70 ± 0.01	0.0164 ± 0.0031		

As with the previous Pt examples data was collected for a Au foil prior to the nanoparticle measurements to enable determination of the amplitude reduction factor. This was found to be 0.85 ± 0.04; all coordination numbers and subsequent results were corrected accordingly.

There were difficulties in fitting the data beyond the first coordination shell for both Au/C samples at 300 K, and for the 16 wt% Au/C sample at 150 K. The disorder measured for these is questionably large, as are the errors associated with the coordination numbers. As discussed earlier, termination effects are liable to complicate higher coordination shell fitting. The degree of disorder present in even the 20 K measurements implies the system is structurally strained. Work by Solliard[30] has shown that whilst Pt nanoparticles retain their monocrystalline structure down to ~1 nm, Au nanoparticles below 6 nm start to change to include polytetrahedral grains in the structure. This change in crystallinity as a function of size may give rise to the increased disorder observed for the Au nanoparticles with respect to the Pt nanoparticles.

Both Au nanoparticle samples exhibit an apparent negative thermal expansion (NTE) over the range of the temperature measurements. This effect has been observed in studies by Comaschi[36,37] and Li *et al*[38], and has been attributed to the balance between the static, the vibrational and the electronic properties of the particle. The small size of the nanoparticles results in the energy levels being separated by only a few meV, this being smaller than the thermal energy of the system; consequently electronic excitations dominate.

The presence of an Au-S first shell scattering path was needed to improve the quality of it for the 4 wt% Au/C nanoparticles as the thiol encapsulating layer was still present. The addition of an Au-C or an Au-O path to the 16 wt% Au/C nanoparticles made no improvement to the overall quality of fit although, as with the previous sample, nothing was done to remove the citrate encapsulating groups. A list of the particle sizes determined from the EXAFS fits for the Au/C samples (data in **Section 6.3**, **Tables 19** and **20**) is in **Table 21** below.

Table 21: Particle sizes for the Au/C samples determined from EXAFS fits.

Sample / wt% Au/C	Average diameter / nm	
	Standard 4 shell fit	**Standard 1 shell fit**
4	1.48 ± 0.52	1.96 ± 0.37
16	4.04 ± 0.43	4.86 ± 0.68

7 Discussion and Conclusions

Each technique determines size differently. For cross-correlation to be a quantitative means of assessing a sample, a clear understanding of how each technique works and how to best weight the determined sizes is important. A full comparison of average particle size for the samples reported in this chapter is presented in **Table 22**.

Table 22: Cross correlation of average particle sizes. Errors in XRD crystallite size not supplied in analytical report.

Sample / wt% Pt/C	Average diameter / nm			
	XRD D_{Vol}	**TEM D_{Vol}**	**EXAFS**	
			Standard 4 shell fit	**Standard 1 shell fit**
10	---	1.61 ± 0.45	1.32 ± 0.09	1.52 ± 0.14
20	1.46	2.43 ± 0.69	1.51 ± 0.15	1.87 ± 0.26
40	1.81	2.57 ± 0.73	2.10 ± 0.29	2.29 ± 0.33
60	2.25	2.95 ± 0.82	2.49 ± 0.43	2.66 ± 0.34

10 wt% Pt/C treatment	Average diameter / nm			
	XRD D_{Vol}	**TEM D_{Vol}**	**EXAFS**	
			Standard 4 shell fit	**Standard 1 shell fit**
None	2.15	4.03 ± 1.10	2.01 ± 0.93	1.38 ± 0.81
973 K	2.93	3.77 ± 0.99	2.86 ± 0.88	2.63 ± 0.85
1273 K	6.91	9.34 ± 2.79	4.77 ± 1.37	4.17 ± 1.27
1473 K	14.40	22.50 ± 6.57	5.07 ± 1.63	4.22 ± 1.03

Table 22 continued: Cross correlation of average particle sizes. Errors in XRD crystallite size not supplied in analytical report.

Sample / wt% Au/C	Average diameter / nm			
	XRD D_{Vol}	TEM D_{Vol}	EXAFS	
			Standard 4 shell fit	Standard 1 shell fit
4	2.41	2.38 ± 1.22	1.48 ± 0.52	1.96 ± 0.37
16	4.19	4.14 ± 1.22	4.04 ± 0.43	4.86 ± 0.68

The conversion of TEM and XRD measurements to D_{Vol} brings the results into good agreement with each other, as it reduces the size determination down to two equivalent parameters, see **Equation 4 Section 3.3**. Both parameters are dependent on the sample quality, most importantly on σ, that is the variance of the size distribution. A sample with a uniform and narrow size distribution (low σ), such as the 4 wt% Au/C will have very good agreement between TEM and XRD, whereas a sample such as the 10 wt% Pt/C heated to 1473 K with a large σ will have very poor agreement between TEM and XRD (**Table 22**). EXAFS is a per-atom averaging technique, with the coordination number being a number weighted average. Unlike standard number weighted TEM that images a 2D projection of a particle to determine average size, the photoelectron wave in EXAFS radiates in 3-dimensions, averaging coordination number in a sphere around the absorber. In this sense, a particle size determined from EXAFS may be compared with a volume weighted size from TEM or XRD as the volume weighting assumes a spherical nature. The comparison cannot be direct though due to the per-atom averaging nature of EXAFS.

The presence and identification of mono- to tri- atomic species in the AC-STEM micrographs greatly aids the understanding of the cross correlation between results. A per-atom averaging technique such as EXAFS would include every atom when calculating the coordination number, whilst XRD would be unable to detect any of the debris, nor the amorphous layers visible on the outside of the particles. With the lack of crystallinity present in the unheated Pt/C series, there is little surprise that XRD gives the smallest measurement of particle (crystallite) size. A typical series of TEM micrographs would also be unable to detect the atomic debris, nor the amorphous surface layer.

Whilst the amorphous nature can be inferred from the quality of the XRD pattern, it is unclear as to whether this is the result of a thin PtO layer on the surface, or poor packing. The AC-STEM micrographs show in great detail the amorphous and crystalline areas of the nanoparticles, but as **Figure 5** illustrates, the beam breaks up the crystallinity of the particles, and so the cause of the reduced size determined by XRD is still not clear. *In situ* reduction with H_2 would be necessary to remove any surface oxide layers, increasing the amount of metallic crystalline Pt and thus the average crystallite size, if indeed the surface oxide is the cause. If no size increase were observed, then it can be concluded that at such small sizes, nanoparticles do not pack together in a uniform crystalline manner.

The question of whether *in situ* XRD measurements were needed for the Pt/C samples is not as applicable for the Au/C samples. The amorphous nature of the Au is a result of the size and not the presence of any other poorly defined oxidic phases. As such the samples offer much better agreement between the XRD and TEM derived average sizes. This supports the theory that the discrepancies observed for the Pt/C samples are caused by a small amorphous Pt oxide surface layer.

For the routine imaging of "as-received" samples of a similar nature to the nanoparticles reported in this work, the results suggest that XRD is not a suitable technique for crystallite size or phase determination A recent study by Uvarov and Popov[39] of the analysis of nanomaterials used a range of freeware and commercial software methods to determine crystallite sizes in the range 3 – 35 nm. All the tested methods provided very close agreement in size determination, confirming that the difficulties of size determination are not software limitations but physical limitations of the approach and the nature of the sample. The heat treated Pt/C samples have a large discrepancy between the XRD and TEM derived sizes. This is attributed to crystallite twinning during the heating process. The Au/C samples exhibit a very good agreement between XRD and TEM; given the poor crystallinity in the XRD patterns this is somewhat surprising, although the good agreement is attributed to the samples having a relatively low Au concentration, good dispersion over the support and a relatively uniform particle size, all of which aid size determination.

All the techniques used display the same trends of increasing size through each series of samples, with the EXAFS determined size almost always being the smallest, for reasons covered earlier. The one discrepancy is for the citrate stabilised Au/C nanoparticles with EXAFS giving the largest size. The XRD determined crystallite size

is also larger than the TEM determined particle size. TEM is only a local probe and therefore if the area under study contains no large particles that are present elsewhere in the sample, the determined size would contain some unknown amount of random error. There is also the potential source of human error in TEM particle size determination where the operator excludes any overly large particles that would distort the simple number weighted distribution that is commonly reported for TEM (i.e. the large particle would be regarded as an outlier). The discrepancy between the results for the 16 wt% citrate stabilised Au/C catalysts is attributed to large particles not observed during the TEM particle size analysis. On the contrary, these particles would be included in the bulk-probe methods of EXAFS and XRD and would increase the average particle/crystallite size measured, resulting in the discrepancy and highlighting one of the shortcomings of TEM.

The strengths and shortcomings of XRD, TEM and EXAFS have been highlighted, with a variety of samples to illustrate the points. Several of the assumptions that underpin EXAFS have not been dealt with so far, and these will be addressed in Chapter Four.

8 References

(1) Díaz-Moreno, S.; Koningsberger, D. C.; Muñoz-Páez, A. *Nuclear Instruments and Methods in Physics Research Section B: Beam Interactions with Materials and Atoms* **1997**, *133*, 15.

(2) Yevick, A.; Frenkel, A. I. *Physical Review B* **2010**, *81*, 115451.

(3) Calvin, S.; Riedel, C. J.; Carpenter, E. E.; Morrison, S. A.; Stroud, R. M.; Harris, V. G. *Physica Scripta* **2005**, 744.

(4) Azaroff, L. V.; Kaplow, R.; Kato, N.; Weiss, R. J.; Wilson, A. J. C.; Young, R. A. *X-Ray Diffraction*; McGraw-Hill, Inc.: USA, 1974.

(5) Warren, B. E. *X-Ray Diffraction*; Dover Publications Inc.: New York, 1990.

(6) Fernandez-Garcia, M.; Martinez-Arias, A.; Hanson, J. C.; Rodriguez, J. A. *Chemical Reviews* **2004**, *104*, 4063.

(7) *Nanoscience and nanotechnologies: opportunities and uncertainties*, The Royal Society, 2004.

(8) Calvin, S.; Luo, S. X.; Caragianis-Broadbridge, C.; McGuinness, J. K.; Anderson, E.; Lehman, A.; Wee, K. H.; Morrison, S. A.; Kurihara, L. K. *Applied Physics Letters* **2005**, *87*.

(9) Li, Z. Y.; Young, N. P.; Di Vece, M.; Palomba, S.; Palmer, R. E.; Bleloch, A. L.; Curley, B. C.; Johnston, R. L.; Jiang, J.; Yuan, J. *Nature* **2008**, *451*, 46.

(10) Shido, T.; Prins, R. *Journal of Physical Chemistry B* **1998**, *102*, 8426.

(11) Cervera-Gontard, L.; et al. *Journal of Physics: Conference Series* **2006**, *26*, 367.

(12) Schroeder, S. L. M.; Moggridge, G. D.; Chabala, E.; Ormerod, R. M.; Rayment, T.; Lambert, R. M. *Faraday Discussions* **1996**, 317.

(13) Smith, M. C.; Gilbert, J. A.; Mawdsley, J. R.; Seifert, S.; Myers, D. J. *Journal of the American Chemical Society* **2008**, *130*, 8112.

(14) Haubold, H. G.; Wang, X. H.; Goerigk, G.; Schilling, W. *Journal of Applied Crystallography* **1997**, *30*, 653.

(15) Meneses, C. T.; Flores, W. H.; Sasaki, J. M. *Chemistry of Materials* **2007**, *19*, 1024.

(16) Sankar, G.; Thomas, J. M. *Topics in Catalysis* **1999**, *8*, 1.

(17) Shaw, E. A.; Rayment, T.; Walker, A. P.; Lambert, R. M.; Gauntlett, T.; Oldman, R. J.; Dent, A. *Catalysis Today* **1991**, *9*, 197.

(18) Bus, E.; Miller, J. T.; Kropf, A. J.; Prins, R.; van Bokhoven, J. A. *Physical Chemistry Chemical Physics* **2006**, *8*, 3248.

(19) Haberkorn, R.; 1.2.1 ed. Saarbrücken, 2004, p ERLRAY_SizeDistSim V1.2.1 and ERLRAY_TEMDist.

(20) Ozkaya, D. *Platinum Metal Reviews* **2008**, *52*, 61.

(21) Hyde, T. I. *Platinum Metal Reviews* **2008**, *52*, 129.

(22) Curley, B. C.; Johnston, R. L.; Young, N. P.; Li, Z. Y.; Di Vece, M.; Palmer, R. E.; Bleloch, A. L. *J. Phys. Chem. C* **2007**, *111*, 17846.

(23) Krill, C. E.; Haberkorn, R.; Birringer, R.; Hari Singh, N.; M.Sc; Ph.D In *Handbook of Nanostructured Materials and Nanotechnology*; Academic Press: Burlington, 2000, p 155.

(24) Ravel, B.; Kelly, S. D. *X-Ray Absorption Fine Structure-XAFS13* **2007**, *882*, 150.

(25) Heald, S. M. In *X-Ray Absorption: Principles, Applications, Techniques of EXAFS, SEXAFS and XANES*; Koningsberger, D. C., Prins, R., Eds.; John Wiley & Sons: New York, 1988, p 87.

(26) Dalba, G.; Fornasini, P. *Journal of Synchrotron Radiation* **1997**, *4*, 243.

(27) Sadaiyandi, K. *Materials Chemistry and Physics*, *In Press, Corrected Proof*.

(28) Beni, G.; Platzman, P. M. *Physical Review B* **1976**, *14*, 1514.

(29) Huang, W. J.; Sun, R.; Tao, J.; Menard, L. D.; Nuzzo, R. G.; Zuo, J. M. *Nature Materials* **2008**, *7*, 308.

(30) Solliard, C.; Flueli, M. *Surface Science* **1985**, *156*, 487.

(31) Benfield, R. E. *Journal of the Chemical Society-Faraday Transactions* **1992**, *88*, 1107.

(32) Jentys, A. *Physical Chemistry Chemical Physics* **1999**, *1*, 4059.

(33) Poole, C. P.; Owens, F. J. *Introduction to Nanotechnology*; John Wiley & Sons Inc: Hoboken, New Jersey, 2003.

(34) Bellisario, D. O.; Jewell, A. D.; Tierney, H. L.; Baber, A. E.; Sykes, E. C. H. *The Journal of Physical Chemistry C* **2010**, *114*, 14583.

(35) Vaarkamp, M. *Catalysis Today* **1998**, *39*, 271.

(36) Comaschi, T.; Balerna, A.; Mobilio, S. *Physical Review B* **2008**, *77*, 10.

(37) Comaschi, T.; et al. *Journal of Physics: Conference Series* **2009**, *190*, 012122.

(38) Li, W. H.; Wu, S. Y.; Yang, C. C.; Lai, S. K.; Lee, K. C.; Huang, H. â. L.; Yang, H. â. D. *Physical Review Letters* **2002**, *89*, 135504.

(39) Uvarov, V.; Popov, I. *Materials Characterization* **2007**, *58*, 883.

CHAPTER FOUR: APPLICATION OF MOLECULAR DYNAMICS TO EXAFS

The work in this chapter seeks to address some of the assumptions underlying the "standard" EXAFS analysis approach, namely those of harmonic disorder brought about by a standard distribution of bond lengths throughout the nanoparticle. As in Chapter Three, "standard" analysis refers to the use of a bulk *fcc* lattice to generate scattering paths, "cumulant" analysis refers to the addition of higher cumulants to the standard analysis, and "MD" analysis refers to the use of an output from a molecular dynamic simulation being used to generate the scattering paths used to fit the experimental data.

1 Introduction

It has been shown that for highly disordered systems, EXAFS underestimates coordination number and thus particle size when compared with the theoretical coordination number based on size determination from other experimental techniques[1-4]. Similarly, when cross-correlating EXAFS with other techniques, such as TEM and XRD[5,6], EXAFS gives smaller sizes. The failure to accurately measure the coordination number is due to a failure to account for the high degree of disorder present. The most common approach to analysing the EXAFS involves quantifying the atom-atom pair distribution extracted from the data by approximating it to a Gaussian or near-Gaussian distribution. This allows for the determination of an average coordination number, relative position from the absorber and the mean square relative disorder, MSRD (also called the Debye Waller term - σ^2), of the absorbing atoms at that distance to be measured. If the Gaussian distribution is skewed or attenuated, additional terms (known as higher cumulants) can be added to the fitting parameters to account for this disorder[7-9], although the use of these has limitations.

1.1 Anharmonicity

In a perfect crystalline monometallic system, at 0 K, there would be only one nearest neighbour bond length throughout. Defects within a bulk system give rise to static disorder, as does decreasing the size down to the nanometre scale. Increasing the temperature increases the amount of dynamic disorder within the system. The Debye temperature is the temperature above which the material behaves classically and where thermal vibrations are more important than quantum effects. Below this temperature, an increase in disorder produces a variation in the nearest neighbour

bond length measured, that is modelled as a Gaussian distribution, and is known as the pair or radial distribution function (RDF)[10]. This is done traditionally to help reduce the number of variables in the EXAFS fitting process. When analysing particles by EXAFS, near-neighbour interactions can be parameterised as a 1D anharmonic potential based on the interatomic distance (**Equation 1**), where *a*, *b*, and *c* are the coefficients of $\psi(r)$.

$$\psi(r) = \frac{1}{2}ar^2 + br^3 + cr^4$$

Equation 1

Many parameters in the EXAFS equation, such as the disorder and coordination number, are highly correlated. As all of the individual inter-atomic distances cannot be measured independently of each other, this distribution is assumed. The width of the distribution is equivalent to the MSRD factor in a traditional *k* space calculation of the EXAFS spectrum[11]. Above the Debye temperature, thermal effects increase in importance and can skew the pair distribution function from harmonic (Gaussian) to anharmonic (log-normal distribution) as a result of dynamic disorder. Structural defects or distortions will also have an effect on the bond length distribution, and can split the single distribution into a bi- or even tri-modal distribution. One significant example of this for nanoparticles is the case of surface atoms. Surface atoms behave differently to core atoms as they are only partially coordinated, and have more freedom to move. This can result in a contraction of surface atoms towards the core to minimise the surface energy, which is true both for bulk materials[12] and nanoparticles[13]. These termination effects are present in both the bond length distribution and the disorder[13], as surface atoms rearrange to reduce the surface energy, whether by smoothing electron density[14] or a change in the metal-metal bond[15], and can be likened to surface tension. For bulk materials, this surface effect is negligible as the bulk contribution dominates.

With nanoparticles below 5 nm, the proportion of surface atoms is approximately 25%, rising rapidly to over 75% below 2 nm and therefore they contribute significantly to the average bond length, as well as being increasingly dominant in the EXAFS signal. With many of the atoms shifted towards shorter bond distances (surface), but the core atoms remaining (more or less) as they were, the radial distribution function will move away from a Gaussian distribution towards a bi-modal distribution, as a result of static disorder. The assumption of a Gaussian distribution in the "standard" EXAFS model breaks down in systems with high disorder, whether through thermal effects or size

effects. This results in errors in bond lengths, coordination numbers and disorder terms[1,11,16,17]. This is a limitation of the technique, as in disordered systems these errors tend to be exaggerated, resulting in particles appearing smaller than they are in reality, manifest by lower average coordination numbers than would be predicted by the true particle size.

1.2 Cumulant Expansions

The first approach to compensate for the anharmonicity present was to introduce higher order cumulants into the calculations. Initially developed in 1983 by Bunker[18], and known then as the ratio method, the introduction of higher cumulants provided a means to address this problem of a non-Gaussian distribution. Cumulant expansions are written in terms of moments of the anharmonic potential $\psi(r)$ (**Equation 1**), and evaluated in terms of a, b and c; these being the parameters used in the EXAFS fitting program. The cumulants equate to:

$$\Delta R = C_1 \approx \frac{-3bk_BT}{a^2}\left[1 + \frac{k_BT}{a^2}\left(\frac{45b^2}{a} - 32c\right)\right]$$

Equation 2

$$\sigma^2 = C_2 \approx \frac{k_BT}{a}\left[1 + \frac{k_BT}{a^2}\left(\frac{36b^2}{a} - 12c\right)\right]$$

Equation 3

$$C_3 \approx \frac{-6b(k_BT)^2}{a^3}\left[1 + \frac{k_BT}{a^2}\left(\frac{144b^2}{a} - 84c\right)\right]$$

Equation 4

$$C_4 \approx \frac{(k_BT)^3}{a^4}\left[\frac{108b^2}{a} - 24c\right]$$

Equation 5

The first cumulant, C_1 (**Equation 2**), relates to the mean value of the inter-atomic distance (R), and the second cumulant, C_2 (**Equation 3**), to its variance (that is the Debye Waller term σ^2). Normally only the first two cumulants are used as they are significant for small degrees of disorder[10], and, if none of the higher order cumulant values are greater than zero, the distribution is Gaussian. In highly disordered systems, like the nanoparticles studied in this work, the disorder is non-Gaussian, and so higher order cumulants are greater than zero. The third cumulant, C_3 (**Equation 4**), measures

the asymmetry of the radial distribution function with respect to a Gaussian distribution (**Figure 1a**), giving rise to a change in the average inter-atomic distance measured. If a positive C_3 is measured, the distance measured without its inclusion was an underestimate and vice versa. The fourth cumulant, C_4 (**Equation 5**), measures the symmetric sharpening and flattening of the radial distribution peak (**Figure 1b**), which is related to the coordination number and Debye Waller term. The inclusion of a positive C_4 will give a larger coordination number than without, and reduce the error associated with it by up to 40 %[7].

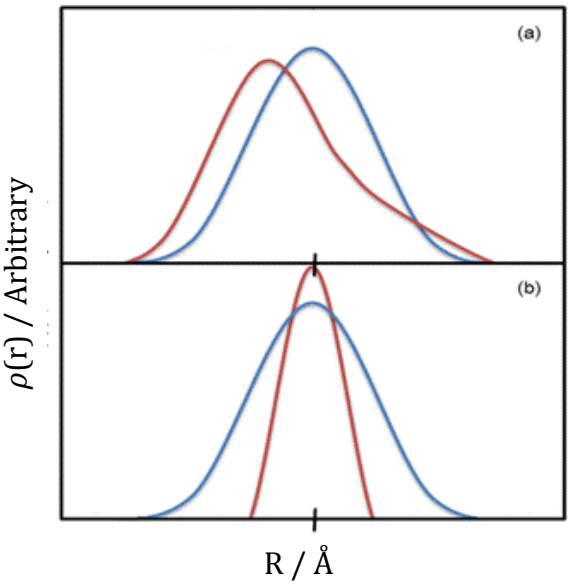

Figure 1: Schematic of effect of a) third cumulants, (C_3 - red) and b) fourth cumulants (C_4 - red) on a Gaussian distribution (blue) with variance C_2.

Low temperature measurements, in particular below the materials' Debye temperature, reduce the thermal disorder in the system, reducing the anharmonic contribution effect[10], notably from the under-coordinated surface atoms. For bulk systems, this can be enough to give an accurate value of the coordination number and disorder. Complications arise due to the fact that Debye temperature of very small particles can differ from the known bulk values[1]. Consequently, measurements must be taken at as low a temperature as possible to ensure the system is below its Debye temperature. With the dynamic (thermal) disorder greatly reduced that which is left is static disorder due to any termination effects brought about by the size of the particles.

1.3 Molecular Dynamic Studies of EXAFS

The inputs for both "standard" and "cumulant" EXAFS fitting of metallic particles are based on a bulk crystalline lattice where anharmonic thermal motion and surface

termination effects are negligible. In nano-sized systems, there is a need for the correct treatment of the distribution of neighbours, to account for the effects of the increasingly high proportion of disordered surface atoms with decreasing particle size[19].

The "standard" and "cumulant" models fit a single distribution for each coordination shell. If the contributions from surface bonds are different enough from the core, the distribution will become bimodal and any attempt to fit a single peak over the split distribution will result in false results.

Much prior work has been done addressing the accurate determination of coordination number from EXAFS, looking at the relationship between surface atom anharmonicity and particle geometry[20-23]. These theoretical studies clearly demonstrate the difference in radial position and intensity of each nearest neighbour shell between the different geometries modelled, yet still assume an even distribution of bond lengths from the core to the surface, with no contraction or other termination effects accounted for.

Work has been reported to simulate EXAFS based on MD simulations, and compare real structural data with MD predictions such as that by Okamoto[20] and Gilbert *et al.* [24,25], although only a few previous studies have attempted to use MD to more accurately determine average coordination number from EXAFS[2,3]. The disorder modelled in these systems however still remained a single pseudo-Gaussian distribution, unlike that reported here. Studies by Clausen *et al.* on nanoparticles below 5 nm have been largely theoretical, although work has been done on larger particles[2,3,17]. Of the previous studies combining MD with EXAFS, all have been for data collected at high temperature, and so thermal disorder dominates any fine structural disorder. As such, the disorder is far less pronounced and can be modelled using higher cumulants to account for small degrees of asymmetry within the distribution, an approach that also works well for disordered radial distributions in liquids[9,18,26]. Below 3 nm, the disorder is significantly non-Gaussian and so the use of higher cumulants will fail to accurately address the problem. Applying the structural information obtained from MD to real EXAFS data is needed determine if the increased disorder has a significant effect on the EXAFS fit, and if the assumption of symmetrical distribution of bond lengths is invalid.

Most recently Yevick and Frenkel[27] have simulated increasing the degree of surface disorder on a small metallic cluster, and how this effects the RDF. This investigates the assumption of bulk-like disorder and a symmetric bond length distribution that the

work in this chapter focuses on, although as with the majority of previous studies their work was purely theoretical. One other important difference is that their work is based on a radial distortion model, multiplying the distance of each atom from the centre of the cluster by a distortion function, rather than the molecular dynamic modelling performed in this work.

The amount of information in the MD output used as the EXAFS fitting input is far larger than that in the "standard" analysis. The total number of atom-atom pair distances measured throughout the simulation makes direct fitting unmanageable due to the number of potential scattering paths. Previously, a histogram approach has been used effectively by Ravel *et al.* to model the bond length distribution in highly disordered bulk materials[28,29]. In this approach all atom-atom pair distributions within a small range are binned into a histogram to reduce the information content of the input to a manageable size. This approach is further developed in this chapter.

The work in this chapter will compare the standard, cumulant and molecular dynamics methods for EXAFS analysis, and identify the current limitations for each approach. Cross-correlation with XRD and TEM will be used as a means to evaluate the effectiveness of each approach for determining coordination number and therefore an estimate of particle size.

2 Cumulant EXAFS

Data was fitted between 2-3 Å in *R* and 3-18 $Å^{-1}$ in *k*. The "cumulant" approach uses the "standard" approach as the basis for the fit, with the third and fourth cumulants as additional parameters. Fitting parameters are reported in **Tables 1a-d.**

Tables 1a-c: Structural parameters for 10 - 40 wt% Pt/C nanoparticles at 20 K, 150 K and 300 K, acquired in a reducing H_2 environment at the Pt L_{III} edge.

Table 1a	**10 wt% Pt/C**						
Temperature	***N***	***R* / Å**	**σ^2 / $Å^2$**	**C_3 / $Å^3$ ($\times10^5$)**	**C_4 / $Å^4$ ($\times10^6$)**	**ΔE_0 / eV**	**R_f**
20 K	8.70 ± 0.83	2.73 ± 0.01	0.0061 ± 0.0009	-9.5 ± 5.0	12.7 ± 9.9	6.92 ± 0.82	0.004
150 K	8.76 ± 0.76	2.73 ± 0.01	0.0073 ± 0.0009	-8.1 ± 5.4	15.1 ± 10.7	6.74 ± 0.72	0.004
300 K	7.61 ± 0.93	2.76 ± 0.01	0.0060 ± 0.0014	115.8 ± 9.3	-13.8 ± 19.1	6.62 ± 0.99	0.009

Table 1b	**20 wt% Pt/C**						
Temperature	***N***	***R* / Å**	**σ^2 / $Å^2$**	**C_3 / $Å^3$ ($\times10^5$)**	**C_4 / $Å^4$ ($\times10^6$)**	**ΔE_0 / eV**	**R_f**
20 K	8.84 ± 1.10	2.74 ± 0.01	0.0064 ± 0.0013	-2.1 ± 7.2	10.3 ± 14.4	7.40 ± 1.03	0.008
150 K	9.12 ± 1.28	2.73 ± 0.01	0.0073 ± 0.0015	-0.6 ± 9.1	13.4 ± 18.1	7.12 ± 1.16	0.012
300 K	8.22 ± 0.89	2.77 ± 0.01	0.0058 ± 0.0012	9.4 ± 8.0	-13.2 ± 16.3	6.40 ± 0.89	0.007

Table 1c	**40 wt% Pt/C**						
Temperature	***N***	***R* / Å**	**σ^2 / $Å^2$**	**C_3 / $Å^3$ ($\times10^5$)**	**C_4 / $Å^4$ ($\times10^6$)**	**ΔE_0 / eV**	**R_f**
20 K	8.92 ± 0.69	2.75 ± 0.01	0.0031 ± 0.0006	-3.9 ± 3.2	-4.7 ± 6.1	8.05 ± 0.70	0.002
150 K	8.68 ± 0.57	2.75 ± 0.01	0.0043 ± 0.0006	-0.1 ± 0.3	-4.0 ± 6.5	8.10 ± 0.57	0.002
300 K	8.02 ± 0.68	2.77 ± 0.01	0.0051 ± 0.0009	8.7 ± 5.5	-14.0 ± 11.1	6.48 ± 0.70	0.004

Table 1d: Structural parameters for 60 wt% Pt/C nanoparticles at 20 K, 150 K and 300 K, acquired in a reducing H_2 environment at the Pt L_{III} edge.

Table 1d	**60 wt% Pt/C**						
Temperature	***N***	***R* / Å**	**σ^2 / Å^2**	**C_3 / Å^3 (×10^5)**	**C_4 / Å^4 (×10^6)**	**ΔE_0 / eV**	**R_f**
20 K	9.13 ± 0.52	2.75 ± 0.01	0.0036 ± 0.0005	-0.1 ± 2.0	-6.1 ± 5.3	7.88 ± 0.50	0.001
150 K	8.82 ± 0.42	2.75 ± 0.01	0.0039 ± 0.0004	1.6 ± 2.4	-1.1 ± 0.6	8.64 ± 0.42	0.001
300 K	8.05 ± 0.58	2.77 ± 0.01	0.0044 ± 0.0008	7.6 ± 4.6	-18.0 ± 10.4	6.62 ± 0.61	0.003

Initially, looking at the quality of fit, the cumulant method appears to improve on the standard method as the R_f values are lower in most cases; however this would be expected on the addition of more variables to the fit. Of more importance is whether the values are physically reasonable, and how they compare with what is already known about the sample through other characterisation techniques.

The trends in coordination number and disorder for the cumulant analysis (**Tables 1a-d** above) are less clear than those for standard analysis of just the first coordination shell and also of the first four coordination shells (**Tables 3a-d** below and **Tables 5-8**, Chapter Three respectively). One cause of this is the inclusion of the fourth cumulant, C_4. In the majority of fits, C_4 is negative, and as such will result in a flattening of the EXAFS signal (**Equation 5**, **Figure 1b**), and a decrease in apparent coordination number. With the disorder directly linked to the coordination, it will follow the trends displayed in the amplitude to give the best fit to the data, if not the most reasonable. In both cases, the errors associated with the variables are increased over the standard fit as the software compensates for the linked behaviour between the variables. Consequently, the particle size determined by the cumulant method differs from that determined by the standard method (**Table 2**).

The third cumulant, C_3, decreases with measurement temperature, though the decrease is not linear and has large errors associated with it. Including too large a C_3 will

overestimate the bond length, and a negative C_3 will underestimate the bond distance[7]. Whilst the bond distances reported in **Tables 1a-d** are reasonable, the variance of C_3 does not appear so.

Overall, the addition of C_3 and C_4 terms to the fit provides inconsistent results (**Table 2**), the results no longer following the trends in particle size and as such worsen the correlation with other methods.

Table 2: Cross correlation of average size; cumulant method vs. standard method. Sizes are determined from average of fits of the EXAFS data at 20, 150 and 300 K; the reported error is the variance.

Sample / wt% Pt/C	Average diameter / nm	
	Standard EXAFS	Cumulant EXAFS
10	1.52 ± 0.14	1.79 ± 0.41
20	1.87 ± 0.26	2.05 ± 0.37
40	2.29 ± 0.33	1.90 ± 0.34
60	2.66 ± 0.34	2.02 ± 0.43

In addition to a worse cross-correlation with the TEM and XRD data the cumulant approach has several limitations. Cumulant expansions are only accurate at low *k* values, as they diverge with increasing *k* values[11]. However, the lowest *k* data is inherently missing in EXAFS[30]. This creates a particular problem for cumulant expansion analysis of heavier metal nanoparticles such as the Pt series in this work, where the quality of structural information increases with useable *k* range. Cumulant expansions can work very well for the first coordination shell, but are limited as they break down when applied to higher coordination shells, as they cannot be applied to multiple scattering effects, nor to systems with mixed coordination shells[10,11]. Thus, for systems with high structural disorder, when more structural information is needed beyond the first shell, and when more than one element is present in the nearest coordination shell, another means is needed to account for the disorder

3 MD EXAFS

3.1 Introduction

The histogram generated by the molecular dynamics (MD) output provides a simple representation of how the standard and cumulant approaches can fail (**Figure 2**).

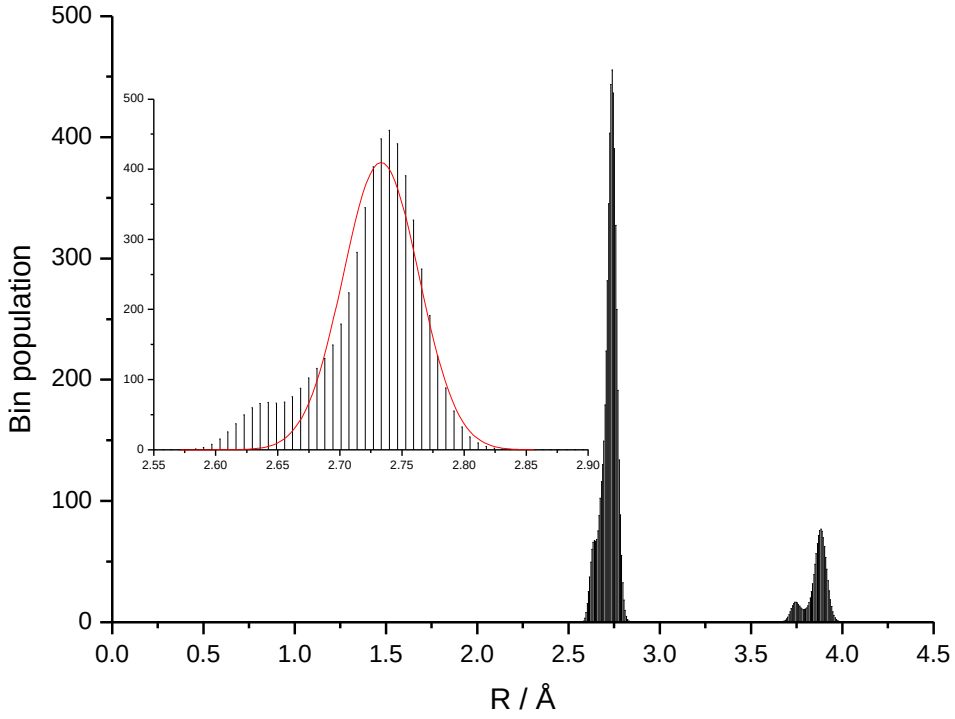

Figure 2: Sample histogram generated from MD output, with Gaussian fit over first shell (red line - inset). Vertical lines are the sum of nearest neighbour bond distances forming a radial distribution function.

Basing the analysis on a Gaussian distribution for the case shown in **Figure 2** would introduce a significant systematic error into the analysis. In the standard model, the MSRD (σ^2) is used to describe the variance of the atomic displacement from the absorbing atom at distance *R*. This variance can be due to both structural disorder and thermal vibrations - averaged out over the whole structure - and is modelled by a Gaussian or near-Gaussian distribution. In nanoparticles, such as those under study here, there is no large structure over which to average out, and so termination effects (surface contraction) are significant and result in a low R tail. Assuming the nanoparticles are nominally *fcc* in packing (as in the standard analysis model), on a very local scale, an atom pair will occasionally have an interatomic distance far larger than the standard value - i.e. 2.772 Å for Pt - giving rise to a high R tail. For particles

≥ 100 nm diameter, these tails in the distribution are insignificant, and a Gaussian approximation for the MSRD is sufficient. For nanoparticles < 10 nm diameter, the lack of long range order and large surface area to volume ratio become significant, especially with regard to termination effects. This is seen in all the MD simulations run where the largest contraction in nearest neighbour distances comes from the surface shell[13,27].

The Gaussian fit across the first shell in **Figure 2** cannot encompass all the scattering paths, as the distribution is clearly bimodal, with a large contribution to the signal at shorter than average bond lengths. These contributions are from nearest neighbour pairs that involve at least one edge or vertex atom (**Figure 3**), and to a lesser extent, atoms on the faces of the nanoparticle surface.

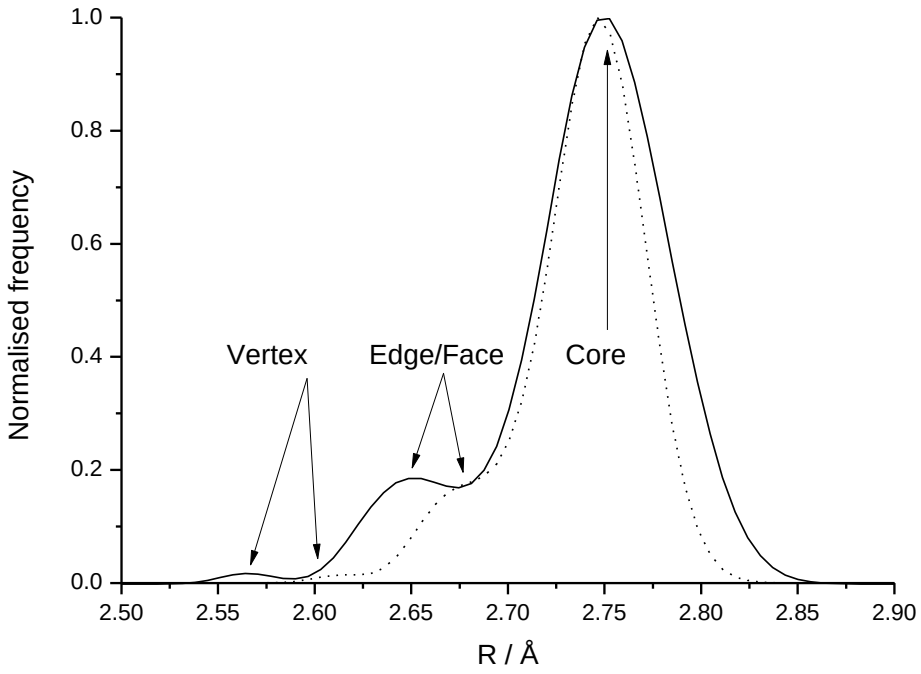

Figure 3: Origin of nearest neighbour pair contributions to histogram in 20 K simulations; Gupta potential (—) and Sutton-Chen potential (···).

As the cluster size increases, the core atom-pair contributions begin to dominate the RDF. As the number of core atoms decrease with decreasing size, the contributions of face and edge atoms increases. The contribution to the overall intensity of the surface atoms is such that a single Gaussian distribution will no longer be able to accurately model the bond-length distribution in nanoparticles, highlighting the shortcomings of

using a standard approach regarding EXAFS analysis of small nanoparticles. Thus, the attempts to fit a single peak over a bimodal distribution would require a larger σ^2 term to fit across the bond length distribution and result in a smaller path degeneracy (amplitude) than is actually the case. The average of the contracted surface bond length and the core bond length throughout the nanoparticle is measureable using the standard model, although due to the possible scale of surface contraction previously reported[13,27], is unlikely to be representative of either.

3.2 Experimental

The raw EXAFS data was processed and fitted to theory as with the standard approach, but instead of using the Pt *fcc* structure to fit the data, the histogram output from the MD output was used. In the standard analysis, each nearest neighbour shell is centred around a single scattering path at distance R_i, assuming a symmetrical bond distribution with disorder σ^2. The histogram contains bins 0.0065 Å wide, with the frequency of each bin being the total number of nearest neighbour pair distances that fall within the specific range during the course of the simulation, and is therefore equivalent to a radial distribution function (RDF) of the simulated nanoparticle. New sections of code for Artemis[31] were provided by Bruce Ravel to enable the generation of scattering paths for each histogram bin. With the MD approach, each bin in the histogram is considered to be a single scattering path, with a contribution towards the total amplitude of each nearest neighbour shell, thus containing a much larger amount of structural information. The total amplitude of all histogram bins for the first coordination shell was normalised to unity. Each histogram bin was therefore parameterised using the same 4 variables as the standard approach; amplitude N, isotropic expansion coefficient α, energy correction ΔE_0 and disorder σ^2. A disorder term was still needed for the fits as the simulations did not fully account for the thermal vibrations within the molecule[32]. All data was fitted over a range in R between 2 and 3.2 Å, and between 3 and 18 $Å^{-1}$ in k.

The scatterers at the different distances within the histogram give rise to a much more complex phase relationship than that of a much simpler Gaussian distribution (**Figure 4**). Whilst the MD simulations do not perfectly model the nanoparticles[32], they provide an improvement over the standard model, and by fitting the EXAFS data with different MD simulation outputs, a means by which to evaluate the simulations ability to model real nanoparticles is available.

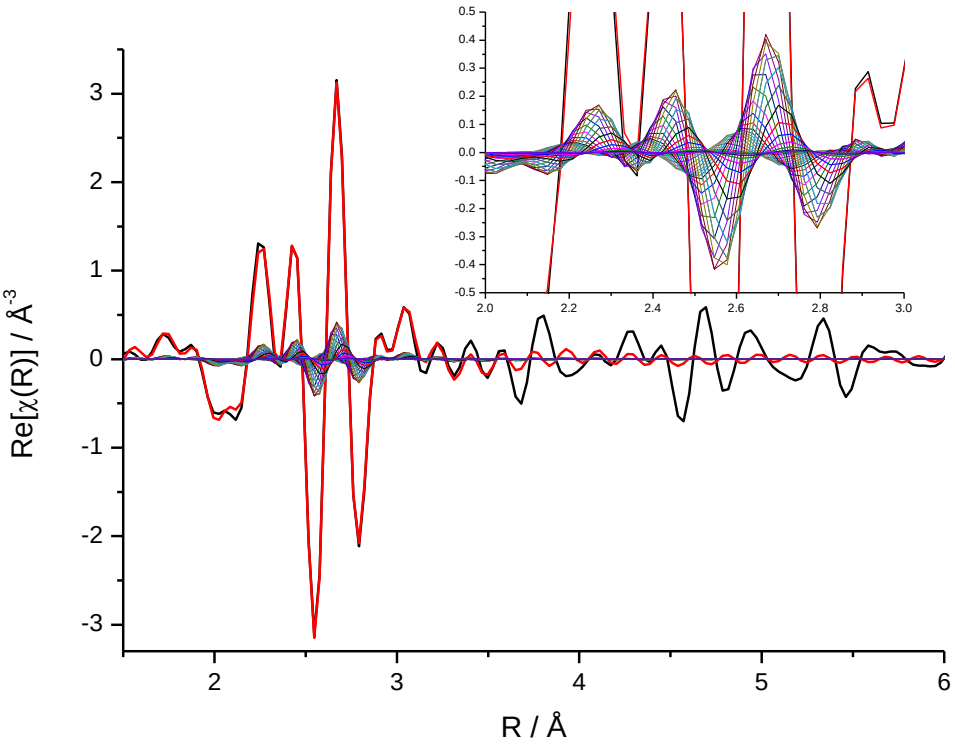

Figure 4: Fourier transform of the phase relationship between scattering paths generated from RDF output for first coordination shell. Black line is data, red line is the fit using the sum of the RDF scattering paths, RDF scattering paths are lower amplitude multi-coloured lines; close-up of RDF scattering paths in inset.

3.3 Results and Discussion

3.3.1 Effect of MD Potential and Simulated Nanoparticle Size

In the analysis reported here, only the first coordination shell is analysed as the current software is incapable of managing the large numbers of scattering paths required for a full multiple scattering analysis. The RDF data was extracted from the Pt simulations run at 20 K, 150 K and 300 K (simulation temperatures corresponding to the EXAFS experimental conditions), and that for the first shell is plotted in **Figure 5**.

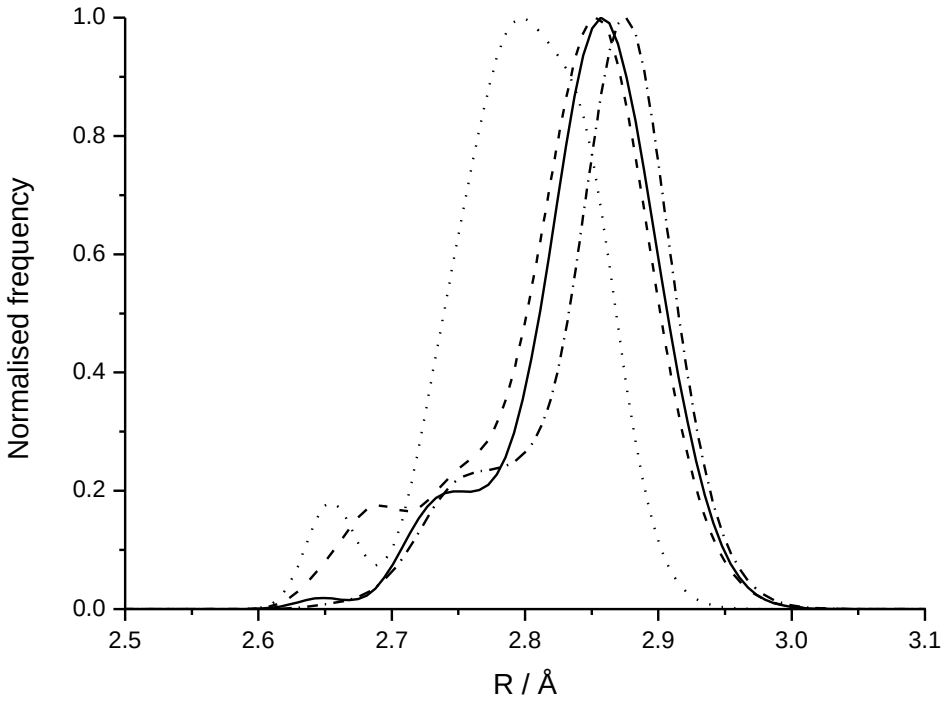

Figure 5: First shell RDFs at 20 K for 55 atom (····), 177 atom (----), 381 atom (—) and 767 atom (- · - ·) "spherical" Pt nanoparticles.

Each permutation of experimental temperature, MD simulation size and MD temperature was tried during the EXAFS analysis; the best fit results are in **Tables 3a-d** below. The 300 K simulations could not be fitted to the data at all. As previously reported[32] the higher temperature simulations overestimate the disorder, and consequently a negative σ^2 term was needed to provide any sort of fit; as this is physically unrealistic these results were discounted. Simulations run at 150 K were able to be fitted to data at 150 K and 300 K within the same error as the 20 K simulation. The smallest (55 atom) and largest (767 atom) simulated clusters had disorder that was too great and too small, respectively, and these too failed to give

physically realistic fits to the data. All best reported fits are to the 381 atom cluster unless otherwise stated.

Tables 3 a-b: Structural parameters for 10 - 20 wt% Pt/C nanoparticles at 20 K, 150 K and 300 K, acquired in a reducing H_2 environment at the Pt L_{III} edge.

Table 3a	Fitting method	10 wt% Pt/C				
		N	α*	σ^2 / Å^{-2} (×10^4)	ΔE_0 / eV	R_f
20 K	Standard	7.89 ± 0.60	-0.012 ± 0.001	50 ± 3	8.11 ± 0.70	0.009
	Gupta*	8.98 ± 0.39	-0.002 ± 0.001	31 ± 2	7.39 ± 0.28	0.004
	Sutton-Chen*	8.08 ± 0.44	0.002 ± 0.001	35 ± 2	7.58 ± 0.46	0.005
150 K	Standard	7.91 ± 0.52	-0.013 ± 0.001	61 ± 3	7.62 ± 0.63	0.009
	Gupta*	8.85 ± 0.39	-0.003 ± 0.001	41 ± 2	6.20 ± 0.40	0.004
	Sutton-Chen*	8.02 ± 0.29	0.001 ± 0.001	44 ± 2	7.23 ± 0.51	0.004
300 K	Standard	8.23 ± 0.62	-0.006 ± 0.002	71 ± 1	5.63 ± 0.69	0.017
	Gupta	8.67 ± 0.85	0.002 ± 0.002	54 ± 6	5.01 ± 0.80	0.023
	Sutton-Chen	8.31 ± 0.75	0.005 ± 0.001	60 ± 5	5.41 ± 0.66	0.015

*177 atom cluster provided best fit

Table 3b	Fitting method	20 wt% Pt/C				
		N	α*	σ^2 / Å^{-2} (×10^4)	ΔE_0 / eV	R_f
20 K	Standard	8.24 ± 0.56	-0.012 ± 0.001	55 ± 3	7.71 ± 0.59	0.009
	Gupta	8.64 ± 0.56	-0.004 ± 0.001	38 ± 3	6.90 ± 0.62	0.010
	Sutton-Chen	8.35 ± 0.54	-0.001 ± 0.001	45 ± 3	7.51 ± 0.56	0.008
150 K	Standard	8.41 ± 0.66	-0.014 ± 0.002	62 ± 4	7.23 ± 0.72	0.014
	Gupta	8.88 ± 0.67	-0.006 ± 0.001	45 ± 4	6.62 ± 0.74	0.015
	Sutton-Chen	8.53 ± 0.65	-0.003 ± 0.001	52 ± 4	7.05 ± 0.68	0.010
300 K	Standard	8.88 ± 0.59	-0.004 ± 0.001	68 ± 4	5.60 ± 0.62	0.015
	Gupta	9.67 ± 1.25	0.004 ± 0.002	52 ± 6	4.51 ± 1.01	0.016
	Sutton-Chen	9.15 ± 0.63	0.007 ± 0.001	58 ± 3	4.96 ± 0.63	0.010

Tables 3 c-d: Structural parameters for 40 - 60 wt% Pt/C nanoparticles at 20 K, 150 K and 300 K, acquired in a reducing H_2 environment at the Pt L_{III} edge.

Table 3c	Fitting method	40 wt% Pt/C				
		N	α*	σ^2 / Å^{-2} (×10^4)	ΔE_0 / eV	R_f
20 K	Standard	9.37 ± 0.43	-0.007 ± 0.001	35 ± 1	8.72 ± 0.50	0.004
	Gupta	10.02 ± 0.58	0.000 ± 0.000	19 ± 2	7.41 ± 0.62	0.005
	Sutton-Chen	9.52 ± 0.39	0.003 ± 0.001	25 ± 1	8.33 ± 0.37	0.003
150 K	Standard	8.96 ± 0.30	-0.008 ± 0.001	46 ± 1	8.14 ± 0.29	0.002
	Gupta	9.45 ± 0.55	-0.001 ± 0.001	29 ± 2	7.14 ± 0.53	0.003
	Sutton-Chen	9.08 ± 0.34	0.002 ± 0.001	36 ± 1	7.88 ± 0.35	0.002
300 K	Standard	8.70 ± 0.45	-0.006 ± 0.001	62 ± 3	5.46 ± 0.52	0.010
	Gupta	9.56 ± 1.27	0.002 ± 0.002	46 ± 6	4.66 ± 1.20	0.014
	Sutton-Chen	9.02 ± 0.65	0.005 ± 0.001	52 ± 3	5.34 ± 0.63	0.009

Table 3d	Fitting method	60 wt% Pt/C				
		N	α*	σ^2 / Å^{-2} (×10^4)	ΔE_0 / eV	R_f
20 K	Standard	9.64 ± 0.31	-0.008 ± 0.001	42 ± 1	7.92 ± 0.29	0.002
	Gupta	10.46 ± 0.79	-0.001 ± 0.001	26 ± 3	6.72 ± 0.73	0.003
	Sutton-Chen	9.85 ± 0.40	0.003 ± 0.001	31 ± 1	7.49 ± 0.44	0.001
150 K	Standard	9.40 ± 0.31	-0.008 ± 0.001	46 ± 1	8.43 ± 0.34	0.002
	Gupta	9.91 ± 0.68	-0.001 ± 0.001	29 ± 3	7.36 ± 0.67	0.009
	Sutton-Chen	9.60 ± 0.44	0.003 ± 0.001	36 ± 2	8.10 ± 0.41	0.002
300 K	Standard	9.04 ± 0.54	-0.004 ± 0.001	59 ± 3	5.79 ± 0.62	0.010
	Gupta	9.96 ± 1.31	0.003 ± 0.002	43 ± 6	4.81 ± 1.23	0.015
	Sutton-Chen	9.36 ± 0.68	0.007 ± 0.001	49 ± 3	5.39 ± 0.62	0.009

*A path length correction term (linear expansion coefficient α) was used as a fitting parameter for the MD input as well as the standard input. The very large number of paths contained in the MD input would make tabulated results of fitted bond lengths

unwieldy, and as such the linear expansion coefficient is reported instead of the fitted bond length.

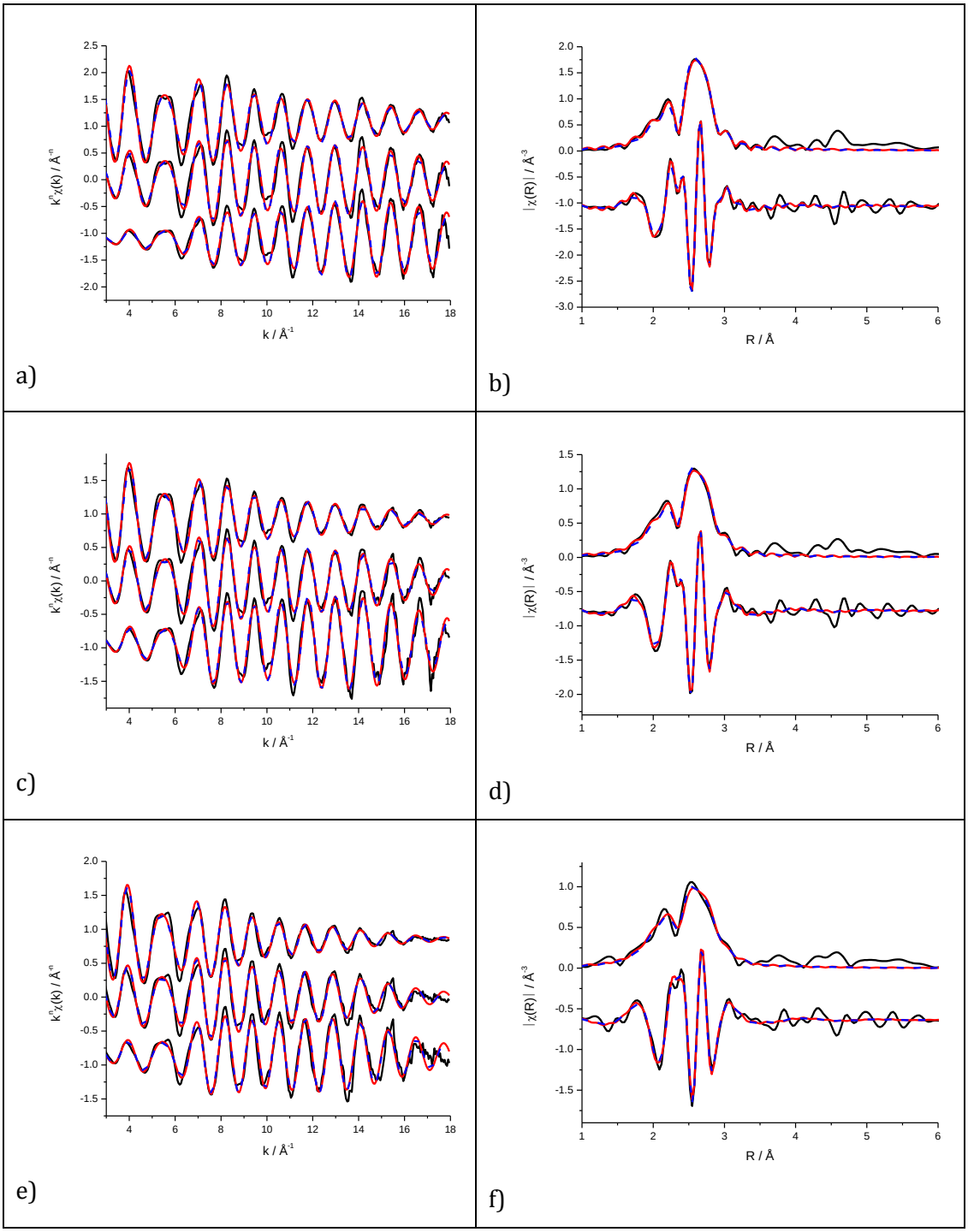

Figure 6: k^n weighted (k^1 top, k^2 middle, k^3 bottom of panel) experimental data (black) and fit to Gupta (red) and Sutton-Chen (blue dashed) potentials, along with k^2 weighted magnitude and real Fourier transform for 10 wt% Pt/C at a-b) 20 K, c-d) 150 K and e-f) 300 K.

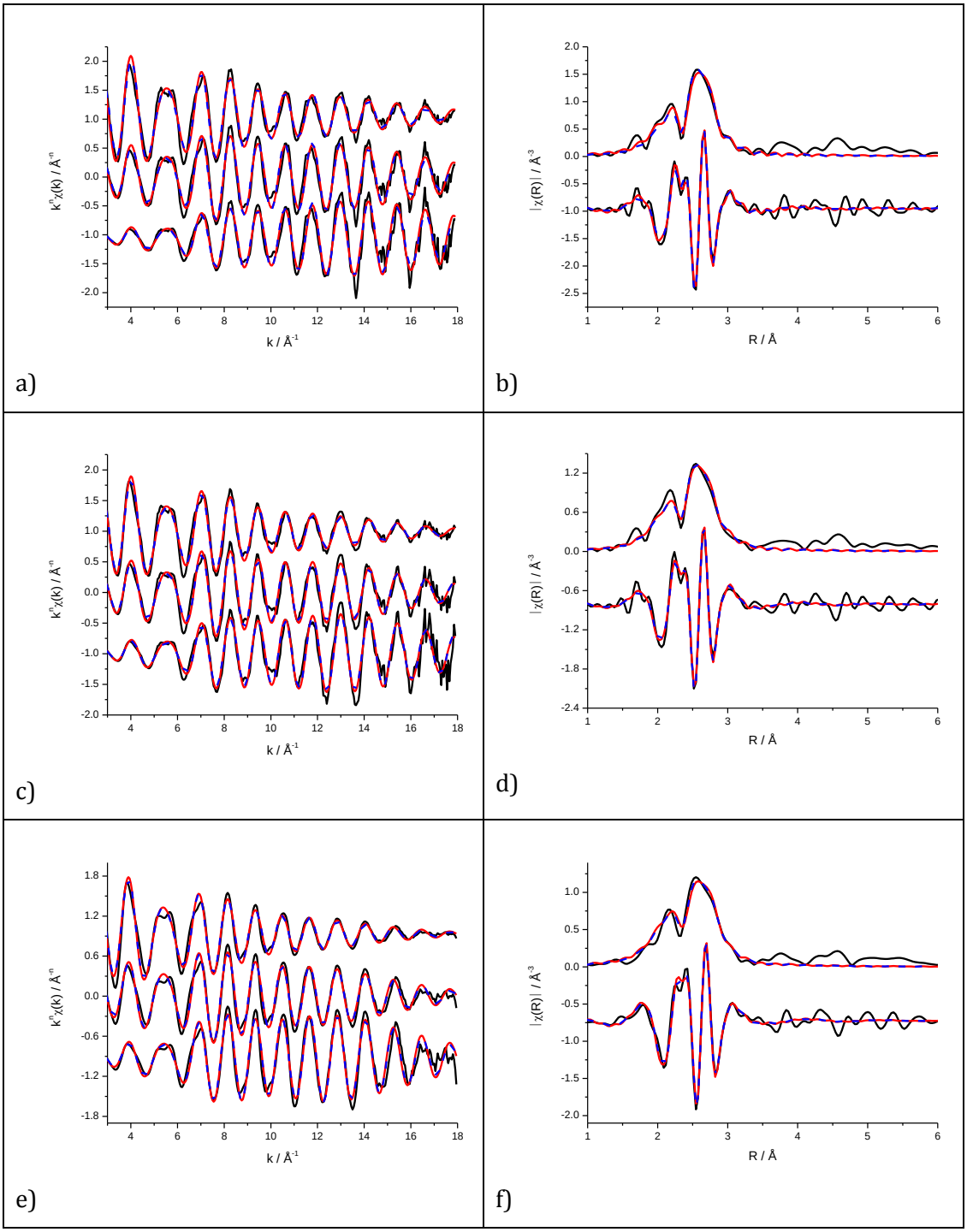

Figure 7: k^n weighted (k^1 top, k^2 middle, k^3 bottom of panel) experimental data (black) and fit to Gupta (red) and Sutton-Chen (blue dashed) potentials, along with k^2 weighted magnitude and real Fourier transform for 20 wt% Pt/C at a-b) 20 K, c-d) 150 K and e-f) 300 K.

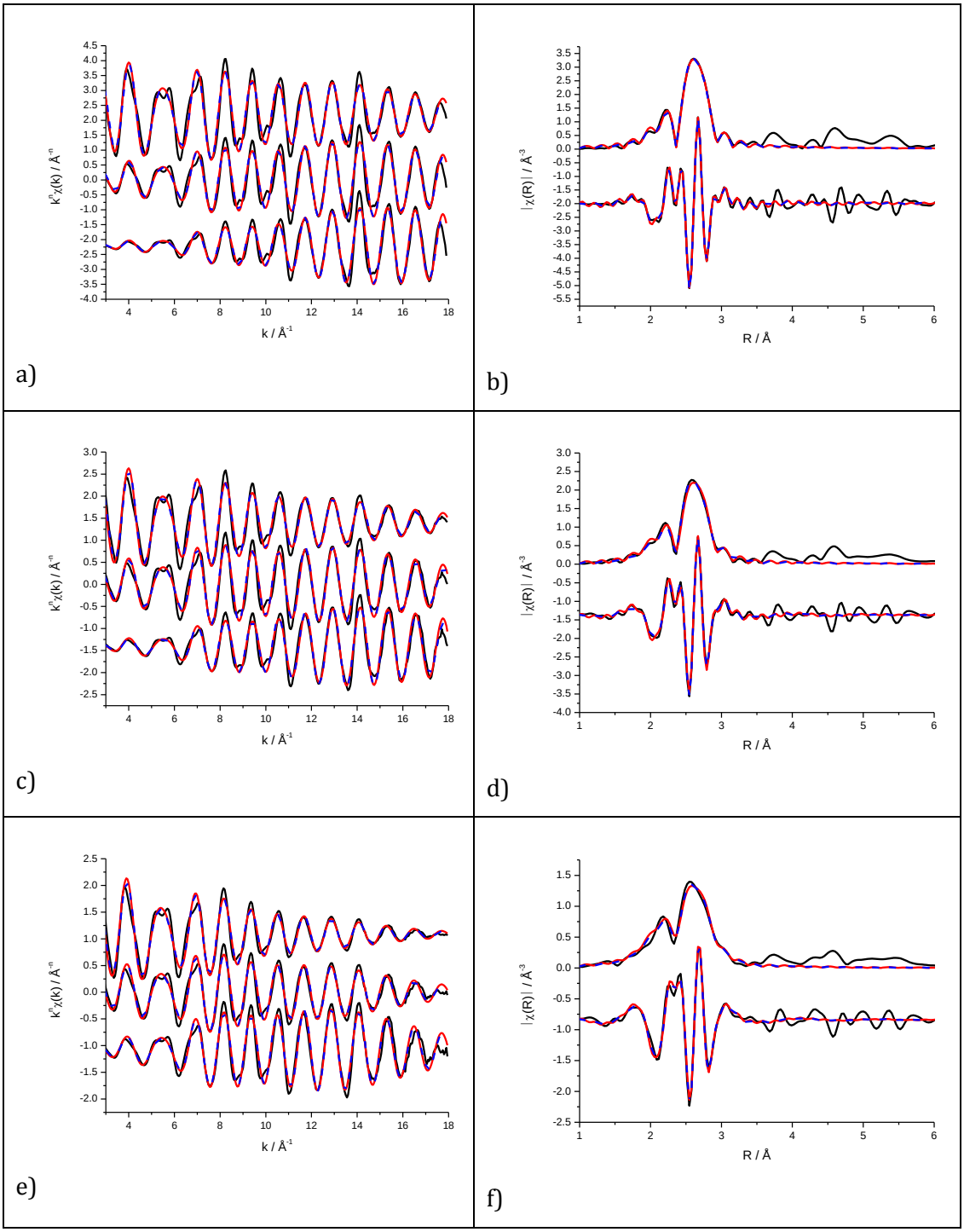

Figure 8: k^n weighted (k^1 top, k^2 middle, k^3 bottom of panel) experimental data (black) and fit to Gupta (red) and Sutton-Chen (blue dashed) potentials, along with k^2 weighted magnitude and real Fourier transform for 40 wt% Pt/C at a-b) 20 K, c-d) 150 K and e-f) 300 K.

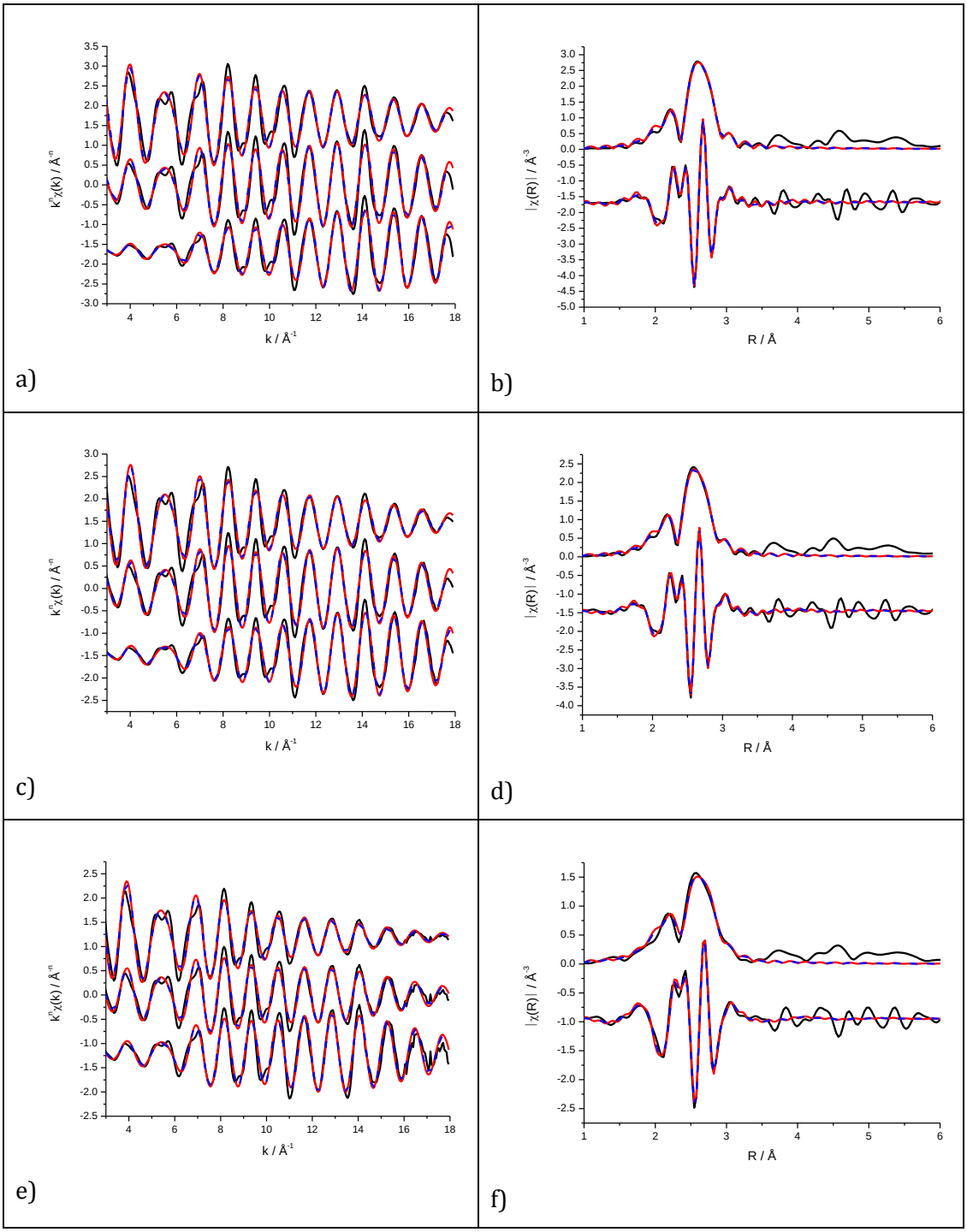

Figure 9: k^n weighted (k^1 top, k^2 middle, k^3 bottom of panel) experimental data (black) and fit to Gupta (red) and Sutton-Chen (blue dashed) potentials, along with k^2 weighted magnitude and real Fourier transform for 60 wt% Pt/C at a-b) 20 K, c-d) 150 K and e-f) 300 K.

The Sutton-Chen potential gave the best quality of fit, and the Gupta potential an inferior quality of fit (**Figure 10**) when compared with the standard fitting approach. This is attributed to the narrower distribution of bond lengths modelled by the Sutton-Chen potential; although the distribution still included a significant low *R* shoulder in the RDF due to surface contraction. The use of molecular dynamic simulations to fit real experimental data can not only provide an improved fitting model, but a measureable metric for evaluating the quality of a particular MD simulation or potential at replicating nanoparticle behaviour, bearing in mind that the empirical potentials used in this work were designed to model bulk metal behaviour.

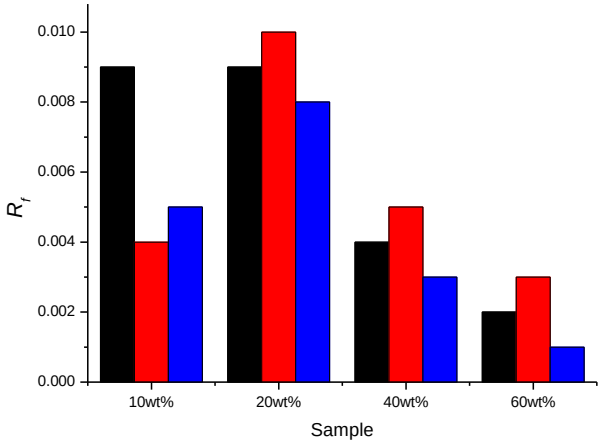

Figure 10: Comparison of quality of fit (R_f) to the first coordination shell between the standard fitting approach (black) and the applied molecular dynamic approaches; Gupta (red) and Sutton-Chen (blue). Fit is of simulation at 20 K to experimental data measured at 20 K.

Whilst visibly there is no significant difference between the two MD fitting approaches, the values in **Tables 3a-d** clearly show the Sutton-Chen potential is superior in this case. With the Sutton-Chen potential giving an improved quality of fit over the standard model and the Gupta model, all results reported from now on will focus on the Sutton-Chen potential. Although the MD simulations provide an improved input for EXAFS analysis, they do not completely account for all the structural and thermal disorder present and the fits using the RDF histogram as an input require a σ^2 parameter. The σ^2 values obtained using the RDF histogram are less than those obtained using the standard model, the difference in all cases between the two can fully be accounted for by the disorder present in the simulation. Plots in both *k* and *R* show

no great difference between the standard approach and the MD approach, although the relationship between coordination number and σ^2 in both models and the improvement that the MD approach offers can be better understood by comparing the relationship between the two parameters (**Figure 11a**).

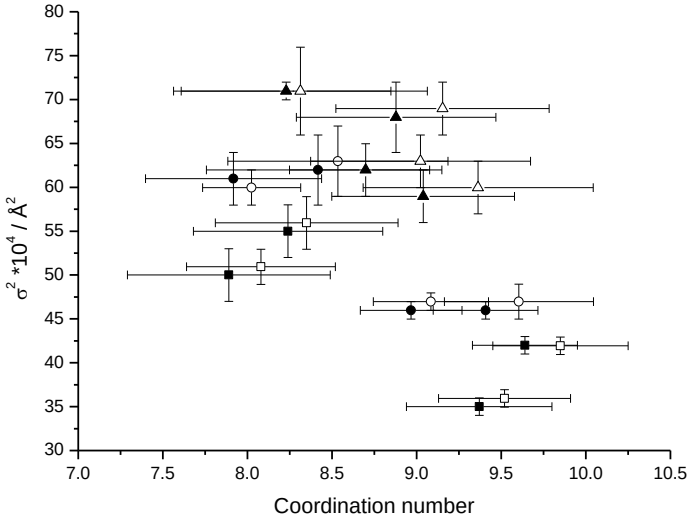

a)

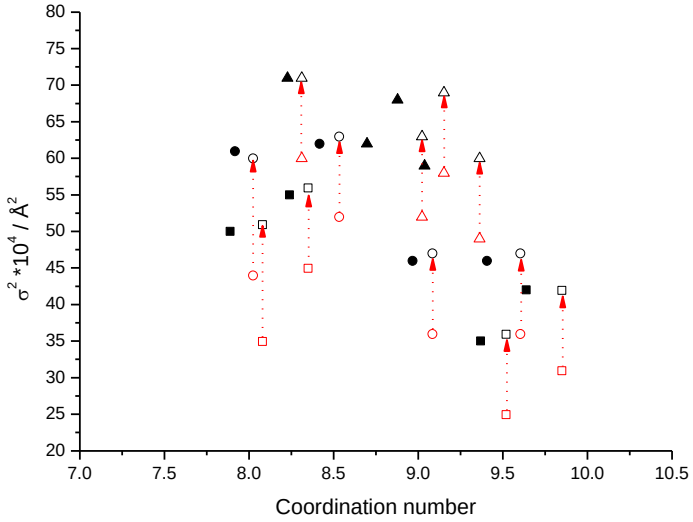

b)

Figure 11: a) Correlation between coordination number and disorder, σ^2, and b) corrections (red) applied to σ^2, for standard fitting approach (closed points - ●) and MD fitting approach (open points - ○). The 20 K MD simulations were used for the MD approach; experimental data at 20 K is represented by a square marker (□), at 150 K by a circular marker (○) and at 300 K by a triangular marker (Δ). Error bars are not included in figure b) for ease of interpretation.

Using a more structurally disordered input from the MD gives an improved model to fit the nanoparticles, and the resultant fits have less disorder and a higher amplitude than the standard model as was discussed earlier. The MD simulations clearly do not completely model the disorder as a σ^2 term is still required in the fit; however it is unlikely that any of the nanoparticles are the perfect "spheres" modelled as evidenced by the AC-STEM images in Chapter Three. The disorder of the first shell was calculated directly from the simulation (dotted red arrows, **Figure 11b**) and combined with the σ^2 determined during the fit (red open points, **Figure 11b**) to provide a more direct comparison with the disorder determined using the standard method.

The combined σ^2 values (open black points, **Figure 11b**) fell in the same range, whereas there was a trend for a general increase in the determined coordination number. Although not a large increase, and within the generally accepted error limits[16] for coordination number determination, the improved qualities of fit indicate that the larger size given by the MD approach is physically reasonable. Indeed when combined with TEM measurements, the MD approach gives a better interpretation of the data than the standard approach and overcomes some of the limitations in applying bulk theory to the analysis of nanoparticles.

The coordination numbers determined from the MD fits were converted into estimated average particle sizes and are reported in **Table 4** alongside those from the standard fit for comparison.

Table 4: Cross correlation of average size; MD methods vs. standard method. Sizes are average of fits at 20, 150 and 300 K; the reported error is the variance.

Sample wt% Pt/C	Average particle size / nm		
	Standard	Gupta	Sutton-Chen
10	1.52 ± 0.14	2.12 ± 0.14	1.60 ± 0.10
20	1.87 ± 0.26	2.38 ± 0.56	2.01 ± 0.36
40	2.29 ± 0.33	3.04 ± 0.41	2.49 ± 0.30
60	2.66 ± 0.34	3.66 ± 0.50	2.94 ± 0.31

One interesting observation for the 10 wt% Pt/C sample at 20 K and 150 K was that the smaller 177 atom simulation provided a better fit than the 381 atom simulation. This simulation output (177 atoms) contained a greater degree of disorder than the larger simulation outputs. The difference between the fitted disorder using the MD

simulation (vs. the standard method) was larger for these two measurements than all the others (**Figure 11b** – furthest left two points; **Table 3a**), equivalent to that contained in the simulation. This is a nice validation of the MD method, with the smaller more disordered particles being fitted best by smaller more disordered simulations and larger particles fitted best by equivalent sized simulations. Also an encouraging result is that the sizes of MD simulation that provides the best fit for each particle size is in reasonable agreement with the TEM derived average particle sizes.

3.3.2 Effect of Histogram Bin Width

To understand whether the improved fit is more dependent on an increased number of scattering paths to parameterise the fit (i.e. the number of bins) or the location of the bins (i.e. the specific shape of the RDF brought about by different size simulated nanoparticles), the MD output histogram was re-binned. The initial set of simulations consisted of 0.0065 Å bin widths, giving a total of 1000 bins up to 6.5 Å i.e. up to and including the fourth nearest neighbour. This radial distance was chosen with the longer term goal of including multiple scattering effects in the MD fits. By fitting every permutation of RDF to experimental temperature, the effect of scattering path location and intensity was investigated, the results having already been discussed. To investigate the effect of the number of bins on the fit, the RDF histogram was re-binned with an order of magnitude more and less scattering paths, i.e. 100 total bins of 0.065 Å width and 10000 of 0.00065 Å width respectively. The standard approach, using one single scattering path for the first nearest neighbour can be thought of in these terms as using a histogram effectively consisting of four bins.

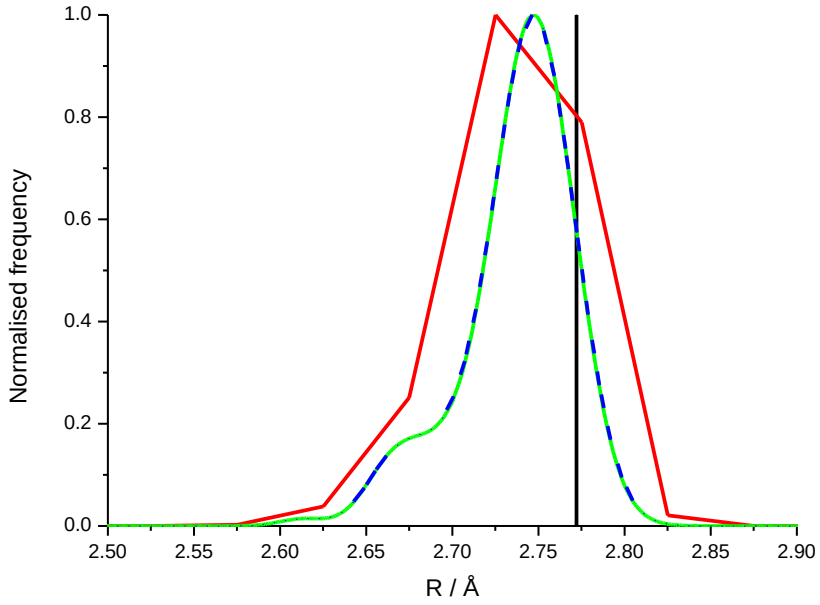

Figure 12: RDFs based on different histogram bin sizes; standard method (single bin)– black line; 0.065 Å bin size – red line, 0.0065 Å bin size – green line; 0.00065 Å bin size – blue dashed line. The similarity of the lines for the two smallest bin sizes is such that they cannot be distinguished from one another.

Figure 12 clearly shows how the histogram with the largest bin size has poorer spatial resolution, jumping roughly from bin to bin instead of the smooth variations observed for the 0.0065 Å and 0.00065 Å bin histograms. That aside, there is enough resolution to model the anharmonicity present in the bond length distribution within the nanoparticle simulation, and provide an improvement over the standard model, the results of the fits are plotted in **Figure 13**, and the results in **Table 5**.

Table 5: Effect of bin size on structural parameters for 20 wt% Pt/C nanoparticles at 20 K, acquired in a reducing H_2 environment at the Pt L_{III} edge.

Number of bins	N	α	σ^2 / Å^{-2} ($\times 10^4$)	ΔE_0 / eV	R_f
Standard	9.32 ± 0.42	-0.0068 ± 0.0006	35 ± 1	8.66 ± 0.45	0.0028
100 bin	9.40 ± 0.37	0.0041 ± 0.0005	22 ± 1	8.39 ± 0.40	0.0023
1000 bin	9.52 ± 0.39	0.0037 ± 0.0005	25 ± 1	8.26 ± 0.41	0.0025
10000 bin	9.52 ± 0.39	0.0037 ± 0.0005	25 ± 1	8.26 ± 0.41	0.0025

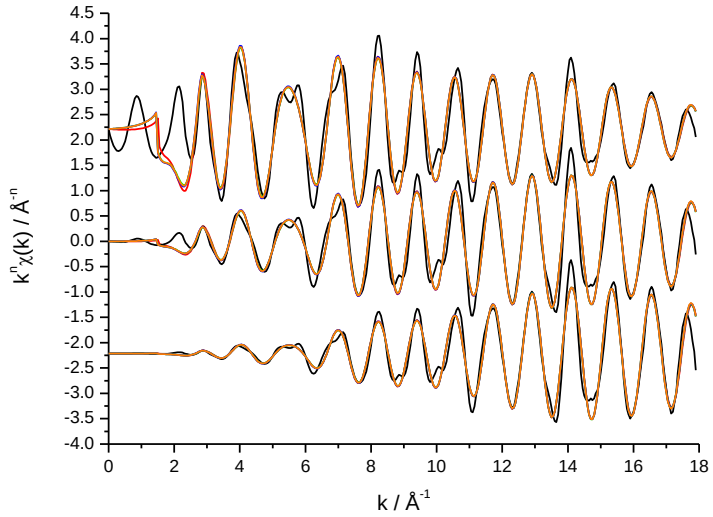

a)

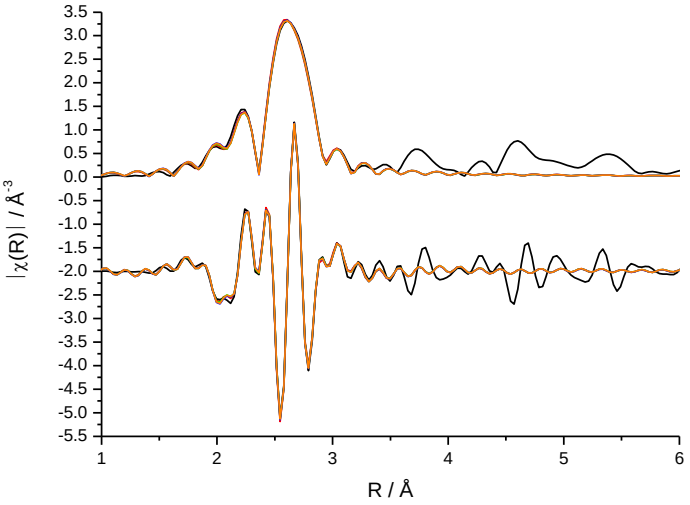

b)

Figure 13: a) k^n weighted (k^1 top, k^2 middle, k^3 bottom of panel, and b) k^2 weighted magnitude and real Fourier transform for 40 wt% Pt/C at 20 K. Experimental data (black) fit to differing histogram bin sizes generated by Sutton-Chen potential; data – black line; standard (single bin)– red line; 0.065 Å bin size – green line, 0.0065 Å bin size – blue line; 0.00065 Å bin size – orange line. The similarity of the lines for each different fit is such that they cannot be distinguished from one another.

There is no visible difference in either plot (*k* or *R*) of the fits using different bin widths (**Figure 13a-b**), as with using different potentials, but it is the quality of fit and evaluated parameters that indicate which model is best (**Table 5**). The change in

goodness of fit is marginal between using different bin sizes, as are the differences in all parameters bar the coordination number, which shows a small increase. Bearing in mind the cross-correlation with TEM, the simulations resulting in the larger coordination numbers appear more physically reasonable. Although the differences are within error values no firm conclusion can be drawn. Clearly there is a point at which increasing the resolution of the histogram makes no difference, as the fits using 0.0065 Å and 0.00065 Å histogram bin widths produce identical results. A truer test of the effect of the number of histogram bins will be when more nearest neighbour shells are added to the fit, and multiple scattering contributions included.

3.3.3 Application to Au/C

As with the Pt/C nanoparticles, the use of an MD input improved the fit, although unlike the Pt/C case, only the Gupta potential was used to fit the Au/C data as it has previously been shown to agree with experimental spectra to a great extent[32]. The results of the fits are in **Table 6** and **Figure 14** below. The lowest temperature measurement was only 85 K as the cold finger of the cryostat unit failed and could not reach 20 K.

Table 6: Structural parameters for 4 wt% Au/C nanoparticles at 85 K, 150 K and 300 K, acquired at the Au L_{III} edge.

	Fitting method	4 wt% Au/C				
		N	α*	σ^2 / Å^{-2} ($\times 10^4$)	ΔE_0 / eV	R_f
85 K	Standard	7.75 ± 0.81	-0.011 ± 0.002	62 ± 5	7.21 ± 0.87	0.017
	Gupta	8.24 ± 0.53	-0.008 ± 0.001	37 ± 3	5.27 ± 0.52	0.009
150 K	Standard	8.05 ± 0.92	-0.014 ± 0.002	79 ± 8	6.60 ± 0.92	0.025
	Gupta	8.24 ± 0.62	-0.009 ± 0.002	51 ± 5	5.01 ± 0.58	0.015
300 K*	Standard	8.60 ± 1.48	-0.021 ± 0.005	124 ± 18	4.43 ± 1.30	0.035
	Gupta	8.65 ± 0.99	-0.014 ± 0.003	89 ± 12	3.50 ± 0.91	0.025

*fitting range finished at k_{max} 14 Å^{-1}

Unlike with the standard model, the Au-S first shell scattering path was unable to be fitted due to a glitch in software; an upgraded version of ARTEMIS was used for the MD approach. At the time of writing this thesis it was in the development stage. Therefore all results were fitted in both the current release of ARTEMIS (ifeffit1.2.11d.exe) and the in development version to check for consistency given the possibility of software

glitches. The Au-S first shell path could be fitted using the standard method, but not during the MD method; beyond this one discrepancy, all other fitting parameters and results were consistent across both software platforms. The cumulant analysis was not performed on the Au/C data given the results observed for the Pt/C data.

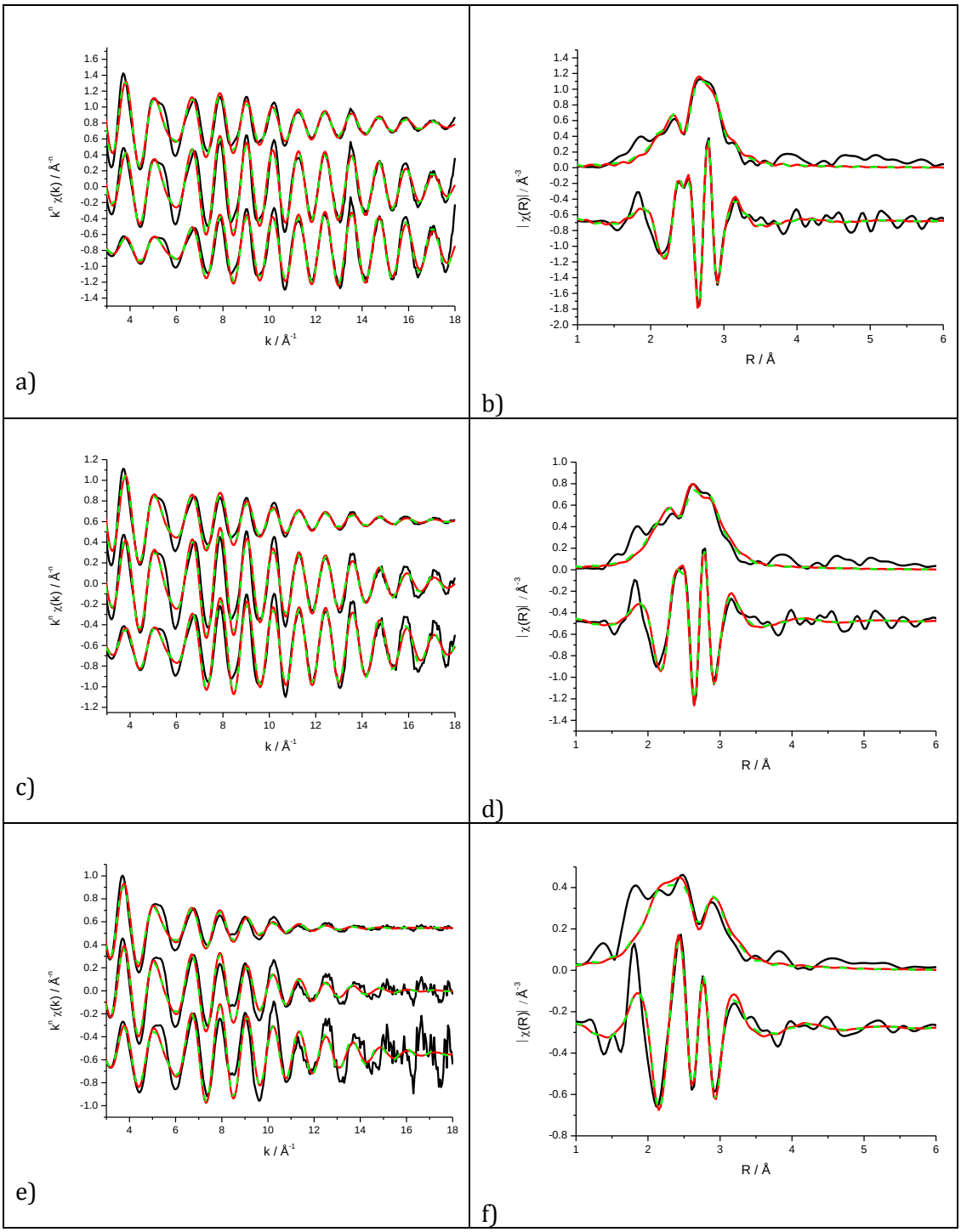

Figure 14: k^n weighted (k^1 top, k^2 middle, k^3 bottom of panel) experimental data (black) and fit to standard (red) and Gupta potential (green dashed), along with k^2 weighted magnitude and real Fourier transform for 4 wt% Au/C at a-b) 85 K, c-d) 150 K and e-f) 300 K. The low *R* misfit is due to the non-inclusion of the first shell Au-S scattering path.

In using the MD output as the basis for the EXAFS fit for the Pt/C series, the simulated cluster size that gave the best fit was slightly smaller than the TEM average particle diameter. For the Au/C the best fit MD output (767 atom simulation - corresponding to a 3.17 nm diameter nanoparticle) was larger than the TEM average particle size. The Au/C nanoparticles still had a dodecanethiol covered surface whilst the Pt/C nanoparticles were bare. Therefore the Au surface atoms were in a more relaxed and less contracted state, due to increased coordination, with more bulk-like properties, i.e. lower disorder and longer bond lengths. These two properties were most represented in the largest simulation, potentially explaining why the 767 atom simulation gave the best fit. Running an MD simulation of the gold nanoparticles with a thiol layer on the surface and seeing how that affected the MD output and subsequent fit to the data would be of great interest.

4 Conclusions

The focus of the work in this chapter has been to take on some of the more interesting challenges facing the analysis of EXAFS data for nanoparticles by combining molecular dynamic simulations with real experimental data. The contraction of the surface layer and anisotropic disorder of the surface atoms (brought about by their reduced coordination) were modelled using semi-empirical potentials, and the results successfully applied.

A full set of characterisation data is included in **Table 7** for cross-correlation purposes. The limitations of the higher cumulant approach to fitting nanoparticles have been exposed for systems with these high levels of structural disorder, as is exhibited in the lack of trend in average particle diameter. The unsuitability of *ex situ* XRD measurements for size determination has previously been discussed (Chapter Three), as has the correlation of TEM derived particle sizes with standard method EXAFS derived particle sizes.

Table 7: Full cross correlation of average particle size by technique.

Sample / wt% Pt/C	Average particle diameter / nm					
	XRD* D_{Vol}	TEM D_{Vol}	EXAFS			
			Standard 4 shell fit	Standard 1 shell fit	Cumulant	MD†
10	---	1.61 ± 0.45	1.32 ± 0.09	1.52 ± 0.14	1.79 ± 0.41	1.60 ± 0.10
20	1.46	2.43 ± 0.69	1.51 ± 0.15	1.87 ± 0.26	2.05 ± 0.37	2.01 ± 0.36
40	1.81	2.57 ± 0.73	2.10 ± 0.29	2.29 ± 0.33	1.90 ± 0.34	2.49 ± 0.30
60	2.25	2.95 ± 0.82	2.49 ± 0.43	2.66 ± 0.34	2.02 ± 0.43	2.94 ± 0.31

† output from Sutton-Chen potential

Sample / wt% Au/C	Average particle diameter / nm				
	XRD* D_{Vol}	TEM D_{Vol}	EXAFS		
			Standard 4 shell fit	Standard 1 shell fit	MD‡
4	2.41	2.38 ± 1.22	1.48 ± 0.52	1.96 ± 0.37	2.15 ± 0.23

*XRD reflects average crystallite size. ‡output from Gupta potential

The use of MD to include anharmonic structural disorder in the EXAFS fit results in a larger average particle size that is in better agreement with TEM data than the standard approach. The new approach detailed in this chapter has shown promise, although clearly is still in the initial stages of development. Extending the analysis to higher coordination shells would provide much more structural information. However the logistical challenges of incorporating the enormous amount of information contained in the full history file from an MD simulation have yet to be overcome.

The assumption of a "spherical" geometry is one limitation of the MD approach in its current form, as it can impose limitations on the relationship between coordination numbers in neighbouring coordination shells. This would likely become more apparent when extending the fit beyond the first nearest neighbour, and leads on to the next stage that could be attempted: modelling nanoparticles of other possible geometries such as icosahedral, cuboctahedral, or hemispherical and using the output from these MD simulations for the EXAFS fit. Different geometries of nanoparticles

have been simulated in many earlier studies[33-35], and the structural properties investigated. Similarly the different ratios between coordination shells have been investigated and the likely consequences this would have on the EXAFS[21,36], however these studies have still assumed an even distribution of bond lengths throughout the nanoparticle.

Determination of particle morphology from EXAFS would be indicated by an improved goodness of fit to the MD output from a particular geometry, e.g. icosahedral. Whilst there are means of estimating particle morphology from EXAFS already from the population of the nearest neighbour coordination shells[37,38], the errors reported for higher coordination shells are such that this method would not stand up by itself.

Further work that can be done could include the investigation of other classical semi-empirical potentials (using the geometries previously run), and more long term, the use of outputs from density functional theory (DFT) calculations as recent advances such as linear scaling[39] now allow for larger clusters to be simulated in achievable time frames.

5 References

(1) Shido, T.; Prins, R. *Journal of Physical Chemistry B* **1998**, *102*, 8426.

(2) Clausen, B. S.; Grabaek, L.; Topsoe, H.; Hansen, L. B.; Stoltze, P.; Norskov, J. K.; Nielsen, O. H. *Journal of Catalysis* **1993**, *141*, 368.

(3) Clausen, B. S.; Topsøe, H.; Hansen, L. B.; Stoltze, P.; Nørskov, J. K. *Catalysis Today* **1994**, *21*, 49.

(4) Curis, E.; Benazeth, S. *Journal of Synchrotron Radiation* **2005**, *12*, 361.

(5) Calvin, S.; Luo, S. X.; Caragianis-Broadbridge, C.; McGuinness, J. K.; Anderson, E.; Lehman, A.; Wee, K. H.; Morrison, S. A.; Kurihara, L. K. *Applied Physics Letters* **2005**, *87*.

(6) Sun, Y.; Frenkel, A. I.; Isseroff, R.; Shonbrun, C.; Forman, M.; Shin, K.; Koga, T.; White, H.; Zhang, L.; Zhu, Y.; Rafailovich, M. H.; Sokolov, J. C. *Langmuir* **2006**, *22*, 807.

(7) Bus, E.; Miller, J. T.; Kropf, A. J.; Prins, R.; van Bokhoven, J. A. *Physical Chemistry Chemical Physics* **2006**, *8*, 3248.

(8) Fornasini, P.; Monti, F.; Sanson, A. *Journal of Synchrotron Radiation* **2001**, *8*, 1214.

(9) Bauer, M.; Bertagnolli, H. *Journal of Physical Chemistry B* **2007**, *111*, 13756.

(10) Dalba, G.; Fornasini, P. *Journal of Synchrotron Radiation* **1997**, *4*, 243.

(11) Daly, K. A.; Penner-Hahn, J. E. *Journal of Synchrotron Radiation* **1998**, *5*, 1383.

(12) Martin, M. R.; Somorjai, G. A. *Physical Review B* **1973**, *7*, 3607.

(13) Huang, W. J.; Sun, R.; Tao, J.; Menard, L. D.; Nuzzo, R. G.; Zuo, J. M. *Nature Materials* **2008**, *7*, 308.

(14) Smoluchowski, R. *Physical Review* **1941**, *60*, 661.

(15) Pauling, L. *Journal of the American Chemical Society* **1947**, *69*, 542.

(16) Vaarkamp, M. *Catalysis Today* **1998**, *39*, 271.

(17) Clausen, B. S.; Topsoe, H.; Hansen, L. B.; Stoltze, P.; Norskov, J. K. *Japanese Journal of Applied Physics Part 1-Regular Papers Short Notes & Review Papers* **1993**, *32*, 95.

(18) Bunker, G. *Nuclear Instruments & Methods* **1983**, *207*, 437.

(19) Marques, E. C.; Sandstrom, D. R.; Lytle, F. W.; Greegor, R. B. *The Journal of Chemical Physics* **1982**, *77*, 1027.

(20) Greegor, R. B.; Lytle, F. W. *Journal of Catalysis* **1980**, *63*, 476.

(21) Frenkel, A. I. *Zeitschrift Fur Kristallographie* **2007**, *222*, 605.

(22) Montejano-Carrizales, J. M.; Aguilera-Granja, F.; Moran-Lopez, J. L. *NanoStructured Materials* **1997**, *8*, 269.

(23) Beale, A. M.; Weckhuysen, B. M. *Physical Chemistry Chemical Physics* **2010**, *12*, 5562.

(24) Okamoto, Y. *Nuclear Instruments and Methods in Physics Research Section A: Accelerators, Spectrometers, Detectors and Associated Equipment* **2004**, *526*, 572.

(25) Gilbert, B.; Zhang, H. Z.; Huang, F.; Banfield, J. F.; Ren, Y.; Haskel, D.; Lang, J. C.; Srajer, G.; Jurgensen, A.; Waychunas, G. A. *Journal of Chemical Physics* **2004**, *120*, 11785.

(26) Eisenberger, P.; Brown, G. S. *Solid State Communications* **1979**, *29*, 481.

(27) Yevick, A.; Frenkel, A. I. *Physical Review B* **2010**, *81*, 115451.

(28) Ravel, B.; Cockayne, E.; Newville, M.; Rabe, K. M. *Physical Review B* **1999**, *60*, 14632.

(29) Ravel, B.; Kim, Y. I.; Woodward, P. M.; Fang, C. M. *Physical Review B* **2006**, *73*.

(30) Stern, E. A.; Ma, Y.; Hanske-Petitpierre, O.; Bouldin, C. E. *Physical Review B* **1992**, *46*, 687.

(31) Ravel, B.; Newville, M. *Journal of Synchrotron Radiation* **2005**, *12*, 537.

(32) Roscioni, O. M.; Zonias, N.; Price, S. W. T.; Russell, A. E.; Comaschi, T.; Skylaris, C. K. *Physical Review B* **2011**, *In Press*.

(33) D'Agostino, G.; Pinto, A.; Mobilio, S. *Physical Review B* **1993**, *48*, 14447.

(34) Mottet, C.; Goniakowski, J.; Baletto, F.; Ferrando, R.; Treglia, G. *Phase Transitions* **2004**, *77*, 101.

(35) Curley, B. C.; Johnston, R. L.; Young, N. P.; Li, Z. Y.; Di Vece, M.; Palmer, R. E.; Bleloch, A. L. *J. Phys. Chem. C* **2007**, *111*, 17846.

(36) Benfield, R. E. *Journal of the Chemical Society-Faraday Transactions* **1992**, *88*, 1107.

(37) Menacherry, P. V.; FernandezGarcia, M.; Haller, G. L. *Journal of Catalysis* **1997**, *166*, 75.

(38) Jentys, A. *Physical Chemistry Chemical Physics* **1999**, *1*, 4059.

(39) Skylaris, C. K.; et al. . *Journal of Physics: Condensed Matter* **2008**, *20*, 064209.

CHAPTER FIVE: APPLICATION OF MOLECULAR DYNAMICS TO EXAFS OF BIMETALLIC SYSTEMS

Chapter Three looked at the cross-correlation of characterisation techniques for monometallic catalysts, and Chapter Four at the application of molecular dynamics to EXAFS and the effect this has on cross-correlation. This chapter looks at both the cross-correlation of techniques for characterisation and the application of molecular dynamics to the EXAFS analysis of bimetallic catalysts.

1 Introduction

Bimetallic catalysts are of interest for reasons including reduced cost, increased catalytic activity[1] and tolerance to poisoning[2]. Core-shell nanoparticles have been demonstrated to be one way to reduce the amount of precious metal used and therefore reduce the cost. For example if the same or improved catalytic activity can be achieved by the use of a Pt shell around a Pd core, then the raw materials cost of the catalyst will be less therefore making it economically more viable.

Crabb *et al.*[3-5] have developed a synthetic method for the controlled deposition of one metal on to a core composed of second metal. The thickness of the deposition can be controlled giving a range of core-shell nanoparticles. The technique was applied for the synthesis of the Pt shell Pd core nanoparticles analysed in this chapter[6].

Characterisation of core- shell nanoparticles is more complex than for monometallic systems. The thinness of the shell is such that it can be amorphous (and XRD invisible), or take on the lattice parameters of the core beneath it and therefore be indistinguishable by XRD, making the technique unsuitable for complete characterisation. The largest indication of a second metal by XRD alone is a subtle shifting[5] or broadening[6] of the diffraction peaks from the core that are attributed to an alloying effect at the core-shell interface. TEM benefits from being able to directly image particles including the amorphous shell structure[7] and, coupled with EDX, is able to confirm the presence of both metals together on the support[3,6].

EXAFS characterisation studies of bimetallic systems[6-8] have focussed primarily on the local coordination environment of the elements present to determine the degree of

segregation or mixing. For example in the work of Hansen *et al*.[9] on Pt core Pd shell nanoparticles, the coordination number of the Pt-Pt bonds has been observed to exceed that of the Pd-Pd bonds, attributed to the segregation of the Pd shell from the Pt core, consistent with computer simulations of the system.

As with monometallic systems, current EXAFS analysis relies on the assumption of Gaussian disorder and bond length distribution. The reality is far more complex for bimetallic systems. The degree of segregation or mixing of the elements present results in four possible atom-atom pairs on the surface. These atom-atom pairs, as well as those beneath the surface, experience the termination effects present in nanoparticles (as a result of the particle size) resulting in a much more complex set of radial distribution functions that is dependent on the particle size, shape and degree of segregation or mixing of the components.

Beale and Weckhuysen have investigated the effect of both shape and mixing on the theoretical coordination numbers of a range of bimetallic nanoparticles[10]. The ratios of coordination numbers simulated provide a means of estimating the degree of mixing, however, like many theoretical EXAFS studies[11-13], these did not take termination effects into account.

As has been discussed in the previous chapter, an incorrect treatment of termination effects results in a decreased coordination number being determined from the EXAFS analysis. The use of higher cumulants cannot be applied, even to systems with a very small degree of surface termination due to the mixed occupancy of coordination shells[14,15]. Therefore the work in this chapter seeks to extend the application of molecular dynamics (described in Chapter Four) to the EXAFS analysis of bimetallic samples and to cross-correlate the results with standard EXAFS analysis, TEM and XRD data.

2 Experimental

A series of well-defined core-shell Pt/Pd/C catalysts (shell/core/support) were supplied by Anna Wise and Johnson Matthey, as suitable candidates for applying the MD approach to analysing the EXAFS of bimetallic systems. The details of all catalysts used in this work are in **Table 1**.

Table 1: Nominal loadings and nomenclature of monometallic nanoparticle catalyst samples investigated.

Sample	Nominal loading / wt%	Sample reference	Temperature measurements / K
Pd/C	20	Core	20, 150, 300
1 monolayer Pt/Pd/C	17.1 (Pt) 16.3 (Pd)	1ML	20, 150, 300
2 monolayer Pt/Pd/C	27.5 (Pt) 14.2 (Pd)	2ML	20, 150, 300

2.1 TEM and XRD

All samples for TEM and XRD were submitted to the Johnson Matthey Technology Centre for analysis. High resolution aberration corrected TEM images (AC-STEM) were recorded by Haibo E at Oxford University

2.2 EXAFS

The absorption edges of interest were the Pd K (24350 eV) and Pt L_{III} (11564 eV) edges. Investigations were carried out on beamline X23A2 for both Pd and Pt measurements. All EXAFS measurements in this chapter were collected in transmission mode using the cryostat cell. The samples were all prepared as boron nitride pellets, and all samples were reduced with H_2 at room temperature.

Data was fitted simultaneously for each edge measurement at a given temperature, e.g. both the Pt and Pd edges at 20 K, over a range in *R* between 2 and 3 Å, and between 3 and 16 $Å^{-1}$ in *k* space. The parameters describing bond length correction and disorder between dissimilar absorber-scatterer pairs (i.e. Pd-Pt and Pt-Pd) were constrained between both data sets to minimise the number of variables in the fit.

2.3 MD

A series of Pd nanoparticle and Pd/Pt bimetallic nanoparticle structures were generated using ATOMS[16] and molecular dynamic simulations carried out using the

Sutton-Chen potential[17] (example structures in **Figure 1**), with the parameters detailed in Chapter Two, **section 6.2**. Full details of all simulations run are in **Table 2**.

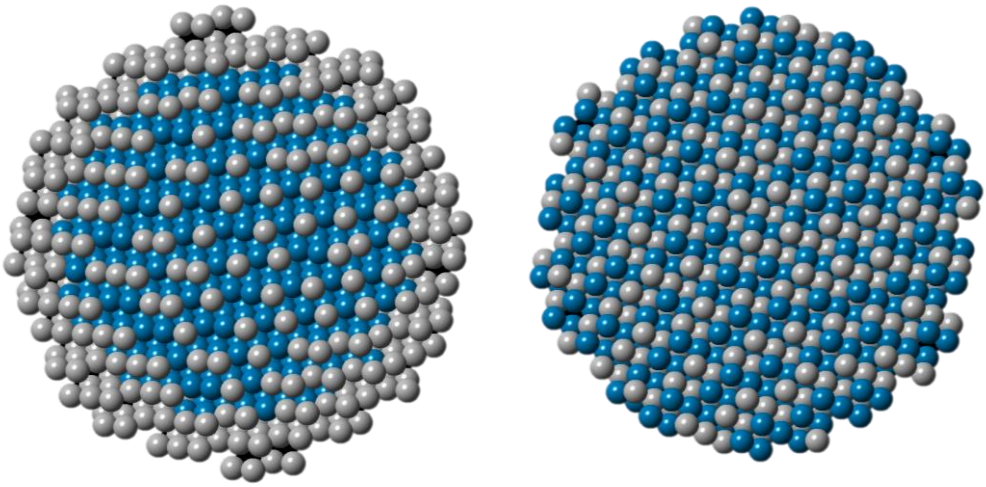

a) **b)**

Figure 1: Starting configurations of a) Pd core-Pt shell and b) Pd:Pt alloy nanoparticles; grey spheres (Pt) and blue spheres (Pd).

Table 2: Details of the cluster compositions used for molecular dynamics simulations.

Simulation	Cluster composition
Core	Pd 177
Core	Pd 381
Core-Shell	Pd177 core Pt 204 Shell
Core-Shell	Pd381 core Pt 386 shell
Alloy	Pd192 Pt189
Alloy	Pd392 Pt375

The alloy compositions are as close to 1:1 as could be achieved whilst keeping a fully mixed structure. The core-shell and alloy structures are larger than the Pd core structures by one complete outer shell of atoms based on the assumption of a complete monolayer coverage of Pt over the Pd core.

Data for the Pd core was fitted to the monometallic simulation outputs, and data for the 1ML and 2ML samples was fitted to the bimetallic simulation outputs.

3 Characterisation

3.1 TEM

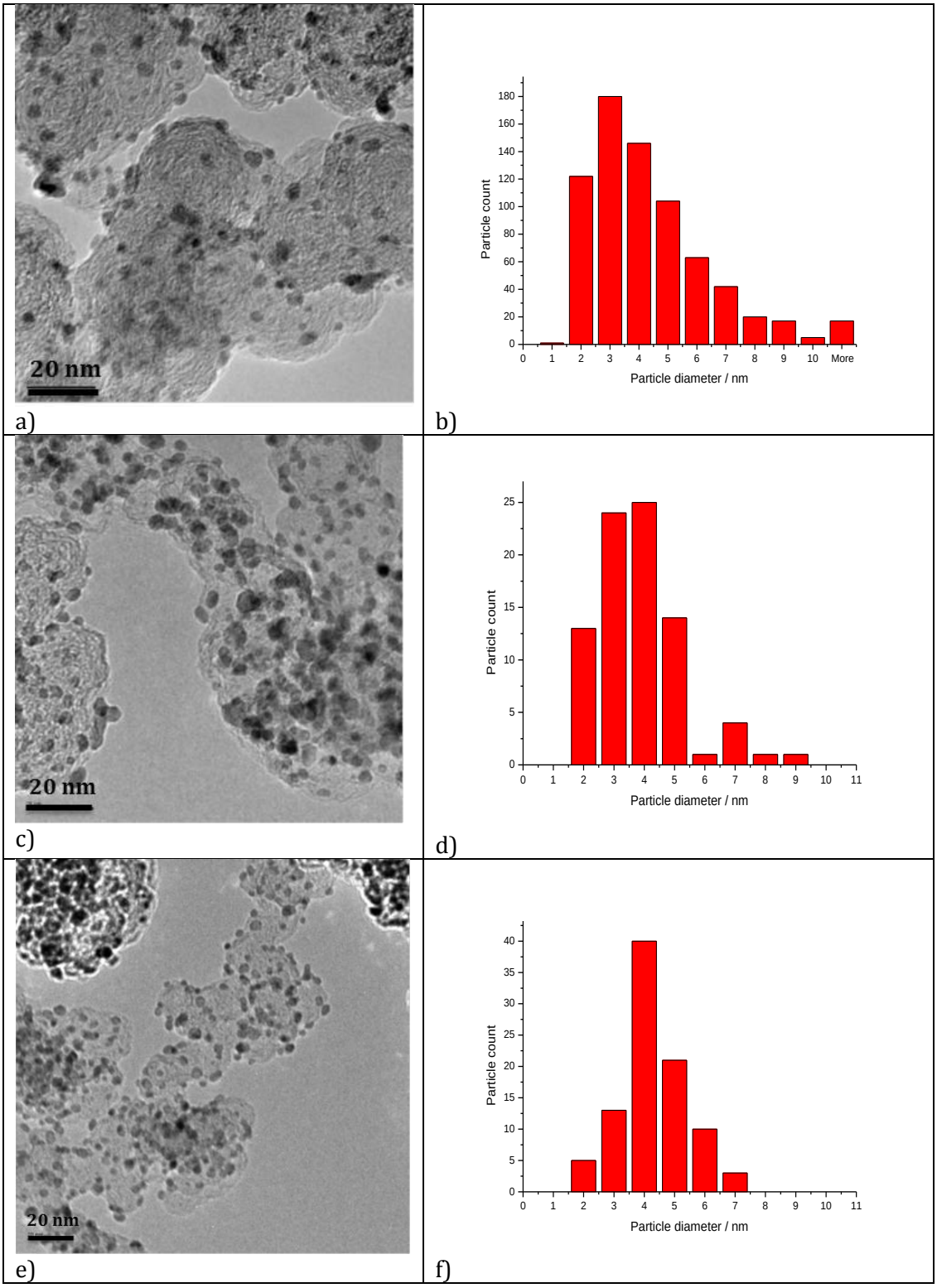

Figure 2: TEM micrographs (left) and corresponding particle size distributions (right) of a-b) Pd core, c-d) 1ML Pt/Pd/C, and e-f) 2ML Pt/Pd/C.

Several very large particles were observed for the core resulting in a skewing of the average size towards larger particles. The largest particles observed during the particle size analysis may have been caused by overlap of adjacent smaller particles. A far greater number of particles were observed for the core than for the core-shell particles, and this will have an influence on the variation (σ) of the data. It is also quite likely that during the size analysis, selective areas of the sample were observed to obtain the best images of the core-shell structure, and therefore were not representative of the sample as a whole. However TEM of the core generally shows the sample is well dispersed over the support, as is the case for the 1ML and 2ML samples (**Figure 2 a**, **c** and **e**). The size distribution is not as uniform as with previous monometallic samples studied in this work, and the different size weightings cover a larger range (**Figure 2 b**, **d** and **f, Table 3**).

Table 3: Comparison of particle size determinations from varying TEM weighting approaches.

Sample	Number of observed particles	Average TEM particle size / nm				Standard deviation / nm
		D_0	D_n	D_a	D_{Vol}	
Core	733	3.46	3.96	6.82	8.95	2.12
1ML	83	3.20	3.51	4.88	5.79	1.57
2ML	95	3.72	3.87	4.59	4.99	1.35

The presence of oxygen in the EDX profile analysis shows that the Pd core is slightly oxidised, most likely on the surface of the nanoparticles (**Figure 3**). EDX line profile analysis of the 1ML and 2ML samples confirms the presence of both Pt and Pd. The counts for Pt coincide with the counts for Pd confirming that there is a correlation between the locations of the two components.

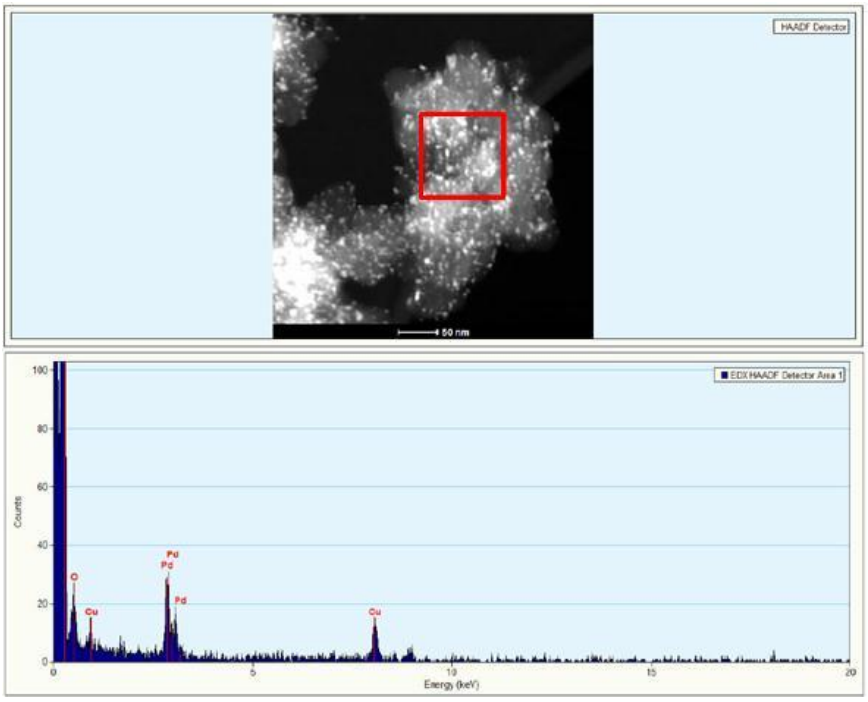

Figure 3: TEM EDX line profile for 20 wt% Pd/C core. The upper box shows the TEM micrograph of the area under investigation. The EDX response for the red box is shown below the TEM micrograph.

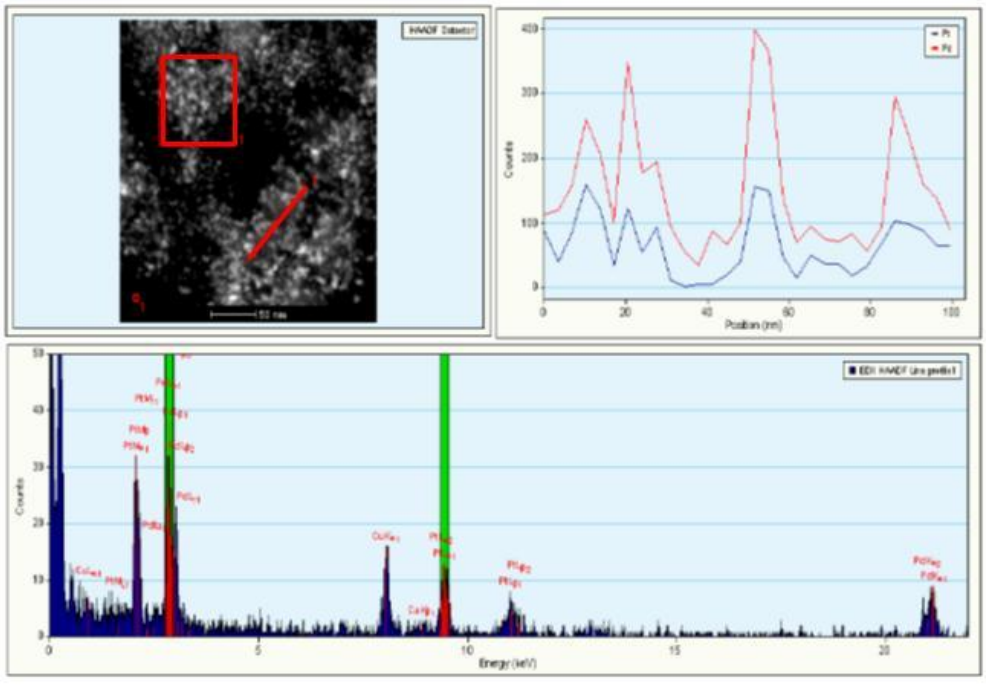

Figure 4: TEM EDX line profile for 1 ML Pt on 20 wt% Pd/C core. The upper left box shows the TEM micrograph of the area under investigation. The EDX response for the red box is shown below the TEM micrograph. The EDX response across the red line labelled "1" in the TEM micrograph is in the upper right box. The counts for both Pt (blue) and Pd (red) are shown.

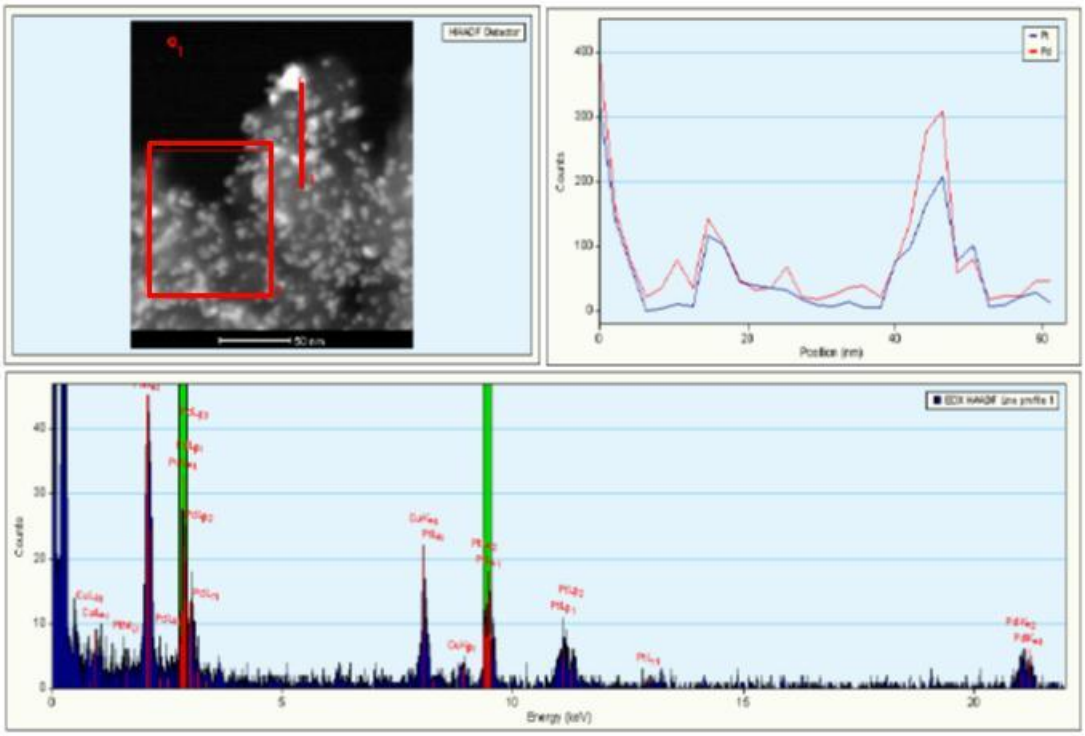

Figure 5: TEM EDX line profile for 2 ML Pt on 20 wt% Pd/C core. The upper left box shows the TEM micrograph of the area under investigation. The EDX response for the red box is shown below the TEM micrograph. The EDX response across the red line labelled "1" in the TEM micrograph is in the upper right box. The counts for both Pt (blue) and Pd (red) are shown.

AC-STEM micrographs (**Figure 6**) of the 2ML sample show a clear core-shell structure. The brighter atoms around the outsides of the particles are the heavier Pt shell (higher atomic mass elements have stronger back-scattering in HAADF mode). The Pt shell is crystalline in the AC-STEM micrographs with lattice fringes clearly defined to the edge of the particles. The Pt contribution appears strongest around the edges of the particles because of perspective. The Pt atoms atop the Pd core as the HAADF detector sees them are at most 2 atoms deep (assuming complete coverage), while those at the edges could be up to 8 atoms deep (assuming a spherical geometry) and thus give a much brighter signal. A similar effect can be seen in the inputs for the MD simulations; **Figure 1a** is a core-shell structure yet as a result of perspective the majority of the Pt shell appears on the edges of the particle.

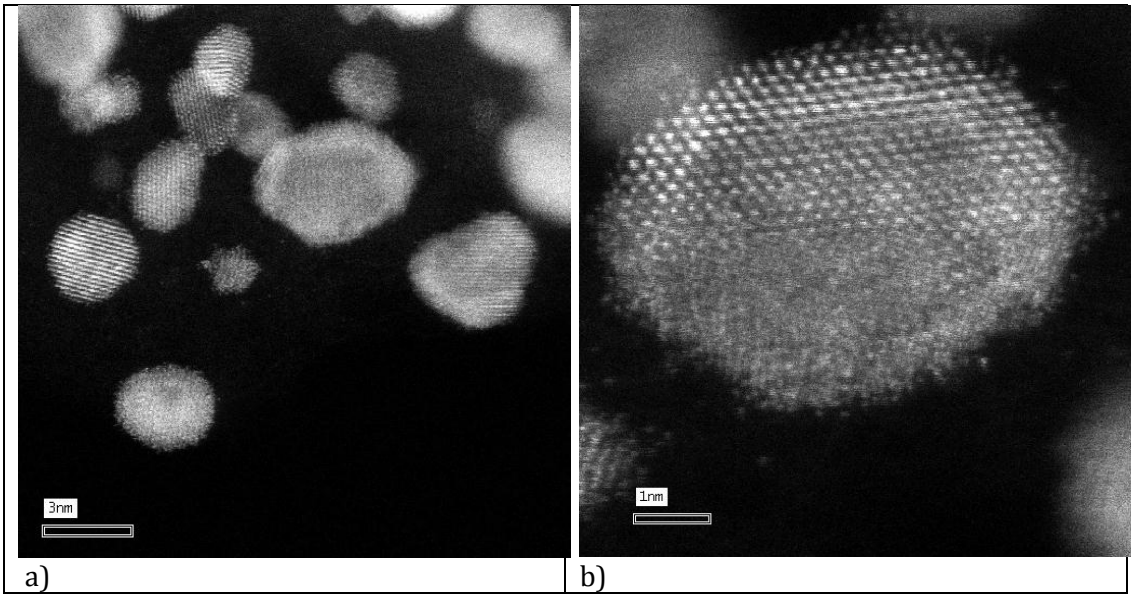

Figure 6: AC-STEM micrographs of 2ML Pt/Pd/C. Scale bar is a) 3 nm and b) 1nm.

3.2 XRD

The broad diffraction peak at $2\theta \sim 25°$ due to the Ketjen carbon support is observed in all patterns. The core is the most poorly crystalline (**Figure 7**), with a small amount of cubic Pd and no other phases present. The small amount of surface oxide detected in the EDX is either amorphous or so thin as not to exhibit diffraction peaks.

The 1ML sample also is poorly crystalline (**Figure 8**), although less so than the core. No crystalline Pt or any other phases were present. The 2ML sample again contains a large amount of poorly crystalline Pd with no other phases present (**Figure 9**).

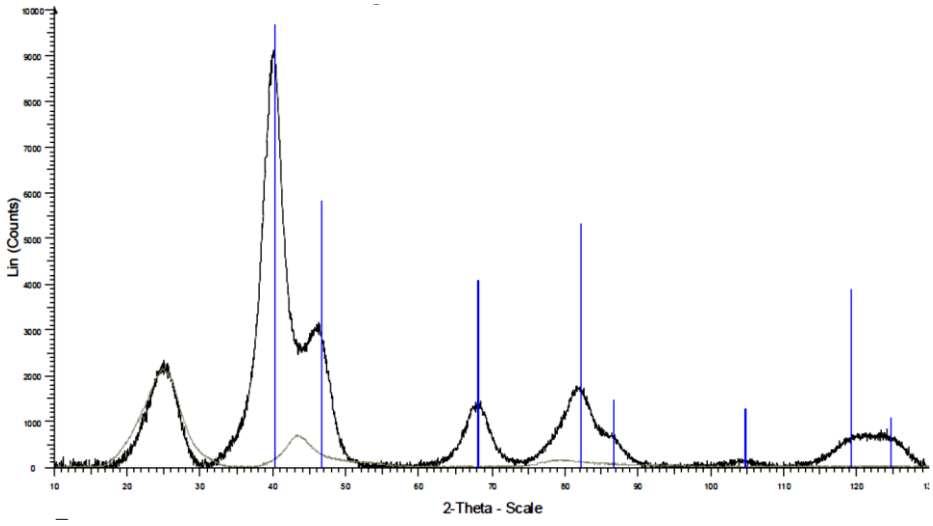

Figure 7: XRD pattern of 20 wt% Pd/C core. Data is the black line, | refers to cubic Pd (PDF No. 00-04-1043, a = 3.89 Å).

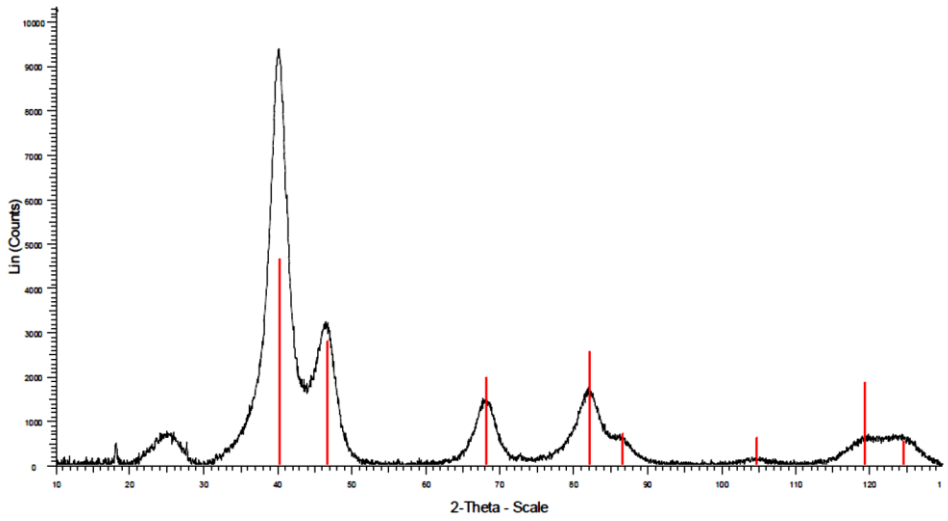

Figure 8: XRD pattern of 1ML Pt/Pd/C. Data is the black line, | refers to cubic Pd (PDF No. 00-04-1043, a = 3.89 Å).

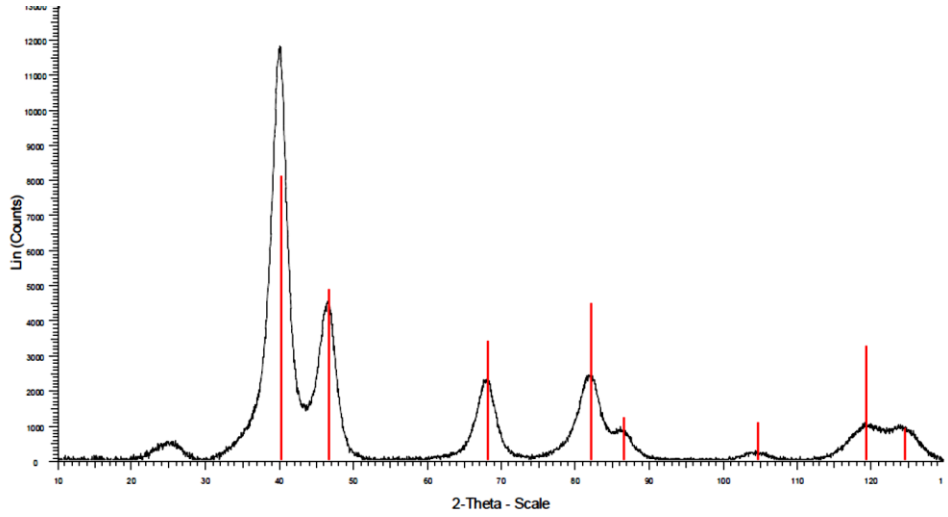

Figure 9: XRD pattern of 2ML Pt/Pd/C. Data is the black line, | refers to cubic Pd (PDF No. 00-04-1043, a = 3.89 Å).

There is a subtle increase observed in the lattice parameter between the 1ML and 2ML samples. Taken by itself this could suggest a possible alloying between the Pd and Pt (Pt lattice parameter 3.92 Å); however the lattice parameter for the core is also larger than expected. Due to the very poor crystallinity of the sample, this is most likely a result of experimental error and highlights the difficulties faced when using XRD for such small samples. Given the crystallinity apparent in the AC-STEM micrographs, it is proposed that the deposited Pt shell adopts the lattice parameters of the Pd core

beneath it; helping to explain the increase in crystallinity observed between the core, 1ML and 2ML samples. A second possible explanation lies with the technique used to synthesise the core-shell structure. The procedure[3-5] involves heating the core to 473 K before the introduction of the shell precursor; during the initial heating phases, some aggregation could occur resulting in the slightly larger and more crystalline particles observed.

As has been the case for all the monometallic samples in Chapter Three, and as a result of the poor crystallinity of the samples the average crystallite sizes (**Table 4**) are, at best, estimates only.

Table 4: Rietveld derived XRD crystallite sizes and estimated lattice parameters.

Sample	Crystallite size / nm		Lattice parameter / Å
	L_{Vol} average crystallite size	D_{Vol} – mean volume weighted diameter	
Core	1.60 ± 0.06	2.13 ± 0.08	3.899 ± 0.001
1ML	2.30 ± 0.05	3.12 ± 0.07	3.890 ± 0.001
2ML	2.54 ± 0.05	3.39 ± 0.07	3.897 ± 0.001

3.4 MD EXAFS

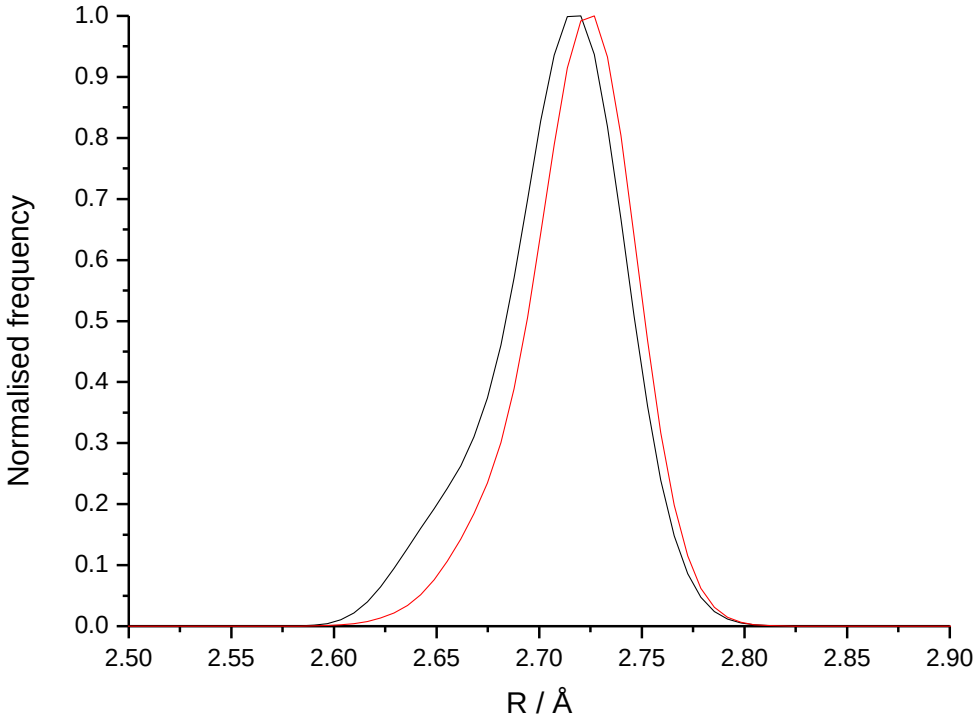

Figure 10: First shell RDFs at 20 K for 177 atom (black) and 381 atom (red) "spherical" Pd nanoparticles

The first shell RDFs for the 177 and 381 atom clusters corresponding to the core are shown in **Figure 10**. There is a contraction in the majority of bond lengths from the bulk Pd value of 2.75 Å (**Figure 10**), but the RDFs are much more Gaussian in their distribution in contrast to the RDFs taken from the Pt simulations (Chapter Four**, Figure 5**). The distribution still exhibits a low-*R* tail, with the 177 atom RDF having a small low-*R* shoulder, but nothing like the asymmetry observed in the Pt simulations.

The data for the core-shell nanoparticles was not analysed using the cumulant expansion approach for reasons detailed in Chapter Four, only being analysed using the standard and MD methods. The results for the Pd core are shown in **Figure 11** and the fit parameters summarised in **Table 5,** below.

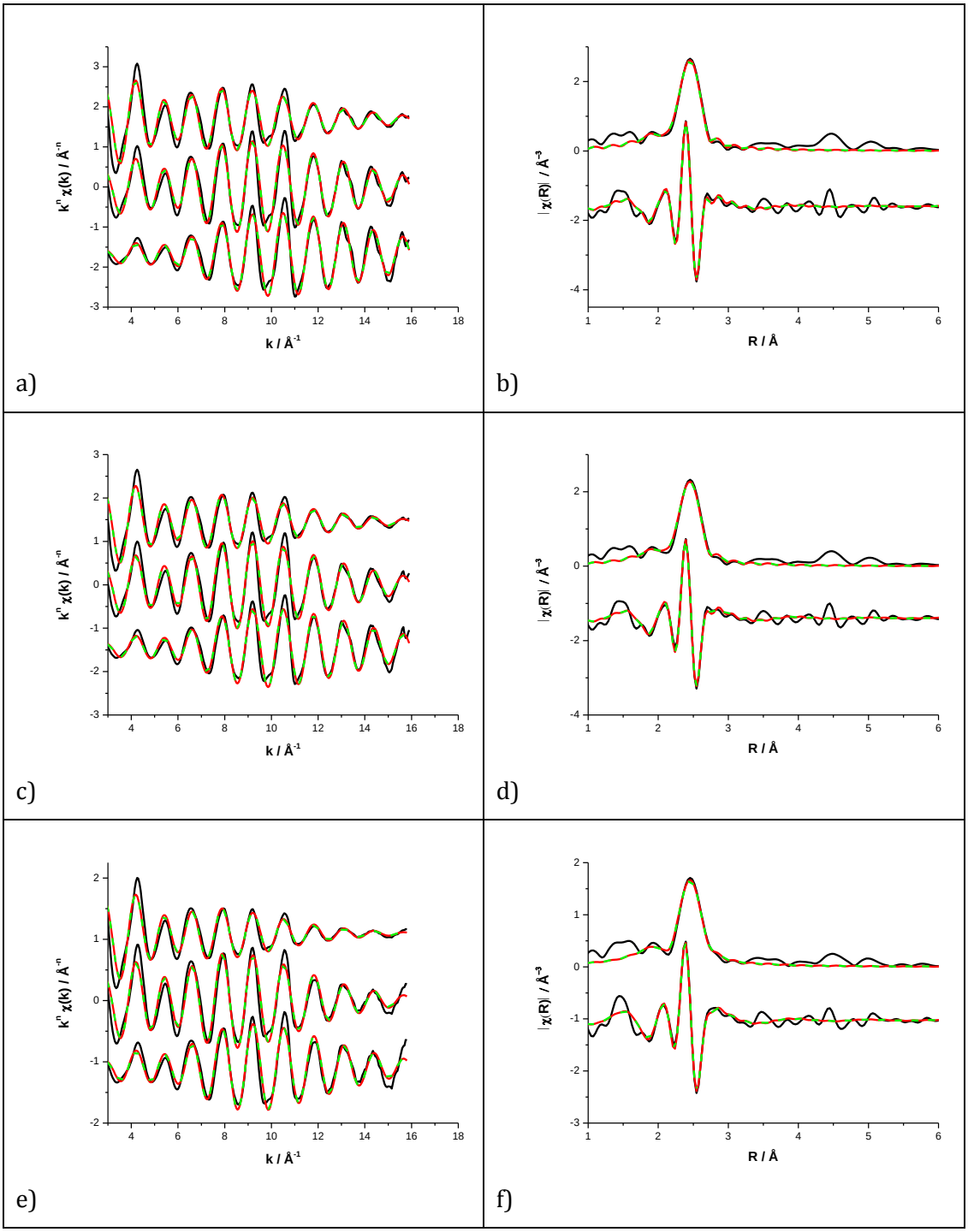

Figure 11: k^n weighted (k^1 top, k^2 middle, k^3 bottom of panel) experimental data (black) and fit to standard (red) and Sutton-Chen (green dash) potentials, along with k^2 weighted magnitude and real Fourier transform for 20 wt% Pd/C at a-b) 20 K, c-d) 150 K and e-f) 300 K. The similarity of the lines for the standard and Sutton-Chen fits is such that they cannot be distinguished from one another.

Table 5: Structural parameters for 20 wt% Pd/C nanoparticles at 20 K, 150 K and 300 K, acquired in a reducing H_2 environment at the Pd K edge.

Condition	20 wt% Pd/C					
	Method	N	α	σ^2 / Å^2	ΔE_0 / eV	R_f
20 K	Standard	6.87 ± 0.60	-0.031 ± 0.001	0.0048 ± 0.0005	-6.74 ± 0.69	0.006
	Sutton-Chen	6.87 ± 0.58	0.012 ± 0.001	0.0037 ± 0.0004	-6.72 ± 0.68	0.005
150 K	Standard	6.80 ± 0.65	-0.004 ± 0.001	0.0055 ± 0.0005	-6.87 ± 0.75	0.008
	Sutton-Chen	6.80 ± 0.64	0.011 ± 0.002	0.0044 ± 0.0005	-6.84 ± 0.74	0.007
300 K	Standard	6.79 ± 0.55	-0.005 ± 0.001	0.0072 ± 0.0006	-6.89 ± 0.61	0.007
	Sutton-Chen	6.80 ± 0.55	0.010 ± 0.002	0.0062 ± 0.0005	-6.84 ± 0.60	0.006

In all cases the 177 atom Pd simulation provided a better fit than the 381 atom simulation, although the difference was minor, giving only a slight improvement in the quality of the MD fit over standard fit. Visibly there is little difference in the plotted fits (i.e. the standard fit (red line) is plotted beneath the MD fit (green dashed line) in **Figure 11** and as such is not clearly visible).

Beyond the minor improvement in quality of fit, there is a slight reduction in the errors associated with each parameter. There is no real change in parameters as there was with the Pt or Au data in Chapter Four. Given that the profile of the MD results is more Gaussian, this is not surprising, as the input is akin to a standard input with a disorder term already applied (the 177 atom simulation has a 0.0009 Å^2 variance in bond length, very similar to the difference in σ^2 between the standard and MD fits). The Pd nanoparticle MD fits to the core (**Table 5**) exhibit a slight negative thermal expansion[18] effect similar to that observed in the Au nanoparticles in Chapter Three**,** although as the value is within the error bars, it may not be realistic.

The core-shell data was fitted initially to the output from core-shell MD simulations (**Figure 12c** and **d**); however the very large distortion in the Pt-Pt bonds present proved problematic and no physically reasonable fitting solution could be reached.

The assumption of a completely "spherical" particle with an evenly distributed complete outer shell of Pt was too restrictive a structural model, and therefore any imperfections in the sample resulted in too large a misfit.

Two of the most important factors used to start an EXAFS fit with are the position and identity of the nearest scattering neighbour. With this in mind, two alloyed well mixed Pt:Pd nanoparticles were simulated; the output RDF of the simulation should contain contributions from all possible atom pairs at all positions from the core through to the surface of the nanoparticle, and therefore provide a more flexible fitting model (**Figure 12a** and **b**). These RDFs have far less contraction of bond lengths, in particular the Pt-Pt bonds, than the core-shell models, yet are still non-Gaussian due to low-*R* contributions.

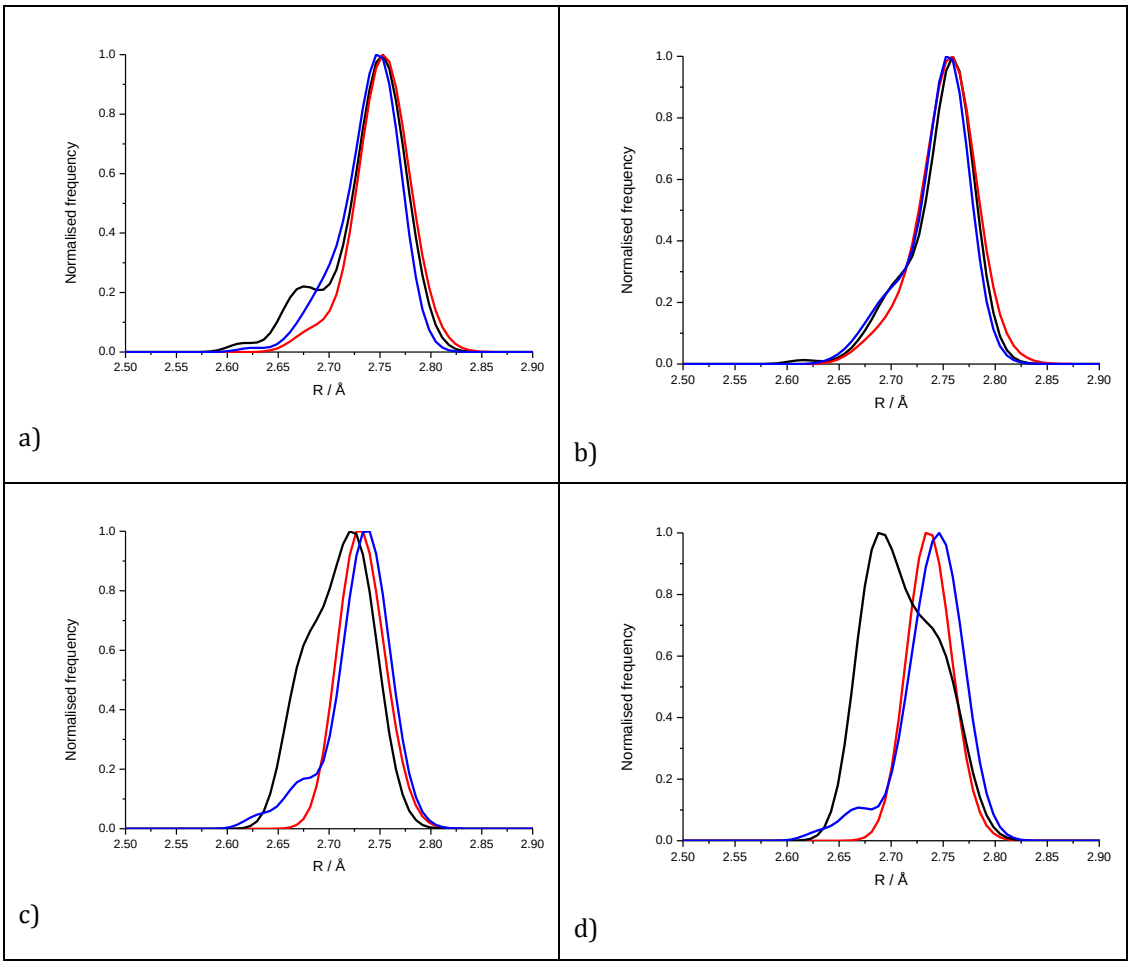

Figure 12: Mixed Pd:Pt alloy RDFs for a) Pt189Pd192, b) Pt375Pd392, and Pd core Pt shell c) Pd177Pt204, and d) Pd381Pt386. Pt-Pt interactions are in black, Pd-Pd interactions in red and Pd-Pt/Pt-Pd interactions in blue.

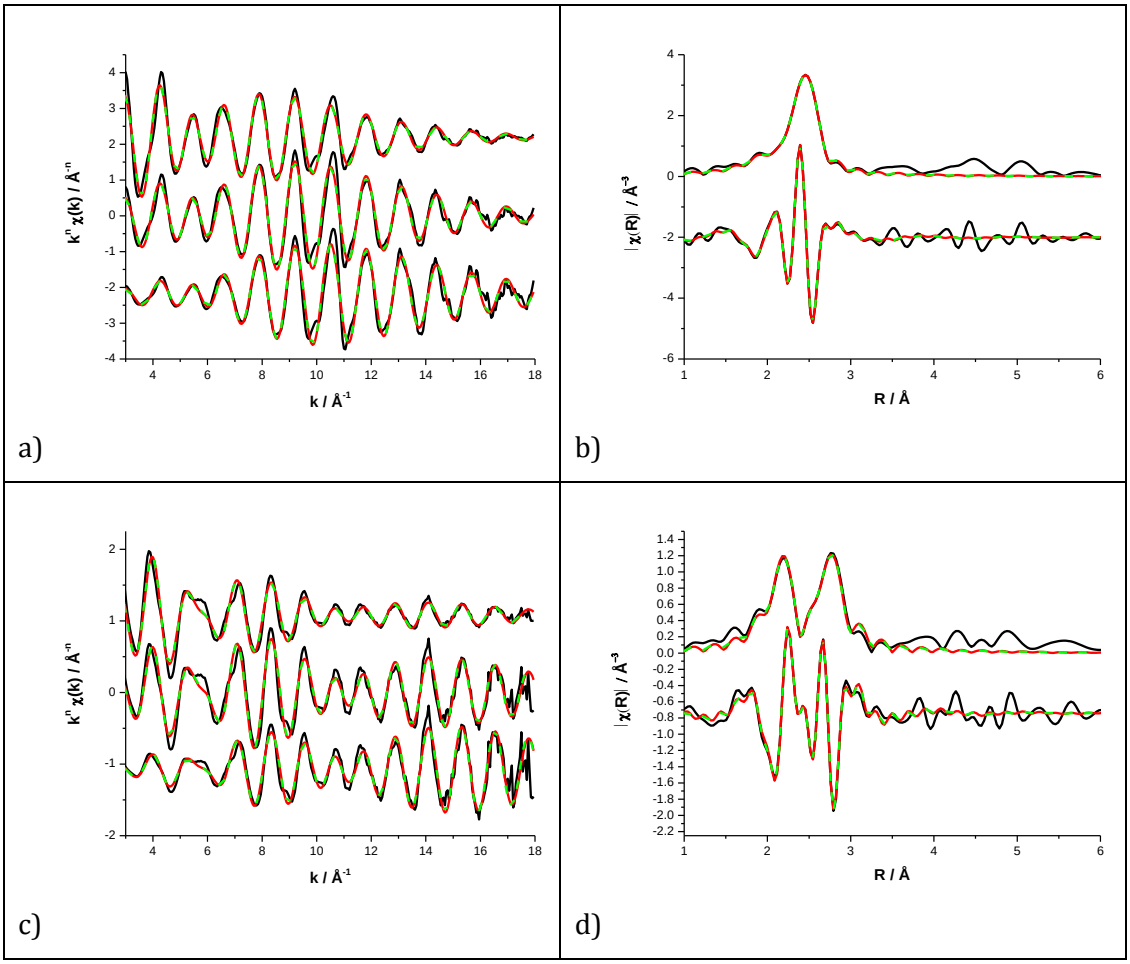

Figure 13: k^n weighted (k^1 top, k^2 middle, k^3 bottom of panel) experimental data (black) and fit to standard (red) and Sutton-Chen (green dashed) potentials, along with k^2 weighted magnitude and real Fourier transform for 1ML Pt/Pd/C at 20 K at a-b) Pd K edge and c-d) Pt L_{III} edge. The similarity of the lines for the standard and Sutton-Chen fits is such that they cannot be distinguished from one another.

Table 6: Structural parameters for 1ML Pt/Pd/C nanoparticles at 20 K, acquired in a reducing H_2 environment at the Pd K edge and Pt L_{III} edge. Fits are to a) standard model and b) MD model

a) Standard 20 K	N	α	σ^2 / Å^2	ΔE_0 / eV	R_f
Pd-Pd	7.80 ± 0.26	-0.007 ± 0.001	0.0037 ± 0.0002	-4.90 ± 0.22	0.0065
Pd-Pt	1.13 ± 0.24	-0.011 ± 0.002	0.0024 ± 0.0005		
Pt-Pd	1.71 ± 0.20			6.38 ± 0.51	
Pt-Pt	6.98 ± 0.49	-0.008 ± 0.001	0.0045 ± 0.0003		

b) MD 20 K	N	α	σ^2 / Å^2	ΔE_0 / eV	R_f
Pd-Pd	7.85 ± 0.27	-0.004 ± 0.001	0.0030 ± 0.0002	-4.93 ± 0.21	0.0008
Pd-Pt	1.26 ± 0.27	-0.003 ± 0.002	0.0023 ± 0.0006		
Pt-Pd	1.96 ± 0.26			6.42 ± 0.49	
Pt-Pt	6.96 ± 0.48	-0.002 ± 0.001	0.0032 ± 0.0003		

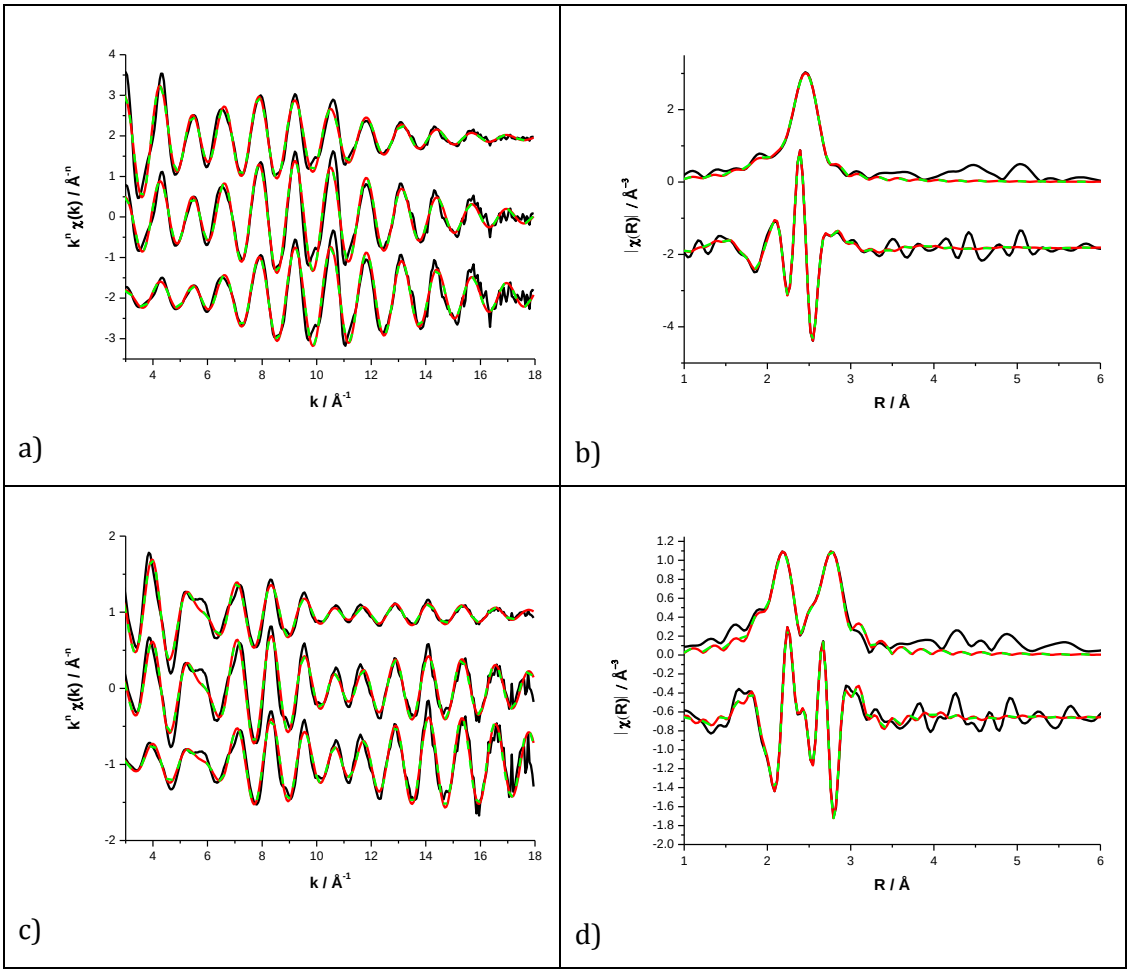

Figure 14: k^n weighted (k^1 top, k^2 middle, k^3 bottom of panel) experimental data (black) and fit to standard (red) and Sutton-Chen (green dashed) potentials, along with k^2 weighted magnitude and real Fourier transform for 1ML Pt/Pd/C at 150 K at a-b) Pd K edge and c-d) Pt L_{III} edge. The similarity of the lines for the standard and Sutton-Chen fits is such that they cannot be distinguished from one another.

Table 7: Structural parameters for 1ML Pt/Pd/C nanoparticles at 150 K, acquired in a reducing H_2 environment at the Pd K edge and Pt L_{III} edge. Fits are to a) standard model and b) MD model

a) Standard 150 K	N	α	σ^2 / Å^2	ΔE_0 / eV	R_f
Pd-Pd	7.85 ± 0.41	-0.007 ± 0.001	0.0043 ± 0.0003	-4.68 ± 0.34	0.0061
Pd-Pt	1.06 ± 0.40	-0.010 ± 0.002	0.0035 ± 0.0008		
Pt-Pd	1.96 ± 0.28			6.52 ± 0.48	
Pt-Pt	6.65 ± 0.41	-0.007 ± 0.001	0.0047 ± 0.0003		

b) MD 150 K	N	α	σ^2 / Å^2	ΔE_0 / eV	R_f
Pd-Pd	7.83 ± 0.39	-0.004 ± 0.001	0.0035 ± 0.0003	-4.74 ± 0.33	0.0013
Pd-Pt	1.22 ± 0.40	-0.003 ± 0.002	0.0030 ± 0.0007		
Pt-Pd	1.98 ± 0.27			6.30 ± 0.45	
Pt-Pt	6.80 ± 0.40	-0.001 ± 0.001	0.0036 ± 0.0003		

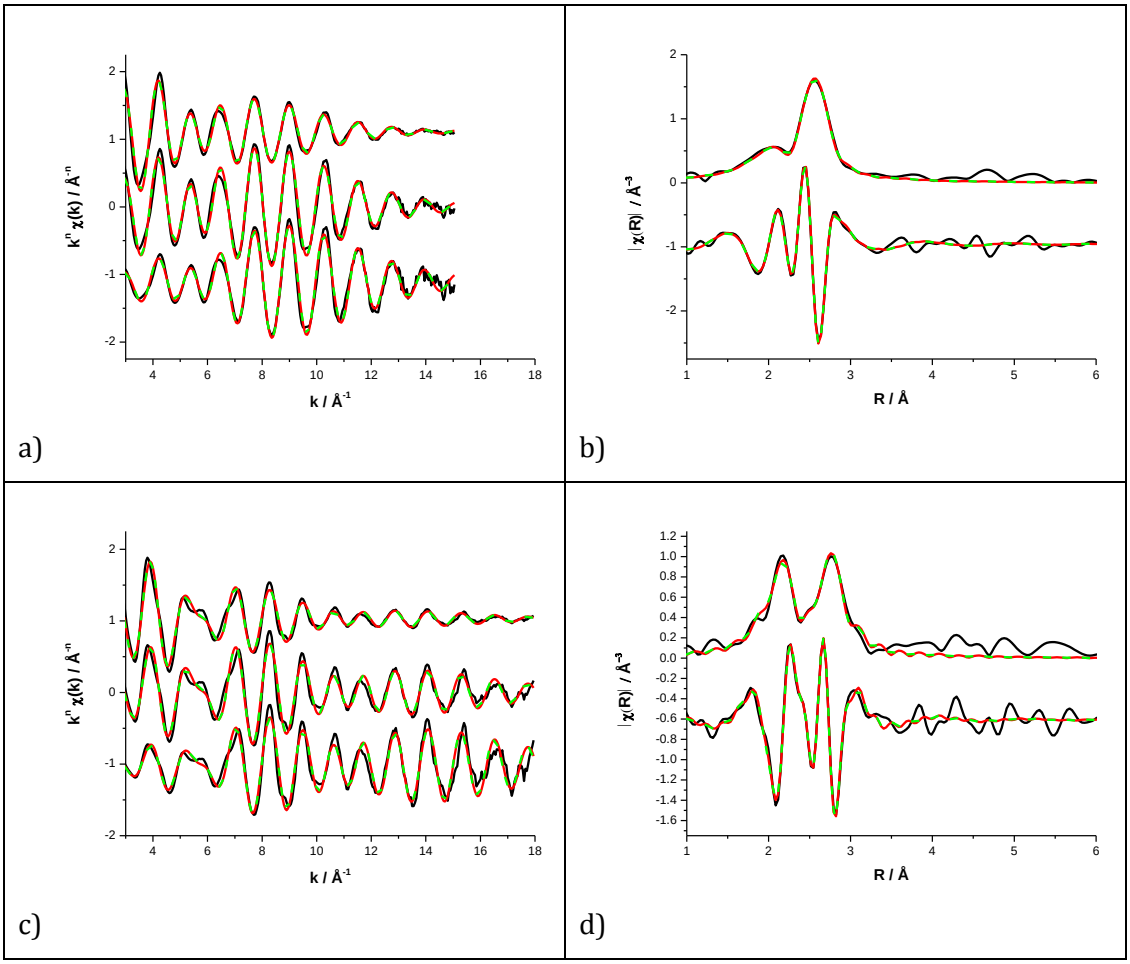

Figure 15: k^n weighted (k^1 top, k^2 middle, k^3 bottom of panel) experimental data (black) and fit to standard (red) and Sutton-Chen (green dashed) potentials, along with k^2 weighted magnitude and real Fourier transform for 1ML Pt/Pd/C at 300 K at a-b) Pd K edge and c-d) Pt L_{III} edge. The similarity of the lines for the standard and Sutton-Chen fits is such that they cannot be distinguished from one another.

Table 8: Structural parameters for 1ML Pt/Pd/C nanoparticles at 300 K, acquired in a reducing H_2 environment at the Pd K edge and Pt L_{III} edge. Fits are to a) standard model and b) MD model

a) Standard 300 K	N	α	σ^2 / Å^2	ΔE_0 / eV	R_f
Pd-Pd	7.52 ± 0.81	-0.007 ± 0.001	0.0076 ± 0.0008	-3.94 ± 0.86	0.0041
Pd-Pt	2.06 ± 0.99	-0.003 ± 0.003	0.0057 ± 0.0010		
Pt-Pd	2.49 ± 0.39			5.20 ± 0.57	
Pt-Pt	7.19 ± 0.55	-0.004 ± 0.002	0.0058 ± 0.0004		

b) MD 300 K	N	α	σ^2 / Å^2	ΔE_0 / eV	R_f
Pd-Pd	7.53 ± 0.90	0.015 ± 0.004	0.0068 ± 0.0009	-3.97 ± 0.98	0.0051
Pd-Pt	2.19 ± 1.17	0.002 ± 0.002	0.0052 ± 0.0011		
Pt-Pd	2.49 ± 0.61			4.97 ± 0.65	
Pt-Pt	7.38 ± 0.45	0.003 ± 0.004	0.0046 ± 0.0004		

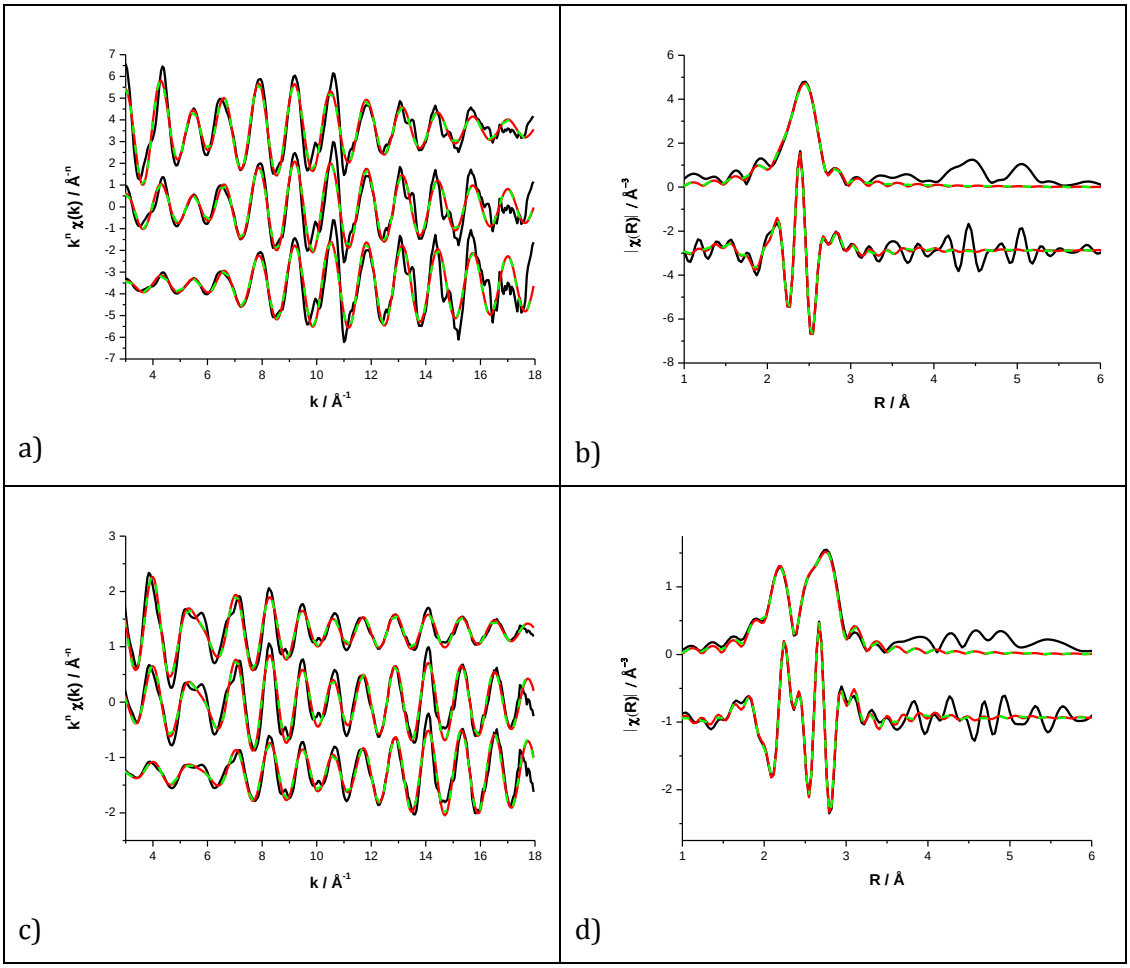

Figure 16: k^n weighted (k^1 top, k^2 middle, k^3 bottom of panel) experimental data (black) and fit to standard (red) and Sutton-Chen (green dashed) potentials, along with k^2 weighted magnitude and real Fourier transform for 2ML Pt/Pd/C at 20 K at a-b) Pd K edge and c-d) Pt L_{III} edge. The similarity of the lines for the standard and Sutton-Chen fits is such that they cannot be distinguished from one another.

Table 9: Structural parameters for 2ML Pt/Pd/C nanoparticles at 20 K, acquired in a reducing H_2 environment at the Pd K edge and Pt L_{III} edge. Fits are to a) standard model and b) MD model

a) Standard 20 K	N	α	σ^2 / Å^2	ΔE_0 / eV	R_f
Pd-Pd	7.75 ± 0.81	-0.007 ± 0.001	0.0018 ± 0.0006	-3.87 ± 0.65	0.0023
Pd-Pt	2.50 ± 0.76	-0.009 ± 0.003	0.0019 ± 0.0010		
Pt-Pd	1.26 ± 0.27			7.03 ± 0.56	
Pt-Pt	7.90 ± 0.51	-0.005 ± 0.002	0.0041 ± 0.0003		

b) MD 20 K	N	α	σ^2 / Å^2	ΔE_0 / eV	R_f
Pd-Pd	7.71 ± 0.82	-0.005 ± 0.001	0.0009 ± 0.0005	-3.99 ± 0.58	0.0019
Pd-Pt	2.83 ± 0.73	-0.003 ± 0.003	0.0013 ± 0.009		
Pt-Pd	1.26 ± 0.25			6.69± 0.48	
Pt-Pt	8.21 ± 0.46	-0.002 ± 0.001	0.0029 ± 0.0003		

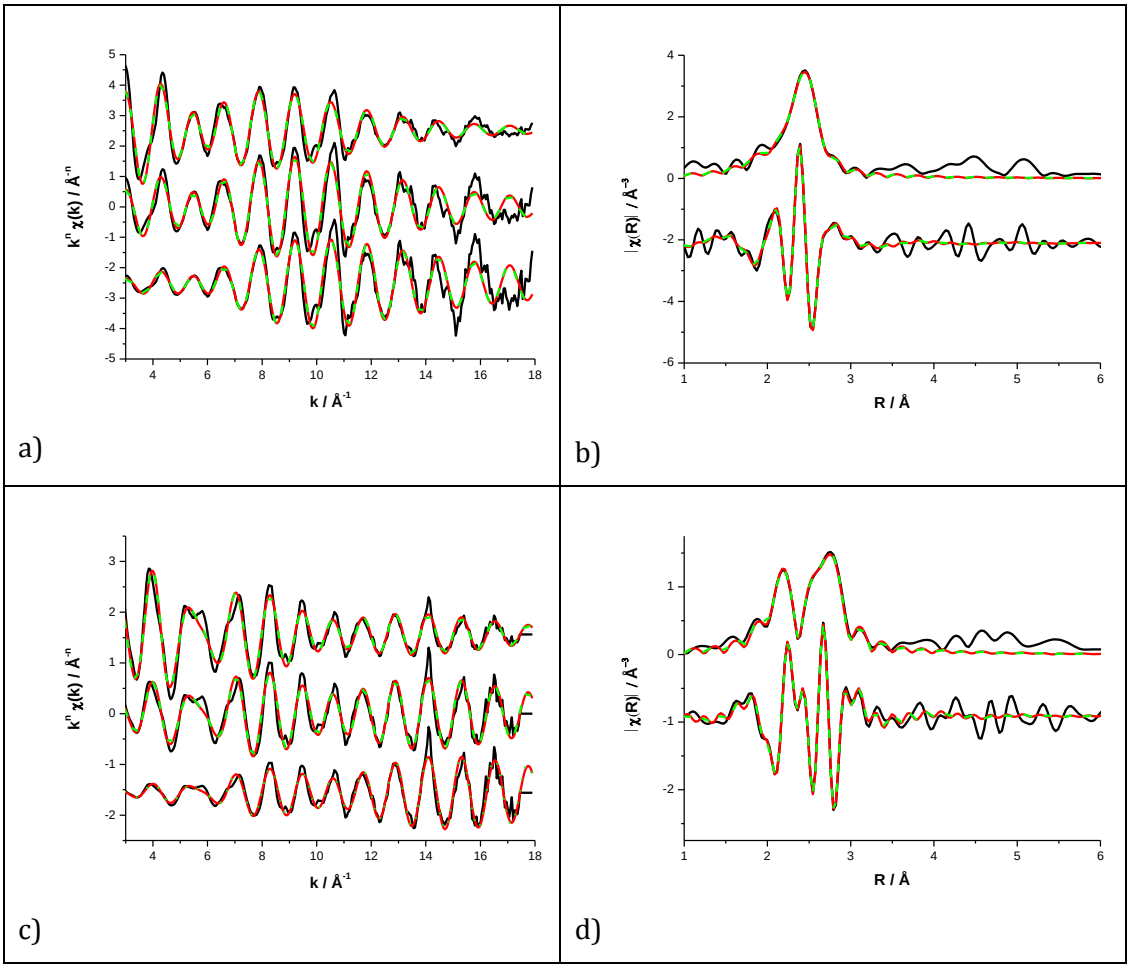

Figure 17: k^n weighted (k^1 top, k^2 middle, k^3 bottom of panel) experimental data (black) and fit to standard (red) and Sutton-Chen (green dashed) potentials, along with k^2 weighted magnitude and real Fourier transform for 2ML Pt/Pd/C at 150 K at a-b) Pd K edge and c-d) Pt L_{III} edge. The similarity of the lines for the standard and Sutton-Chen fits is such that they cannot be distinguished from one another.

Table 10: Structural parameters for 2ML Pt/Pd/C nanoparticles at 150 K, acquired in a reducing H_2 environment at the Pd K edge and Pt L_{III} edge. Fits are to a) standard model and b) MD model

a) Standard 150 K	N	α	σ^2 / Å^2	ΔE_0 / eV	R_f
Pd-Pd	7.77 ± 0.65	-0.007 ± 0.001	0.0031 ± 0.005	-4.06 ± 0.51	0.0026
Pd-Pt	2.19 ± 0.62	-0.008 ± 0.003	0.0024 ± 0.0009		
Pt-Pd	1.38 ± 0.27			7.10 ± 0.56	
Pt-Pt	7.57 ± 0.53	-0.005 ± 0.001	0.0040 ± 0.0003		

b) MD 150 K	N	α	σ^2 / Å^2	ΔE_0 / eV	R_f
Pd-Pd	7.69 ± 0.58	-0.005 ± 0.001	0.0022 ± 0.0004	-4.18 0.46	0.0022
Pd-Pt	2.47 ± 0.60	-0.003 ± 0.003	0.0018 ± 0.0008		
Pt-Pd	1.34 ± 0.24			6.75 ± 0.49	
Pt-Pt	7.76 ± 0.48	0.005 ± 0.001	0.0028 ± 0.0003		

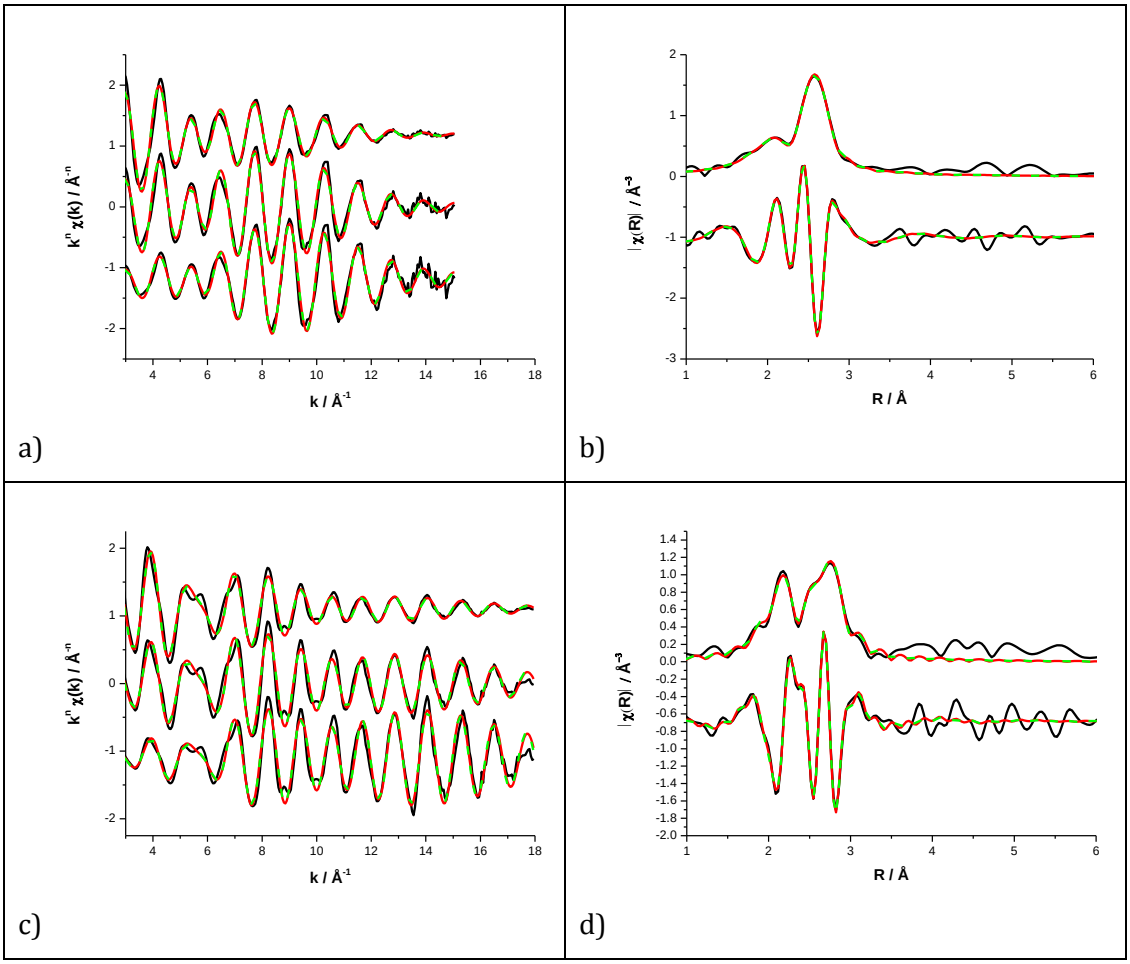

Figure 18: k^n weighted (k^1 top, k^2 middle, k^3 bottom of panel) experimental data (black) and fit to standard (red) and Sutton-Chen (green dashed) potentials, along with k^2 weighted magnitude and real Fourier transform for 2ML Pt/Pd/C at 300 K at a-b) Pd K edge and c-d) Pt L_{III} edge. The similarity of the lines for the standard and Sutton-Chen fits is such that they cannot be distinguished from one another.

Table 11: Structural parameters for 2ML Pt/Pd/C nanoparticles at 300 K, acquired in a reducing H_2 environment at the Pd K edge and Pt L_{III} edge. Fits are to a) standard model and b) MD model

a) Standard 300 K	***N***	***α***	***σ²* / Å²**	***ΔE₀* / eV**	***R_f***
Pd-Pd	7.29 ± 0.87	0.012 ± 0.004	0.0071 ± 0.0009	-3.00 ± 0.86	0.0027
Pd-Pt	2.48 ± 1.02	-0.001 ± 0.003	0.0052 ± 0.0011		
Pt-Pd	1.62 ± 0.29			5.64 ± 0.46	
Pt-Pt	8.05 ± 0.42	-0.002 ± 0.001	0.0055 ± 0.0003		

b) MD 300 K	***N***	***α***	***σ²* / Å²**	***ΔE₀* / eV**	***R_f***
Pd-Pd	7.32 ± 0.96	0.015 ± 0.004	0.0063 ± 0.0010	-3.05 ± 0.97	0.0034
Pd-Pt	2.67 ± 1.19	0.005 ± 0.004	0.0047 ± 0.0013		
Pt-Pd	1.59 ± 0.33			5.32 ± 0.51	
Pt-Pt	8.27 ± 0.51	0.004 ± 0.001	0.0043 ± 0.0003		

The Pd $\chi(k)$ signals and Fourier transforms of the Pd/C core and the Pt/Pd/C core-shell samples (**Figure 11** and **Figures 13-18** respectively) are similar; the Pd-Pd interactions dominate indicating that the Pd-Pt contributions are small. At the Pt L_{III} edge, there is a large change from a typical Pt χ(k) signal and Fourier transform. The Pt-Pd interactions and Pt-Pt interactions are out of phase, and a "beating" effect is seen in the $\chi(k)$ corresponding to a splitting of the first shell peak in the Fourier transform.

There is an improvement in the quality of fit at 20 and 150 K in all cases, most notably for the 1ML sample when the MD input is used. At 300 K however the quality of fit worsens slightly. The R_f is reported to an extra significant figure in this chapter to reflect the more subtle differences between the standard and MD methods. The energy shift ΔE_0 is consistent between the standard and MD method in all fits, which is not significant in itself, but a good verification that applying the MD approach to a multi-edge fit doesn't fundamentally change anything during the fit.

The lattice parameter used to generate the alloyed simulations was calculated from the XRD pattern of a 1:1 Pd:Pt alloy. The calculated parameter, 3.902 Å, lay between the expected lattice values of Pd (3.890 Å) and Pt (3.923 Å), giving an average first shell bond length of 2.759 Å for all possible interactions. The measured contraction from this length at all temperatures can be explained by the size dependent lattice contraction that is common for nanoparticles[19,20], as well as contraction with temperature. The normal thermal expansion observed in the core-shell nanoparticles, suggests either that the effect seen in **Table 5** for the MD fits were not realistic, or that the Pt shell has modified the properties of the core.

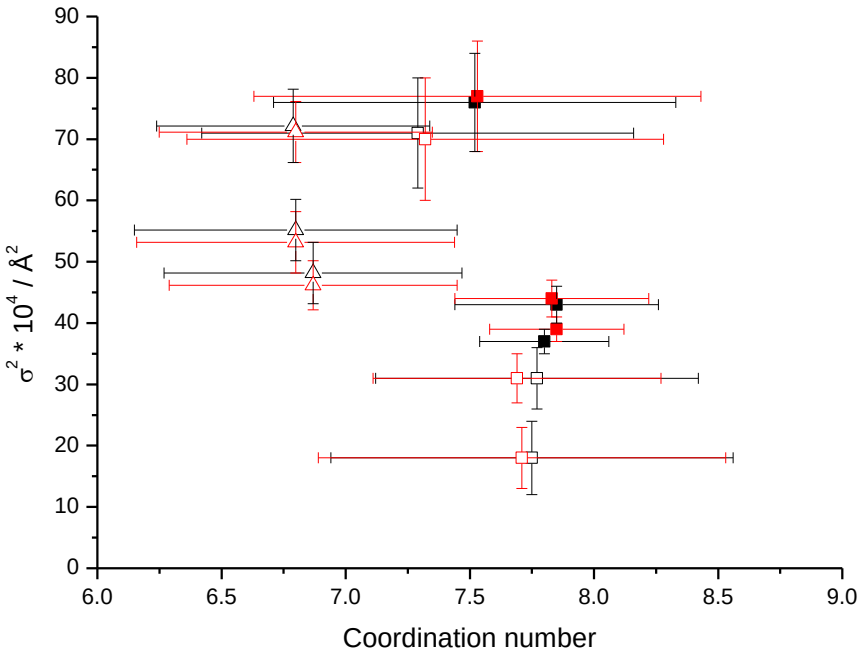

Figure 19: Correlation between coordination number and σ^2 for Pd-Pd nearest neighbour bond. Standard method is in black, MD method in red; Pd core is represented by an open triangle (Δ), 1ML Pt/Pd/C is represented by a closed square (▪), and 2ML Pt/Pd/C is represented by an open square (□).

There is a noticeable increase in Pd-Pd coordination number between the core and core-shell samples (**Figure 19**). The method used to deposit Pt onto the Pd core involved some heating of the catalysts and, therefore, may have caused aggregation giving the slightly larger reported Pd-Pd coordination numbers (and therefore sizes) for core-shell nanoparticles than for the untreated core. The 2ML sample has a very similar Pd-Pd coordination number to the 1ML sample but with lower disorder. This

suggests an increased crystallinity of the core as it becomes more coordinated, and indeed agrees nicely with the larger crystallite sizes determined by XRD (**Table 4**). Similar to the Pd core there is no real change in the Pd-Pd coordination number between the two fitting methods, explained by the near-Gaussian nature of the Pd-Pd RDF from the MD simulation (as previously discussed for the core). The disorder of the Pd-Pd bond decreases as the Pt shell thickens. The addition of a shell increases the average coordination of the Pd atoms, reducing the number of degrees of freedom the surface atoms experience, making the bond disorder more harmonic and therefore reducing the σ^2 determined.

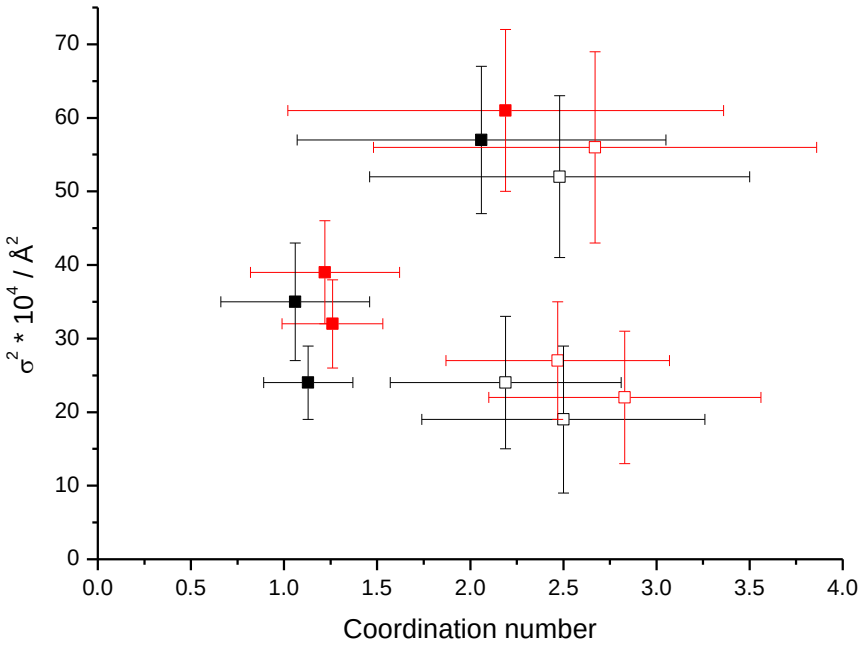

Figure 20: Correlation between coordination number and σ^2 for Pd-Pt nearest neighbour bond. Standard method is in black, MD method in red; 1ML Pt/Pd/C is represented by a closed square (▪), and 2ML Pt/Pd/C is represented by an open square (□).

The Pd-Pt nearest neighbour coordination number is clearly larger in the MD method in all cases, but there is also a corresponding increase in disorder (**Figure 20**). The increase in the average number of Pt atoms seen by each Pd atom in the 2ML sample suggests that there was not complete surface coverage in the 1ML sample. It appears the increased Pt coordination restricts the number of degrees of freedom of each Pt atom and results in a reduction in the disorder of the 2ML sample with respect to the 1ML sample.

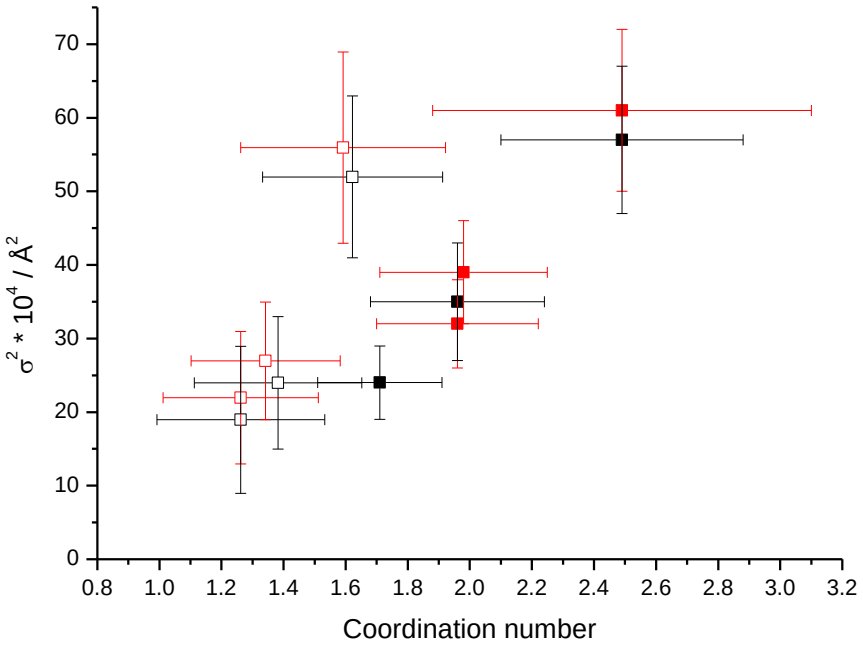

Figure 21: Correlation between coordination number and σ^2 for Pt-Pd nearest neighbour bond. Standard method is in black, MD method in red; 1ML Pt/Pd/C is represented by a closed square (▪), and 2ML Pt/Pd/C is represented by an open square (□).

The same effect is seen from the Pt-Pd bond point of view, with the 2ML sample having a lower disorder (**Figure 21**). The coordination number for Pt-Pd is lower for the 2ML sample than for the 1ML sample, however there is no change in the values calculated between the MD method and standard method. With an increased coverage, the Pt atoms on average see more Pt neighbours than Pd thus reducing the average Pt-Pd coordination number.

The Pt-Pt nearest neighbour coordination number increases from the 1ML to 2ML sample as would be expected with a thicker layer of Pt present (**Figure 22**). There is a corresponding decrease in disorder as the thicker Pt layers are becoming more bulk-like. For all nearest neighbour interactions studied, there is a small increase in disorder measured using the MD method compared with the standard method, although this change is within the error estimates. There is enough of a trend however to say that for the systems under study here, the use of the MD method results in a larger disorder being measured.

The local structure around the Pd is Pd rich, and similarly Pt has a Pt rich local structure consistent with there being segregation of the two metals instead of an alloy as has been predicted by Christoffersen *et al.*[21]

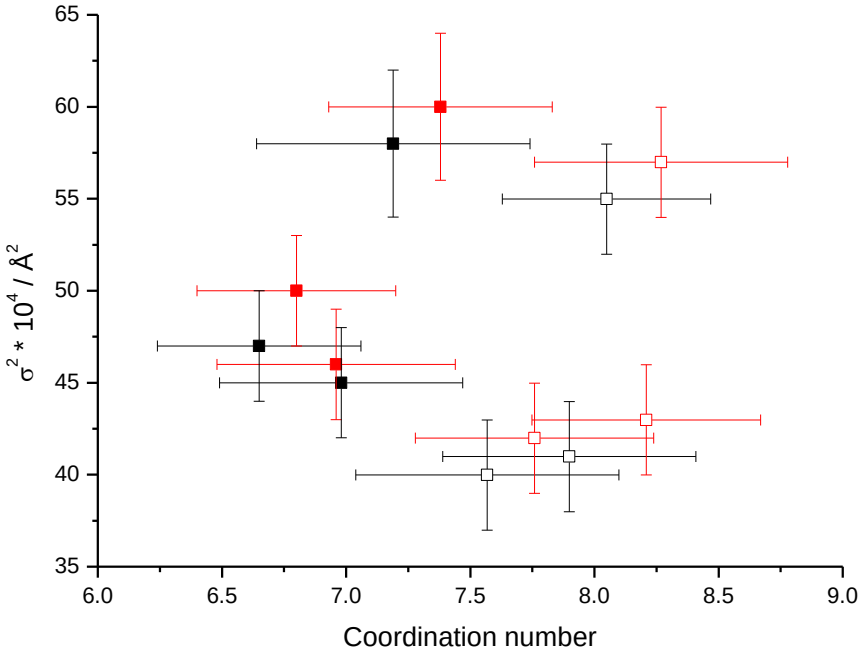

Figure 22: Correlation between coordination number and σ^2 for Pt-Pt nearest neighbour bond. Standard method is in black, MD method in red; 1ML Pt/Pd/C is represented by a closed square (▪), and 2ML Pt/Pd/C is represented by an open square (□).

Size determination from EXAFS for the core-shell samples is problematic. On top of the problems detailed in Chapter Three (**Section 3.5**) there is an unknown error associated with the size determination of the Pt/Pd/C nanoparticles as the average thickness of the Pt layer is unknown. As a first approximation the total Pd first shell coordination number was used to determine particle size; i.e. Pd-Pd and Pd-Pt interactions. The results of the EXAFS estimated particle size is in **Table 12**.

Table 12: Estimated particle sizes derived from EXAFS first shell Pd coordination numbers.

Sample	Average particle diameter / nm	
	EXAFS	
	Standard fit	MD fit
Core	1.02 ± 0.13	1.02 ± 0.13
1ML Pt/Pd/C	2.36 ± 0.39	2.52 ± 0.41
2ML Pt/Pd/C	3.39 ± 0.37	3.79 ± 0.50

4 Discussion and Conclusions

The AC-STEM micrographs (**Figure 6a** and **b**) appear to show the shell formed more on the edges and vertices of the Pd core. Whilst this can be explained by the perspective of the micrograph (end of section 3.1 c.f. **Figure 1a**), it may also be the case that the Pt shell forms first on the vertices and edges of the core (**Figure 23**). The rate of diffusion of the Pt atoms to the core during the synthesis is greatest at the vertices, with the Pt atoms initially clustering together before completing the shell formation.

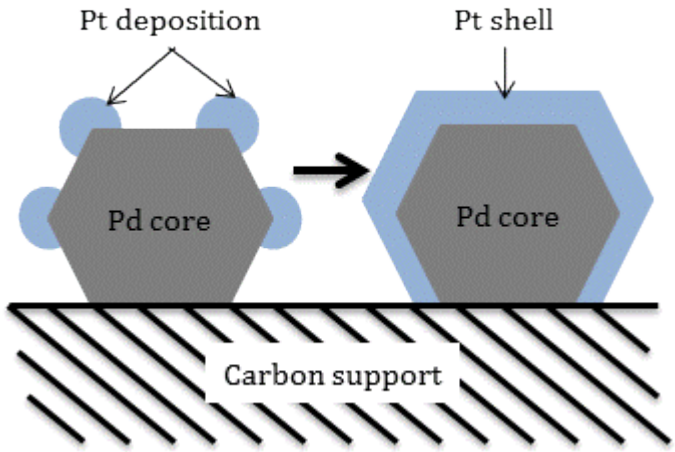

Figure 23: Schematic of Pt shell formation around Pd core.

Based on the work of Beale[10], the ratios of coordination numbers determined from the EXAFS are partway between those predicted for core-shell and for "single-half" structures (**Figure 24**). It is unlikely that the Pt shell would form between the Pd core and the carbon support, where by a near complete core shell structure would be formed, explaining the trends in coordination number observed.

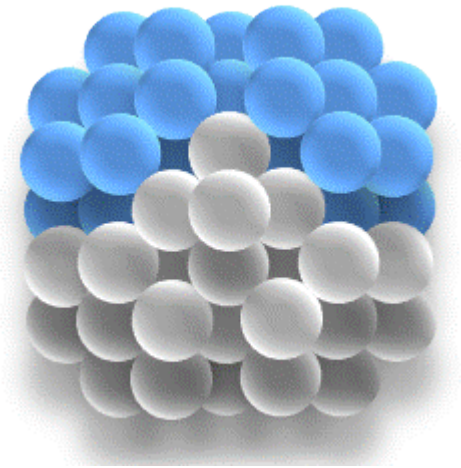

Figure 24: Bimetallic "single-half" clusters simulated to determine hypothetical coordination numbers, adapted from Beale[10]; grey spheres (Pd) and blue spheres (Pt).

A full cross-correlation of estimated particle size is in **Table 13**.

Table 13: Cross correlation of average particle size by technique.

Sample	Average particle diameter / nm			
	XRD D_{Vol}	TEM D_{Vol}	EXAFS	
			Standard fit	MD fit
Core	2.13 ± 0.08	8.95 ± 2.12	1.02 ± 0.13	1.02 ± 0.13
1ML Pt/Pd/C	3.12 ± 0.07	5.79 ± 1.57	2.36 ± 0.39	2.52 ± 0.41
2ML Pt/Pd/C	3.39 ± 0.07	4.99 ± 1.35	3.39 ± 0.37	3.79 ± 0.50

The average size for the core (estimated by EXAFS) is far below that determined by XRD and TEM. There are several possibilities that could cause this:

1) The synthesis of the Pd nanoparticles left a significant amount of Pd atomic debris scattered on the support that aggregated together during the heating process (for Pt shell deposition) increasing the Pd core size, explaining the improved agreement in the diameter of the core-shell particles compared to the core alone (Chapter Three, **Section 3.2**).

2) Pd acts as a hydrogen sponge, forming a hydride in the subsurface region[22]. The Pd/C samples in this work were reduced at room temperature for 30 minutes to remove any oxide, and the amount of hydrogen absorbed in that time could have been enough to force apart the Pd structure, thereby reducing the local coordination. This seems unlikely however as there was little change in the Pd-Pd bond length and the disorder remained relatively low.

3) The reduction of the Pd particles caused them to flatten out on the surface into non-spherical shapes. Not only would this reduce the first shell coordination number, but the means by which the size is estimated would be invalidated and give erroneous results. A higher coordination shell analysis of the Pd core gave a third shell coordination number of 7.23 ± 1.16. The ratio between the first and third coordination shell numbers can be used as an estimate of particle morphology[13]. Such a low third shell coordination number suggests that the particles are indeed non-spherical, tending towards a flatter structure, and is the most likely cause for the EXAFS greatly underestimating the size. One test of this would be to simulate flattened or other distorted shapes of Pd nanoparticle and see what difference in coordination number or quality of fit is observed with the MD method. The reduction at 473 K during the Pt

shell formation may have provided enough energy for the particle to reform into approximately spherical shapes, improving the agreement between the size determination methods for the core-shell catalysts.

Given that the TEM micrographs for the core show a 2D "spherical" geometry, and have a larger average size than the core-shell particles, possibility 3) seems the most plausible explanation.

The calculation of the D_{Vol} average particle size by the TEMdist software assumes a spherical particle size. The flattened nature of the nanoparticles on the support (described above) introduces a systematic error into the TEM size analysis that is seen in the much larger D_{Vol} weighted TEM size for the core (**Table 13**).

As has been the case for all the nanoparticles analysed in this work, crystallite size determination by XRD can only be regarded as an approximation due to the poor crystallinity of the samples. The improvement in crystallinity observed in the XRD patterns as the Pt shell thickness is increased indicate a well-defined shell is formed. The lack of a distinct Pt diffraction pattern is attributed to the Pt shell conforming to the lattice structure of the Pd core beneath. As the Pt shell thickness is further increased it is anticipated that the lattice parameter would become more Pt-like (i.e. a small increase).

The improved fit to the EXAFS data offered in most cases by the MD approach helps to address the question of which is more important for the fit: the relative location of the scattering paths (histogram bins that form the RDF taken from the MD output) or the number of scattering paths used (histogram bin width - Chapter Four, **Section 3.3.2**). Both the core-shell and alloy inputs contained the same number of histogram bins and generated the same number of scattering paths in Artemis, however the core shell input failed to give a fit. This was attributed to there being too great a disorder in the Pt shell, resulting in too great a proportion of shorter bond lengths in the input. Therefore it is the position (and degeneracy) of the extra scattering paths used and not just an increased number that contributes to the improved quality of fit.

When studying the monometallic systems (Chapter Four), an approximately spherical particle was a good enough approximation to the actual geometry of the nanoparticle to provide a noticeable improvement in both fit quality and cross-correlation with other techniques. As became apparent early on in the fitting process for the bimetallic systems the initial core-shell geometry simulated (whilst being more similar to the

actual morphology of the nanoparticles than the alloy) was too rigid a structural input for the fit and, therefore, failed to give physically reasonable parameters. The alloy structure provided a reasonable structural approximation for the initial application of the MD methodology since, at the nearest neighbour distance an alloy and a core-shell are effectively the same. Only upon moving beyond the first shell, or taking coordination number ratios into account, do the real differences between alloys and core-shell structures become apparent. It is clear however that more realistic structures for improved MD simulations are needed to generate an output that is most representative of the particles studied here. This is anticipated to improve the cross correlation of results between techniques, as has been achieved with the monometallic systems. Simulations of hemispherical clusters on the support would help address the nature of the Pd core-support interaction and shape. Simulation of single-half clusters non-spherical geometries would provide a range of other inputs with which to fit the EXAFS data.

One fact that is apparent throughout is the increased difficulty in determining particle size for core-shell systems. The use of XRD alone presents more problems than for monometallic systems. Without the benefit of AC-STEM to show the crystalline shell (**Figure 6**), the nature of the shell (amorphous or crystalline) cannot be confirmed. EXAFS gives indirect information on size and structure, although information on the exact thickness and uniformity of the shell is currently not possible. TEM provides the best means for direct particle size determination, however it is limited by the area of sample imaged, and also the random error introduced by the human operator choosing which areas to image. The two dimensional nature of TEM proved a limitation for the samples reported in this chapter. The nature of the particle support interaction was not clearly defined, and resulted in further discrepancies between the sizes determined. The use of HAADF tomography[23] would provide a direct means of determining the morphology of the core and core-shell particles on the support. The technique however is more time-consuming and local in scale than TEM. Simulation of different geometries and using the MD outputs as the basis for fitting the EXAFS would provide a means of determining the most likely shape of the nanoparticles, although as has been discussed earlier, EXAFS by itself currently provides an estimation of particle size and shape for core-shell systems, and not a structural solution.

5 References

(1) Wang, S.; Lin, W.; Zhu, Y.; Xie, Y.; Chen, J. G. *Chinese Journal of Catalysis* **2006**, *27*, 301.

(2) Yoshimura, Y.; Toba, M.; Matsui, T.; Harada, M.; Ichihashi, Y.; Bando, K. K.; Yasuda, H.; Ishihara, H.; Morita, Y.; Kameoka, T. *Applied Catalysis A: General* **2007**, *322*, 152.

(3) Crabb, E. M.; Marshall, R.; Thompsett, D. *Journal of The Electrochemical Society* **2000**, *147*, 4440.

(4) Crabb, E. M.; Ravikumar, M. K. *Electrochimica Acta* **2001**, *46*, 1033.

(5) Crabb, E. M.; Ravikumar, M. K.; Thompsett, D.; Hurford, M.; Rose, A.; Russell, A. E. *Physical Chemistry Chemical Physics* **2004**, *6*, 1792.

(6) Wells, P. P.; Crabb, E. M.; King, C. R.; Wiltshire, R.; Billsborrow, B.; Thompsett, D.; Russell, A. E. *Physical Chemistry Chemical Physics* **2009**, *11*, 5773.

(7) Chen, H. M.; Liu, R. S.; Jang, L. Y.; Lee, J. F.; Hu, S. F. *Chemical Physics Letters* **2006**, *421*, 118.

(8) Morlang, A.; Neuhausen, U.; Klementiev, K. V.; Schütze, F. W.; Miehe, G.; Fuess, H.; Lox, E. S. *Applied Catalysis B: Environmental* **2005**, *60*, 191.

(9) Hansen, P. L.; Molenbroek, A. M.; Ruban, A. V. *The Journal of Physical Chemistry B* **1997**, *101*, 1861.

(10) Beale, A. M.; Weckhuysen, B. M. *Physical Chemistry Chemical Physics* **2010**, *12*, 5562.

(11) Frenkel, A. I. *Zeitschrift Fur Kristallographie* **2007**, *222*, 605.

(12) Benfield, R. E. *Journal of the Chemical Society-Faraday Transactions* **1992**, *88*, 1107.

(13) Jentys, A. *Physical Chemistry Chemical Physics* **1999**, *1*, 4059.

(14) Dalba, G.; Fornasini, P. *Journal of Synchrotron Radiation* **1997**, *4*, 243.

(15) Daly, K. A.; Penner-Hahn, J. E. *Journal of Synchrotron Radiation* **1998**, *5*, 1383.

(16) Ravel, B. *Journal of Synchrotron Radiation* **2001**, *8*, 314.

(17) Sutton, A. P.; Chen, J. *Philos. Mag. Lett.* **1990**, *61*, 139.

(18) Comaschi, T.; et al. *Journal of Physics: Conference Series* **2009**, *190*, 012122.

(19) Miller, J. T.; Kropf, A. J.; Zha, Y.; Regalbuto, J. R.; Delannoy, L.; Louis, C.; Bus, E.; van Bokhoven, J. A. *Journal of Catalysis* **2006**, *240*, 222.

(20) Solliard, C.; Flueli, M. *Surface Science* **1985**, *156*, 487.

(21) Christoffersen, E.; Liu, P.; Ruban, A.; Skriver, H. L.; Nørskov, J. K. *Journal of Catalysis* **2001**, *199*, 123.

(22) Sykes, E. C. H.; Fernández-Torres, L. C.; Nanayakkara, S. U.; Mantooth, B. A.; Nevin, R. M.; Weiss, P. S. *Proceedings of the National Academy of Sciences of the United States of America* **2005**, *102*, 17907.

(23) Cervera-Gontard, L.; et al. *Journal of Physics: Conference Series* **2006**, *26*, 367.

CHAPTER SIX: EXAFS STUDIES OF THE UNDERPOTENTIAL DEPOSITION OF Cu ON Au NANOPARTICLES

1 Introduction

EXAFS has proven to be a powerful and flexible characterisation technique and has been applied to studies of heteroepitaxial film growth[1-3], nanoparticle characterisation[4-6] and potential dependent studies[7-9]. The coordination number measured by EXAFS is the average number of neighbours surrounding each atom in the sample. For bulk materials such as powders, crystals or metals, these values are at the theoretical maximum value for the specific crystal structure of the compound being investigated e.g. face centred cubic (*fcc*) has a nearest neighbour coordination of 12. The previous chapters detailed the termination effects present in nanoparticles due to the high proportion of surface atoms[10-12]. These surface atoms have greatly reduced coordination, as a result of which the average coordination number will be significantly less than for bulk materials. By capping the surface of the nanoparticle, the surface atoms will become fully coordinated and exhibit values similar to those of the bulk material. The differences in the EXAFS between the core and the capped core will allow for the determination of the contribution to the EXAFS from the surface atoms to be isolated, and for a better understanding of the structure of the nanoparticle.

One means of capping the nanoparticle surface is the underpotential deposition (UPD) of another metal. UPD has received much attention as a means of electrochemical heteroepitaxial growth on single crystal surfaces[1-3,13,14], and is the deposition of typically one monolayer of a metal onto a different metal electrode at potentials positive to the bulk deposition potential, the initial stages forming a two dimensional film. The adlayers deposited by the UPD method may also be used as a template for the deposition of a more noble metal by spontaneous exchange, thus providing a means to synthesise a range of layered substrates and core-shell materials.

Studies on the UPD of Cu on Pt electrodes in sulphuric acid by Bruckenstein[15,16] noted that the deposition of two monolayers of Cu^0 on the electrode surface were necessary before Cu could be reduced exhibiting Nernstian behaviour. The underpotential deposited Cu^0 occurred at the potential at which Cu^{2+} is reduced to Cu^{1+} and was

independent of the Cu^{2+} concentration in the range studied. This was followed by extensive work by Kolb *et al.*[17-19] on the UPD of metals onto foreign metal substrates in both aqueous and non-aqueous solutions.

Cu UPD on Au surfaces from a sulphate supporting electrolyte is one of the more extensively studied systems. The process of deposition on Au (111) and Au (100) surfaces is well documented[20-22], although little work has been done on nanoparticle systems.

During the initial stages of Cu deposition on Au (111), it is known that the sulphate anion is co-adsorbed with the Cu onto the Au surface, represented in **Figure 1a**[13,21], and that the Cu still retains a partial yet unknown charge. Surface X-ray scattering (SXS) combined with scanning tunnelling microscopy (STM) and atomic force microscopy (AFM) have shown that the Cu atoms and sulphate molecules occupy 3-fold hollow sites during the initial deposition stage of Cu on Au (111) surfaces in acidic medium [14].

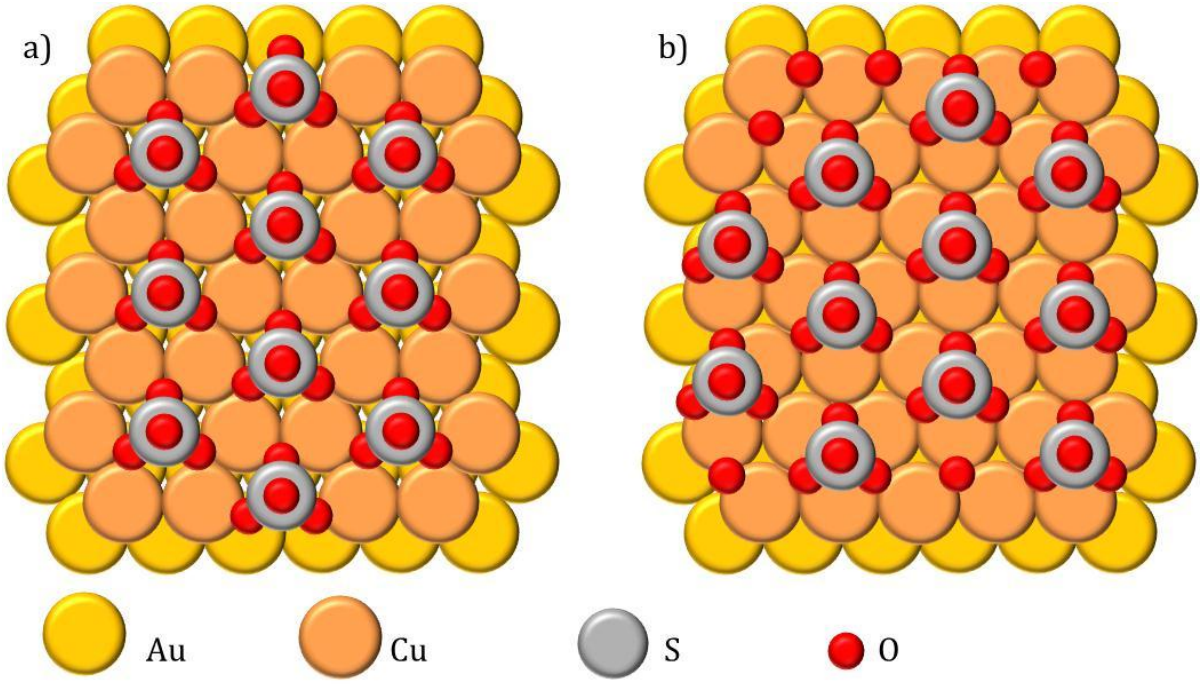

Figure 1: Schematic of deposition of Cu on Au (111) with sulphate anions, a) first stage and b) full Cu monolayer.

EXAFS studies by Lee *et al.*[2] of Cu UPD on Au (111) gave results consistent with the model of Cu coadsorbed with sulphate. They showed that at more negative potentials (before the bulk deposition) the surface structure rearranged to be a complete Cu monolayer of Cu with sulphate anions atop (**Figure 1b**). The adsorption of Cu in 2-fold

and atop sites was also investigated during this study; however the EXAFS quality of fit was noticeably reduced in both cases, indicating that these adsorption sites were less favoured than the 3-fold site.

Recent theoretical studies by Oviedo[23] predict the number of Ag adsorption sites on ideal truncated octahedral Au nanoparticles; they highlight the decreasing percentage of adsorption sites on the nanoparticle face as a function of both the available number of surface atoms and the nanoparticle radius. Based on this study, the total Cu coverage by UPD on an idealised Au nanoparticle would be expected to be less than the total number of Au surface atoms, although a uniform surface coverage could still be attained. This computational study has implications for the interpretation of EXAFS data and coordination number determination and interpretation. The functions proposed by Oviedo are such that for a 6 nm diameter (truncated cuboctahedron) Au nanoparticle, only 75 % of possible adsorption sites are on the faces. Based on the accepted interfacial structure of Cu adsorbing in 3-fold sites, this reduced degree of surface coverage would result in the coordination number for Au-Cu and Cu-Cu interactions being significantly less than the theoretical maximum.

Zhang *et al*.[24] synthesised bimetallic Ag/Au nanoparticles by the UPD-redox displacement method. However the nanoparticles were much larger than those studied here (c. 40 nm determined by scanning electron microscopy - SEM), and EDX was the only means of quantifying the Ag coverage as a weight percentage value. No apparent effort was made to determine the extent or environment of the deposition, only attributing the small amount of deposition and negligible change in size to monolayer deposition. A similar study by Tang *et al.*[25] characterised the nanoparticles in a similar way confirming the co-presence of the core and Cu UPD adlayer. They were not however able to quantify the extent of surface coverage.

UPD is currently receiving considerable attention as a means of synthesising and modifying core-shell electrocatalysts. The UPD adlayer of Cu on an electrode surface (core) can undergo spontaneous exchange with a more noble metal such as Pt to form a Pt monolayer (shell) on the substrate (core). It has been proposed that not only will this result in a reduction of the amount of the more expensive metal, but that a modification in the catalytic properties of the surface monolayer might be achieved by varying the nature of the underlying metal substrate[26,27]. Adzic *et al*.[28-30] have used this Cu UPD method to prepare core-shell nanoparticle electrocatalysts. The initial shell depositions were performed using controlled surface deposition reactions[29], or by

thermal treatment of metal salt slurries[28], to ensure a noble metal was atop a non-noble core. Cu was then deposited atop the noble metal shell and displaced by Pt to form a multi layered structure. The core-shell particles initially synthesised by Adzic *et al*.[26] averaged between 12-15 nm diameter; particles of this size behave in a much more bulk-like manner than nanoparticles <5 nm and therefore the faces of the nanoparticle are much more like crystal surfaces; the more recent work[29] involved particles between 4 and 8 nm in diameter. The Au nanoparticles used in this study have an initial diameter of between 2 and 2.5 nm, are very poorly crystalline and this may have an effect on the Cu deposition.

The work in this chapter aims to cap the surface of Au nanoparticles via Cu UPD and to measure the EXAFS before, during and after the deposition to investigate both the structure of the core-shell nanoparticles and to determine the contribution arising from the surface atoms of the core.

2 Experimental

2.1 Preparation

The sample used for the UPD measurements was the 4 wt% Au/C (thiol) sample as characterised in Chapters Three and Four. Painted electrodes were prepared as detailed in section 5.4 of Chapter Two with a Au loading of 0.07 mg cm^{-2}. The three electrode cell and *in situ* cell were set up as reported in Chapter Two (sections 7.1.2 and 2.2.7, respectively). Firstly cyclic voltammograms were collected using a Au disc electrode followed by the Au nanoparticle painted electrode using 0.5 M H_2SO_4 as the supporting electrolyte and then using 0.5 M H_2SO_4 with 2 mM $CuSO_4$, as detailed in Chapter Two section 7. All potentials quoted in this chapter are reported versus a $Hg/HgSO_4$ reference electrode calibrated to +0.695 V vs. RHE. Four regions of interest were identified based on peaks identified for both the Au disc and painted electrode using the three electrode cell. The experiment was repeated using the *in situ* cell in the lab before the EXAFS measurements were collected.

The geometric surface area of the Au working electrode contact in the *in situ* cell was far less than 0.001% the estimated surface area of the Au nanoparticles (based on spherical nanoparticles with a diameter of 4.3 nm) and therefore its contribution to the overall current response can be neglected. The Cu^{2+} concentration was sufficient to ensure a complete monolayer coverage based on the *in situ* cell volume alone (~ 1 ml), and the excess in the electrolyte being pumped through the cell was nearly 2000 times

that for a monolayer coverage, sufficient for bulk deposition on the nanoparticles surface.

2.2 Beamline

The absorption edges of interest were the Au L_{III} (11919 eV) and Cu K (8979 eV) edges. Investigations were carried out on beamline X23A2 of the NSLS and measurements collected by myself and Jon Speed (University of Southampton). The station scientist present was Bruce Ravel. All EXAFS measurements in this chapter were collected in fluorescence mode using the *in situ* cell.

The 0.5 M H_2SO_4 electrolyte was purged with N_2 for 20 minutes, and then pumped through the *in situ* cell using a peristaltic pump for 20 minutes to ensure hydration of the painted electrode. Three voltammograms were collected between -0.625 and +0.925 V vs. $Hg/HgSO_4$ at 50 mVs^{-1} sweep rate, followed by three voltammograms at 10 mVs^{-1}. The upper potential limit was reduced to +0.200 V vs. $Hg/HgSO_4$ and the scans repeated.

To record EXAFS whilst the electrode was held at potential in 0.5 M H_2SO_4 the following procedure was followed. To avoid large jumps in current the potential was gradually moved to the desired value and the current vs. time profile recorded as the peristaltic pump circulated the electrolyte through the cell. After 5 minutes and providing the current vs. time profile had stabilised the pump was switched off and the EXAFS collected. After the EXAFS had been collected the pump was restarted and two voltammograms collected between -0.625 and +0.925 V vs. $Hg/HgSO_4$ followed by two between -0.625 and +0.200 V vs. $Hg/HgSO_4$.

The procedure for the EXAFS in 2 mM $CuSO_4$ in 0.5 M H_2SO_4 (purged with N_2 for 20 minutes) was as above with the following alteration; the deposition time was increased to 30 minutes to allow for formation of the adlayers.

3 Results

3.1 Electrochemistry

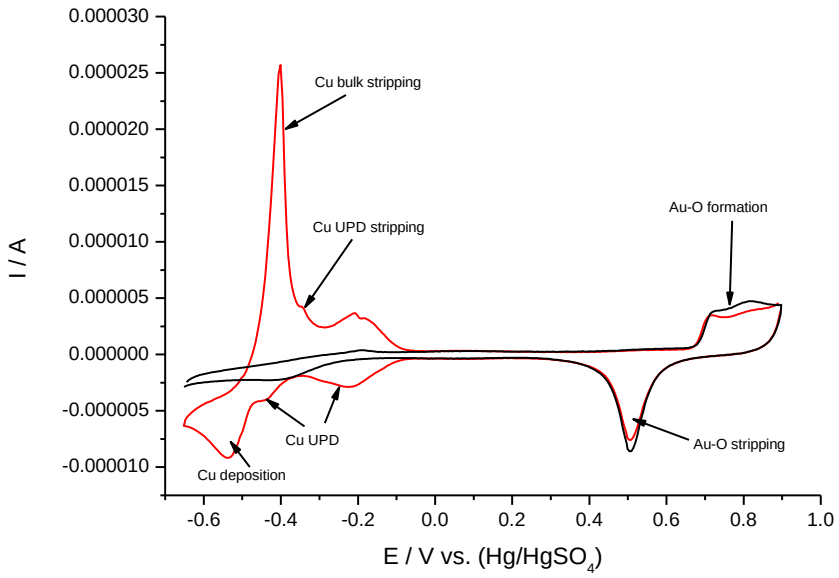

Figure 2: Cyclic voltammogram of 0.20 cm² Au disc in 0.5 M H_2SO_4 (black) and in 0.5 M H_2SO_4 with 2 mM $CuSO_4$ (red). Sweep rate 10 mVs^{-1}.

Figure 2 highlights the potential regions where Cu deposits on to the Au surface using a (bulk) Au disc electrode. The peak at -0.21 V represents the first deposition stage, an adlayer structure involving both the Cu atoms and SO_4 anions[14], followed by a complete Cu adlayer deposition at -0.42 V. Bulk deposition of Cu occurs by -0.51 V.

Previous studies[2,3,14,31] have used Cu^{2+} solutions containing between 0.02 mM to 0.1 M Cu^{2+}, in 0.1 to 1 M H_2SO_4 concentrations. The concentrations used in this study were chosen to ensure there was enough Cu^{2+} in the solution to give the full theoretical coverage of the nanoparticles, whilst dilute enough for minimal Cu^{2+} left in solution after the deposition. The latter would complicate the EXAFS analysis due to the small amount of sample in the X-ray beam.

The cyclic voltammograms of the Au nanoparticles recorded using the three electrode cell are less clearly defined than the Au disc because of the increased capacitance of the carbon support and the low loading of Au on the electrode. However the deposition regions are still identifiable (**Figure 3**). The first adlayer deposition is far less well defined and this attributed to the smaller size of the crystal facets on the nanoparticles compared to the polycrystalline Au electrode.

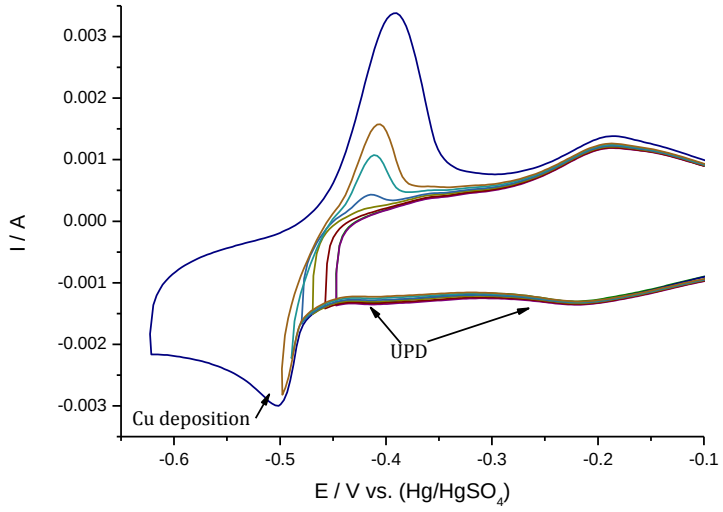

Figure 3: Cyclic voltammogram of 4 wt% Au/C nanoparticles on 1.32 cm² electrode in 0.5 M H_2SO_4 with 2 mM $CuSO_4$. Three electrode electrochemical cell used. Change in line colour corresponds to increase of the negative potential limit. Sweep rate 10 mVs^{-1}.

3.2 In Situ Cell Electrochemistry

The *in situ* cell has a very thin layer of electrolyte between the window and electrode to ensure that the largest fraction of the incident X-rays reach the sample (and are not absorbed by the solution). This thin layer configuration increases the resistance of the cell causing further distortion to the voltammogram. Whilst the peaks are broadest and least well defined using the *in situ* cell, the position of the peaks are very similar between the disc and nanoparticle electrode, and also between the three electrode cell and the *in situ* cell. **Figure 4** shows the cyclic voltammograms in 0.5 M H_2SO_4 (black line) and in 0.5 M H_2SO_4 with 2 mM $CuSO_4$ (red line) obtained in the *in situ* EXAFS cell.

A small change in the double layer capacitance is observed when the electrolyte is changed from 0.5 M H_2SO_4 to 2 mM $CuSO_4$ in 0.5 M H_2SO_4. The Cu bulk stripping peak in the *in situ* cell is not as well defined as in the three electrode cell, or for the Au disc. A window opening experiment was performed, increasing the negative potential limit however no clearly defined bulk stripping peak was observed (**Figure 5**).

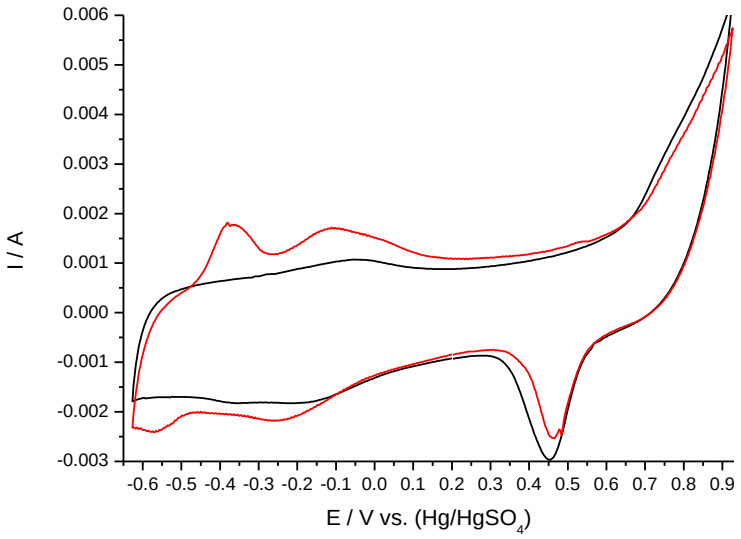

Figure 4: Cyclic voltammogram of 4 wt% Au/C nanoparticles on 1.32 cm² electrode in 0.5 M H_2SO_4 (black) and in 0.5 M H_2SO_4 with 2 mM $CuSO_4$ (red). *In situ* EXAFS cell used. Sweep rate 10 mVs^{-1}.

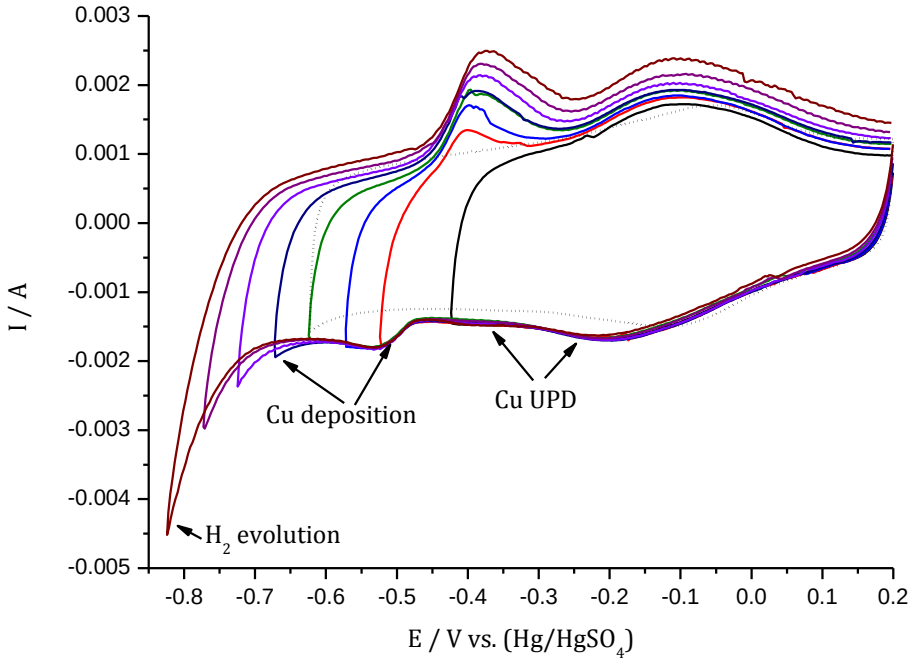

Figure 5: Cyclic voltammogram of 4 wt% Au/C nanoparticles on 1.32 cm² electrode in 0.5 M H_2SO_4 with 2 mM $CuSO_4$. *In situ* EXAFS cell used. Change in line colour corresponds to increase of the negative potential limit, dotted line is 0.5 M H_2SO_4 only scan. Sweep rate 10 mVs^{-1}.

Figures 6, **7** and **8** show cyclic voltammograms obtained in the *in situ* cell during the EXAFS measurements. The structure of the nanoparticles does not appear to change during cycling in 0.5 M H_2SO_4, as there was no evidence of dissolution of the Au or significant sintering of the particles over the course of the experiment; the voltammograms collected show very little change in the Au-O stripping peak after each potential hold.

The addition of $CuSO_4$ to the electrolyte resulted in the appearance of Cu deposition peaks in the voltammograms (compare **Figures 6** and **7**). The small differences between the voltammograms obtained after the potential holds during EXAFS collection are attributed to the variation in the flow rate of the peristaltic pump used. Whilst every effort was made to keep the flow rate constant throughout the experiment it varied slightly and therefore the amount of Cu coming into contact with the electrode varied between each voltammogram collected (resulting in the small changes in current). These slight differences were only noticeable for the voltammograms and not when the potential was held during the EXAFS measurements.

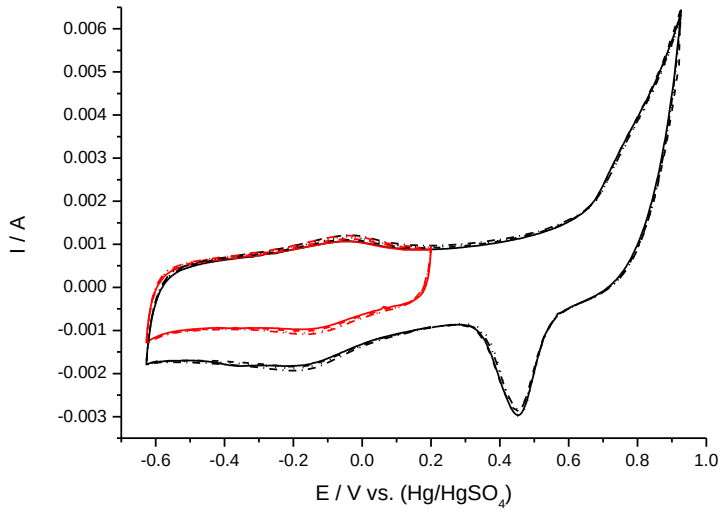

Figure 6: Cyclic voltammogram of 4 wt% Au/C nanoparticles on 1.32 cm² electrode in 0.5 M H_2SO_4. *In situ* EXAFS cell used. Black denotes potential limits between -0.65 to 0.9 V, and red between -0.65 to 0.2 V. Cyclic voltammograms were collected after the Au L_{III} edge EXAFS was measured at +0.20 V (—), -0.21 V (---), -0.42 V (···) and at -0.51 V (-·-·-). Sweep rate 10 mVs^{-1}. The second cycle after each potential is reported to show no restructuring of the nanoparticles has occurred.

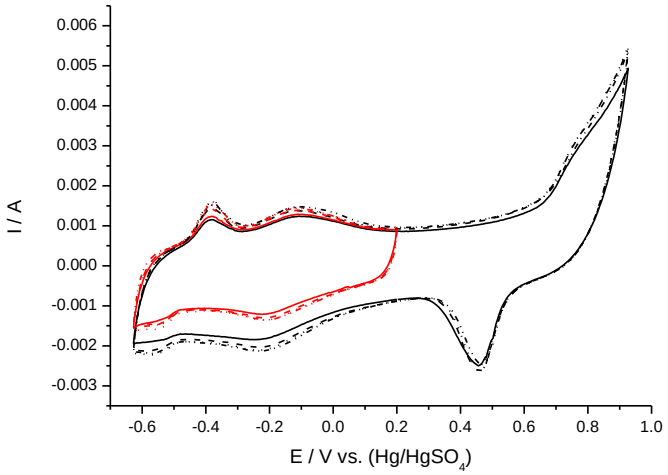

Figure 7: Cyclic voltammogram of 4 wt% Au/C nanoparticles on 1.32 cm^2 electrode in 0.5 M H_2SO_4 with 2 mM $CuSO_4$. *In situ* EXAFS cell used. Black denotes potential limits between -0.65 to 0.9 V, and red between -0.65 to 0.2 V. Cyclic voltammograms were collected after the Au L_{III} edge EXAFS was measured at +0.20 V (—), -0.21 V (---), -0.42 V (···) and at -0.51 V (-·-·-). Sweep rate 10 mVs^{-1}. The second cycle after each potential is reported to show no restructuring of the nanoparticles has occurred.

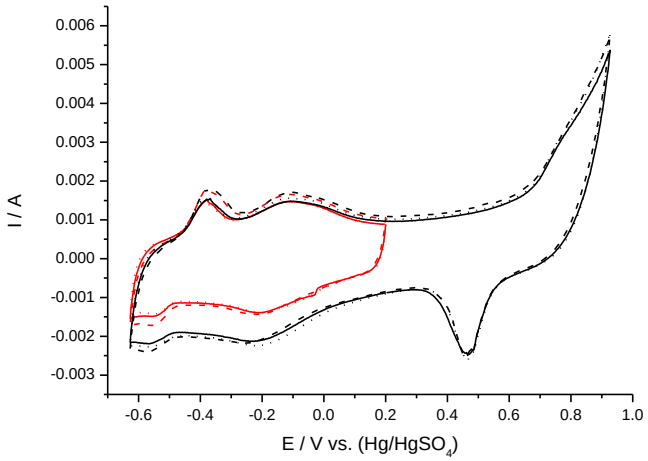

Figure 8: Cyclic voltammogram of 4 wt% Au/C nanoparticles on 1.32 cm^2 electrode in 0.5 M H_2SO_4 with 2 mM $CuSO_4$. *In situ* EXAFS cell used. Black denotes potential limits between -0.65 to 0.9 V, and red between -0.65 to 0.2 V. Cyclic voltammograms were collected after the Cu K edge EXAFS was measured at +0.20 V (—), -0.21 V (---), and at +0.20 V (···). The electrode was not cycled after the -0.42 V and -0.51 V measurements to preserve the deposited structure. Sweep rate 10 mVs^{-1}. The second cycle after each potential is reported to show no restructuring of the nanoparticles has occurred.

The surface area of the Au nanoparticles was determined by measuring the charge of the Au-O stripping peak at+0.45 V. This was found to be 61.32 mC., corresponding to 1.92 x 10^{17} surface Au atoms.

Au-O formation/stripping and Cu adsorption/desorption are both 2 electron processes. The charge associated with the Cu stripping peak after holding the potential at -0.42 V (UPD adlayer) for 30 minutes is 27.15 mC corresponding to 8.48 x 10^{16} Cu atoms, whilst that after 30 minutes at -0.51 V is 62.77 mC, corresponding to 1.96 x 10^{17} Cu atoms. The stripping voltammograms are shown in **Figure 9**. This gives a theoretical UPD coverage of 44% after the -0.42 V hold. Given the large excess of Cu^{2+} ions in solution, the incomplete coverage cannot be attributed to the unavailability of Cu. The charge after holding the potential at -0.51 V indicates that enough Cu atoms were deposited to cover the surface fully, and increase the thickness of the coverage; the uniformity of the deposition cannot be confirmed from these measurements alone.

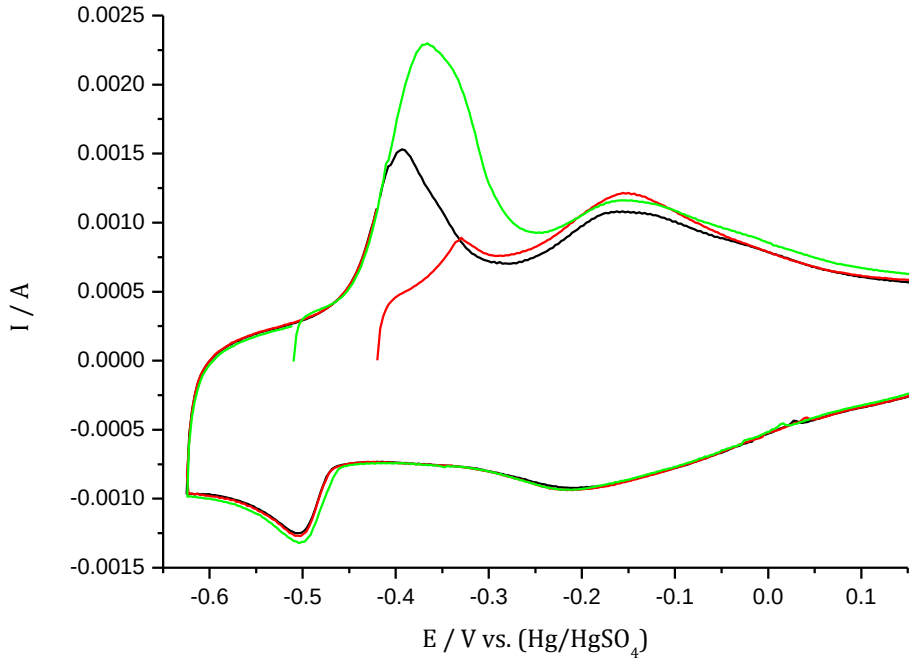

Figure 9: Stripping voltammograms for 4 wt% Au/C nanoparticles on 1.32 cm^2 electrode in 0.5 M H_2SO_4 with 2 mM $CuSO_4$. *In situ* EXAFS cell used. Sweep rate 5 mVs^{-1}. Standard voltammogram (black), stripping after -0.42 V hold for 30 minutes (red), stripping after -0.51 V hold for 30 minutes (green).

3.3 EXAFS

The fluorescence cell cannot record a transmission measurement at the same time as a fluorescence measurement (a result of a narrow beam exit window). Therefore it was not possible to record a simultaneous reference measurement as was the case for data collected in transmission mode presented in previous chapters. Alignment of the energy scale for the spectra was, therefore, achieved by use of features inherent from the monochromator that are energy dependent, and detectable in I_0. A Au foil was used to reference these features and the I_0 reading was then used to calibrate the energy of all the fluorescence measurements. Miscalibration between mono and position recorder gives an expected energy value for the Au L_{III} edge e.g. 11919 and a recorded value e.g. 11924.49919. The monochromator held position well throughout the series of measurements, i.e. the major feature in the mono at 12689.7 eV (before calibration) was consistent in all scans, and therefore this procedure was used to align all the measurements.

Data were fitted using the standard method detailed in Chapter Three, between 2-6 Å in *R*, 3-15 $Å^{-1}$ in *k*, with multiple *k*-weighting. The measurement at -0.42 V was fitted between 3-14 $Å^{-1}$ in *k*. To minimise the number of parameters in the fit the multiple scattering path σ^2 parameters were constrained based on the photoelectron mean free path length (Chapter Three, **section 3.4**).

Prior to collecting the nanoparticle data, a Au foil spectrum was obtained to determine the amplitude reduction factor (S_0^2), without which the coordination number cannot be accurately determined[32]. The amplitude reduction factor was found to be 0.85 ± 0.04 at the Au L_{III} edge and all Au coordination numbers reported in this work were corrected using this amplitude reduction.

3.3.1 Au L_{III} edge – 0.5 M H_2SO_4 electrolyte

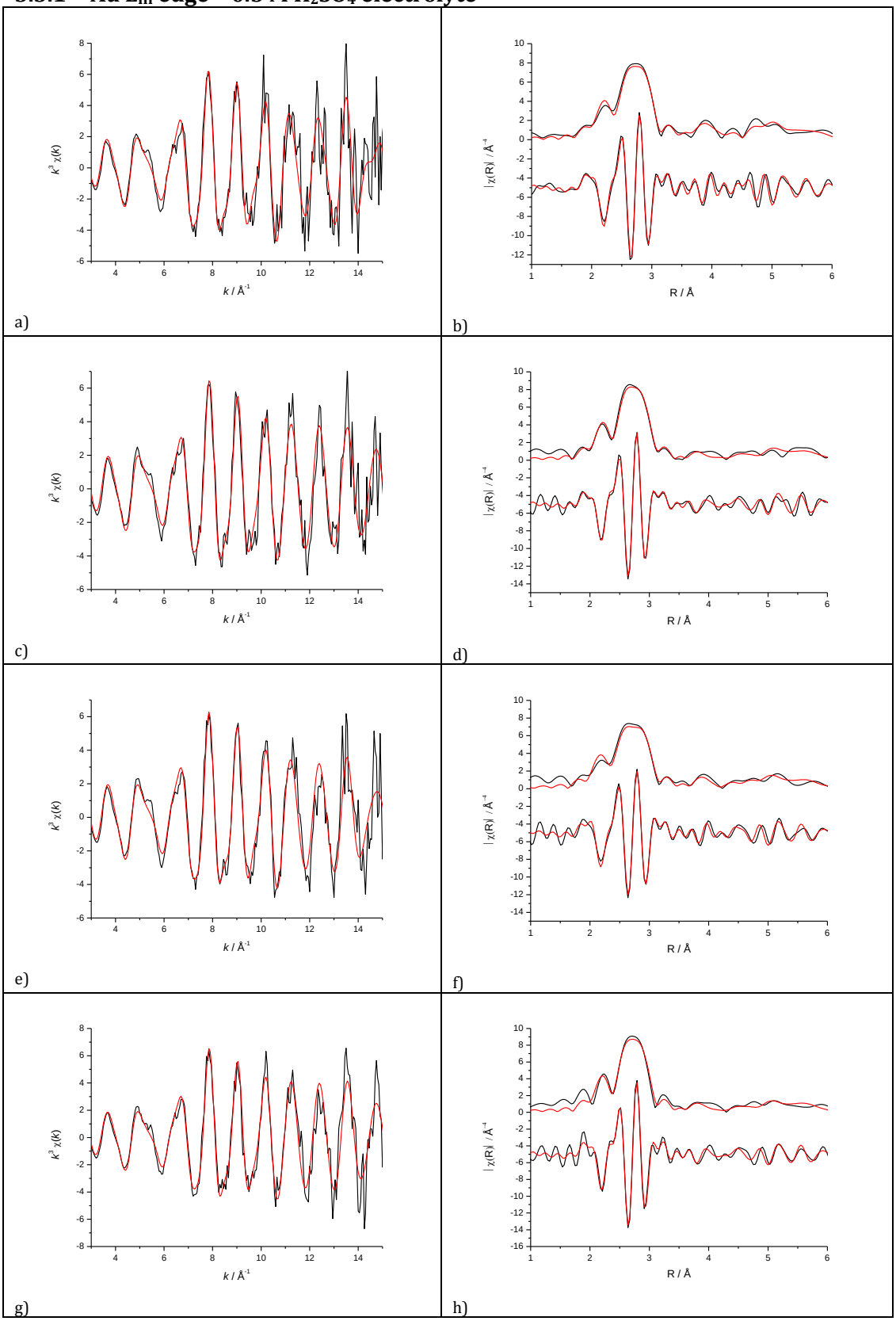

Figure 10: k^3 weighted Au L_{III} edge experimental data (black) and fit (red), along with k^3 weighted magnitude and real Fourier transform for 4 wt% Au/C on 1.32 cm² electrode in 0.5 M H_2SO_4, *in situ* EXAFS cell used, at a-b) +0.20 V, c-d) -0.21 V, e-f) -0.42 V and at g-h) -0.51 V.

Table 1a: Structural parameters for room temperature 4 wt% Au/C nanoparticles at +0.20 and -0.21 V in 0.5 M H_2SO_4 acquired at the Au L_{III} edge, corresponding to the data in Figure 10a-10d.

+0.20 V vs. ($Hg/HgSO_4$)					
Shell	***N***	***R* / Å**	**σ^2 / Å^2**	**ΔE_0 / eV**	**R_f**
Au-Au_1	10.33 ± 0.75	2.85 ± 0.01	0.0085 ± 0.0005	3.72 ± 0.45	0.033
Au-Au_2	0.68 ± 0.75	4.04 ± 0.01	0.0015 ± 0.0036		
Au-Au_3	11.27 ± 6.49	4.95 ± 0.01	0.0094 ± 0.0034		
Au-Au_4	7.19 ± 1.78	5.71 ± 0.01	0.0632 ± 0.2060		

-0.21 V vs. ($Hg/HgSO_4$)					
Shell	***N***	***R* / Å**	**σ^2 / Å^2**	**ΔE_0 / eV**	**R_f**
Au-Au_1	10.05 ± 0.64	2.85 ± 0.01	0.0081 ± 0.0004	5.03 ± 0.39	0.023
Au-Au_2	1.43 ± 1.39	4.03 ± 0.01	0.0082 ± 0.0071		
Au-Au_3	21.26 ± 13.10	4.93 ± 0.01	0.0150 ± 0.0048		
Au-Au_4	6.76 ± 1.51	5.70 ± 0.01	0.1005 ± 0.4462		

Table 1b: Structural parameters for room temperature 4 wt% Au/C nanoparticles at -0.42 and -0.51 V in 0.5 M H_2SO_4 acquired at the Au L_{III} edge, corresponding to the data in Figure 10e-10h.

-0.42 V vs. ($Hg/HgSO_4$)					
Shell	***N***	***R* / Å**	**σ^2 / Å^2**	**ΔE_0 / eV**	**R_f**
Au-Au_1	10.23 ± 0.74	2.85 ± 0.01	0.0086 ± 0.0005	4.57 0.42	0.026
Au-Au_2	0.64 ± 0.97	4.03 ± 0.01	0.0032 ± 0.0063		
Au-Au_3	21.15 ± 12.42	4.93 ± 0.01	0.0137 ± 0.0042		
Au-Au_4	7.34 ± 1.78	5.70 ± 0.01	0.0849 ± 0.3253		

-0.51 V vs. ($Hg/HgSO_4$)					
Shell	***N***	***R* / Å**	**σ^2 / Å^2**	**ΔE_0 / eV**	**R_f**
Au-Au_1	9.74 ± 0.66	2.85 ± 0.01	0.0078 ± 0.0004	4.25 ± 0.42	0.027
Au-Au_2	1.17 ± 1.35	4.02 v 0.01	0.0061 ± 0.0055		
Au-Au_3	21.46 ± 13.84	4.93 ± 0.01	0.0148 ± 0.0049		
Au-Au_4	6.17 ± 1.44	5.69 ± 0.01	0.0657 ± 0.2423		

The first shell coordination number (**Table 1a** and **b**) is 10.01 averaged over all four potential measurements. This is significantly larger than the average measured for the untreated 4 wt% Au/C sample obtained using the standard method (first shell coordination = 8.13) and the MD method (first shell coordination = 8.38) in Chapter Four. This increase is attributed to the effects of cycling the electrode prior to collecting the EXAFS data. Prior to the EXAFS measurements the prepared electrode was cycled in 0.5 M H_2SO_4 until there was no change in the oxide forming or stripping peaks (i.e. the scans overlaid). The cycling process can either cause aggregation of

nanoparticles in close proximity or dissolution of the smaller particles resulting in the increase in coordination numbers observed.

The ratio between the first and third shell coordination numbers at +0.20 V is near 1 due to the low third shell coordination. This low ratio is attributed to a flattening of the particles on the surface of the support[33]. At all negative potential measurements the third shell coordination number increases, with the ratio being above 2 which is attributed to a return to an approximately spherical particle shape.

The second shell proved difficult to fit in all cases, with both amplitude and disorder terms being small, and the respective errors large. As has been the case for most measurements reported in previous chapters, the disorder in the fourth coordination shell is abnormally large, attributed to termination effects caused by the under-coordination of the fourth shell.

Both Au-O and Au-S scattering paths could not be fitted to the data; therefore the cause of the poor fit could not be attributed to these paths. These scattering paths were considered because of the thiol used during the nanoparticle synthesis (that provided an improved fit for the untreated nanoparticles – Chapter Three), and the H_2SO_4 electrolyte. The lack of an Au-S scattering contribution indicates that the cycling removed all traces of thiol from the surface of the nanoparticles.

3.3.2 Au L_{III} edge – 0.5 M H_2SO_4 with 2 mM $CuSO_4$ electrolyte

The data collected at the Au L_{III} edge during the Cu deposition stage were fitted as in the previous section, with the exception of the +0.20 V measurement having a reduced *k* range of 3-14 $Å^{-1}$.

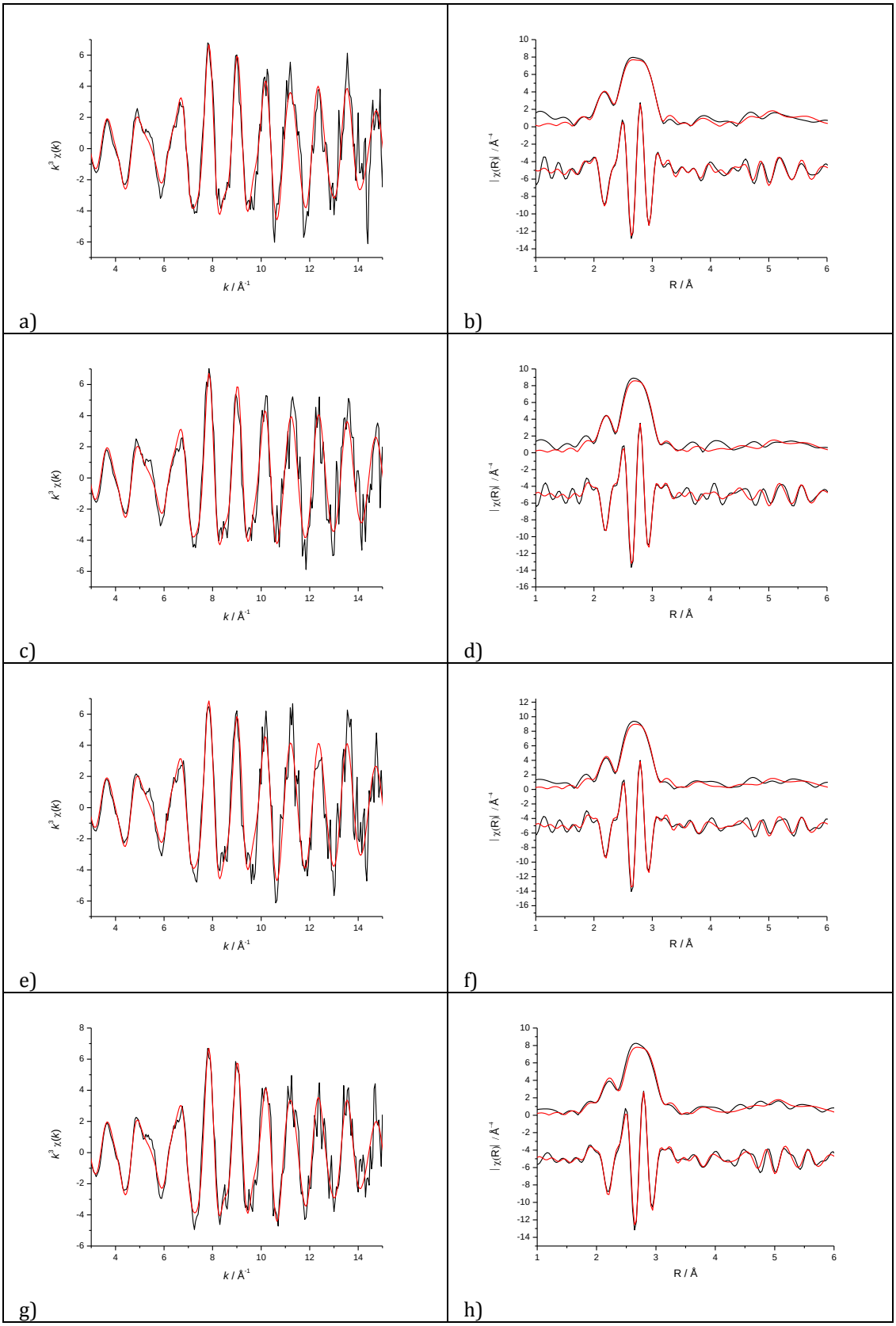

Figure 11: k^3 weighted Au L_{III} edge experimental data (black) and fit (red), along with k^3 weighted magnitude and real Fourier transform for 4 wt% Au/C on 1.32 cm² electrode in 0.5 M H_2SO_4 with 2 mM $CuSO_4$, *in situ* EXAFS cell used, at a-b) +0.20 V, c-d) -0.21 V, e-f) -0.42 V and at g-h) -0.51 V.

Table 2a: Structural parameters for room temperature 4 wt% Au/C nanoparticles at +0.20 and -0.21 V in 0.5 M H_2SO_4 and 2 mM $CuSO_4$ acquired at the Au L_{III} edge, corresponding to the data in Figure 11a-11d.

+0.20 V vs. ($Hg/HgSO_4$)					
Shell	***N***	***R* / Å**	**σ^2 / Å^2**	**ΔE_0 / eV**	**R_f**
Au-Au_1	10.48 ± 0.66	2.85 ± 0.01	0.0082 ± 0.0004	4.46 ± 0.39	0.018
Au-Au_2	1.74 ± 1.68	4.03 ± 0.01	0.0099 ± 0.0083		
Au-Au_3	13.83 ± 7.17	4.94 ± 0.01	0.0107 ± 0.0032		
Au-Au_4	7.92 ± 1.54	5.70 ± 0.01	0.0754 ± 0.2228		

-0.21 V vs. ($Hg/HgSO_4$)					
Shell	***N***	***R* / Å**	**σ^2 / Å^2**	**ΔE_0 / eV**	**R_f**
Au-Au_1	10.33 ± 0.75	2.85 ± 0.01	0.0081 ± 0.0005	4.28 ± 0.49	0.029
Au-Au_2	3.67 ± 3.96	4.03 ± 0.01	0.0183 ± 0.0179		
Au-Au_3	22.18 ± 14.88	4.94 ± 0.01	0.0158 ± 0.0053		
Au-Au_4	7.60 ± 1.76	5.70 ± 0.01	0.0926 ± 0.4229		

Table 2b: Structural parameters for room temperature 4 wt% Au/C nanoparticles at -0.42 and -0.51 V in 0.5 M H_2SO_4 and 2 mM $CuSO_4$ acquired at the Au L_{III} edge, corresponding to the data in Figure 11e-11h.

-0.42 V vs. ($Hg/HgSO_4$) in 0.5 M H_2SO_4 / 2 mM $CuSO_4$					
Shell	***N***	***R* / Å**	**σ^2 / Å^2**	**ΔE_0 / eV**	**R_f**
Au-Au_1	10.39 ± 0.75	2.85 ± 0.01	0.0079 ± 0.0004	3.67 ± 0.46	0.028
Au-Au_2	2.14 ± 2.09	4.03 ± 0.01	0.0090 ± 0.0065		
Au-Au_3	18.55 ± 13.13	4.94 ± 0.01	0.0136 ± 0.0051		
Au-Au_4	6.83 ± 1.65	5.70 ± 0.01	0.0685 ± 0.2584		

-0.51 V vs. ($Hg/HgSO_4$) in 0.5 M H_2SO_4 / 2 mM $CuSO_4$					
Shell	***N***	***R* / Å**	**σ^2 / Å^2**	**ΔE_0 / eV**	**R_f**
Au-Au_1	11.01 ± 0.71	2.85 ± 0.01	0.0087 ± 0.0004	4.39 ± 0.39	0.023
Au-Au_2	2.02 ± 1.98	4.03 ± 0.01	0.0097 ± 0.0071		
Au-Au_3	20.56 ± 9.88	4.94 ± 0.01	0.0126 ± 0.0033		
Au-Au_4	8.16 ± 1.79	5.70 ± 0.01	0.0981 ± 0.3770		

As was the case with the Au L_{III} edge measurements in acid, the particles appear flattened out on the support at positive potentials, and more spherical at negative potentials, although the errors associated with the third shell coordination number are somewhat higher. Again the second shell coordination number proves difficult to fit and the error in the fourth shell disorder remains high.

Au-O and/or Au-S scattering paths were fitted to all data sets again, but made no physically realistic improvements to the fits (i.e. negative amplitudes or disorder terms), but much more interestingly, the addition of an Au-Cu first shell scattering path also failed to produce a physically realistic fit. The upper *k* limit was reduced to minimise the Au relative contribution and increase Cu relative contribution to the backscattering amplitude (in case the Au-Au signal was dominating any Au-Cu contribution) but this also resulted in no change to either the overall fit quality or the physical viability of the scattering path. The absence of a Cu contribution will be discussed in more depth after the Cu K edge data is presented below.

3.3.3 Cu K edge – 0.5 M H_2SO_4 with 2 mM $CuSO_4$ electrolyte

The data were fitted using the standard method detailed in Chapter Three, between 1-3 Å in *R*, 3-11 $Å^{-1}$ in *k*, with multiple *k*-weighting. A Cu foil reference was measured, as was a 2 mM $CuSO_4$ reference sample. An S_0^2 of 0.82 ± 0.20 was determined from solution reference sample and 0.89 ± 0.05 from the Cu foil. Fitting models were based on a *fcc* Cu foil and a *fcc* 1:1 Cu:Au alloy for the potentials corresponding to Cu UPD, and an octahedral Jahn-Teller distorted $Cu(H_2O)_6$ solvated copper ion[34-36] for the Cu^{2+} in the electrolyte.

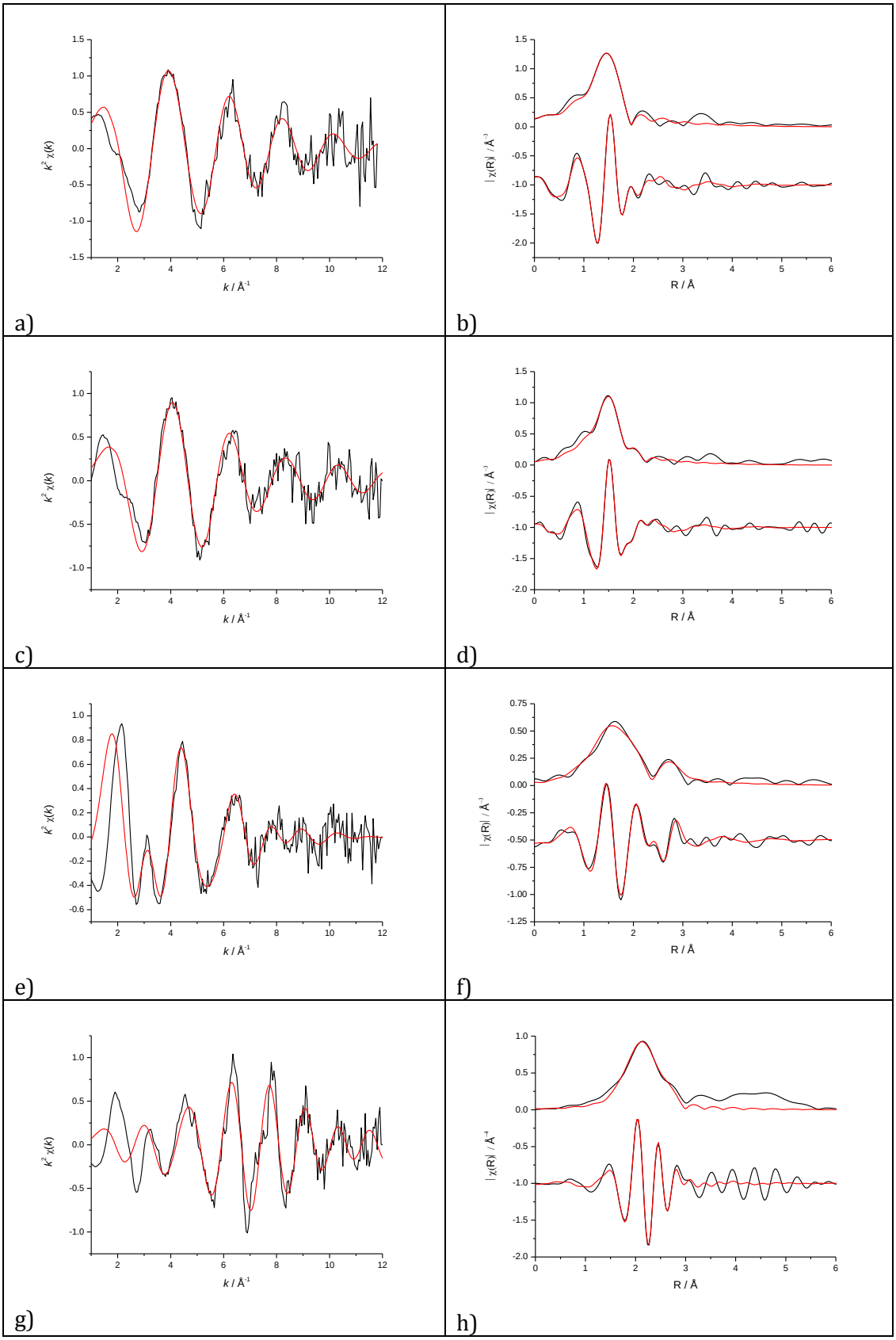

Figure 12: k^2 weighted Cu K edge experimental data (black) and fit (red), along with k^2 weighted magnitude and real Fourier transform for 4 wt% Au/C on 1.32 cm² electrode in 0.5 M H_2SO_4 with 2 mM $CuSO_4$, *in situ* EXAFS cell used, at a-b) +0.20 V, c-d) -0.21 V e-f) -0.42 V and at g-h) -0.51 V.

Table 3: Structural parameters for room temperature 4 wt% Au/C nanoparticles at +0.20 to -0.51 V in 0.5 M H_2SO_4 and 2 mM $CuSO_4$ acquired at the Cu K edge, corresponding to the data in Figure 12a-12h.

+0.20 V vs. ($Hg/HgSO_4$)					
Shell	***N***	***R* / Å**	**σ^2 / Å^2**	**ΔE_0 / eV**	**R_f**
Cu-O_{eq}	4.52 ± 1.82	1.96 ± 0.02	0.0070 ± 0.0031	-7.45 ± 2.59	0.010
Cu-O_{ax}	2.26 ± 0.91	2.33 ± 0.04	0.0063 ± 0.0065		

-0.21 V vs. ($Hg/HgSO_4$)					
Shell	***N***	***R* / Å**	**σ^2 / Å^2**	**ΔE_0 / eV**	**R_f**
Cu-O_{eq}	3.22 ± 0.34	1.94 ± 0.01	0.0046 ± 0.0014	-5.76 ± 1.38	0.010
Cu-O_{ax}	1.96 ± 0.17	2.50 ± 0.04	0.0058 ± 0.0063		

-0.42 V vs. ($Hg/HgSO_4$)					
Shell	***N***	***R* / Å**	**σ^2 / Å^2**	**ΔE_0 / eV**	**R_f**
Cu-O	2.32 ± 0.91	1.93 ± 0.02	0.0219 ± 0.0047	-0.97 ± 2.18	0.037
Cu-Cu	---	---	---		
Cu-Au	6.44 ± 2.41	2.60 ± 0.03	0.0219 ± 0.0053		

-0.51 V vs. ($Hg/HgSO_4$)					
Shell	***N***	***R* / Å**	**σ^2 / Å^2**	**ΔE_0 / eV**	**R_f**
Cu-O	---	---	---	-4.25 ± 3.08	0.024
Cu-Cu	2.63 ± 1.07	2.49 ± 0.02	0.0104 ± 0.0039		
Cu-Au	2.20 ± 1.09	2.59 ± 0.03	0.0073 ± 0.0038		

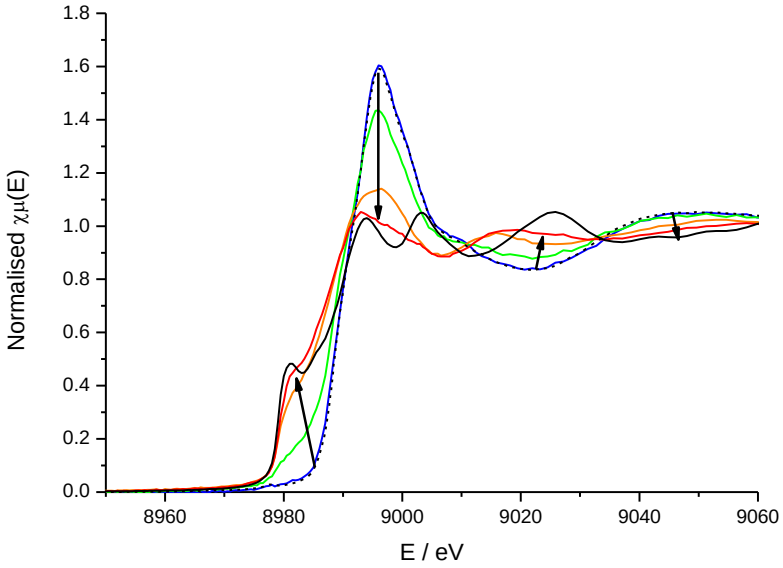

Figure 13: Cu K edge XANES. 2 mM CuSO4 reference solution (···), +0.20 V (—), -0.21 V (—), -0.42 V (—), -0.51 V (—) and Cu foil (—). Black arrows indicate change in edge features with decreasing potential .

The XANES region of the Cu K edge spectrum shows a clear change in the oxidation state of the Cu as the potential is decreased, corresponding to reduction from Cu^{2+} to Cu^{0} (**Figure 13**). Linear combination fitting (LCF) was performed using Athena[37] between -50 and +200 eV over the Cu K absorption edge (8979 eV) and between 50 to 400 eV beyond the edge (**Table 4**). The presence of a pre-edge shoulder (attributed to metallic Cu) required a Cu foil for LCF of the XANES; however beyond the absorption edge, the relative proportions determined by the LCF changed corresponding to less Cu^{0} than that inferred by the pre-edge peak. The lack of a CuAu alloy reference sample hinders the fitting to standards for the -420 mV and -510 mV measurements where Cu-Au neighbours are expected, however the Cu foil was still used to account for the presence of metallic Cu. The intensity of the EXAFS oscillations for a few atomic layers of Cu is far less than that for bulk Cu. Consequently, the amplitude of the EXAFS oscillations for the -510 mV measurements are more similar to those of the $CuSO_4$ reference sample, even though EXAFS analysis only fits to metallic Cu. Therefore such LCF analysis is presently limited in its usefulness for this system. It has previously been reported[13,14] that the adsorption of the Cu^{2+} ion onto the metal surface does not fully discharge to Cu^{0}, and therefore XANES analysis alone won't be able to quantify the relative amount of metallic copper on the surface.

Table 4: Linear combination fitting results for Cu K edge data showing relative weighting to each reference sample

Potential XAS measured at / V vs. ($Hg/HgSO_4$)	Fitting range			
	-50 to 200 eV (XANES)		50 to 400 eV (EXAFS)	
	2 mM $CuSO_4$ in 0.5 M H_2SO_4	Cu Foil	2 mM $CuSO_4$ in 0.5 M H_2SO_4	Cu Foil
+0.20	>0.99	<0.01	>0.99	<0.01
-0.21	0.69	0.31	0.95	0.05
-0.42	0.21	0.79	0.87	0.13
-0.51	0.03	0.97	0.56	0.44

Previous EXAFS studies of Cu UPD on bulk Au surfaces have focussed only on the Cu K edge since the Au-Au first shell contribution from bulk Au would dominate over any Au-Cu contributions, making determination of the Au-Cu coordination impossible. Even for nanoparticles that are expected to have a reduced first shell coordination number (and therefore the detection of an Au-Cu scattering path becomes more likely) the lack of any Au-Cu contribution in the Au L_{III} edge measurements highlights the difficulties.

The ordered structures proposed for Cu deposition on Au single crystal surfaces[2,14] were used as the initial fitting models, however these did not give realistic EXAFS fit results. On a single crystal surface (for example Au(111)) a mixed Cu and SO_4^{2-} adlayer is expected to form[14] at around -0.21 V. This adlayer would have no Cu-Cu first shell neighbours but Cu-O (from the sulphate) and Cu-Au would be present. Decreasing the potential to -0.42 V would result in a complete Cu monolayer forming on the crystal surface, with sulphate atop the Cu[2,3]. Theoretically there should now be Cu-O, Cu-Cu and Cu-Au contributions to the first shell. Finally, at the bulk deposition potential, Cu-Cu contributions will begin to dominate over any Cu-O and Cu-Au contributions.

4 Discussion

The initial aim of the study presented in this chapter was to measure the surface disorder of the Au nanoparticles by capping the surface with a second metal. The lack of any Cu neighbours in the Au L_{III} edge EXAFS means this is not possible. It is possible that the Cu solution was not able to penetrate the electrode fully and therefore the bottom layers of the Au nanoparticles remained un-capped by Cu. A much lower Au

loading on the electrode would decrease the thickness and therefore any contribution to the EXAFS from un-capped Au nanoparticles, and increase the sensitivity towards Au-Cu scattering. The shape of the Au nanoparticles is potential dependent, with reorganisation of the Au nanoparticles between +0.20 V and -0.21 V. This restructuring may result in a loss of structural sensitivity from the Au perspective as the surface of the nanoparticle may be different between one cycle and the next.

Analysis of the Cu K edge EXAFS measured at +0.20 V is consistent with an octahedrally coordinated Cu^{2+} ion. The analysis at -0.21 V reveals the presence of Cu-O first shell neighbours but no Cu-Au or Cu-Cu, in contrast to previously reported studies for bulk Au[2]. The Cu-O contributions fitted reasonably well to the octahedral solvated Cu^{2+} model, although the pre-edge region of the XANES has a Cu^0 component – up to 30% based on the LCF. No Cu^0 could be fitted to the EXAFS, suggesting that the proportion of Cu^0 deposited on the surface was too small to be detected in relation to the Cu^{2+} in solution. Attempts to fit Cu-Au and Cu-Cu failed resulting in negative coordination numbers and/or disorder terms.

The presence of both Cu-Au and Cu-O first shell neighbours is expected for the EXAFS measured at -0.42 V with a Cu monolayer on the Au surface, the sulphate groups forming an adlayer with the deposited Cu and solvated Cu^{2+} still in solution. The quantity and quality of available data prohibits determination of the exact nature of the Cu-O environment (limited by the Nyquist criterion).

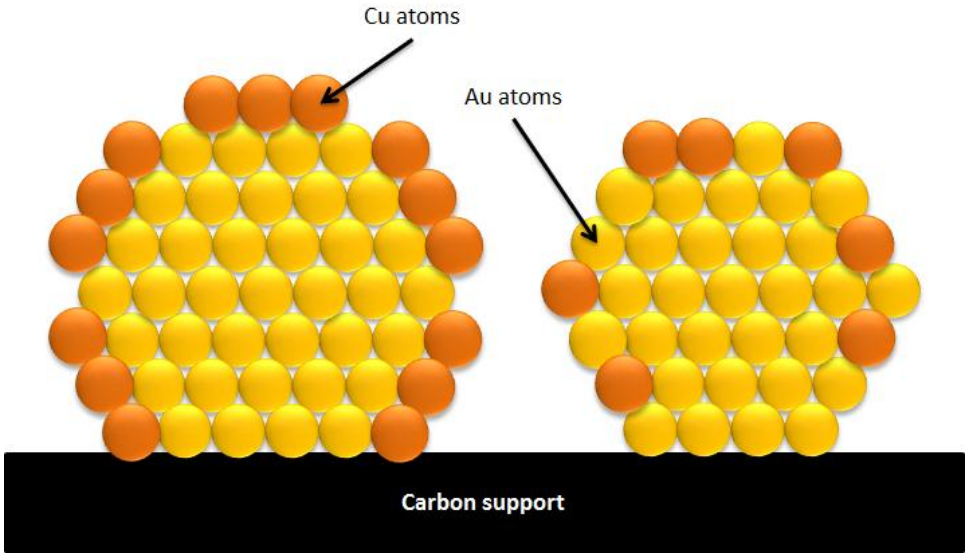

Figure 14: Schematic of Cu deposition on Au nanoparticle based on complete outer shell (left) and incomplete outer shell (right).

Previous Cu UPD studies have used a single crystal surface e.g. Au (111)[2,3]. Being a bulk crystal, any possible defects have less effect on the overall Cu deposition. Directly transferring the UPD method to nanoparticles, relies on the assumption of a complete outer shell of atoms for each nanoparticle (all with perfect crystal faces e.g. Au (111) for icosahedral particle). Real nanoparticles rarely have complete outer shells and therefore each face of the nanoparticle surface will contain defects. The large Cu-Au first shell and lack of Cu-Cu first shell coordination numbers for the -0.42 V measurement are attributed to the Cu preferentially depositing in these defects, thus minimising the surface energy of the nanoparticle by completing the outer shell of atoms (**Figure 14**). Consequently the Cu will have a far higher Au first shell coordination number (Cu-Au contribution) and far lower Cu first shell coordination number (Cu-Cu contribution) than if on a perfect surface. This also means that the corresponding Au L_{III} edge measurement will have a much lower Au-Cu coordination number due to the decreased amount of Cu present. The lack of a detectable Au-Cu first shell coordination number for the Au L_{III} edge measurements taken at -0.42 V is consistent with this analysis. The Cu-Au coordination number of 6.44 ± 2.41 is also comparable to that of alloyed Cu-Au, suggesting that a surface alloy may be formed as these surface defect sites are occupied. The charge calculated from the stripping peak (**Figure 9**) equates to only a 44% surface coverage by the Cu, consistent with the incomplete coverage observed in the EXAFS data.

The EXAFS collected with the potential held at -0.51 V corresponds (theoretically) to the deposition of more than one layer of Cu atoms. The corresponding Au-Cu coordination numbers should therefore be the same as the Cu-Au first shell, if coverage was complete in 3-fold sites; the surface even of a perfect icosahedral nanoparticle however does not consist of only 3-fold sites. A Cu-Au first shell coordination number of 3 would be expected if deposition occurred in a 3-fold site; a coordination number of 2 would be expected if in a 2-fold bridged site and a Cu-Au first shell coordination number of only 1 if directly atop an Au atom. The uncertainty in the coordination numbers measured (**Table 3**) could put the actual value between 1 and 3 for both Cu-Cu and Cu-Au making it not possible to distinguish between the various possible Cu deposition sites on the surface of the Au nanoparticle. However a reduced coverage on a larger Au nanoparticle would result in a marked decrease in Au-Cu first shell coordination number. Given the inability to fit an Au-Cu first shell neighbour for the Au L_{III} edge measurements, it is concluded that the Cu coverage, even at the bulk deposition potential, is very low. The number of counts for the Au measurements is at

least four times the number recorded for the Cu measurements confirming that much more Au is present than Cu, even at -0.51 V where bulk deposition of Cu is occurring.

The inability to fit an Au-Cu scattering path to the EXAFS collected at the Cu bulk deposition potential, and the Cu-Cu first shell coordination number of 2.63 ± 1.07 indicate that the Cu may be clustering together in areas on the Au nanoparticle surface instead of forming a more evenly distributed shell around the Au. When combined with the charge calculated from the stripping peak in **Figure 9**, it is concluded that enough Cu was deposited to completely cover the Au surface. However if bulk deposition had occurred, the Cu-Cu first shell coordination number would be far higher. Therefore it is concluded that the Cu deposition did not form a uniform monolayer but partially covered the Au nanoparticle surface, initially as clusters of Cu atoms.

5 Conclusions

The use of UPD was initially intended as a means to investigate the contribution of the surface disorder to the EXAFS signal. Although a Au-Cu bond is not identical to an Au-Au bond, complete coverage would ensure all Au atoms were fully coordinated to metal atoms and therefore behave in a similar way to atoms in the core of the nanoparticle. The difference in the Au-Au disorder calculated from the EXAFS between the Au core and the Au with a Cu capped surface would be attributed to the surface Au atoms, giving an indication of the extent of the surface disorder contribution to the overall EXAFS signal determined.

This was based on several assumptions, all of which have been challenged by the results reported in this chapter: a) deposition on nanoparticles occurs in the same manner as on a single crystal surface, and b) the nanoparticles are all evenly sized, geometric structures with complete outer shells and therefore defined crystal faces. Before starting out these assumptions were known to be ideal cases, but the degree to which the results indicate the assumptions are overly-idealised was not expected, and illustrates the need for far more detailed studies into underpotential deposition on nanoparticles.

6 References

(1) Tamura, K.; Oyanagi, H.; Kondo, T.; Koinuma, M.; Uosaki, K. *The Journal of Physical Chemistry B* **2000**, *104*, 9017.

(2) Lee, J. R. I.; O'Malley, R. L.; O'Connell, T. J.; Vollmer, A.; Rayment, T. *The Journal of Physical Chemistry C* **2009**, *113*, 12260.

(3) Blum, L.; Abruna, H. D.; White, J.; Gordon, J. G.; Borges, G. L.; Samant, M. G.; Melroy, O. R. *Journal of Chemical Physics* **1986**, *85*, 6732.

(4) Calvin, S.; Miller, M. M.; Goswami, R.; Cheng, S. F.; Mulvaney, S. P.; Whitman, L. J.; Harris, V. G. *Journal of Applied Physics* **2003**, *94*, 778.

(5) Frenkel, A. I. *Journal of Synchrotron Radiation* **1999**, *6*, 293.

(6) Russell, A. E.; Rose, A. *Chemical Reviews* **2004**, *104*, 4613.

(7) Rose, A.; Bilsborrow, R.; King, C. R.; Ravikumar, M. K.; Qian, Y.; Wiltshire, R. J. K.; Crabb, E. M.; Russell, A. E. *Electrochimica Acta* **2009**, *54*, 5262.

(8) Rose, A.; Crabb, E. M.; Qian, Y.; Ravikumar, M. K.; Wells, P. P.; Wiltshire, R. J. K.; Yao, J.; Bilsborrow, R.; Mosselmans, F.; Russell, A. E. *Electrochimica Acta* **2007**, *52*, 5556.

(9) Crabb, E. M.; Ravikumar, M. K.; Thompsett, D.; Hurford, M.; Rose, A.; Russell, A. E. *Physical Chemistry Chemical Physics* **2004**, *6*, 1792.

(10) Roscioni, O. M.; Zonias, N.; Price, S. W. T.; Russell, A. E.; Comaschi, T.; Skylaris, C.-K. *Physical Review B* **2011**, *83*, 115409.

(11) Huang, W. J.; Sun, R.; Tao, J.; Menard, L. D.; Nuzzo, R. G.; Zuo, J. M. *Nature Materials* **2008**, *7*, 308.

(12) Yevick, A.; Frenkel, A. I. *Physical Review B* **2010**, *81*, 115451.

(13) Omar, I. H.; Pauling, H. J.; Juttner, K. *Journal of The Electrochemical Society* **1993**, *140*, 2187.

(14) Toney, M. F.; Howard, J. N.; Richer, J.; Borges, G. L.; Gordon, J. G.; Melroy, O. R.; Yee, D.; Sorensen, L. B. *Physical Review Letters* **1995**, *75*, 4472.

(15) Cadle, S. H.; Bruckenstein, S. *Analytical Chemistry* **1971**, *43*, 932.

(16) Tindall, G. W.; Bruckenstein, S. *Analytical Chemistry* **1968**, *40*, 1051.

(17) Gerischer, H.; Kolb, D. M.; Przasnyski, M. *Surface Science* **1974**, *43*, 662.

(18) Kolb, D. M.; Gerischer, H. *Surface Science* **1975**, *51*, 323.

(19) Kolb, D. M.; Przasnyski, M.; Gerischer, H. *Journal of Electroanalytical Chemistry and Interfacial Electrochemistry* **1974**, *54*, 25.

(20) Magnussen, O. M.; Hotlos, J.; Nichols, R. J.; Kolb, D. M.; Behm, R. J. *Physical Review Letters* **1990**, *64*, 2929.

(21) Shi, Z.; Lipkowski, J. *Journal of Electroanalytical Chemistry* **1994**, *365*, 303.

(22) Nakamura, M.; Endo, O.; Ohta, T.; Ito, M.; Yoda, Y. *Surface Science* **2002**, *514*, 227.

(23) Oviedo, O. A.; Mariscal, M. M.; Leiva, E. P. M. *Electrochimica Acta* **2010**, *55*, 8244.

(24) Zhang, G.; Kuang, Y.; Liu, J.; Cui, Y.; Chen, J.; Zhou, H. *Electrochemistry Communications* **2010**, *12*, 1233.

(25) Tang, H.; Chen, J. H.; Wang, M. Y.; Nie, L. H.; Kuang, Y. F.; Yao, S. Z. *Applied Catalysis A: General* **2004**, *275*, 43.

(26) Zhang, J.; Vukmirovic, M. B.; Xu, Y.; Mavrikakis, M.; Adzic, R. R. *Angewandte Chemie International Edition* **2005**, *44*, 2132.

(27) Zhang, J.; Mo, Y.; Vukmirovic, M. B.; Klie, R.; Sasaki, K.; Adzic, R. R. *The Journal of Physical Chemistry B* **2004**, *108*, 10955.

(28) Zhang, J.; Lima, F. H. B.; Shao, M. H.; Sasaki, K.; Wang, J. X.; Hanson, J.; Adzic, R. R. *The Journal of Physical Chemistry B* **2005**, *109*, 22701.

(29) Shao, M.; Sasaki, K.; Marinkovic, N. S.; Zhang, L.; Adzic, R. R. *Electrochemistry Communications* **2007**, *9*, 2848.

(30) Knupp, S.; Vukmirovic, M.; Haldar, P.; Herron, J.; Mavrikakis, M.; Adzic, R. *Electrocatalysis* **2010**, *1*, 213.

(31) Brankovic, S. R.; Wang, J. X.; Adzic, R. R. *Surface Science* **2001**, *474*, L173.

(32) Ravel, B.; Kelly, S. D. *X-Ray Absorption Fine Structure-XAFS13* **2007**, *882*, 150.

(33) Jentys, A. *Physical Chemistry Chemical Physics* **1999**, *1*, 4059.

(34) Benfatto, M.; D'Angelo, P.; Della Longa, S.; Pavel, N. V. *Physical Review B* **2002**, *65*, 174205.

(35) Inada, Y.; Ozutsumi, K.; Funahashi, S.; Soyama, S.; Kawashima, T.; Tanaka, M. *Inorganic Chemistry* **1993**, *32*, 3010.

(36) Korshin, G. V.; Frenkel, A. I.; Stern, E. A. *Environmental Science & Technology* **1998**, *32*, 2699.

(37) Ravel, B.; Newville, M. *Journal of Synchrotron Radiation* **2005**, *12*, 537.

CHAPTER SEVEN:

CONCLUSIONS AND FUTURE WORK

The principal aim of this thesis has been to improve the characterisation of nanoparticle catalysts in order to aid in the understanding of the particle size effect, beginning with an initial assessment of three key techniques (TEM, XRD, EXAFS), highlighting their strengths and weaknesses and to provide a framework to enable quantitative comparison of the particle size (distributions) obtained using each method. Several of the assumptions underlying EXAFS analysis were then addressed in depth through the application of molecular dynamics to both monometallic and bimetallic systems.

Chapter One described the particle size effect, the importance of understanding nanoparticle catalyst size and how it is determined. The need for cross-correlation of analytical techniques if one wishes to fully understand a nanoparticle system was highlighted in **Chapter Three**. Each technique offers a different approach to imaging a given sample, each with its own strengths and limitations. Understanding how TEM, XRD and EXAFS may be used to calculate average particle size allows for a rational comparison between the techniques, particularly useful if only one technique has been used for size determination. XRD is limited as a method of size determination for nanoparticles below 5 nm, as a result of the lack of long range order. In particular, the amorphous surface layer present on oxidised or core-shell nanoparticles is not directly detectable by XRD. TEM coupled with EDX proved to be a useful technique to compliment the XRD analysis, in particular for identification of amorphous regions and the composition of surface layers. Recent studies have shown the degree of surface contraction present in nanoparticles[1-3]; the current standard method of EXAFS analysis does not account for the degree of distortion present and, therefore, introduces a systematic error into the determination of coordination number, underestimating particle size. The effect of this was highlighted by comparing the average particle sizes determined by the three techniques used.

Chapters Four and **Five** moved on to tackle the challenge posed by non-uniform bond length distributions, and proved that the consideration of surface disorder and termination effects must be considered to interpret accurately EXAFS data for nanoparticles. The RDF outputs from molecular dynamics simulations were

successfully introduced into the EXAFS analysis, resulting in changes in the quality of fit. On the whole there was an improvement in the quality of fit; however in some cases the quality decreased. One notable example would be the worse fit given by the use of the Gupta potential to model the Pt-Pt interactions. Both semi-empirical potentials used were derived from modelling bulk metal behaviour rather than nanoparticle behaviour and the worse fit from the Gupta potential was attributed to the potential failing to accurately model nanoparticle behaviour. The molecular dynamics approach to EXAFS analysis may be used as a means to evaluate the effectiveness of other semi-empirical potentials at modelling nanoparticle behaviour by simulating the same structural input and applying it to the data. As previously stated, the approach may be taken further still by using quantum mechanical modelling of nanoparticles to provide improved structural inputs.

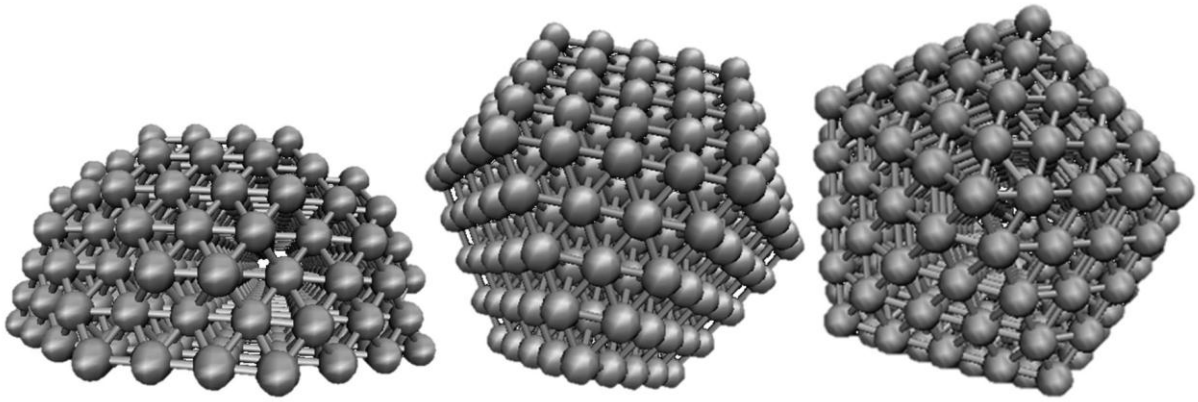

Figure 1: Hemispherical (387 atom), cuboctahedral (309 atom) and icosahedral (309 atom) Pt nanoparticles.

Figure 1 illustrates several potential nanoparticle geometries, and **Figure 2** the radial distribution functions corresponding to the nanoparticle structures (simulated using the Sutton-Chen potential). The icosahedral geometry in particular has a greatly distorted distribution with three clear peaks whilst the hemispherical and cuboctahedral geometries are less distorted (although still non-Gaussian). Use of these RDFs as inputs for the EXAFS analysis would be of great interest as an improved quality of fit from any one particular input would give an indication of particle geometry as well as size from the first shell alone. This could be taken further still by simulating the different geometries with other potentials to see the effect on the quality of fit.

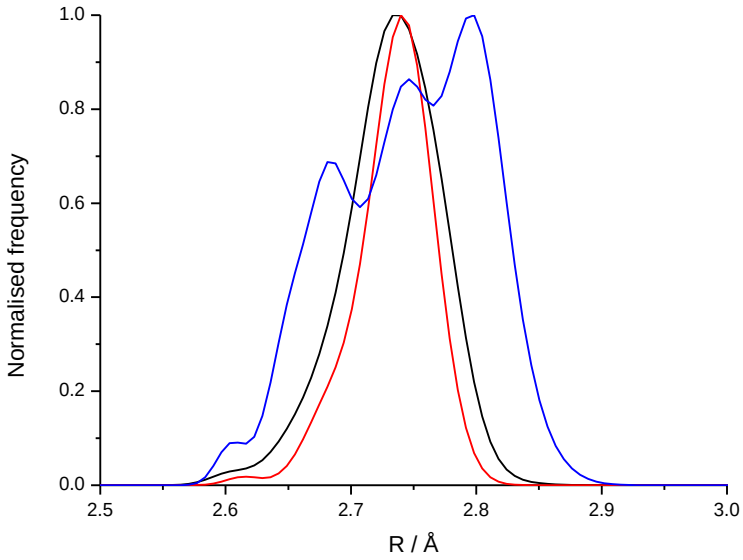

Figure 2: Radial distribution functions for hemispherical (—), cuboctahedral (—) and icosahedral (—) Pt nanoparticles based on diameters of approximately 2.50 nm.

Currently only the first coordination shell may be fitted using the input from the molecular dynamics simulations. The inclusion of higher coordination shells and multiple scattering effects would allow more structural information to be determined from the analysis and would extend the potential usefulness and number of applications of the approach.

The application of the approach to bimetallic systems is more complicated but possible. The implementation of the structural input is very similar to that for monometallic systems, the main difference being the number of different atom-atom interactions (i.e. four for a bimetallic system; Pt-Pt, Pt-Pd, Pd-Pt and Pd-Pd). However, as a result of the increased number of interactions, more so than with monometallic systems, the structural input for the molecular dynamics simulations is critically important. The bimetallic nanoparticles investigated were reasonably well defined core-shell structures, although they were neither completely spherical nor uniformly covered. This complicated the modelling of the interactions between the two metals. More work needs to be done investigating the effectiveness of other semi-empirical potentials at modelling the interatomic interactions, and also simulating different bimetallic structures, such as those proposed by Beale[4], and using these as structural inputs for the EXAFS fit.

With the UPD technique being increasingly used in the synthesis of core-shell nanoparticles[5,6], there is still very little structural characterisation of these structures. Similar to the assumptions in the standard analysis of EXAFS data, the understanding of the mechanism of UPD on nanoparticles is based on perfect crystalline structures and this clearly is not the case for real nanoparticles. Consequently the UPD of Cu on Au nanoparticles reported in **Chapter Six** failed to cap the core to provide an insight into the contribution to the disorder from the surface atoms, as was initially intended. The non-uniform nature of the surface structure of the nanoparticles was apparent through the EXAFS analysis, indicating that structural characterisation UPD on nanoparticles merits further investigation. One potential route is AFM characterisation of the UPD adlayers on nanoparticles, similar to the characterisation of Cu UPD on the Au (111) surface by Toney *et al*.[7] AC-STEM coupled with EDX would help provide direct information on the location and uniformity of the Cu coverage for both the monolayer and bulk deposition (cf. Pt/Pd/C nanoparticles in **Chapter Five**).

This work has shown that nanoparticles are more structurally complex than their bulk material counterparts, and this complexity needs to be accounted for to ensure accurate structural characterisation. The application of molecular dynamics to the interpretation of EXAFS data has been practically demonstrated, resulting in an improved quality of fit to the data. The further development of this technique holds promise for more complete morphological determination from EXAFS data alone.

1 References

(1) Roscioni, O. M.; Zonias, N.; Price, S. W. T.; Russell, A. E.; Comaschi, T.; Skylaris, C.-K. *Physical Review B* **2011**, *83*, 115409.

(2) Yevick, A.; Frenkel, A. I. *Physical Review B* **2010**, *81*, 115451.

(3) Huang, W. J.; Sun, R.; Tao, J.; Menard, L. D.; Nuzzo, R. G.; Zuo, J. M. *Nature Materials* **2008**, *7*, 308.

(4) Beale, A. M.; Weckhuysen, B. M. *Physical Chemistry Chemical Physics* **2010**, *12*, 5562.

(5) Knupp, S.; Vukmirovic, M.; Haldar, P.; Herron, J.; Mavrikakis, M.; Adzic, R. *Electrocatalysis* **2010**, *1*, 213.

(6) Zhang, J.; Lima, F. H. B.; Shao, M. H.; Sasaki, K.; Wang, J. X.; Hanson, J.; Adzic, R. R. *The Journal of Physical Chemistry B* **2005**, *109*, 22701.

(7) Toney, M. F.; Howard, J. N.; Richer, J.; Borges, G. L.; Gordon, J. G.; Melroy, O. R.; Yee, D.; Sorensen, L. B. *Physical Review Letters* **1995**, *75*, 4472.

APPENDIX

1 XANES Observations

An interesting change in the white-line was observed in the XANES regions of all the Pt measurements run using the cryostat. There was a reduction in intensity and a broadening of the white line when comparing the spectra between the 300 K measurements and the cooled measurements (**Figure 1**, dotted arrows between black and red lines).

Theoretical studies by Ankudinov on the multiple scattering contributions to the XANES region of the absorption spectrum have been published[1,2]. They proposed that a large number of multiple scattering contributions from short bonds (such as the "rattle" multiple scattering path where the photoelectron scattering between the absorber an atom in the first coordination shell twice - Pt_{abs}-Pt_1-Pt_{abs}-Pt_1-Pt_{abs}) lead to a strong white line intensity.

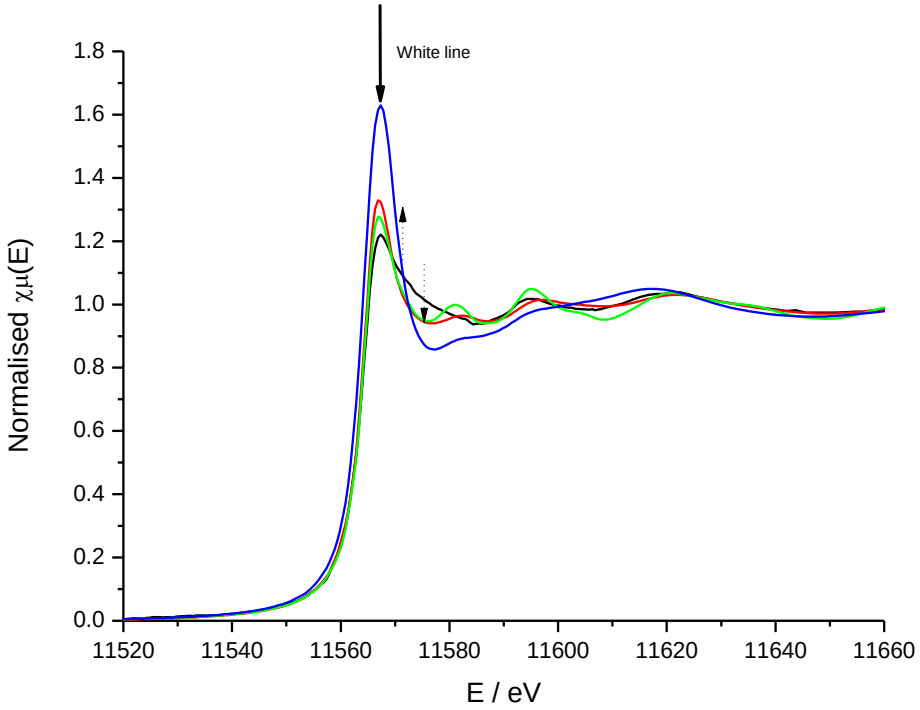

Figure 1: Change in Pt L_{III} XANES spectrum as dependent on oxidation state of Pt; hydrogen reduced Pt nanoparticles (black line), Pt nanoparticles under vacuum conditions (red line), oxidised Pt nanoparticles (blue line), and Pt foil (green line). Solid arrow indicates white line and dotted arrows the observed changes in the XANES shape.

Given the termination effects present in the fourth coordination shell, it was initially thought the change in the XANES was a result of a change in multiple scattering contributions with respect to temperature, i.e. a freezing of the structure at lower temperatures enhancing the aforementioned contribution. A full multiple scattering analysis was performed and showed no change, indicating that this was not the case.

The intensity of the "white line" above the Pt L_{III} absorption edge correlates to the d-band vacancies of the Pt[3]. The more oxidised the Pt is, the more intense the white line feature. An intense white line complicates background removal during the EXAFS processing stage, and therefore reducing the Pt with H_2 greatly reduces the white line and amongst other factors helps simplify the background removal. **Figure 1** illustrates the change in white line intensity at 300 K between fully oxidised and reduced Pt nanoparticle samples, a nanoparticle sample under vacuum in the cryostat with the observed difference in the XANES, as well as comparing these with a Pt foil. The Pt foil has a small oxide layer (Pt-O) on the surface, but the proportion of oxidised atoms with respect to the whole sample is so small (the majority being metallic Pt) the effect on the white line is negligible. The reduced Pt nanoparticles exhibit a less intense white line than a bare Pt foil, with an increased absorption in the region of 11570-11580 eV. The amplitude of the oscillations over and beyond the edge for the nanoparticle is damped with respect to the foil, as has been reported by Ankudinov *et al*[4] and Bus[5].

A series of theoretical calculations[6-8] have been carried out modelling the XANES of both bare Pt and Pt-H; the features present in these spectra are in good agreement with the features observed in **Figure 1**. It is proposed that the change observed in the XANES region is the result of hydrogen desorbing from the Pt surface once the cryostat vacuum unit has been activated. A similar effect has been observed by Ramaker *et al*[9], but in their study flowing He (instead of a vacuum) was used to intentionally remove the chemisorbed hydrogen. Whilst there is some debate[10,11] as to the exact nature of the hydrogen atop the Pt surface, the results presented here confirm the effect chemisorbed hydrogen has on Pt XANES.

2 References

(1) Ankudinov, A. L.; Ravel, B.; Rehr, J. J.; Conradson, S. D. *Physical Review B* 1998, *58*, 7565.

(2) Ankudinov, A. L. *Journal of Synchrotron Radiation* 1999, *6*, 236.

(3) Lytle, F. W.; Wei, P. S. P.; Greegor, R. B.; Via, G. H.; Sinfelt, J. H. *Journal of Chemical Physics* 1979, *70*, 4849.

(4) Ankudinov, A. L.; Rehr, J. J.; Low, J. J.; Bare, S. R. *Journal of Chemical Physics* 2002, *116*, 1911.

(5) Bus, E.; van Bokhoven, J. A. *The Journal of Physical Chemistry C* 2007, *111*, 9761.

(6) Ankudinov, A. L.; Rehr, J. J.; Low, J. J.; Bare, S. R. *Journal of Synchrotron Radiation* 2001, *8*, 578.

(7) Ankudinov, A. L.; Rehr, J. J.; Low, J. J.; Bare, S. R. *Physical Review Letters* 2001, *86*, 1642.

(8) Asakura, K.; Kubota, T.; Chun, W. J.; Iwasawa, Y.; Ohtani, K.; Fujikawa, T. *Journal of Synchrotron Radiation* 1999, *6*, 439.

(9) Ramaker, D. E.; Mojet, B. L.; Garriga Oostenbrink, M. T.; Miller, J. T.; Koningsberger, D. C. *Physical Chemistry Chemical Physics* 1999, *1*, 2293.

(10) Ramaker, D. E.; Koningsberger, D. C. *Physical Review Letters* 2002, *89*, 139701.

(11) Ankudinov, A. L.; Rehr, J. J.; Low, J. J.; Bare, S. R. *Physical Review Letters* 2002, *89*, 139702.